



MONASH University

Precipitation of Sc-containing phases in Al-Si-Sc alloys

Jayshri Dumbre

M. Tech. in Process Engineering

Indian Institute of Technology (IIT) Bombay, India

A thesis submitted for the degree of Doctor of Philosophy

Department of Materials Science and Engineering

Monash University, Victoria, Australia

November 2020

Copyright notice

© The author (2020).

I certify that I have made all reasonable efforts to secure copyright permissions for third-party content included in this thesis and have not knowingly added copyright content to my work without the owner's permission.

Abstract

In a number of aluminium (Al) alloys to date, the addition of a small quantity of scandium (Sc) has revealed a significant and beneficial effect on strengthening due to the formation of nano-sized, coherent Al₃Sc precipitates. However, the strengthening response of the ternary Al-Si-Sc (4xxx series Al-alloys) and quaternary Al-Si-Mg-Sc (6xxx series Al-alloys) alloy systems has been hampered by an apparent unfavourable interaction between silicon (Si) and Sc; forming the deleterious V-phase (AlSc₂Si₂) and thus limiting the allowable Si content to ~ 0.15 wt. % for Sc-containing Al-alloys.

The present research was aimed at elucidating and understanding the evolution of phases that form due to the Si-Sc interaction in Al-alloys – whilst seeking ways to achieve enhanced alloy strength without compromising other properties (such as corrosion resistance).

Model Al-Si-Sc alloy compositions and heat treatment parameters were designed using CALPHAD (CALculation of PHase Diagrams). The production of model Al-Si-Sc alloy sheets with varying Si:Sc ratio was carried out by lab-scale casting and processing using a conventional route for wrought aluminium semi-products with T6 condition. The Si-Sc interaction was studied at various processing stages. Firstly, during the casting of model alloys, a difference in the precipitation of nano-sized (Al,Si)₃Sc phase was dependent on the Si content of the alloys. Secondly, during low-temperature homogenisation treatments (pre-heat treatment) which led to desirable, coherent (Al,Si)₃Sc spherical precipitates, hardening resulted depending on the Si to Sc ratio. Thirdly, upon a high-temperature solutionising treatment, the formation of rod-shaped and deleterious V-phase (AlSc₂Si₂) resulted, with an unrecoverable softening. *In situ* transmission electron microscopy (TEM) studies were conducted at the formation temperatures of (Al,Si)₃Sc and V-phase to study the respective precipitation mechanism. Various analytical techniques including electron microscopy, small-angle x-ray

scattering (SAXS), atom probe tomography (APT), precession electron diffraction (PED), and Vickers hardness testing were utilised to characterise the phases formed following the said processing conditions of the Sc-containing alloys.

Beyond this work, the comprehensive understanding of desirable and undesirable Si, Sc-containing phases will be useful to design suitable Al-Si-Mg-Sc alloy compositions and heat treatment conditions. This study indicates that there exists a compositional and processing window to design the future high strength Al-Si-Mg-Sc alloys. Co-precipitation of $(Al,Si)_3Sc$ and Mg_2Si in these alloys can be obtained by optimising the ageing heat treatment conditions below the V-phase nucleation temperature to avoid its formation and to maximise bulk mechanical properties.

Publications

Publications and their status

1. **Jayshri Dumbre**, Timothy Langan, Thomas Dorin, Nick Birbilis, “Optimised composition and process design to develop Sc-enhanced wrought Al-Si alloys”, *Light Metals*, 2019, pp. 1431-1438 (**Published** - Chapter 5)
2. **Jayshri Dumbre**, Shravan Kairy, Elaf Anber, Timothy Langan, Mitra L. Taheri, Thomas Dorin, Nick Birbilis, “Understanding the formation of $(Al,Si)_3Sc$ and V-phase $(AlSc_2Si_2)$ in Al-Si-Sc alloys via *ex situ* heat treatments and *in situ* transmission electron microscopy studies”, *Journal of Alloys and Compounds*, 861, 2021, 158511 (**Published** – Chapter 6)
3. **Jayshri Dumbre**, Lu Jiang, Daniel Foley, Timothy Langan, Mitra L. Taheri, Thomas Dorin, Nick Birbilis, “Effect of Si on $(Al,Si)_3Sc$ phase following low-temperature heat treatment of Al-Si-Sc alloys” (**ready for submission** – Chapter 7)

Publications in collaboration

1. S. K. Kairy, B. Rouxel, **J. Dumbre**, J. Lamb, T. J. Langan, T. Dorin, N. Birbilis, “Simultaneous improvement in corrosion resistance and hardness of a model 2xxx series Al-Cu alloy with the microstructural variation caused by Sc and Zr additions”, *Corrosion Science*, 158, 2019, 108095 (**Published**)

Conference presentations

1. Jayshri Dumbre, Timothy Langan, Thomas Dorin, Nick Birbilis, “Optimised composition and process design to develop Sc-enhanced wrought Al-Si alloys”, 148th TMS (The Minerals, Metals and Materials Society) Annual Meeting and Exhibition – 2019, March 10-14, 2019, San Antonio, Texas, USA
2. C. Salehi, J. Dumbre, P. Nakashima, N. Birbilis, “Exploring machine learning in the design of high strength aluminium alloys” 5th World Congress on Integrated Computational Materials Engineering (ICME 2019), July 21–25, 2019, Indianapolis, Indiana, USA.
3. Jayshri Dumbre, Shravan Kairy, Timothy Langan, Thomas Dorin, Nick Birbilis, ‘Understanding the formation of $(Al,Si)_3Sc$ and $AlSc_2Si_2$ phases in novel Al-Si-Sc alloys via the use of CALPHAD, electron microscopy and atom probe tomography’, CALPHAD-2019, Singapore, 2019.

Awards and recognitions

1. Winner of 3-minute thesis competition at 2020 Tri-University Research Workshop on Advanced Engineering.
2. Selected to represent Monash University at Borland Forum - 2020 to present PhD research work.
3. Certificate of participation for ‘Visualise Your Thesis (VYT 2020) – a one-minute video competition on the PhD work’ by Monash University, Australia.
4. Finalist of MGA (Monash Graduate Association) volunteer award in the category of ‘Leadership and Innovation’, 2019 for the contribution towards post-graduates at Monash University.
5. Recipient of Larry Kaufman scholarship award to attend and present PhD research work at CALPHAD – 2019, an international conference, Singapore
6. ‘Early career researcher award’ by Sparrho to attend and present PhD research work at TMS - 2019, an international conference, San Antonio, USA.
7. Recipient of Graduate Research International Travel Award (GRITA), 2019, Monash University, to conduct collaborative research with Drexel University, USA
8. Winner of MGA volunteer award in the category of ‘Exceptional Skills’, 2018.
9. First place for the best poster award at Materials Science and Engineering (MSE) summer conference - 2018, Monash University.

Positions held:

1. ‘Student representative’ on the Engineering Graduate Research Committee to represent student cohort at the Faculty of Engineering, Monash University, 2019-20.
2. ‘Student representative’ for the Materials Science and Engineering Department, Monash University, 2017-18.

Table of content

Abstract.....	iii
Publications.....	v
Awards and recognitions.....	vi
Table of content	vii
List of figures.....	x
List of tables.....	xiv
Thesis including published works declaration	xv
Acknowledgements.....	xvii
1 Introduction	1
2 Literature review.....	3
2.1 Al-Sc binary alloy system	3
2.2 Effects of Sc in Al-alloys	4
2.3 Precipitates evolution during processing.....	8
2.3.1 Casting process	9
2.3.2 Homogenisation treatment	10
2.3.3 Hot-working	17
2.4 Effect of Sc in multi-component systems	19
2.4.1 Commercially available Sc-bearing Al-alloys	19
2.4.2 Other beneficial elements	20
2.4.3 Other detrimental elements	20
2.5 Sc in Al-Si and Al-Mg-Si alloys	21
2.5.1 Precipitation of (Al,Si) ₃ Sc in Al-Si-(Mg)-Sc alloys	25
3 Research aims.....	27
4 Experimental procedures	30
4.1 Alloy composition and heat treatment design	30
4.1.1 Alloy compositions	30
4.1.2 Heat treatment design	32
4.2 Processing of alloys.....	35
4.2.1 Ingot casting.....	35
4.2.2 Homogenisation / pre-heat treatment of cast ingots	37
4.2.3 Hot and cold rolling of ingots	38
4.2.4 Solutionising and ageing of sheets.....	39

4.3	Characterisation techniques used	41
4.3.1	Hardness testing	41
4.3.2	Microstructure analysis	41
4.3.3	X-ray diffraction (XRD)	43
4.3.4	Small-angle x-ray scattering (SAXS)	43
4.3.5	Atom probe tomography	44
5	Design and development of Sc-containing Al-Si alloys.....	46
5.1	Synopsis	46
5.2	Abstract	47
5.3	Introduction	47
5.4	Experimental procedure.....	48
5.4.1	Alloy compositions.....	48
5.4.2	Processing of alloys.....	48
5.4.3	Equilibrium phase prediction using CALPHAD.....	49
5.4.4	Characterisation techniques.....	49
5.5	Results and discussions.....	49
5.5.1	Phase diagrams.....	49
5.5.2	Equilibrium phase analysis in Sc-containing Al-Si alloys	50
5.5.3	Hardness results	51
5.5.4	Microstructure analysis	51
5.6	Conclusion	53
	References.....	54
6	Sc-containing phases in Al-Si-Sc alloys.....	55
6.1	Synopsis	55
6.2	Abstract.....	56
6.3	Introduction.....	56
6.4	Materials and methods.....	57
6.4.1	Alloy synthesis.....	57
6.4.2	Hardness testing.....	57
6.4.3	Microstructural characterisation.....	57
6.4.4	In situ TEM heating.....	58
6.5	Results.....	58
6.5.1	Equilibrium phase diagram.....	58
6.5.2	Hardness results.....	59
6.5.3	XRD results.....	59
6.5.4	Microstructure analysis.....	59

6.5.5	In situ TEM heating results.....	64
6.6	Discussion.....	65
6.6.1	Phase transformation mechanisms.....	66
1.	The formation mechanism for (Al,Si) ₃ Sc phase.....	66
2.	The formation mechanism for V-phase.....	66
6.7	Conclusions.....	67
	References.....	67
7	Effect of Si to Sc ratio on (Al,Si) ₃ Sc nano-precipitates	69
7.1	Chapter synopsis	69
7.2	Abstract	70
7.3	Introduction	71
7.4	Materials and methods	74
7.4.1	Alloys composition	74
7.4.2	Alloys processing.....	74
7.4.3	Characterisation	75
7.5	Results.....	78
7.5.1	Hardness results	78
7.5.2	Precipitation prediction using ThermoCalc®	79
7.5.3	Transmission electron microscopy	81
7.5.4	Quantification of nano-precipitates.....	84
7.5.5	Local strain distribution	90
7.5.6	Composition of nano-precipitates	92
7.6	Discussions.....	96
7.6.1	Effect of Si to Sc ratio on (Al,Si) ₃ Sc precipitation	96
7.6.2	Effect of Si content on local strain.....	97
7.6.3	Effect of Si to Sc ratio on hardening response.....	99
7.6.4	Strengthening mechanisms	100
7.7	Conclusions	105
8	Summary and future work	107
8.1	Summary	107
8.2	Future work	110
	References.....	112
	Appendix 1:.....	120

List of figures

Figure 2.1: Schematic diagram of the Al-rich end of the Al–Sc binary phase diagram (reprinted from [8] with permission from Elsevier).	3
Figure 2.2: Effect of Sc content on as-cast grain size (reprinted from [13] with permission from Elsevier).	4
Figure 2.3: Recrystallization temperature change versus TM addition in Al-TM cold rolled alloys (reprinted from [7] with permission from Elsevier).	6
Figure 2.4: DF-TEM micrograph of Al ₃ Sc precipitate in Al-0.5Sc alloy aged at 400 °C for 17 minutes (reprinted from [25] with permission from Elsevier).	6
Figure 2.4: Hardening of (a) Al-0.41Sc-0.01Fe-0.1Si alloy (reprinted from [7] with permission from Elsevier), (b) as a function of Sc concentration (reprinted from [26] with permission from Elsevier).	7
Figure 2.5: Schematic representation of a manufacturing process sequence for wrought Al semi-products.	9
Figure 2.6: Al ₃ Sc primary particles at a cooling rate of (a) 1 K s ⁻¹ (b) 100 K s ⁻¹ (c) 1000 K s ⁻¹ (reprinted from [45] with permission from Elsevier).	10
Figure 2.7: Changes in strain contrast arising from the level of coherency of precipitates with the matrix (reprinted from [25] with permission from Elsevier).	12
Figure 2.8: An example of discontinuous precipitation in Al-0.3Sc alloy: (a) bright-field (BF) and (b) corresponding dark-field (DF) TEM images of Al ₃ Sc precipitates nucleated heterogeneously at dislocations (reprinted from [49] with permission from Elsevier).	12
Figure 2.9: Evolution of Al ₃ Sc precipitate in Al-0.1Sc alloy viewed along [100] _{α-Al} aged at 350 °C with varying time (reprinted from [49] with permission from Elsevier).	13
Figure 2.10: A Great Rhombicuboctahedron (a) 3D precipitate (b) [100] and (c) [110] projection (reprinted from [49] with permission from Elsevier).	13
Figure 2.11: Size of Al ₃ Sc versus (aging time) ^{1/3} (t ^{1/3}) at 350 °C, 400 °C, 450 °C, and 500 °C (reprinted from [13] with permission from Elsevier).	14
Figure 2.12: Ratio of semi-coherent particles versus the particle radius (reprinted from [25] with permission from Elsevier).	15
Figure 2.13: Hardness change for Al-Sc-(Zr) alloys with respect to annealing time at 350 °C (reprinted from [7] with permission from Elsevier).	16
Figure 2.14: Strain hardening effect in (a) commercial pure aluminium (b) Al-1Sc alloy both rolled at 200 °C (reprinted from [68] with permission from Elsevier).	18
Figure 2.15: Improvement in hardness as a function of ageing treatment for Al-Si-Sc alloys (reprinted from [84] with permission from Elsevier).	23
Figure 2.16: 3DAP studies of Al-0.16Sc-0.05Si heat-treated at 300 °C: (a) individual precipitate mapping, (b) concentration profiles of the elements (reprinted from [83] with permission from Elsevier).	24

Figure 4.1: Al-rich end of the Al-Sc binary phase diagram calculated using ThermoCalc®	31
Figure 4.2: Al-rich end of the Al-Si binary phase diagram calculated using PANDAT®	32
Figure 4.3: Al-rich end of the pseudo-binary Al-Si phase diagram with 0.3 wt. % Sc calculated using ThermoCalc®	34
Figure 4.4: Block flow diagram for Al-Si-(Sc) alloys processing sequence	35
Figure 4.5: (a) Muffle furnace used for the melting of raw materials, (b) liquid metal being poured into the rectangular-shaped mild steel mould, (c) Al-Si-(Sc) cast ingots after cooling	36
Figure 4.6: (a) Buehler four-high lab-scale rolling mill used for hot and cold rolling of ingot samples, (b) the rolled sheet of Al-Si-(Sc) alloys	38
Figure 4.7: Schematic of processing sequence and process parameters followed for Al-Si-(Sc) alloys	40
Figure 5.1: Processing parameters and sequence followed for all the alloys	49
Figure 5.2: Calculated Al-rich side of the (a) binary phase diagram of Al-Sc system (b) pseudo-binary Al-Si system for constant 0.3 wt. % Sc	49
Figure 5.3: Calculated equilibrium phase fractions (a) in Al-0.8Si-0.2Sc-0.08Fe (b) in Al-0.4Si-0.25Sc-0.08Fe (c) in Al-0.1Si-0.3Sc-0.08Fe model alloys and (d) with respect to Sc:Si ratio in Al-Si-Sc alloy system at 350 °C	50
Figure 5.4: Hardness evolution of Sc-free and Sc-containing Al-Si alloys with respect to processing stages	51
Figure 5.5: Secondary electron images of the Al-0.8Si-0.3Sc alloy after low-temperature homogenisation treatment at 350 °C for 30 minutes showing (a) segregation of Si-precipitates and intermetallic phases at the dendrite boundaries (b) presence of primary Si and corresponding energy dispersive spectroscopy maps of Al and Si	51
Figure 5.6: Secondary electron image of intermetallic phases (Fe-rich $Al_9Fe_2Si_2$ indicated with a darker arrow and ScSi phase indicated with the white arrows) found together in Al-0.8Si-0.2Sc alloy after low-temperature homogenisation treatment at 350 °C for 30 minutes	51
Figure 5.7: BF TEM image of $(Al,Si)_3Sc$ nano-dispersoids in the Al-0.1Si-0.3Sc alloy in as-homogenised condition (a) showing large number density (b) nano-dispersoids appear as coffee-bean shaped particles due to Ashby-Brown strain contrast effect which confirms their coherency with α -Al matrix and the inset image shows an FFT of the corresponding micrograph	53
Figure 5.8: BF TEM images of Al-0.1Si-0.3Sc alloy hot rolled at 350 °C (a) showing sub-grain formations and tangled dislocations (b) the coherency of $(Al,Si)_3Sc$ nano-dispersoids is retained after the hot rolling. Inset image shows a corresponding SADP	53

Figure 6.1: Alloy production and processing diagram. The Al-0.4Si-0.25Sc alloy was solutionised at 450 °C for 0.5 h, and Al-0.8Si-0.2Sc was solutionised at 550 °C for 0.5 h....	58
Figure 6.2: Pseudo-binary phase diagram of Al-Si system with 0.25 wt. % Sc. Diagram calculated using ThermoCalc®, indicating the ScSi phase region in α -Al matrix	58
Figure 6.3: Evolution of hardness as a function of processing during the thermo-mechanical treatments for both alloys studied	59
Figure 6.4: Comparison of phases with the XRD results of Al-0.8Si-0.2Sc alloy in the pre-heat treated (350 °C for 0.5 h) and solutionised conditions (550 °C for 0.5 h)	59
Figure 6.5: Al-0.8Si-0.2Sc following pre-heat treatment at 350 °C for 0.5 h. (a) SEI-SEM image of the microstructure showing distribution of phases. White arrows indicate the coarse intermetallics (b) magnified SEI-SEM image of secondary Si particles marked by a rectangle in (a); (c) BF-TEM image of Si-precipitates and (d) corresponding SADP; (e) BF-STEM image of (Al,Si) ₃ Sc nano-precipitates; (f) atomic-scale HAADF-STEM image showing the structure of coherent, nano-sized (Al,Si) ₃ Sc faceted precipitate	60
Figure 6.6: SEI-SEM images of microstructure in (a) Al-0.8Si-0.2Sc alloy solution treated at 550 °C for 0.5 h (b) magnified view of Al-0.8Si-0.2Sc alloy solution treated at 550 °C for 0.5 h (c) Al-0.4Si-0.25Sc solution treated at 450 °C for 0.5 h	62
Figure 6.7: (a) BF-STEM, (b) corresponding HAADF-STEM image, and (c) EDS line-scan results of the V-phase in the α -Al matrix in Al-0.8Si-0.2Sc solutionised at 550 °C for 0.5 h, with the corresponding EDS mapping results	63
Figure 6.8: BF-STEM images of Al-0.8Si-0.2Sc alloy solutionised at 550 °C for 0.5 h. (a) Low-magnification image of (Al,Si) ₃ Sc precipitates and V-phase and (b) semi-coherent (Al,Si) ₃ Sc precipitates. Red and white arrows indicate (Al,Si) ₃ Sc precipitates and V-phase respectively	63
Figure 6.9: Atomic resolution BF-STEM image of the V-phase in Al-0.8Si-0.2Sc alloy	64
Figure 6.10: Crystallographic ORs of the V-phase with the α -Al matrix in Al-0.8Si-0.2Sc alloy solutionised at 550 °C for 0.5 h. (a-f) BF-TEM images of the V-phase, (a'-f') respective SADPs of the images	65
Figure 6.11: (a-c) Images from in situ TEM heating experiment conducted on Al-0.4Si-0.25Sc alloy at 350 °C for 1 h showing nucleation and growth of (Al,Si) ₃ Sc nano precipitates (d) respective change in precipitate diameter as a function of holding time	65
Figure 6.12: Snapshots of video during in-situ TEM heating of Al-0.8Si-0.2Sc alloy revealing (a1-a6) dissolution sequence for the secondary Si particle (b1-b3) dissolution sequence of the nano-sized (Al,Si) ₃ Sc precipitates (c1-c3) nucleation and growth sequence for the rod-shaped	68

V-phase. Red, white and black arrows indicate the (Al,Si)₃Sc nano-precipitates, Si-particle, and V-phase rods respectively. Note: As-cast Al-0.8Si-0.2Sc alloy was first ex situ heat-treated at 350 °C for 30 min and then in situ heated at 550 °C 65

Figure 7.1: Vickers hardness results with respect to Si to Sc ratios of the Al-Si-Sc alloys in as-cast and heat-treated conditions. 78

Figure 7.2: Al₃Sc precipitation simulation results at 350 °C for 30 minutes using ThermoCalc[®]: (a) size distribution, (b) radius, number density, and volume fraction with respect to Si to Sc ratios of the alloys. 80

Figure 7.3: (Al,Si)₃Sc nano-precipitates following heat treatment at 350 °C, 0.5 h: (a) uniform local distribution of precipitates, (b) precipitates revealing coherency as seen with the AB strain contrast, (c) coarser precipitates, (d) DF image indicating faceted precipitates, (e) relatively fine precipitates, and (f) lattice fringes in the high-resolution TEM image showing coherency of precipitate with Al matrix. 82

Figure 7.4: (Al,Si)₃Sc nano-precipitate in Al-0.8Si-0.2Sc alloy heat-treated at 350 °C for 0.5 h: (a) HRTEM image, (b) corresponding diffraction pattern obtained by the Fourier transformation of the image in (a), (c) Fourier-filtered image of (a) after masking diffraction spots from L1₂ phase, (d) colourmap revealing atomic arrangement in L1₂ crystal structure with interplanar spacings: $d_{[200]} = 2.08\text{\AA}$ and $d_{[220]} = 1.41\text{\AA}$ 84

Figure 7.5: SAXS analysis for the effect of Si:Sc ratios on (Al,Si)₃Sc precipitates characteristics: (a) radius, (b) change in precipitate radius (cast precipitate radius – heat-treated precipitate radius), (c) invariant Q which is proportional to the volume fraction and (d) number density. 86

Figure 7.6: Precipitates volume comparison in as-cast and heat-treated conditions for the Al-Si-Sc alloys using Kratky plots. 87

Figure 7.7: Comparison of Kratky plots in all the three alloys in (a) as-cast condition and (b) after heat treatment at 350 °C for 0.5 h. 88

Figure 7.8: Comparison using TEM, SAXS, and ThermoCalc[®] for (Al,Si)₃Sc precipitate characteristics in heat-treated alloys: (a) size, (b) volume fraction, (c) number density, and (d) magnified view of the data in the dashed rectangle in the graph in (c). 90

Figure 7.9: Area selected for the strain mapping in (a) Al-0.1Si-0.3Sc, (b) Al-0.4Si-0.25Sc, (c) Al-0.8Si-0.2Sc alloys in heat-treated condition, (A, B, and C) respective normalised strain maps of scan size 100 × 100 nm along [001]_{α-Al}, (d) 2D plots of the average strain distribution of the white rectangles marked in A, B, and C. 92

Figure 7.10: 3DAP volume constructed for heat-treated (a) Al-0.4Si-0.25Sc, (b) Al-0.8Si-0.2Sc alloys. 93

Figure 7.11: Proxygrams of the nano-precipitates from Figure 7.10: (a) Al, Si, and Sc in Al-0.4Si-0.25Sc, (b) Al, Si, and Sc in Al-0.8Si-0.2Sc, (c) overlay of Si concentration. 95

Figure 7.12: Maximum strain as a function of Si content and hardness following the heat treatment of Al-Si-Sc alloys. 99

List of tables

Table 4.1: Nominal composition of the model Al-alloys.	31
Table 4.2: Raw material additions to the respective alloy ingots and actual chemical composition of the alloys measured using ICP-OES.	36
Table 4.3: Gravity die casting process parameters.	37
Table 4.4: Hot and cold rolling process parameters.	39
Table 4.5: Solutionising and ageing process parameters.	39
Table 5.1: Chemical composition for the six alloys under study measured using ICP-OES ^(A)	48
Table 5.2: Vickers microhardness values for the alloys in four different processing conditions	51
Table 6.1: Chemical composition (wt. %) of the two Sc-containing Al-alloys measured using ICP-OES test	57
Table 6.2: Experimental and calculated interplanar spacings (d-spacings) for the ternary V-phase	64
Table 6.3: Comparison of experimental and theoretical lattice parameters of V-phase	64
Table 6.4: Misfit between matching crystallographic planes for the identified ORs of the AlSc ₂ Si ₂ (V-phase) and α -Al matrix	65
Table 7.1: Chemical composition (wt. %) of Al-Si-Sc alloys measured using ICP-OES test.	74
Table 7.2: Effect on volume fraction, size and number density of precipitates with increasing Si content in the Al-Si-Sc alloys analysed using SAXS.	85
Table 7.3: Maximum strain from various scans collected for the three Al-Si-Sc alloys in heat-treated condition along $[001]_{\alpha\text{-Al}}$	90

Thesis including published works declaration

I hereby declare that this thesis contains no material which has been accepted for the award of any other degree or diploma at any university or equivalent institution and that, to the best of my knowledge and belief, this thesis contains no material previously published or written by another person, except where due reference is made in the text of the thesis.

This thesis includes 2 original papers published in peer reviewed journals, and 1 ready for submission paper titled '*Effect of Si to Sc ratio on (Al,Si)₃Sc nano-precipitates and related local strain fields in Al-Si-Sc alloys following low-temperature heat treatment*' as chapter 7. The core theme of the thesis is scandium-containing Al-Si alloys. The ideas, development and writing up of all the papers in the thesis were the principal responsibility of myself, the student, working within the Material Science and Engineering Department, Faculty of Engineering under the supervision of Professor Nick Birbilis.

The inclusion of co-authors reflects the fact that the work came from active collaboration between researchers and acknowledges input into team-based research. The alloy design using CALPHAD tools and their processing was conducted independently by myself, the student, in addition to the use of various characterization techniques that includes scanning electron microscopy (SEM), (high resolution) transmission electron microscopy (TEM), x-ray diffraction (XRD), and small-angle x-ray scattering (SAXS). The collaborative approach was taken for the use of atom probe tomography (APT), in situ TEM and precession electron diffraction (PED) techniques.

In the case of chapter 5 and 6 my contribution to the work involved the following:

Thesis Chapter	Publication Title	Status <i>(published, in press, accepted or returned for revision, submitted)</i>	Nature and % of student contribution	Co-author name(s) Nature and % of Co-author's contribution	Co-author(s), Monash student Y/N
5	<i>Optimised composition and process design to develop Sc-enhanced wrought Al-Si alloys</i>	<i>Published</i>	<i>Concept and collecting data and writing first draft (88%)</i>	1) Timothy Langan, input into manuscript 2% 2) Thomas Dorin, evaluation of manuscript and supervision 5%	No No No

				3) Nick Birbilis, evaluation of manuscript and supervision 5%	
6	Understanding the formation of (Al,Si) ₃ Sc and V-phase (AlSc ₂ Si ₂) in Al-Si-Sc alloys via ex situ heat treatments and in situ transmission electron microscopy studies	Published	Concept and collecting data and writing first draft (84%)	1) Shravan K. Kairy, methodology 2% 2) Elaf Anberb, methodology 2% 3) Timothy Langan, input into manuscript 1% 4) Mitra L. Taheri, input into manuscript 1% 5) Thomas Dorin, evaluation of manuscript and supervision 5% 1) Nick Birbilis, evaluation of manuscript and supervision 5%	No No No No No No

I have not renumbered sections of submitted or published papers in order to generate a consistent presentation within the thesis.

Student name: Jayshri Dumbre

Student signature:

Date: 05-Feb-2021

I hereby certify that the above declaration correctly reflects the nature and extent of the student's and co-authors' contributions to this work. In instances where I am not the responsible author I have consulted with the responsible author to agree on the respective contributions of the authors.

Main Supervisor name: Prof. Nick Birbilis

Main Supervisor signature:

Date: 05-Feb-2021

Acknowledgements

I am grateful to my supervisors Prof. Nick Birbilis for allowing me to conduct this research work under his guidance. He is a constant source of inspiration with great clarity on research requirements who tirelessly guided, helped, and shaped me both personally and professionally throughout my research journey at Monash University.

I am also thankful to my co-supervisor Dr. Thomas Dorin (Deakin University) for providing me an opportunity to collaborate with the Institute for Frontier Materials at Deakin University. His knowledge and the technical inputs in this research field was extremely useful to plan and shape the research work undertaken. I would also like to appreciate all the help and support from my co-supervisor, Dr. Yuman Zhu.

I would like to take this opportunity to thank Prof. Mitra Taheri (John Hopkins University, USA) for allowing me to form the collaboration with Drexel University, USA which proved to be the most valuable contribution to this research. The collaborative work could not have been completed without the support from Ms. Elaf Anber and Mr. Daniel Foley who helped me with conducting microscopy work. I sincerely acknowledge for allowing me to work at the Centralized Research Facility (CRF), Drexel University, Philadelphia, USA which has world-class electron microscopy facilities.

I acknowledge the Monash Centre for Electron Microscopy (MCEM) for allowing me to use their state-of-the-art electron microscopy facilities to analysis microstructures of aluminium alloys. This research used equipment funded by the Australian Research Council grant (LE110100223). I would like to acknowledge the valuable contribution of Dr. Tim Williams, Dr. Flame Burgmann, Dr. Xi-Ya Fang, Dr. Yu Chen for helping me understand the use of electron microscopy techniques which were vital for this research. I would like to thank Dr. Russel King, and Mr. Renji Pan, MCEM, for training on sample preparation techniques as well as handling of various electron microscopes.

The Monash X-Ray Platform (MXP) is also acknowledged for the use of their facilities and the research-related help received from Dr. James Griffith and Dr. Jisheng Ma was useful for developing an understanding of phases in the microstructures studied. I am grateful to Dr. T. J. Langan, M/S Clean TeQ Holdings Ltd. for providing me with an insight into the industrial requirements for the Sc-bearing aluminium alloys, for supplying Al-Sc master alloys. I would like to thank my colleagues Dr. Shravan Kairy (Monash University), Dr. Mahendra Ramajayam

(Deakin University), Dr. Lu Jiang (Deakin University), and Dr. Baptiste Rouxel (École Polytechnique, France) for much useful advice and discussions.

I am thankful to Monash University for providing me the financial support via MGS (Monash Graduate Scholarship), IMPRS (International Monash Postgraduate Research Scholarship), GRITA (Graduate Research International Travel Award), and GRCA (Graduate Research Completion Award). I also acknowledge financial support through the ARC Linkage Project scheme (LP160100104).

I acknowledge all my lab-mates and friends who helped me directly and indirectly with my ongoing research work. Lastly but majorly, my heartfelt thanks to my father (Mr. Shankar Karande), my mother (Mrs. Shakuntala Karande), my sisters (Ujjwala, Swati, Jyoti, Chhaya, Dipika, and Arti), and my brother (Mayur) for their unconditional love without which the dream of being a researcher would not have been possible.

1 Introduction

Light weighting remains an ongoing and important trend in the automotive sector in order to increase fuel efficiency and reduce CO₂ emissions. The required weight saving is generally achieved through the use of low-density materials such as aluminium (Al) alloys, magnesium (Mg) alloys, carbon-based composites, and other lightweight materials. Aluminium alloys are of particular importance and specifically, the conventional 6xxx series (Al-Mg-Si) Al-alloys are most widely used due to the balance of good corrosion resistance and moderate strength. Attempts to increase the strength of the 6xxx series Al-alloys are popular in the context of automotive use. Some of the copper (Cu) containing 6xxx series Al-alloys that demonstrate the highest strength of 6xxx series Al-alloys are also being considered for aircraft applications [1]. However, the strength enhancement by the addition of Cu is associated with degradation in corrosion performance. On the other hand, studies indicate that alloying with scandium (Sc) in small quantities has the potential to simultaneously achieve significantly higher strength in commercial Al-alloys, while maintaining corrosion resistance [2–5].

The use of Sc as an alloying element has been documented since the 1960s and the first patent on this system was filed in 1968 by the Aluminum Company of America (ALCOA). This initial work emphasised the useful benefits of alloying Al with Sc in multicomponent alloys and the strengthening benefits were found to occur during carefully designed thermal treatments due to the formation of L1₂ structured nano-precipitates [6]. Further studies resulted in successfully designed high strength Sc-bearing 5xxx (Al-Mg) and 7xxx (Al-Zn) series Al-alloys and are being used commercially for a few applications. On the contrary, very little work has been done in the development of Sc-containing 6xxx series Al-alloys; majorly due to the cost implications resulting from the addition of comparatively expensive elements like Sc as well as due to the detrimental effects of Si on Sc-bearing phases forming the deleterious V-phase (AlSc₂Si₂) [7]. The present work was aimed at both elucidating and understanding these detrimental effects

due to the presence of higher levels of Si content in the Al-Sc alloys via detailed characterisation of desirable and undesirable Sc-containing phases. The identification of processing conditions at which these phases form was done to formulate the mitigation strategies which can help develop Sc-containing 6xxx series Al-alloys.

2 Literature review

This chapter provides a review of the available literature on Sc-containing Al-alloys and multiple effects caused by the addition of Sc. The Sc-containing nano-precipitates and their evolution during key manufacturing stages of wrought Al-alloy production are discussed in a later part. The final part of the literature survey outlines the effect of Sc addition in multi-component Al-alloys.

2.1 Al-Sc binary alloy system

The binary system of Al-Sc alloys is well understood and studied in detail. The maximum solubility of Sc in the face centred cubic (FCC) α -Al at the temperature of eutectic transformation (659 °C) is ~ 0.35 wt. %, a eutectic composition is 0.6 wt. % Sc, and the solidification has a very narrow range of ~ 5 °C [8–10] as given in Figure 2.1. The alloy is hyper-eutectic for the Sc composition beyond the eutectic point, whereas in hypo-eutectic alloys the Sc composition is lower than the eutectic point.

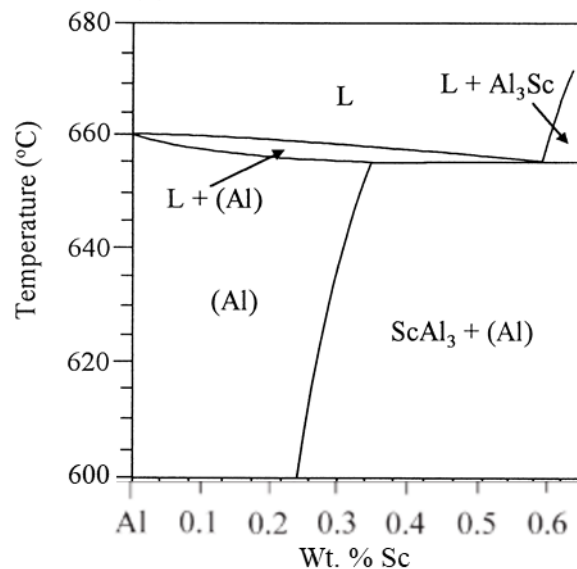
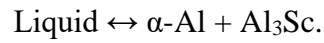


Figure 2.1: Schematic diagram of the Al-rich end of the Al–Sc binary phase diagram (reprinted from [8] with permission from Elsevier).

The equilibrium coherent Al_3Sc (scandium aluminide) phase is formed during the following eutectic reaction occurring at 655 °C to 660 °C.



The formation of Guinier-Preston (GP) zones and other metastable phases during the precipitation sequence has not been observed so far [11].

2.2 Effects of Sc in Al-alloys

The addition of Sc in Al-alloys results in multiple beneficial effects which are explained in this section. These effects can be helpful while designing and processing the Al-Sc alloys due to their direct relationship with the end properties of the Al semi-products.

2.2.1 Refined microstructure

Scandium is one of the most effective grain refiners and modifiers in Al-alloys when added with a concentration greater than 0.55 wt. % (hypereutectic concentration) [8,11–16]. The relationship between grain size and Sc concentration is shown in Figure 2.2. The modifying effect of Sc forms dendrite free, equiaxed grains in the cast condition [7].

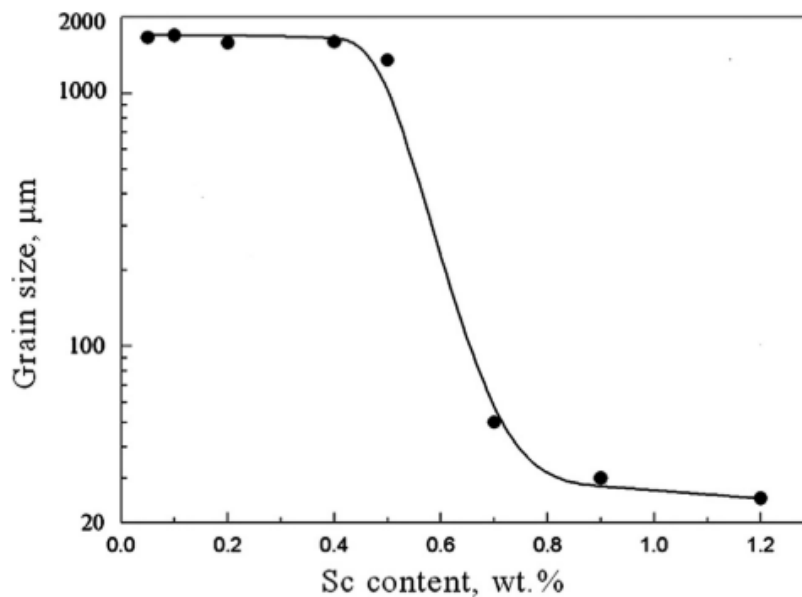


Figure 2.2: Effect of Sc content on as-cast grain size (reprinted from [13] with permission from Elsevier).

Scandium additions in more common Al-Si-Mg foundry alloys have refined the as-cast grain size, reduced dendritic arm spacing (DAS), refined eutectic Si phase, and converted iron (Fe) rich β -Al₅FeSi phase into less deleterious, soft, nodular Sc-containing phases such as Al₁₂Si₆Fe₂(Mg,Sc)₅ [2,17–20].

2.2.2 Improved quench sensitivity

Lower quench sensitivity is important for cast products in order to get uniform mechanical properties at varying thicknesses of the component. It also indicates that relatively slow cooling rates are enough to get a saturated solid solution during casting. In the case of Al-Sc alloys, a supersaturated solution of Sc in α -Al was achieved even at lower cooling rates (of the order of 10⁵ K/s) similar to those being used at an industrial scale for continuous casting of Al-alloys [21,22]. Scandium was found to improve the quench sensitivity of Al–7Si–0.6 Mg alloy by 60% due to the formation of Al₃Sc precipitates even at low cooling rates, with a similar hardness reached for a range of cooling rates. The formation of Al₃Sc precipitates also retards the formation of β' -Mg₂Si [23].

2.2.3 Anti-recrystallization

Recrystallization occurs in Al-alloys wherein deformed grains are replaced by new strain-free grains when heated to a high enough temperature [1]. The transition metal (TM) elements, when added to Al-alloy, increase the recrystallization temperature of the respective alloy, known as the ‘anti-recrystallization effect’. This effect is important since the worked texture of the component can be retained during subsequent high-temperature thermal treatments without the formation of recrystallized grains. As can be seen in Figure 2.3, Sc is the most effective of all other TM elements due to the large number density of homogeneous coherent Al₃Sc precipitates. The anti-recrystallization effect disappears after coarsening and loss of coherency of these precipitates [7].

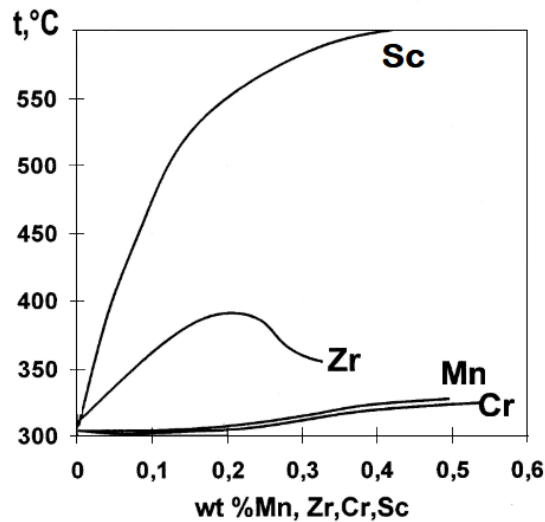


Figure 2.3: Recrystallization temperature change versus TM addition in Al-TM cold rolled alloys (reprinted from [7] with permission from Elsevier).

2.2.4 Precipitation hardening

A significant hardening effect in Al-Sc alloys was seen as a result of precipitation of spherical, coherent, Al_3Sc precipitates with an optimum diameter of 1.5 nm [12,24]. A dark field (DF) TEM image of the Al_3Sc precipitates is given in Figure 2.4.

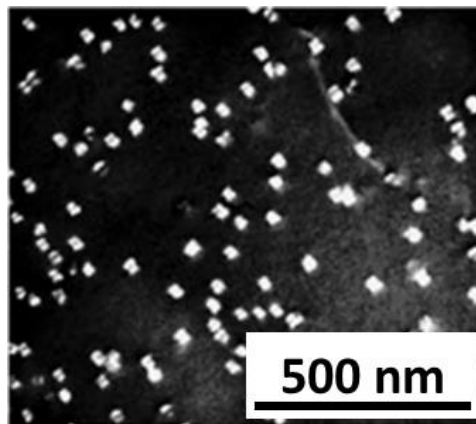


Figure 2.4: DF-TEM micrograph of Al_3Sc precipitate in Al-0.Sc alloy aged at 400 °C for 17 minutes (reprinted from [25] with permission from Elsevier).

In general, precipitation experiences three stages [1]:

1. Early-stage with an incubation period, which indicates delayed nucleation of precipitates
2. Rapid growth stage, which is the period of highest hardening rate

3. Gradual growth stage which has a lower hardening rate

The hardening response mainly depends on - (1) treatment temperature, (2) holding time at the temperature, and (3) Sc concentration in the alloy. As the treatment temperature and time are changed, the kinetics of precipitation changes, as shown in Figure 2.5 (a). The maximum hardness can remain similar even with the change in treatment temperature; however, with increasing temperature, a sharp peak of maxima appeared along with the disappearance of the plateau [7,24,26]. It is thus important to achieve the right trade-off between treatment temperature and time in order to get optimum sized precipitates.

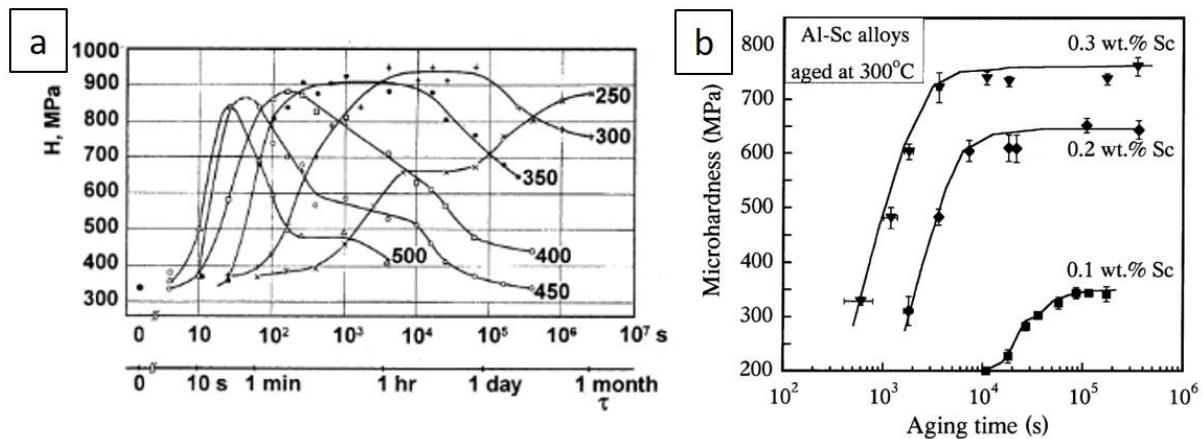


Figure 2.5: Hardening of (a) Al-0.41Sc-0.01Fe-0.1Si alloy (reprinted from [7] with permission from Elsevier), (b) as a function of Sc concentration (reprinted from [26] with permission from Elsevier).

With increasing Sc content, the incubation time decreases, and the value of peak hardness increases [11,26] as shown in Figure 2.5 (b), for the Sc concentrations of 0.1, 0.2, and 0.3 wt. % at 300 °C. As compared to the usual age hardenable alloys like Al-Mn and Al-Zr, the Al-Sc alloys were reported to have a higher precipitation temperature [26], decomposition rate [24], resistance to softening [12], and a shorter incubation time [24,27,28].

2.2.5 Corrosion resistance

The limited research that explored the effect of Sc on corrosion reported an improvement in the corrosion properties resulting from refined, non-recrystallized microstructure and modified

grain boundary precipitate characteristics due to Al_3Sc precipitates [5,29–31]. The Al_3Sc phase was found to be slightly cathodic to the α -Al matrix and hence should have only little impact on the corrosion resistance of Al-alloys when added in low concentrations [5]. For instance, the additions of Sc and zirconium (Zr) were reported to improve the corrosion performance of 7xxx series Al-alloys [30] and 2xxx series Al-alloys [32]. Similarly, Sc:Zr addition of 1:2 in Al-Cu-Mg alloys was found to reduce intergranular corrosion susceptibility resulting from non-recrystallized refined grain size, increased grain boundary precipitate spacing, and decreased Cu containing phases at grain boundaries [31]. Only one study reported a degradation in corrosion properties and concluded that Sc addition in AA7010 alloy facilitates corrosion initiation due to the formation of a coarse $\text{Al}_3\text{Sc}_x\text{Zr}_{1-x}$ phase [33].

2.2.6 Other properties

The Al_3Sc precipitates are also known for their high thermal resistance and therefore, they have been found to improve the creep performance of Al-alloys [26]. The creep properties are a function of Sc content, precipitate size, and heat treatment conditions [34–37]. The addition of Sc and Zr improved the superplastic behaviour of Al-Mg-Sc-(Mn)-(Zr) alloys [38–41]. The 01570 commercial Al-alloy was found to exhibit superplastic properties at 475 °C and under a strain rate of $6 \times 10^{-3} \text{ s}^{-1}$, an elongation of 600% was reported with flow stress of 11 MPa. Under the same conditions, the 01571 Al-alloy was reported to exhibit an elongation of 1000% [42]. These alloys were also proved to have better wear resistance [43] and weldability [44].

2.3 Precipitates evolution during processing

The Sc-containing precipitates are of great importance since they result in improved properties and thus an overall performance enhancement of the alloys as explained in section 2.2. This section describes their evolution through some key stages of the conventional wrought Al semi-product manufacturing process which is schematically illustrated with respect to temperature and time of respective process steps in Figure 2.6.

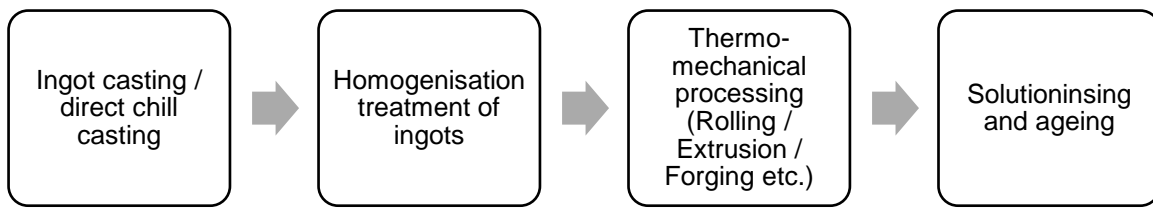


Figure 2.6: Schematic representation of a manufacturing process sequence for wrought Al semi-products.

2.3.1 Casting process

A fine grain size, a lower amount of Fe-rich grain boundary constituent particles, non-dendritic structure, fine intermetallics, and lower elemental segregation are the desirable microstructural features in cast structures in order to get improved strength in the end product. The Sc concentration and casting process conditions directly affect these microstructural features in Al-alloys.

In the case of hyper-eutectic Al-alloys, primary, faceted, cubic Al_3Sc particles form during solidification. The particles have an $L1_2$ crystal structure with a lattice parameter ' a ' of 0.4104 nm [8]. The presence of an oxide inclusion at the centre of the Al_3Sc particles was observed, which indicated that the primary particles tend to nucleate on the inclusions [8,33].

An effect of cooling rate on the primary Al_3Sc phase in an Al-0.7 wt. % Sc system was reported by Hyde et al. [45]. The as-cast grain size and Al_3Sc primary particle size were both found to be decreasing with increasing solidification rate. One of the effects of increasing the cooling rate was a change in the surface morphology of Al_3Sc primary particles from faceted cubic to non-faceted cellular structure growing in [111], [110], and [100] directions as shown in Figure 2.7 [45].

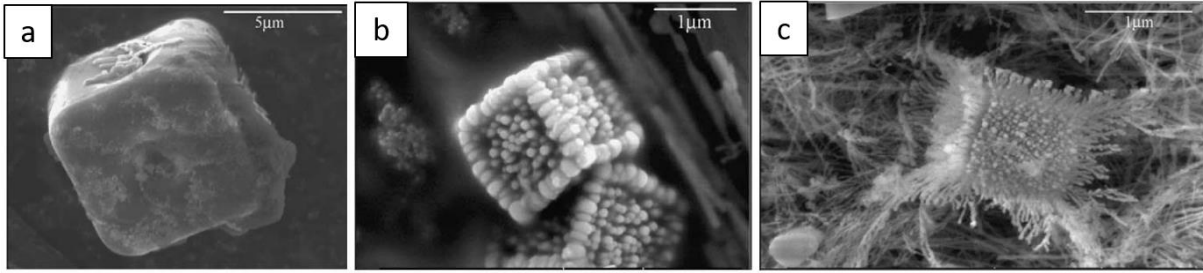


Figure 2.7: Al_3Sc primary particles at a cooling rate of (a) 1 K s^{-1} (b) 100 K s^{-1} (c) 1000 K s^{-1} (reprinted from [45] with permission from Elsevier).

In hypo-eutectic conditions, the Sc stays largely supersaturated in the Al matrix during solidification. However, few studies reported the presence of eutectic Al_3Sc or $\text{Al}_3(\text{Sc,Zr})$ nano-precipitates formed due to discontinuous precipitation in the as-cast condition. The precipitation is referred to as ‘discontinuous’ if the precipitates form heterogeneously at the moving high angle boundaries [46]. The degree of discontinuous precipitation of Al_3Sc is proportional to Sc supersaturation and melt temperature [24,47,48]. A study by Elagin et al. [24] showed that a small amount of Al_3Sc nano-precipitates of $\sim 20 \text{ nm}$ size were formed during solidification in the case of an Al-0.41 wt. % Sc alloy, indicating that the solid solution of Sc in Al was unstable.

Although there exists some knowledge about the precipitation of primary Al_3Sc during the solidification, the studies relating the solidification parameters with the changes in eutectic Al_3Sc nano-precipitates are scarce.

2.3.2 Homogenisation treatment

Cast structures in Al-alloys are not desirable when it comes to superior strength performance. Therefore, homogenisation treatment generally becomes necessary to improve the cast structure and to make it suitable for subsequent thermo-mechanical processing. The major objectives of conducting homogenisation treatment on cast ingots are [1]: (1) to reduce microsegregation of elements throughout the ingot, (2) to remove the low melting point (LMP)

phases, (3) to dissolve and/or to spheroidise and/or to convert deleterious Fe-rich coarse intermetallic phases into less harmful phases (4) to form precipitates of hardening phases to control grain structure during subsequent hot working process.

In Sc-containing Al-alloys, Sc remains supersaturated after casting, and hence a separate thermal treatment is usually required to precipitate the Al_3Sc phase. Usually, there are two approaches to precipitate the Sc-containing phases. In a first approach, the precipitation of the Al_3Sc phase was obtained by annealing heat treatment of the cast ingots (low-temperature homogenisation treatment). Whereas, in the second approach, the Al_3Sc phase can be dissolved first during the solutionising treatment of the thermo-mechanically processed alloys and a suitable ageing treatment can be performed to form the Al_3Sc phase [27]. Such a treatment condition is called as 'T6 temper' which involves solution treating of an alloy at high temperature followed by artificial ageing at a certain temperature to achieve precipitation hardening. However, comparative studies of resultant strength with these two different approaches are missing. In general, to achieve high strength Sc-containing wrought Al-alloys, the process sequence given here (T6 temper) is considered as more appropriate: heat treatment of cast ingots to form nano-precipitates → hot working of ingots to form non-recrystallized structure due to presence of nano-precipitates → cold working to get required size and shape of the alloy → solutionising treatment to get solid solution of other hardening elements in the case of ternary alloys or quaternary alloys → ageing treatment to co-precipitate second or third hardening phases while maintaining coherency of Al_3Sc nano-precipitates.

The information presented subsequently is about the Al_3Sc characteristics and precipitation kinetics irrespective of whether the precipitation occurred during a low-temperature homogenisation treatment to cast ingots or T6 treatment.

2.3.2.1 Nucleation and growth of precipitates

The type of nucleation, size, and the growth morphology of precipitates were found to be a function of the Sc concentration and thermal treatment cycle given to the alloy [11,13,49].

The continuous precipitation due to homogeneous nucleation of coherent Al_3Sc precipitates occurred when precipitation treatment was conducted from 225 °C to 300 °C. The coherency strain of the precipitates was stable as would be expected from the fact that they were in their equilibrium state and the diffusion rate of Sc in Al is low [11]. Coherency of precipitates was qualitatively judged by Ashby and Brown (AB) strain contrast method as shown in Figure 2.8 [25].

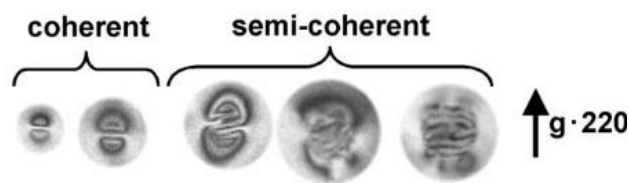


Figure 2.8: Changes in strain contrast arising from the level of coherency of precipitates with the matrix (reprinted from [25] with permission from Elsevier).

The discontinuous precipitation (due to heterogeneous nucleation and therefore not so desirable mode of precipitation) of the Al_3Sc phase along the dislocation occurred when the precipitation treatment between 300-500 °C was conducted [50] (Figure 2.9) or when the Sc concentration in the alloy was low [48].

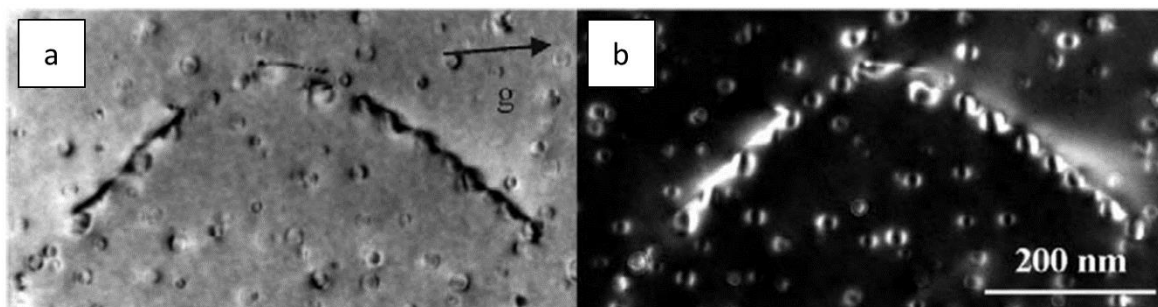


Figure 2.9: An example of discontinuous precipitation in Al-0.3Sc alloy: (a) bright-field (BF) and (b) corresponding dark-field (DF) TEM images of Al_3Sc precipitates nucleated heterogeneously at dislocations (reprinted from [49] with permission from Elsevier).

For low Sc concentrations, lobes and cusps at the corner of cubic shaped Al_3Sc precipitates were formed when treated at $300\text{ }^\circ\text{C}$ for a very long time of 72 h. The lobes were grown in non-specific crystallographic orientation as shown in Figure 2.10. For longer ageing treatment at $350\text{ }^\circ\text{C}$ for 130 h, Al_3Sc precipitates with rod shape were formed [49].

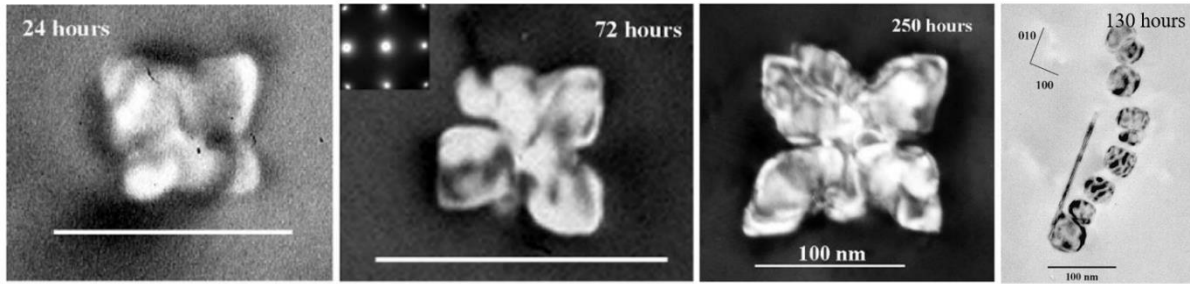


Figure 2.10: Evolution of Al_3Sc precipitate in Al-0.1Sc alloy viewed along $[100]_{\alpha\text{-Al}}$ aged at $350\text{ }^\circ\text{C}$ with varying time (reprinted from [49] with permission from Elsevier).

On the other hand, for higher Sc concentrations, the shape of the Al_3Sc precipitate was found to be a function of precipitate size. The facets on Al_3Sc precipitate are not developed when the precipitate is too small (less than 2 to 3 nm); whereas, the facets on $\{100\}$ and $\{110\}$ planes for an increased precipitate size were observed under a transmission electron microscope (TEM). The development of facets is related to the interface boundary energy (γ), which was found to be orientation and temperature-dependent for $\text{Al}_{(\text{FCC})}:\text{Al}_3\text{Sc}_{(\text{L}_{12})}$ interface. At 0 K, with zero applied pressure, the γ was 32.5, 51.3, 78.2 mJ/m^2 for (100), (110) and (111) respectively [51]. This indicated that the Al_3Sc was likely to develop cuboidal shaped precipitates with interfaces in (100) as against (110) or (111) planes.

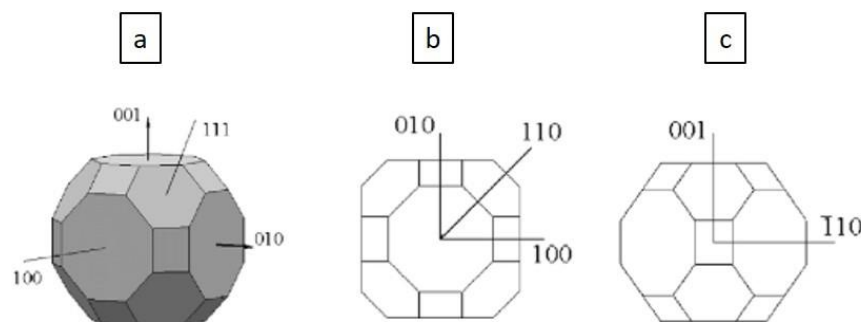


Figure 2.11: A Great Rhombicuboctahedron (a) 3D precipitate (b) $[100]$ and (c) $[110]$ projection (reprinted from [49] with permission from Elsevier).

The equilibrium Al_3Sc precipitate has 6 {100} planes (cube), 12 {110} planes (rhombohedral dodecahedron), and 8 {111} planes (octahedron), which is called a Great Rhombicuboctahedron and schematically shown in Figure 2.11 [49].

The strengthening due to precipitates was not significant when aged at below 300 °C for Al-0.11 at. % Sc and Al-0.19 at. % Sc alloys and theoretical calculations indicated that the Orowan mechanism was operative for ageing above 300 °C [52].

2.3.2.2 Coarsening and coherency loss of precipitates

Precipitate size, coherency, and precipitation treatment temperature are strongly related to each other. Coarsening and coherency loss in Al_3Sc precipitates was observed when the alloys were exposed to temperatures higher than 400 °C to 500 °C resulting in softening [13,25,26,53–55]. Yet in another study, the coherency of Al_3Sc precipitates was maintained even after a heat treatment at 300 - 450 °C for 168 h [56]. It was seen that with increasing temperature and/or holding time, the precipitate size increases (refer Figure 2.12) with reduced number density. The coarsening rate increases with the increase in temperature and is controlled by bulk diffusion of elements [55].

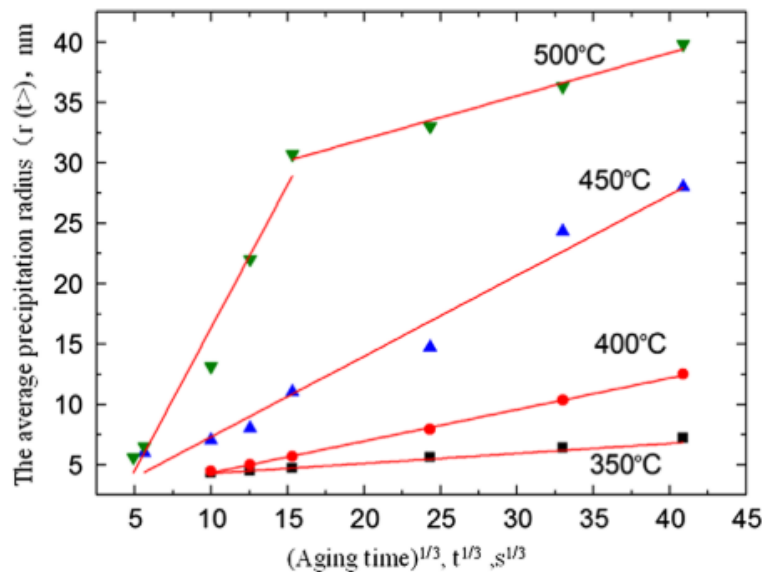


Figure 2.12: Size of Al_3Sc versus (aging time)^{1/3} ($t^{1/3}$) at 350 °C, 400 °C, 450 °C, and 500 °C (reprinted from [13] with permission from Elsevier).

The qualitative observation of changes in AB strain contrast can be used to estimate the coherency loss as shown in Figure 2.13. Precipitates below 15 nm in diameter were coherent whereas those between 15 to 40 nm in diameter were mixed with coherent as well as semi-coherent precipitates, and those greater than 40 nm diameter were all semi-coherent. The coherency loss was also associated with the presence of dislocations at the matrix-precipitate interface [25].

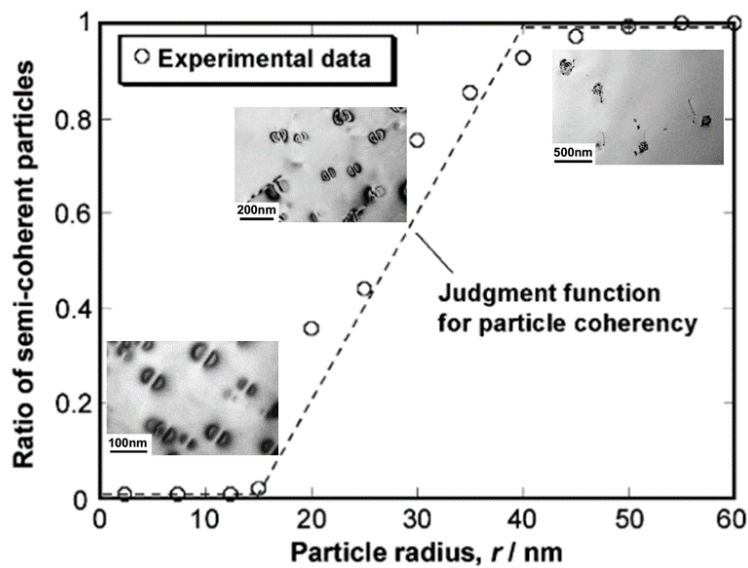


Figure 2.13: Ratio of semi-coherent particles versus the particle radius (reprinted from [25] with permission from Elsevier).

The coarsening and coherency loss of Al_3Sc precipitates are to be considered when it comes to precipitate strengthening utilizing heat treatment in the case of Al-Sc-X ternary alloys (where X can be Mg, Si, Cu, and other similar hardening elements). The solutionising temperature for these ternary alloys is 450-550 °C which is not sufficient to form a saturated solid solution of Sc in the α -Al matrix. Instead, exposure to conventional solutionising temperatures results in coherency loss and coarsening of Al_3Sc degrading the strengthening performance [57].

2.3.2.3 Improvement of thermal stability of nano-precipitates

There is a need to increase the thermal stability of Al_3Sc precipitates in order to conduct successful solutionising and ageing for the co-precipitation of other hardening phases and to

maintain coherency of Al_3Sc precipitates in Al matrix. To improve the coarsening resistance, the minor addition of other elements (individually and combined) such as titanium (Ti) [58,59], vanadium (V) [60], hafnium (Hf) [61], and Zr were studied, and Zr was found to be most common and efficient of all. Zirconium can be dissolved in Al_3Sc precipitate substituting Sc up to 50%, which forms a shell around the Sc-rich core of the $\text{Al}_3(\text{Sc}_{1-x}\text{Zr}_x)$ precipitates [62]. Similarly, up to 10% Ti can be dissolved in Al_3Sc substituting Sc, which also forms a shell around the Sc-rich core of precipitate [57].

1. Addition of Zr

The coherent, core-shell type, $\text{Al}_3(\text{Sc}_{1-x}\text{Zr}_x)$ precipitates are less susceptible to coagulation. This helps in retaining the anti-recrystallization effect of the alloy. Zirconium also helped to improve the modifying effect of Sc in Al-alloys by reducing the required critical addition of Sc from 0.55 wt. % to 0.18 - 0.25 wt. % [63].

Several studies indicated that Zr improved thermal stability without changing the hardening effect, as shown in Figure 2.14 [7,53,64,65]. However, a study conducted by Knipling et al. [54] indicated that the hardness increase for the addition of Sc and Zr was much higher than that of Sc addition.

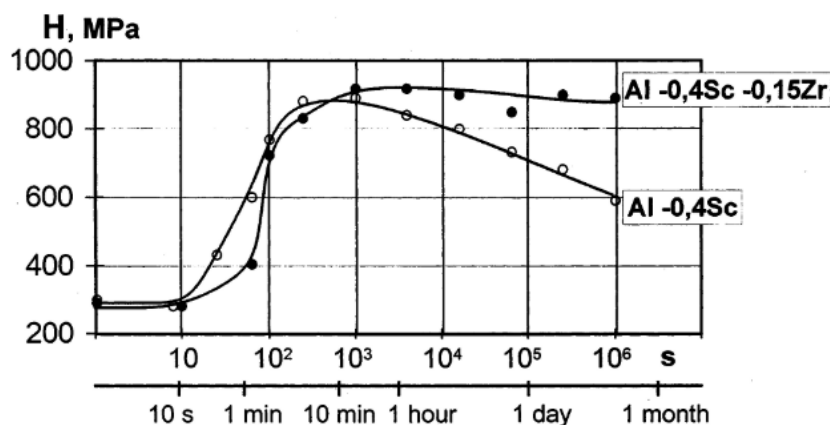


Figure 2.14: Hardness change for Al-Sc-(Zr) alloys with respect to annealing time at 350 °C (reprinted from [7] with permission from Elsevier).

As compared to Al_3Sc , Al_3Zr precipitates need higher precipitation temperature and time [54]. The calculated time-temperature-transformation (TTT) diagram indicated that a homogenisation temperature of 450 °C for a holding time of 10 h should be sufficient to form a 0.05% volume fraction of Al_3Zr [66].

2. Addition of Mg

Very few studies indicated that Mg addition can also be beneficial in improving the thermal stability of Al_3Sc precipitates. Magnesium increases the lattice parameter of aluminium solid solution and hence effectively reduces the coherency strain around Al_3Sc precipitates. The structural mismatch between the α -Al matrix and precipitates is reduced by 50% with a 6.5 wt. % Mg addition [57].

The coherent Al_3Sc precipitates were thermally stable up to 450 °C with an Mg addition of 6.3 wt. % as confirmed by Drits et al. [22]. It is quite well established that the Al_3Sc precipitates in binary Al-Sc alloys are stable up to 350 °C. The maximum Mg addition of up to 6.5 wt. % can be made to Al-alloys, which is a limit for most 5xxx series Al-alloys. Thus, thermal stability can be increased by 100 °C maximum with a 6.5 wt. % Mg addition. So far, there are no studies conducted with an Mg addition greater than 6.5 wt. % to the binary Al-Sc alloys and hence the full potential of Mg for improving thermal stability is unknown.

2.3.3 Hot-working

The strain hardening behaviour of Al-Sc alloys depends on the amount of strain and deformation temperature [67–69]. The strain hardening effect of Al-Sc in comparison to commercially pure Al-alloy (CPAl) after hot rolling at 200 °C was studied by Jindal et al. [69]. As indicated in Figure 2.15, the alloy free from Sc (CPAl) showed increasing work hardening with increasing strain due to increased dislocation density. However, Al-1.0Sc alloy showed two separate modes of work hardening. In the initial mode, increasing work hardening response

was seen for up to 10% deformation probably due to the formation of dislocation tangles confined by precipitates. In the subsequent mode, at a deformation level greater than 10%, no work hardening effect was observed possibly due to the non-uniform interaction of dislocations with precipitates.

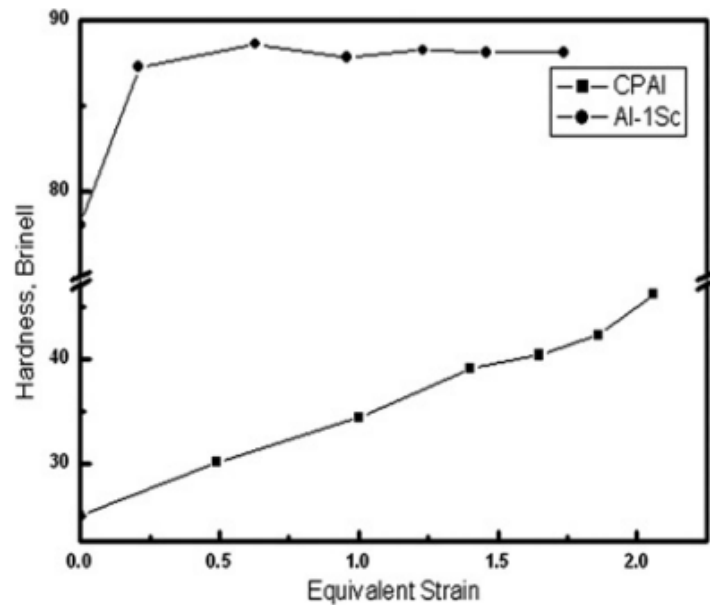


Figure 2.15: Strain hardening effect in (a) commercial pure aluminium (b) Al-1Sc alloy both rolled at 200 °C (reprinted from [68] with permission from Elsevier).

The recrystallization temperature of the alloy increases with Sc concentration [7]. Due to a homogeneous distribution of $\text{Al}_3(\text{Sc,Zr})$ precipitates, Al-Mg-Si [64], Al-Cu-Li-Sc-Zr [70], and Al-Mn-Zr-Sc [71] alloys showed recrystallization resistance up to 450 °C, 470 °C, and 550 °C respectively. However, the study conducted by Ihara et al. [72] indicated that the dynamic recrystallization occurs more frequently in Al-Mg-Sc alloy as compared to Al-Mg alloy for deformation temperatures above 450 °C. The high degree of dislocation density around Al_3Sc precipitates was found to be the main source of nucleating new recrystallized grains. On the other hand, the hot working also is seen to affect the morphology of $\text{Al}_3(\text{Sc,Zr})$ precipitates, and three different morphologies after hot rolling at 400 °C were seen [73]: (1) a rod-shaped

precipitate, (2) spherical precipitate with spherical core and (3) a spherical precipitate with a cylindrical core.

The literature on determining the ease of hot working operation in terms of applied pressure during forming due to the presence of the Al_3Sc phase are scarce. There exists a study on analysing the extrudability of AA6082 and AA7108 alloys, which was degraded marginally due to Sc and/or Zr addition [74].

2.4 Effect of Sc in multi-component systems

Scandium is more useful in Al-alloys when added in ternary or quaternary alloy systems. Reviews of the Al-Sc alloy literature can be found in [75,76]. This section deals with the effects of other common main alloying elements on the Al-Sc system.

2.4.1 Commercially available Sc-bearing Al-alloys

The main alloying additions to aluminium are Si, Cu, zinc (Zn), Mg, and lithium (Li). Out of these elements only Zn, Mg, and Li do not react with Sc. Hence, most of the commercial alloys are based on Al-Mg-Sc (1570, 1571, 1545, 1535, 1523, and 1511), Al-Zn-Mg-Sc (1970, 1975), and Al-Mg-Li-Sc (1421, 1422, and 1424) systems. The performance of all these alloys is superior to their counterparts [7].

In the peak aged condition, the 01570 alloy (Al-6Mg-0.25Sc-0.1Zr-0.4Mn) had an ultimate tensile strength (UTS) of 400 MPa, a yield strength (YS) of 300 MPa, and an elongation of 15%. The observed high strength was attributed to the stable and non-recrystallized microstructure after the hot working process, which was maintained even after solution annealing at 300 °C [42].

2.4.2 Other beneficial elements

Magnesium is found to be most effective in achieving high strength properties due to refined grain size during casting, precipitate strengthening due to coherent $\text{Al}_3(\text{Sc,Zr})$ precipitates, and non-recrystallized substructure after hot rolling. The YS of 433 MPa and UTS of 503 MPa for Al-6Mg-0.5Sc alloy after ageing at 288 °C for 4 h was observed in a study conducted by Sewtell et al. [40]. The alloys were found to be thermally stable up to 288 °C for 100 h without degrading the hardness; however, YS was found to be decreasing rapidly with an exposure of 1 h to 260 °C possibly due to thermally activated dislocation bypass of Al_3Sc particles. An increase of 150 MPa in UTS of Al-Mg alloy with an alloying of 0.2 wt. % Sc and 0.1 wt. % Zr was achieved with a drop in elongation by 10% in a study by Yin et al. [47].

Manganese (Mn) does not react with Sc and improves strength, stabilises polygonised structure, and improves corrosion performance [77]. For Li containing Al-alloys, marginal improvement in mechanical properties has been achieved. In the case of AA8090, hardness increased marginally by 3 HV and 10 HV with an Sc addition of 0.11 and 0.22 wt. % respectively. Similarly, YS increased by 18 MPa and TS increased by 27 MPa in the case of 0.11 wt. % Sc addition. The alloys with Sc addition showed the presence of Al_3Li , non-uniform composite precipitates of $\text{Al}_3\text{Li}/\text{Al}_3(\text{Sc,Zr})$, and precipitate free zones (PFZ) [3].

2.4.3 Other detrimental elements

Chromium (Cr) addition increases exfoliation corrosion susceptibility of Al-Zn-Mg-Sc alloys and hence is undesirable. Iron does not react with Sc and hence when added below 0.8 wt. % does alter the strengthening, anti-recrystallization, or modifying effect of Sc [7]. In another study, the effect of 0.2 and 0.4 wt. % Fe on Al-(5.8-6.8)Si-(0.2-0.35)Mg alloy with 0.2 and 0.4 wt. % Sc was evaluated. Increasing Fe content decreased the modification effect of Sc, whereas the effect of Sc on Fe-intermetallics was found to be beneficial. Iron-rich $\beta\text{-Al}_5\text{FeSi}$

intermetallics were changed to α -Al₈Fe₂Si and other Sc-rich intermetallics with a less harmful morphology [78,79].

Copper can react with Sc to form W-phase (ScCu₇₋₄Al₅₋₈) intermetallics decreasing the strength, plasticity, and crack resistance. Thus, for Cu-containing Al-alloys, lower Sc addition is desirable [7] and studies indicate the possible formation of L₁₂ structured precipitates to improve the strengthening response [80]. For Al-0.72Cu-0.48Sc alloy, the effective temperature for maximum hardening was found to be 200-350 °C with the formation of θ (CuAl₂) and Al₃Sc precipitates; both showing growth and coherency loss at above 400 °C. The coherent θ'' and semicoherent θ' had (100)_p || (100)_m ; [010]_p || [010]_m orientation relationships. The phenomenon of natural hardening i.e. ageing of an alloy at room temperature was almost absent in these alloys [21,80].

Silicon is another detrimental element in the Al-alloys for Sc addition [7]. The interactions of Si and Sc are important for this project and hence detailed discussions about the same are carried out in section 2.5.

2.5 Sc in Al-Si and Al-Mg-Si alloys

Both the heat treatable as well as non-heat treatable category alloys are available in the 4xxx series (Al-Si) alloys. The precipitation kinetics of Si in an Al-1.7 wt. % Si alloy were studied by Lasagni et al. [81] when solutionised at 540 °C for 1 hr. When aged at 270 °C, a mix of globular and platelet Si particles were observed while at 300 °C mostly unstable, globular Si was precipitated which dissolved once heated to 370 °C indicating the unstable nature of Si-precipitates in this alloy system at higher ageing temperatures.

The strengthening response of the ternary Al-Si-Sc alloy system was much different than that of the binary Al-Sc system. Silicon reacted with Sc forming V-phase (AlSi₂Sc₂) which neutralised the effect of Sc addition. Hence, it was recommended to limit Si content to 0.15

wt. % max. [7]. Thus, the Si-Sc interactions are less studied for Al-alloys having higher Si content. Ageing studies on Al-9.72Si-0.45Sc cast alloy done by Kharakterova et al. [21] indicated that an increase of 150 MPa in hardness can be obtained after thermal treatment at 200 °C for 2 to 4 h. Both the non-coherent Si particles and ternary V-phase contributed to this hardening. The two orientation relationships (ORs) of V-phase and the Al matrix were $(\bar{1}2\bar{2})_p \parallel (010)_m ; [221]_p \parallel [100]_m$ and $(\bar{1}\bar{3}4)_p \parallel (010)_m ; [221]_p \parallel [100]_m$.

Commercial Al-alloys usually have some impurity level Si (< 0.2 wt. %) and Fe (< 0.1 wt. %). The impurity Si can be introduced in the Al-alloys from the starting material i.e. primary aluminium of the wrought Al-alloy and/or from the erosion and contamination from the refractory materials lining of the smelter. The source of Fe in Al-alloys is usually from the ores and are not always completely removed during the production and refining of primary aluminium. The presence of these impurities often leads to the formation of insoluble phases like $Al_6(Mn,Fe)$ and $Al_{15}Si_2(Fe,Mn)$ which usually have detrimental effects on the other mechanical properties such as fracture toughness and fatigue resistance [82]. Silicon is of particular importance here, since Si replaces Al atoms in the $L1_2$ crystal structure [83–85], the precipitates formed in these commercial Al-alloys are actually $(Al,Si)_3Sc$ even though they have been broadly reported as Al_3Sc . Throughout this thesis, the nano-precipitates formed in Si-free Al-Sc alloys are referred to as Al_3Sc , whereas those formed in Si-containing Al-Sc alloys are referred to as $(Al,Si)_3Sc$.

Some studies are done focusing on the dilute addition of Si in Al-Sc alloys. Q. Yao [86] indicated that the calculated shear modulus of 62.64 GPa for $(Al,Si)_3Sc$ precipitates as against that of Al (26.1 GPa) can result in a good strengthening effect. The calculations further showed that the $(Al,Si)_3Sc$ precipitate was less brittle than Al_3Sc . The strengthening effect of Al-Sc alloys with the dilute addition of Si was superior to that of alloys without Si addition [85]. It was also noticed that the dilute simultaneous addition of Si and Fe resulted in enhanced

precipitation kinetics and microhardness [87]. The higher Si content (0.06 at. %) was found to be more beneficial than the lower Si content (0.02 at. %) in the alloys upon ageing heat treatment, as indicated in Figure 2.16 [84]. Similarly, in another study [37], a substantial improvement in creep resistance was seen for the Al-Si-Sc-Zr-Er alloy having a higher Si content than the alloy with a lower Si content. The creep improvement was attributed to the formation of a chemically homogeneous core-shell L_{12} nano-precipitates which modified the elastic strain field around them.

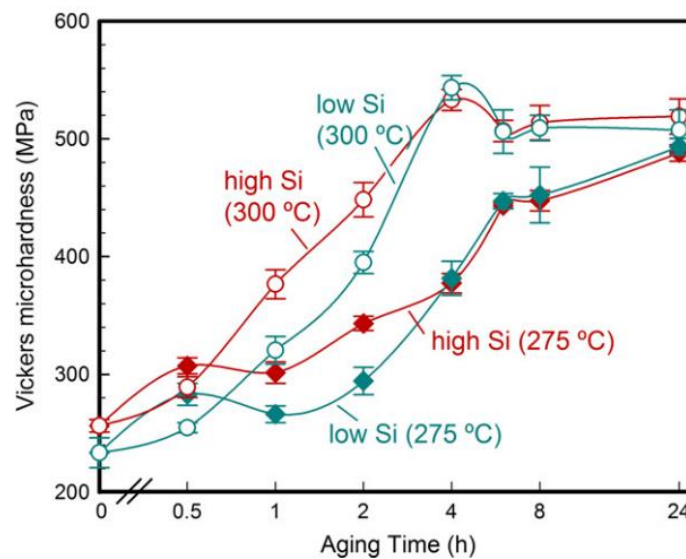


Figure 2.16: Improvement in hardness as a function of ageing treatment for Al-Si-Sc alloys (reprinted from [84] with permission from Elsevier).

The L_{12} structured $(Al,Si)_3Sc$ precipitates were formed at the beginning of decomposition when aged at 300 °C. The alloy experienced a strong hardening effect due to coherent $(Al,Si)_3Sc$ precipitates with a mean diameter of 6 nm. The concentration profile through a single precipitate in Figure 2.17 (c) produced using atom probe tomography (APT) confirmed the composition of precipitate as Al - 25 at. % Sc - 6 at. % Si. Silicon was found to be uniformly distributed throughout the precipitate without any segregation at the interface. Hence, the authors indicated that Si may not produce the effect of anti-coarsening like Zr and Ti does [83]. In another study [88] of 6xxx series Al-alloy, the substitution of Al-sublattice sites by Si was

seen to be much higher of the order of 20 to 25 at. % as compared to the earlier studies [83,84,89] where such substitution was reported to be lesser than 10 at. %.

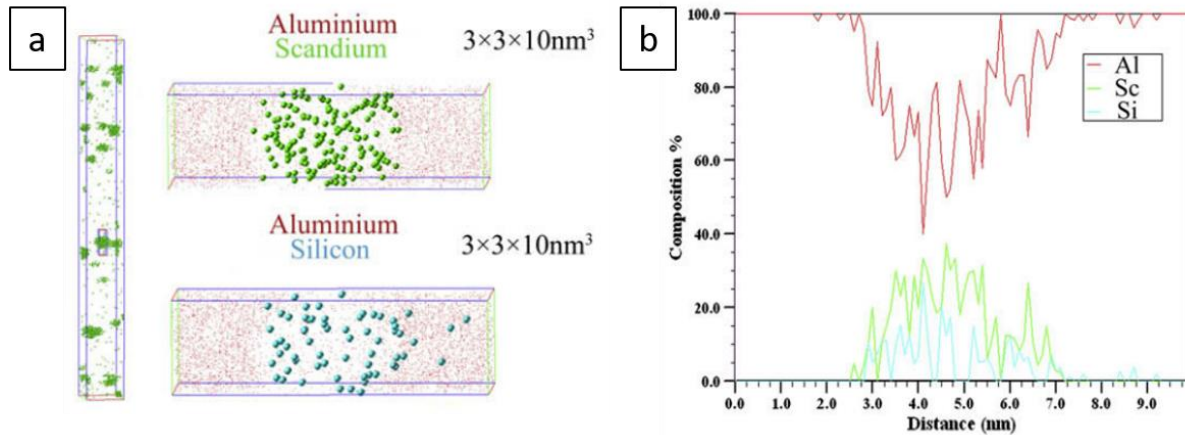
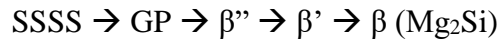


Figure 2.17: 3DAP studies of Al-0.16Sc-0.05Si heat-treated at 300 °C: (a) individual precipitate mapping, (b) concentration profiles of the elements (reprinted from [83] with permission from Elsevier).

Having said this, $(\text{Al,Si})_3\text{Sc}$ precipitates appeared to be coarsening faster than that of Al_3Sc . There exists a study [85] which indicated that Si addition (0.05 wt. %) reduced precipitate coarsening resistance of $\text{Al}_3\text{Sc}_{(1-x)}\text{Zr}_x$. The possible explanation given by the authors was that the Si-Sc pairing might have increased Sc diffusivity in the Zr-enriched shell as well as in the α -Al matrix. Secondly, Si could have also increased Zr diffusion kinetics reducing the coarsening resistance of the Zr-rich shell. The study also indicated that Si was found to eliminate the presence of distinct zones in the case of core-double shell precipitates of AlScZrEr . It was believed that the addition of Si evens out the differences in diffusivities ($D_{\text{Er}} < D_{\text{Sc}} < D_{\text{Zr}}$) and hence the said precipitates did not show the non-flat concentration profiles in the presence of Si. The precipitates constructed using APT revealed that the Si concentration was greater in Sc-rich core than Zr-rich shell in both high- and low-Si alloys [84]. However, no evidence in the literature was found for the change in coherency strain and lattice parameter of $(\text{Al,Si})_3\text{Sc}$ precipitates due to Si addition.

The precipitation sequence in 6xxx series Al-alloys can be given as:



where SSSS is a supersaturated solid solution of an α -Al matrix, and GP zones are a precursor to precipitation. The Sc addition in these alloys is not very well studied probably due to the formation of deleterious phases rather than the desirable $L1_2$ nano-precipitates. Marginal implications of Sc addition on the precipitation strengthening in the 6xxx series Al-alloys are seen [74]. The recrystallization resistance was not improved in the AA6082 alloy due to Sc addition. Further, the extruded and heat treated AA6082 alloy had shown to have a marginal improvement in the tensile strength due to the changes that occurred in the recrystallization structure after extrusion, however, the contribution of Sc and/or Zr was not evident [74]. Yet in another study conducted on extruded AA6082 alloy rods could show a significant increase in yield strength (~ 100 MPa) and UTS (of ~ 85 MPa) due to Sc addition [90]. The needle-like β -phase co-existed with $\text{Al}_3(\text{Sc,Zr})$ nano-precipitates in the solutionised and aged Al-1 wt. % Mg-0.6 wt. % Si alloy resulting in an increased hardness [91], indicating a potential to co-precipitate the hardening phases originally present in these alloy systems and the nano-precipitates of $L1_2$ crystal structure. Commercially available AA1370 alloy (equivalent to AA6056 with additions of Ni, Sc, and Zr) with optimised heat treatment could provide the UTS of 400-420 MPa [92].

2.5.1 Precipitation of $(\text{Al,Si})_3\text{Sc}$ in Al-Si-(Mg)-Sc alloys

The presence of Si in the Al-Sc alloys assisted the nucleation of $(\text{Al,Si})_3\text{Sc}$ nano-precipitates during solidification [27], which was attributed to the attractive Si-Sc binding energies resulting in a strong tendency to form Si-Sc clusters [84]. The Sc migration energy was reduced by 39% in presence of Si in the matrix, where the Si-Sc pairing occurred after the solute-vacancy exchange resulting in accelerated precipitation of Sc atoms and hence Sc-containing phases. A significant amount of Si-Sc and Si-Si clustering at a near-neighbour distance was revealed [84]. The substitution of Si at Al sub-lattice sites in the Al_3Sc precipitate was most

favourable resulting in more relaxed $(\text{Al,Si})_3\text{Sc}$ precipitates; this also accelerated the precipitation kinetics of Sc in $(\text{Al,Si})_3\text{Sc}$ precipitates [83–85].

The studies conducted so far have been focusing on the Al-Sc binary alloy systems and the ternary alloy systems are less explored except those with Mg, Zn, and Li since these elements do not react with Sc. The precipitate evolution is much more complex for the elements which react with Sc, such as Si and Cu. Especially the presence of Si was seen to be deleterious to the hardening effect produced by Al_3Sc precipitates and hence most studies so far on Al-Si-Sc alloy systems are conducted with Si levels lesser than 0.1 wt. % [83,84]. However, most industrially relevant 6xxx series Al-alloys have a Si content of 0.6 to 0.8 wt. %. Hence the effect of Sc addition in Al-Si alloys containing Si level from 0.1 to 0.8 wt. % will be primarily studied in this work. Even if Si is known to be deleterious for the Sc addition in Al-alloys, this deleterious effect is not well studied in the existing literature. Chapter 6 in this thesis will thus examine various characteristics of deleterious phases in Al-Si-Sc alloys and related precipitation mechanisms. There exists limited knowledge about the $(\text{Al,Si})_3\text{Sc}$ precipitate and related effects which will be of main interest for chapter 7.

3 Research aims

A review of the available literature indicates that Sc additions can remain successful in multi-element Al-alloy systems including the 2xxx (Al-Cu), 5xxx (Al-Mg), and 7xxx (Al-Zn-Cu) series systems, with good potential for applications requiring a high specific strength (i.e. aerospace and automotive applications). Although such aforementioned Al-alloys have good mechanical properties, their balance of strength to ductility and their corrosion performance is known to be not optimum. The present research seeks to address the development of a well-balanced Al-alloy, by namely enhancing the strength of alloys, such as the 6xxx series (Al-Mg-Si) Al-alloys. Scandium containing 6xxx series Al-alloys would be ideal candidates for enhanced automotive applications, in addition to extruded products (or Al products that are anodised). However, previous work has highlighted a poor response to Sc additions in 6xxx series Al-alloys mainly due to interactions of Si with Sc. It is necessary to better understand these interactions, to conduct the detailed characterisation of Sc-containing phases and to determine the precipitation mechanisms and processing conditions that will lead to the formation of these phases in Sc-containing 6xxx-series Al-alloys.

The principal aim of this work is to understand the interaction of Sc with Si in the model Al-Si-(Sc) alloys via characterisation of Sc-containing phases, in order to develop strategies to maximise the bulk mechanical properties without compromising other properties. This research work will support the long-term goal of achieving significantly improved strength in Al-Si-Mg-Sc alloys.

One traditional approach to study the effect of Sc is to directly add the required Sc amount into commercial alloys available in the market. However, studies of Sc interactions within such a system are likely to become more complex due to the presence of main alloying elements along with some trace elements added for various purposes (such as Mn, Ti, Zr, etc.)

In the approach herein, model alloys of Al-Si were studied in order to determine the effects of Si on Sc-containing phases. Laboratory scale casting of compositions similar to industrial alloys and subsequent thermo-mechanical processing has been conducted to form wrought alloys in sheet form.

In order to achieve the main objective, the following tasks were conducted:

1. Alloy design:

- Selection of Al-Si-Sc model alloy compositions based on current knowledge from literature, thermodynamic databases, and commercially available alloy databases.
- Development of suitable processing conditions for the thermomechanical processes suitable for the selected alloy compositions.

2. Use of high-end microstructure evaluation techniques:

- Scanning electron microscopy (SEM) and SEM-energy dispersive spectroscopy (EDS): to understand bulk microstructure, intermetallic phases, and primary as well as secondary precipitates.
- TEM and scanning TEM (STEM): to study the micron to atomic level interaction of Sc with Si, which results in Sc-containing precipitates.
- *In situ* TEM: to study the precipitation mechanisms for Sc-containing phases.
- Small-angle x-ray scattering (SAXS): to understand precipitation kinetics by quantifying diameter, number density, and volume fraction of precipitates.
- Atom probe tomography (APT): to understand the composition within nano-sized (Al,Si)₃Sc precipitates.
- Precession electron diffraction (PED): to understand local strain fields at nano-scale due to the presence of coherent (Al,Si)₃Sc precipitates in the α -Al matrix.

3. Evaluation of bulk properties:

- Hardness: to understand the hardness evolution of the alloys as a function of chemical composition and processing conditions.

4 Experimental procedures

This chapter provides details on the design of Al-Si model alloys with and without Sc addition, their manufacturing, and various characterisation techniques utilised to understand their properties and microstructure.

4.1 Alloy composition and heat treatment design

4.1.1 Alloy compositions

Many commercial 6xxx series Al-alloys have Si content up to 0.8 wt. % to get improved fluidity and ductility during the casting process. Literature indicated that the maximum safe limit for Si addition in the Al-Sc alloys is 0.15 wt. % Si to avoid the formation of Sc-containing deleterious phases [7]. Hence, Si concentration used in this study was 0.1, 0.4, and 0.8 wt. % in order to cover both safe and unsafe Si addition. The higher level of Si content was used in order to match that with the conventional AA6xxx series alloys. The Sc-free Al-Si alloys were produced in order to compare the effect of Sc-addition in Al-Si alloys.

The maximum solid solubility of Sc in α -Al at eutectic temperature is 0.33 wt. %, as shown in Figure 4.1. It has been known that Al-Sc alloys have improved quench sensitivity [23], and hence a slow solidification rate of cast ingots in the mild steel mould was considered to be enough to get the required saturated solid solution of Sc in the α -Al matrix. However, due consideration was given to the fact that, upon solidification, a complete solid solution of Sc in α -Al might not be possible if the additions are made close to the maximum solubility limits. Therefore, a slightly reduced Sc concentration of 0.3 wt. % was used for all the three Sc-containing Al-Si model alloys. The Sc content was still on the higher side in order to maximise the Si and Sc interaction effects.

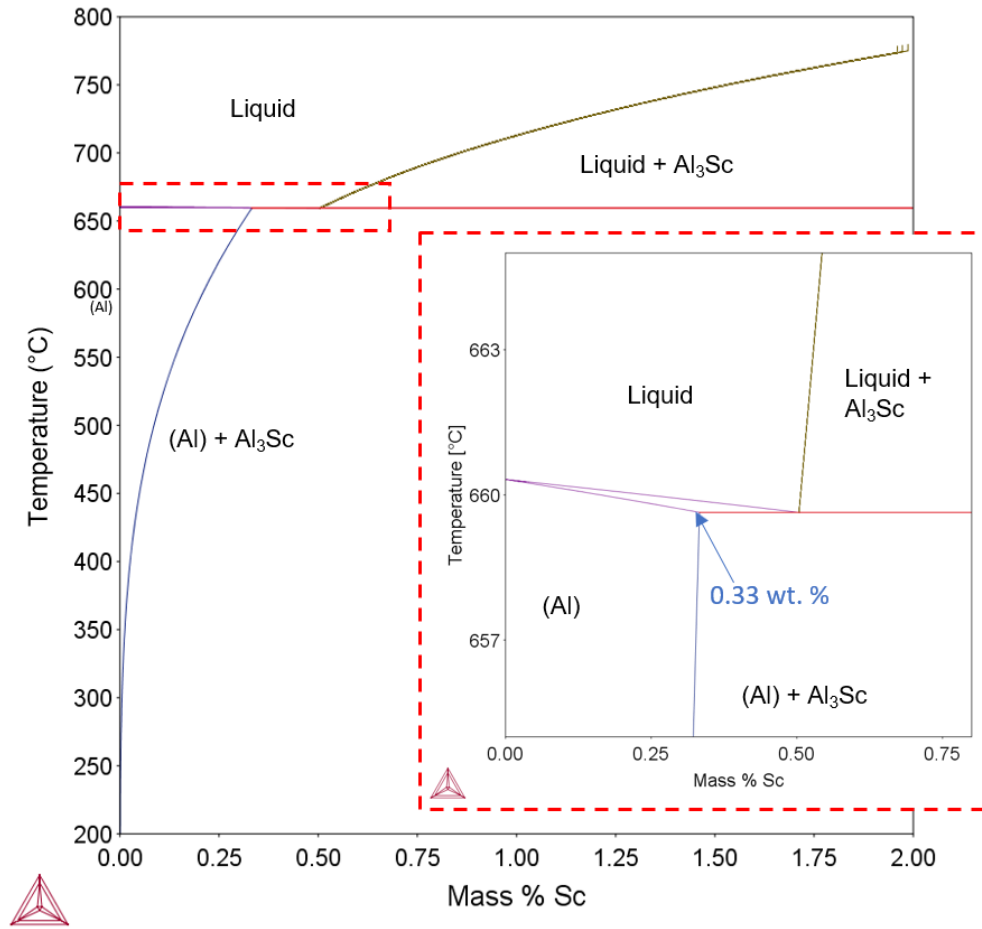


Figure 4.1: Al-rich end of the Al-Sc binary phase diagram calculated using ThermoCalc[®].

The six alloys designed for this study with their nominal compositions are given in Table 4.1.

Table 4.1: Nominal composition of the model Al-alloys.

Model alloy system	Nominal composition (wt. %)
Sc-free alloys	Al-0.1Si
	Al-0.4Si
	Al-0.8Si
Sc-containing alloys	Al-0.1Si-0.3Sc
	Al-0.4Si-0.3Sc
	Al-0.8Si-0.3Sc

4.1.2 Heat treatment design

The equilibrium pseudo-binary phase diagrams were constructed using PANDAT[®] software, version 2012.1.1 from CompuTherm, LLC, USA as well as ThermoCalc[®] software, based on the TCAL-4 thermodynamic database. The software aided in predicting probable phases and designing heat treatments for the Sc-free and Sc-containing alloys.

The binary phase diagram of Al-Si as constructed using PANDAT[®] is represented in Figure 4.2. It can be seen that the solubility of Si in α -Al solid solution increases with increasing Si concentration and temperature. This indicates that the alloys with selected Si concentrations can be heated above the solvus line to get a single-phase α -Al solid solution rich in Si content and upon ageing below the solvus line, a hardening effect can be achieved due to precipitation of Si. Homogenization at 600 °C for 12 h holding time was found to be best for AA4006 alloy (Al-0.86 wt. % Si) and hence similar treatment can be employed for the Al-Si model alloys in this study [93].

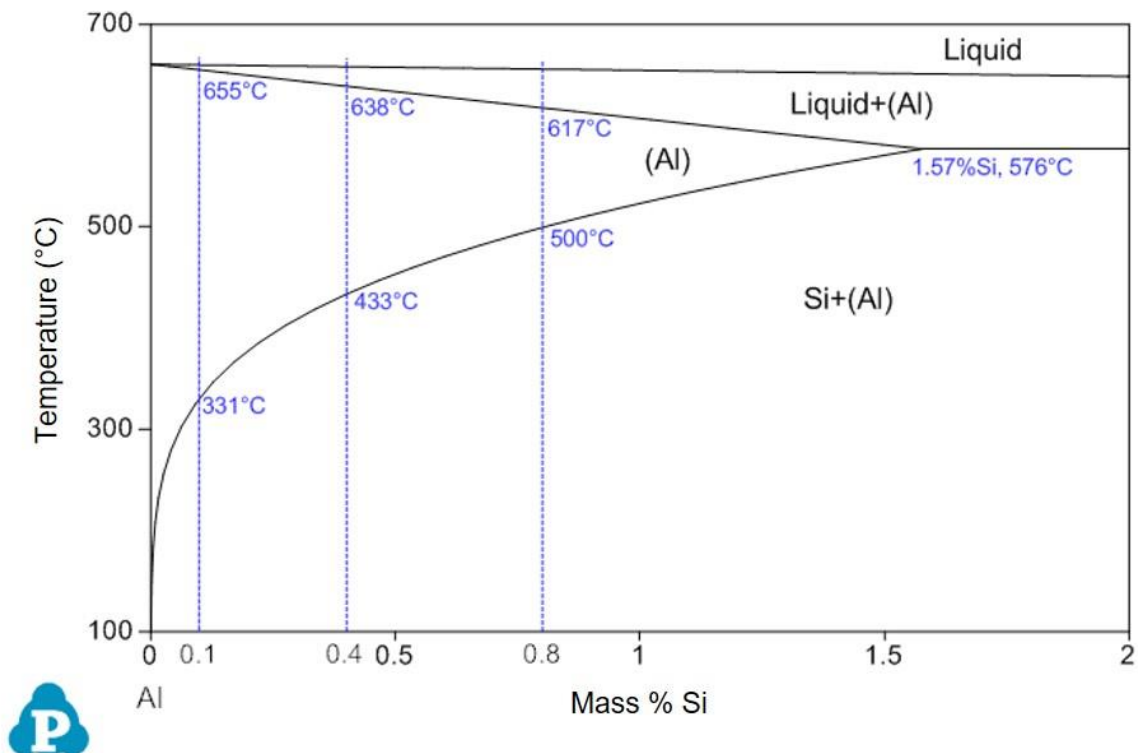


Figure 4.2: Al-rich end of the Al-Si binary phase diagram calculated using PANDAT[®].

In Sc-containing alloys, the phase diagram constructed using PANDAT[®] could not calculate the V-phase (AlSi_2Sc_2) possibly due to the database limitation of the software. On the other hand, ThermoCalc[®] predicted the stable regions for binary Al_3Sc and the ScSi phases, however, the software was unable to predict the ternary V-phase shown in Figure 4.3. In contrast, the formation of V-phase was reported in Al-Si-Sc alloys in previous literature [57,94]. In order to design the heat treatment parameters for the Sc-containing alloys, the ScSi phase stability region was assumed to be equivalent to the V-phase formation region.

The solvus line of Si remains unchanged with Sc-addition. However, a single-phase α -Al solid solution can only be obtained above 648 °C for Si content up to 0.21 wt. % making homogenisation treatment of Al-Si-Sc alloys practically difficult without increasing the risk of local melting. Thus, a low-temperature homogenisation treatment called ‘pre-heat treatment’ was employed in the case of Sc-containing alloys to precipitate out the L_{12} structured $(\text{Al,Si})_3\text{Sc}$ phase without obtaining a saturated solid solution of elements in the α -Al matrix. Due consideration to the thermal stability of Al_3Sc phase was given. It is known that when exposed to a temperature higher than 400 °C, Al_3Sc precipitates do experience coarsening and coherency loss [25]. At 350 °C, some degree of softening, as a result of Al_3Sc precipitate growth and coherency loss, was seen when exposed for a prolonged time [13,25,26,53,54]. Therefore, a pre-heat treatment at 350 °C for a short duration was considered to be the limiting treatment for Sc-containing Al-alloys and is indicated by a horizontal dotted purple line in Figure 4.3. The recrystallization temperature of Al-0.25Sc is 575 °C [55], giving a larger window of operating temperature for hot rolling in the case of Sc-containing Al-Si alloys.

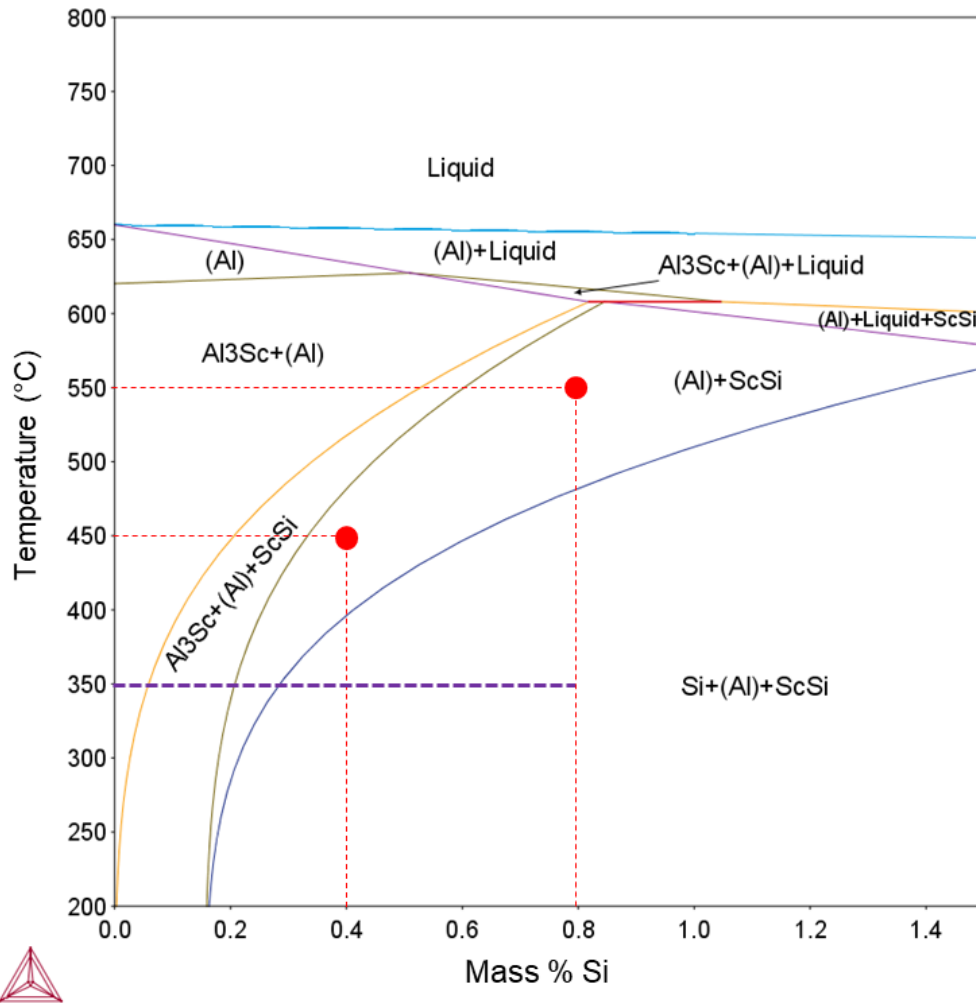


Figure 4.3: Al-rich end of the pseudo-binary Al-Si phase diagram with 0.3 wt. % Sc calculated using ThermoCalc[®].

4.2 Processing of alloys

In order to study the interactions between Si and Sc, the model alloys were made in the wrought form as it is the most common form of the Al-alloys for high strength automotive and aerospace applications. For the thermomechanical processing, a rolling practice has been included depending on the availability of the lab-scale rolling facility. The pre-heat treatment to cast ingots and the final solutionising ageing heat treatments applied to the rolled sheets were performed since heat treatment optimisation is an important aspect of the Sc-containing alloy development. The conventional metallurgical processing route given in Figure 4.4 was adopted for the alloys to form sheets.

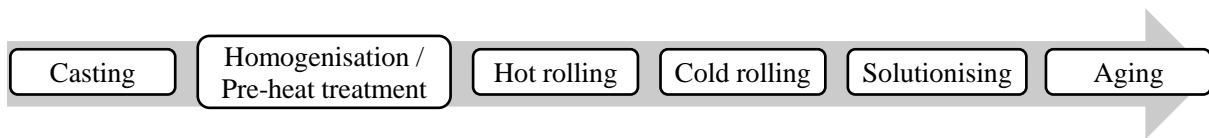


Figure 4.4: Block flow diagram for Al-Si-(Sc) alloys processing sequence.

4.2.1 Ingot casting

All six alloys were cast using a lab-scale gravity die casting facility as per the alloying additions mentioned in Table 4.2. The raw material in their required quantity was added in graphite crucible which was then heated up to 720 °C in a muffle furnace shown in Figure 4.5 (a) to form a liquid melt. An intermittent stirring of the liquid melt for 1 minute was done by the use of a graphite rod and dross was skimmed from the top of the liquid melt. The liquid melt at 720 °C after a holding time of 30 minutes was poured into a rectangular-shaped mild steel mould of dimensions 150 × 50 × 10 mm maintained at room temperature as shown in Figure 4.5 (b). The solidified cast ingots of weight 300 gm were then cooled in the water bath maintained at room temperature within a quench delay of 10 seconds and are shown in Figure 4.5 (c). The casting process parameters were kept similar for all the cast ingots and are given in Table 4.3. The actual chemical composition of all the six alloys was tested in the as-cast condition using inductively coupled plasma – optical emission spectroscopy (ICP-OES) and is given in Table

4.2. It can be seen that the actual composition does not exactly match with the target composition likely due to the use of a lab-scale basic facility for alloy casting and a more sophisticated facility with precise control on casting process parameters can result in a composition closer to the target composition of alloys.

Table 4.2: Raw material additions to the respective alloy ingots and actual chemical composition of the alloys measured using ICP-OES.

Nominal composition (wt. %)	Pure Al (gm)	Pure Si (gm)	Al-2Sc master alloy (gm)	Actual composition (wt. %)		
				Si	Sc	Al
Al-0.8Si	297.6	2.4	0	0.83	--	Balance
Al-0.8Si-0.3Sc	252.6	2.4	45	0.86	0.20	Balance
Al-0.4Si	298.8	1.2	0	0.43	--	Balance
Al-0.4Si-0.3Sc	253.8	1.2	45	0.48	0.25	Balance
Al-0.1Si	299.7	0.3	0	0.13	--	Balance
Al-0.1Si-0.3Sc	254.7	0.3	45	0.14	0.32	Balance

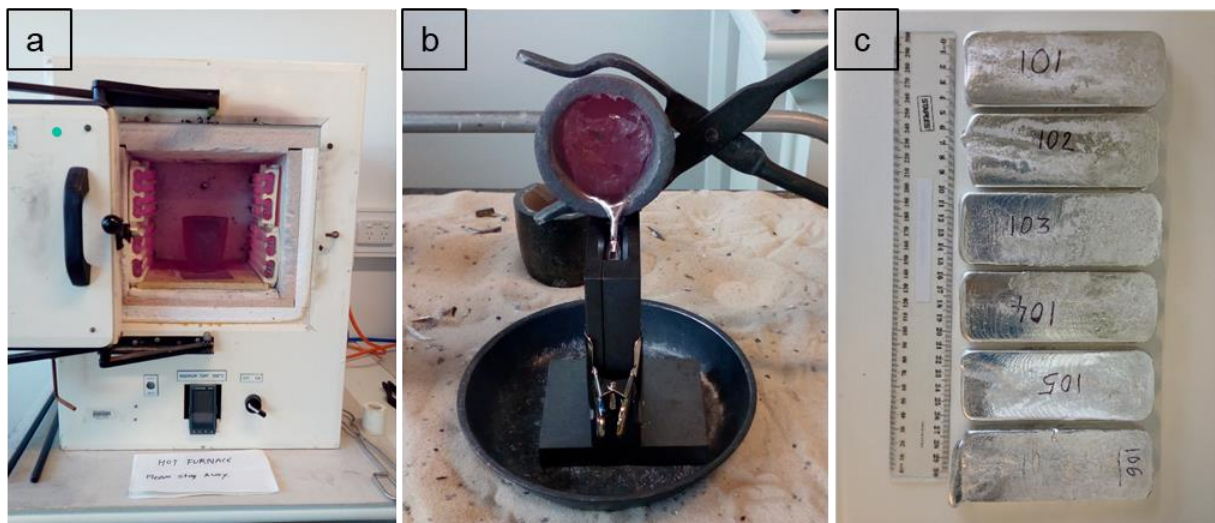


Figure 4.5: (a) Muffle furnace used for the melting of raw materials, (b) liquid metal being poured into the rectangular-shaped mild steel mould, (c) Al-Si-Sc cast ingots after cooling.

Table 4.3: Gravity die casting process parameters.

Sr. No.	Casting parameter	Value
1	Melt temperature (°C)	720
2	Liquid metal hold time (minutes)	30
3	Stirring time (minutes)	1
4	Pouring temperature (°C)	720
5	Ingot size (L × W × T)* (mm)	(150 × 50 × 10)

*L: length; W: Width; T: Thickness

4.2.2 Homogenisation / pre-heat treatment of cast ingots

The Sc-free Al-Si alloys were homogenised at 600 °C for 16 h in a salt bath furnace followed by water quenching with a quench delay of less than 10 s.

The homogenisation treatment is referred as ‘pre-heat treatment’ for the Sc-containing alloys since an effective homogenisation of the microstructure is probably not achieved due to the selection of lower heat treatment temperature for these alloys as compared to that for Sc-free alloys. To find the optimum pre-heat treatment time for the Sc-containing alloys, few trials at 250 °C, 300 °C, and 350 °C temperature, each with varying treatment time (0.5, 1, 2, 4, 8 h) were conducted on the Al-0.1Si-0.3Sc alloy. In order to restrict the coarsening of (Al,Si)₃Sc dispersoids, the shortest feasible holding time of 0.5 h at 350 °C corresponding to the peak hardness of the alloy, was selected and utilised for the pre-heat treatment of other Al-Si-Sc alloys. Thus, the three Sc-containing alloys were pre-heat-treated at 350 °C for 0.5 h in a salt bath furnace followed by quenching in a water bath maintained at room temperature within a quench delay of 10 s.

4.2.3 Hot and cold rolling of ingots

All the homogenised / pre-heat-treated alloy samples were hot-rolled at 350 °C down to 4 mm and then cold-rolled down to 1 mm using a Buehler four-high lab-scale rolling mill facility shown in Figure 4.6 (a). The rolls were cold during the hot rolling passes. A separate muffle furnace was used to heat the samples between each pass at the desired temperature of 350 °C for a soaking duration of 10 minutes. The rolling schedule was performed only once and is given in Table 4.4. All the alloys were formed easily during the rolling and no rolling defects were observed during the processing (refer Figure 4.6 b).

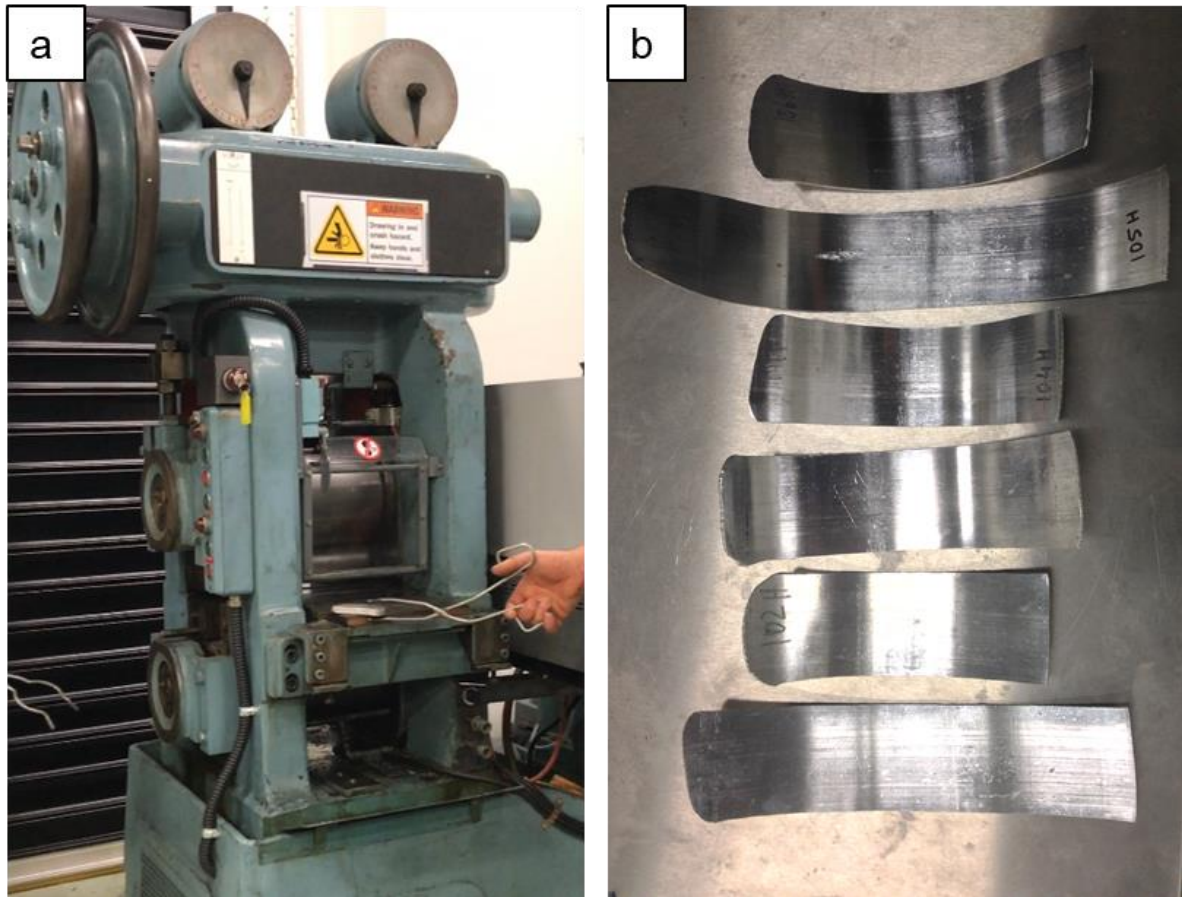


Figure 4.6: (a) Buehler four-high lab-scale rolling mill used for hot and cold rolling of ingot samples, (b) the rolled sheet of Al-Si-(Sc) alloys.

Table 4.4: Hot and cold rolling process parameters.

Process	Rolling speed (rpm)	Temperature (°C)	No. of passes	% reduction in each pass	Initial T* (mm)	Final T* (mm)
Hot rolling	68	350	4	1 st pass: 18 2 nd pass: 22 3 rd pass: 29 4 th pass: 20	11 mm	4 mm
Cold rolling	68	Room temperature	3	1 st pass: 25 2 nd pass: 33 3 rd pass: 50	4 mm	1 mm

*T: Thickness

4.2.4 Solutionising and ageing of sheets

In order to study the Si and Sc interactions and to form the deleterious V-phase, a higher solutionising temperature was selected for the Sc-containing alloys having a medium (0.4 wt. %) and high (0.8 wt. %) Si content. Differing solutionising temperatures were used for the two alloys depending on Si concentration. The solutionising temperatures utilised were just above the solvus line i.e. 550 °C, and 450 °C for Al-Si-Sc alloys with 0.8 wt. % Si, and 0.4 wt. % Si respectively (refer phase diagrams in Figure 4.3). The ageing treatment at 250 °C with varying soaking time was performed subsequently to produce sheets of T6 temper (i.e. solution heat-treated and artificially aged condition).

Table 4.5: Solutionising and ageing process parameters.

Alloy composition (wt. %)	Solutionising cycle	Ageing cycle
Al-0.8Si-0.2Sc	550 °C / 0.5 h	250 °C for 0.5, 1, 2, 4, 8, 24 h
Al-0.4Si-0.25Sc	450 °C / 0.5 h	250 °C for 0.5, 1, 2, 4, 8, 24 h

The solutionising treatment was performed in a salt bath furnace followed by water bath quenching at room temperature within a quench delay of 10 seconds. All the samples were naturally aged for 3 days before the artificial ageing. The ageing treatment was conducted in a muffle furnace with an air atmosphere followed by air cooling.

The entire processing sequence for the alloys has been illustrated in Figure 4.7.

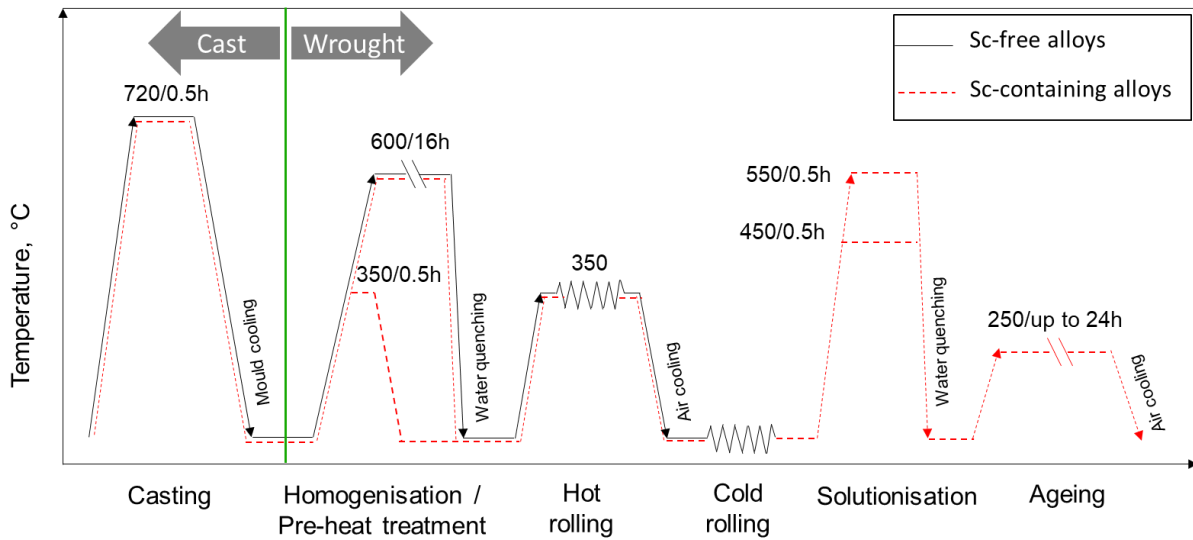


Figure 4.7: Schematic of processing sequence and process parameters followed for Al-Si-(Sc) alloys.

4.3 Characterisation techniques used

Various characterisation techniques were used to evaluate the Al-Si-(Sc) alloys in various processing conditions for their properties as well as related microstructural characteristics.

4.3.1 Hardness testing

Bulk hardness measurements were conducted using Struers[®] Duramin A-300 Vickers hardness tester. The samples for measurement were cut at the centre from the cast ingots as well as rolled sheets. The measurements were conducted at the centre of the cross-section to eliminate any associated surface hardening effects. The sample surface was polished on both sides of the alloy sheet using silicon carbide (SiC) emery paper up to 800 μm before measurements. Hardness values were taken at 7 different locations at 1 kg applied load. The hardness was plotted for the average of the 7 measurements and error bars represent the standard deviation calculated for these measurements for each sample.

4.3.2 Microstructure analysis

Scanning electron microscopy

The bulk samples for microstructure study were cut from the centre of the cast ingots as well as rolled strips using slow speed saw cutting machine and polished using 1200 μm SiC emery papers. Polishing of the sample surface till the mirror finish was achieved using a 3 μm and 1 μm diamond suspension on Struers[®] automatic sample polishing machine. The samples were then analysed for the microstructural features using JEOL[®] 7001F SEM in the secondary electron imaging (SEI) mode. The EDS mode was used to assess the chemical composition of the phases and the matrix with an uncertainty ranging from 30 to 50%. The SEM was operated at a standard operating condition of 15 kV.

Transmission electron microscopy

The structural and chemical characterisation of various phases in the alloys was conducted using TEM imaging, *in situ* TEM and PED techniques. The samples were cut from the middle

of the ingots and rolled strips to avoid surface and edge defects. The 3 mm discs were punched from thin alloy sheets of an initial thickness of 200 μm and then ground to 120 – 170 μm thickness. Two techniques were utilised to prepare TEM foils: (1) electropolishing, (2) ion milling. The discs were electro-polished with 30% nitric acid – 70% methanol electrolyte at - 30 °C until forming a central hole in the foil. The Struers[®] Tenupol electro-polishing unit uses a twin-jet flow system for the electrolyte. The cell voltage was 12.7 V, the current was 180-190 mA and approximate electro-polishing time was 3 to 4 minutes depending on the foil thickness. The ion milling was done using Gatan[®] 691 precision ion polishing systems at - 100 °C.

The thin foil samples were then observed in the bright-field (BF) and dark-field (DF) modes using FEI[®] Tecnai G² T20 TEM and FEI[®] Tecnai G² F20 STEM operated at 200 KV. Additionally, high-angle annular dark-field (HAADF)-STEM image mode was utilised. All the images were analysed using Digital Micrograph software. The EDS mode was used to understand the elemental analysis using a Bruker[®] Quantax 400 detector in the FEI[®] Tecnai G² F20 STEM. To study the crystal structure characteristics of the phases, the Crystal Maker[®] software was utilised.

In situ TEM heating

For the *in situ* TEM heat treatment experiments, a JEOL[®] 2100 LaB₆ TEM was utilised. Specimens were prepared by ion milling 3 mm diameter discs of 45 μm thickness using a Fishione Model 110. The heating was conducted using a Gatan[®] heating holder model 628 which utilises the electrical heating system. The microstructures were recorded *in situ* via a Debut digital screen capture software using a Gatan[®] Orius 832 fiber optic 10.7-megapixel CCD detector.

Local strain field mapping

The strain distributions in the TEM foils at the nanometer scale were measured using PED NanoMEGAS[®] DigiSTAR[™] system on a JEOL[®] 2100 F TEM. Appropriate specimen areas of size $100 \times 100 \text{ nm}^2$ and $50 \times 50 \text{ nm}^2$ containing nano-scale $(\text{Al,Si})_3\text{Sc}$ precipitates were selected for measurements with a scan step size of 1 nm and 0.5 nm respectively. The strain analysis was conducted using a Topspin[®] software package.

4.3.3 X-ray diffraction (XRD)

Samples of $20 \times 20 \times 10 \text{ mm}$ dimensions were polished using SiC emery paper until $800 \mu\text{m}$ for XRD analysis. The XRD equipment with a Cu $K\alpha$ radiation at 40 kV and 40 mA of Bruker[®] D8 Advance - DAVINCI design was utilised for conducting the scans. The 2θ range used was 5° to 80° with a step size of 0.015° . The international centre for diffraction data (ICDD) PDF-4 + 2018 RDB database with an analytical software Bruker[®] DIFFRAC.EVA V4.3 was utilised for the analysis of phases.

4.3.4 Small-angle x-ray scattering (SAXS)

Thin samples of size $9 \times 9 \mu\text{m}$ were cut from the middle of the ingot samples using a low speed saw cutting machine along the transverse section. The samples were then manually thinned down to $\sim 75 \mu\text{m}$ thickness with a SiC emery paper of $800 \mu\text{m}$ size. The SAXS instrument of Bruker[®] N8 Horizon with Cu microbeam radiation and Vantec-500 2D detector was utilised. The data analysis was conducted using Bruker[®] DIFFRAC.SAXS V1.0 software. For simplicity, all the precipitates were considered to be spherical. Initially, Porod and Laue corrections for the background noise were done to the imported raw data [95]. The Guinier plot was used to estimate the Guinier radius (R_g) and the nano-precipitate radius (R). The slope of the linear part of the Guinier plot equals to [95],

$$\frac{R_g^2}{3}, \text{ and } R_g = \sqrt{\frac{3}{5}} R \quad \text{Equation 1}$$

The values of $q_{\min} R_g$ to $q_{\max} R_g$ were maintained between 0.87 to 2.58 to have consistency between different samples while comparing. Here, q is the amplitude of the scattering vector. The Kratky plots (Iq^2 vs q) were used to compare the precipitate volume fractions [95] where an integrated area under the curve, also known as the invariant (Q), was calculated first, which was then utilised to estimate the volume fraction (f_v) of the precipitates using the equation,

$$Q = 2\pi^2 (\rho_p - \rho_m)^2 f_v (1-f_v) \quad \text{Equation 2}$$

Where ρ_p and ρ_m are the scattering length densities of precipitates and matrix respectively. To calculate ρ_p , the presence of Si in the precipitate was ignored to simplify the calculations. Thus, ρ_p was calculated using,

$$\rho_p = \frac{1}{4} (3\rho_{Al} + \rho_{Sc}) \quad \text{Equation 3}$$

where, ρ_{Al} was $22.437 \times 10^{-6} \text{ \AA}^{-2}$ and ρ_{Sc} was $24.071 \times 10^{-6} \text{ \AA}^{-2}$ for the x-ray source. The $(Al,Si)_3Sc$ precipitate number density (N) was calculated from the estimated radius and volume fraction of the precipitates using,

$$N = \frac{3f_v}{4R^3} \quad \text{Equation 4}$$

4.3.5 Atom probe tomography

Thin needle samples were first wire cut from the middle of the ingot samples using the electron discharge machining (EDM) technique to a cross-section of $300 \times 300 \mu\text{m}$ and a length of 1 cm. The electropolishing of the needles was then carried out in two stages at room temperature using the Struers[®] Lectropol 5 electrolytic polishing unit. The first stage of electropolishing was done using an electrolyte composed of 33% nitric acid and 67% methanol at a cell voltage of 7-10 V. The second stage of electropolishing was conducted using 2% perchloric acid and 98% methanol solution at a cell voltage of 10-20 V under an optical microscope. The APT was carried out on a CAMECA[®] LEAP 4000 HRTM instrument at a pulse rate of 200 kHz, a temperature of 25 K, and a pulse fraction of 20%. The three-dimensional atom probe (3DAP)

reconstruction of the acquired data was done using IVAS™ 3.8.2 software. The default image compression factor of 1.40 and the default electric field factor of 4.3 was used.

5 Design and development of Sc-containing Al-Si alloys

5.1 Synopsis

This chapter is focused on the details of the design and manufacturing of Sc-containing and Sc-free Al-Si alloys. Phase diagrams to predict the possible phases that can form in the solidified microstructure during the casting process for the respective alloys was carried out with the aid of ThermoCalc[®]. The thermomechanical processing of all the cast ingots was done in accordance with the wrought aluminium semi-products to make rolled sheets of F-temper. The temperatures for heat treatments and hot rolling were designed considering the phase diagrams for the respective alloys. The alloys were then characterised for the bulk hardness and microstructure analysis. The Sc-containing Al-Si alloys showed an average 30% improvement in the hardness results as compared to that of the Sc-free Al-Si alloys, which was correlated to the microstructural observations. The coherent (Al,Si)₃Sc nano-precipitates were formed during the low-temperature homogenisation treatment at 350 °C for 30 minutes in the case of the Al-Si-Sc alloys. These nano-precipitates retained their coherency with the α -Al matrix during the subsequent thermomechanical processing and was seen to be the main attribution to the increased hardness.



Optimised Composition and Process Design to Develop Sc-Enhanced Wrought Al-Si Alloys

Jayshri Dumbre, Timothy Langan, Thomas Dorin, and Nick Birbilis

Abstract

In a number of aluminium (Al) alloys to date, scandium (Sc) additions have revealed a significant and beneficial effect on strengthening, even when added in small quantities. However, the strengthening response of the ternary Al-Si-Sc alloy system has been hampered by an apparent unfavourable interaction between silicon (Si) and Sc; forming the deleterious V-phase (AlSc_2Si_2) and thus limiting the allowable Si-content to ~ 0.15 wt.%. In this study, phase diagrams were calculated using CALPHAD and utilised to design Al-Si-Sc alloy compositions and heat treatment parameters. The Al-Si-Sc alloys were processed using a conventional route of wrought aluminium semi-products. A hardness improvement of up to 30% was achieved for the alloys containing Si as high as 0.8 wt.% in the F-temper. The improved hardness was mainly attributed to the homogeneously distributed, coherent, $(\text{Al,Si})_3\text{Sc}$ nano-dispersoids in the α -Al matrix formed during a low temperature annealing treatment and retained in the F-temper condition.

Keywords

Al-alloys ■ $(\text{Al,Si})_3\text{Sc}$ ■ CALPHAD ■ Nano-dispersoids

J. Dumbre (&) N. Birbilis

Department of Materials Science and Engineering, Monash University, Clayton, VIC 3800, Australia
e-mail: jayshri.dumbre@monash.edu

T. Langan
Clean TeQ Ltd., Notting Hill, Australia

T. Dorin
Institute for Frontier Materials, Deakin University, Geelong, VIC 3216, Australia

Introduction

The conventional AA6xxx series (Al-Mg-Si) alloys are most widely used due to their good corrosion resistance and moderate strength. Traditionally strength improvement in AA6xxx alloys is achieved by addition of copper (Cu) [1], however, Cu is associated with degradation in corrosion performance. On the other hand, studies indicate that alloying with Sc in small quantities has a potential to achieve significantly higher strength in commercial Al-alloys while maintaining corrosion resistance [2, 3]. The improved strength in Al-alloys due to the addition of Sc is principally attributed to the formation of coherent and homogeneously distributed, Al_3Sc nano-dispersoids with an optimum precipitate size of 1.5 nm in the alloy matrix [4, 5]. As a result, Sc-containing (and therefore Sc-enhanced) Al-Mg alloys known as Scal-malloy[®], Al-Zn-Mg alloys (AA1970, AA1975) and Al-Mg-Li alloys (AA1421, AA1422, AA1424) have been developed. On the contrary, very little work has been reported in the development of Sc-containing Al-Si and Al-Si-Mg alloys; not only due to the cost implications resulting from the addition of Sc, but the detrimental effects of Si on beneficial Sc-bearing phases [6]. A complete review of the Al-Sc literature can be found in [7]. In the case of Al-Si-Sc alloys, the V-phase (AlSc_2Si_2), Al_3Sc and Si phases are found to be in equilibrium with α -Al solid solution [8]. The intermetallic V-phase is known to be a deleterious phase resulting in the degradation of mechanical properties leading to a recommended maximum Si addition of 0.15 wt.% in these alloys [6]. As opposed to this, both the V-phase and the non-coherent Si precipitates were reported to be enhancing the strength of Al-9.72Si-0.45Sc cast alloy during ageing at 200 °C for 2–4 h [9]. Superior strengthening was found in the case of dilute addition of Si (0.02–0.06 at.%) to Al-Sc alloys [10–12]. These alloys show the decomposition phase upon ageing to be L1_2 structured coherent $(\text{Al,Si})_3\text{Sc}$ dispersoids. The composition of these dispersoids was measured as

Al—25 at.% Sc—6 at.% Si using Atom Probe Tomography (APT). Silicon was found to be uniformly distributed throughout the dispersoid without any segregation at the interface [13]. The shear modulus of 62.64 GPa was calculated for $(\text{Al,Si})_3\text{Sc}$ dispersoids as against that of Al (26.1 GPa) indicating that a good strengthening effect can be achieved with the homogeneous distribution of these dispersoids in Al-matrix. The calculations also showed that the $(\text{Al,Si})_3\text{Sc}$ dispersoid was less brittle than Al_3Sc [12]. The precipitation rate, as well as the coarsening rate, was appeared to be faster in case of $(\text{Al,Si})_3\text{Sc}$ dispersoids than that of Al_3Sc dispersoids [10, 11], which was mainly attributed to the reduced Sc migration energy. The calculations further confirmed that the substitution of Si at Al sub-lattice sites in the Al_3Sc precipitate forming the more relaxed $(\text{Al,Si})_3\text{Sc}$ precipitate was most favourable; this also accelerated the precipitation kinetics of Sc in $(\text{Al,Si})_3\text{Sc}$ precipitates [10, 11, 13]. Recent work showed that the presence of 0.6 wt.% Si resulted in the formation of $(\text{Al, Si})_3\text{Sc}$ during casting. The content of Si in the dispersoids was also found to decrease as a function of ageing time which confirms that Si mainly plays a role during the nucleation and early ageing stages [14].

To date, the success for the Sc-addition to Al-alloys was achieved for Al-Mg-Sc and Al-Zn-Sc since Mg and Zn in respective alloys do not react with Sc. On the other hand, due to unfavourable Si-Sc interactions, although Si is a major and traditional alloying addition to most Al-alloys, the Al-Si-(Mg)-Sc alloys were hardly studied. The scarce studies on Al-Si-Sc alloy systems are conducted with Si levels lesser than 0.1 wt.% [10, 13]. However, most industrially relevant wrought Al-alloys have a Si content of 0.6–0.8 wt.% and there exists limited approaches to mitigate the formation of V-phase. This work deals with Al-Si-Sc alloys with Si-content up to 0.8 wt.% to get improved hardening effect due to $(\text{Al,Si})_3\text{Sc}$ dispersoids.

Experimental Procedures

Alloy Compositions

Commercial AA6xxx alloys have Si content up to ~0.8 wt.% for improved fluidity during casting, and balanced ductility in the final form. The literature indicates 0.15 wt.% Si as the maximum ‘safe’ limit for Al-Sc-Si alloys to avoid Sc-Si interactions [6]. Hence, Si concentration of 0.1, 0.4 and 0.8 wt.% were used in the alloys in order to cover both so-called safe and unsafe Si-content. A Sc-concentration of 0.3 wt.% was chosen for all the three Sc-containing Al-Si alloys. Table 1 gives the chemical composition for all the six alloys under study which were tested using Inductively Coupled Plasma-Optical Emission Spectroscopy (ICP-OES) in the as-cast condition.

Processing of the Alloys

All the alloys were prepared using a 99.86 wt.% pure Al, pure Si and Al-2 wt.% Sc master alloy. The alloys were cast using a lab-scale casting facility into a rectangular shaped mild steel mould of size 150 × 50 × 10 mm from a superheat temperature of 720 °C and were then cooled in a water bath maintained at room temperature. The Sc-free Al-Si alloys were homogenised at 600 °C for 16 h in a salt bath furnace followed by water quenching with a quench delay of less than 10 s. In the case of Sc-containing Al-Si alloys, the optimised heat treatment cycle of 350 °C for 30 min holding time was conducted in order to form $(\text{Al,Si})_3\text{Sc}$ nano-dispersoids.

All the homogenised ingots were hot rolled at 350 °C from 10 mm thickness until 4 mm and then subsequently cold rolled to form F-temper sheets of 1 mm thickness. The schematic representation of the processing route is given in Fig. 1.

Table 1 Chemical composition for the six alloys under study measured using ICP-OES^a

Model alloy system	Nominal composition (wt.%)	Si		Sc		Al
		wt. %	at. %	wt. %	at. %	wt. %, at. %
Sc-free alloys	Al-0.1Si	0.13	0.13	–	–	Balance
	Al-0.4Si	0.43	0.42	–	–	Balance
	Al-0.8Si	0.83	0.80	–	–	Balance
Sc-containing alloys	Al-0.1Si-0.3Sc	0.14	0.14	0.32	0.19	Balance
	Al-0.4Si-0.3Sc	0.48	0.46	0.25	0.15	Balance
	Al-0.8Si-0.3Sc	0.86	0.83	0.20	0.12	Balance

^aAll the alloys had iron (Fe) content of 0.08 wt.% (0.04 at.%)

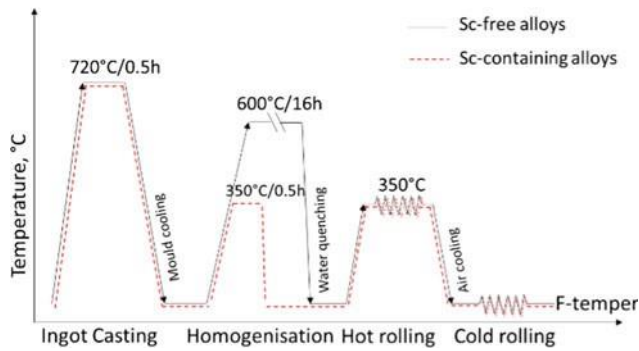


Fig. 1 Processing parameters and sequence followed for all the alloys

Equilibrium Phase Prediction Using CALPHAD

The equilibrium phase diagrams for the alloys under study were constructed using ThermoCalc™ with the use of the TCAL-4 thermodynamic database. In order to understand the effect of actual Si and Sc-content on the phases formed in the model alloy systems, the equilibrium phase fractions were also calculated against the solidification temperatures for all the three Sc-containing alloys. Further, the equilibrium phase fractions in Al-Si-Sc alloys at 350 °C were analysed.

Characterisation Techniques

Bulk hardness measurements were conducted using Struers Duramin A-300 Vickers hardness tester. The sample surface

was polished on both the sides up to 800 μm prior to measurements. Hardness values were taken at 10 different spots at 1 kg applied load and then averaged. The analysis of phases was conducted using SEI (Secondary Electron Imaging) and EDS (Energy Dispersive Spectroscopy) modes of JEOL 7001F™ SEM (Scanning Electron Microscope). The samples for TEM (Transmission Electron Microscope) were prepared by manual thinning to 120–170 μm thickness followed by punching of 3 mm discs. The discs were then electro-polished with 30% Nitric acid–70% Methanol electrolyte at –30 °C until the formation of a central hole in the foil. The Struers Tenupol 5™ electro-polishing unit uses a twin-jet flow system for the electrolyte. The cell voltage was 12.7 V, the current was 180–190 mA and approximate electro-polishing time was 3–4 min depending on the foil thickness. The thin foil samples were then observed in BF (Bright Field) mode using FEI Tecnai G² T20™ TEM at 200 kV at Monash Centre for Electron Microscopy (MCEM).

Results and Discussion

Phase Diagrams

The binary phase diagram of Al-Sc in Fig. 2a indicates that the maximum solubility of Sc in Al at the temperature of eutectic transformation is ~ 0.33 wt.%, a eutectic composition is 0.5 wt.% Sc, and the solidification has a very narrow

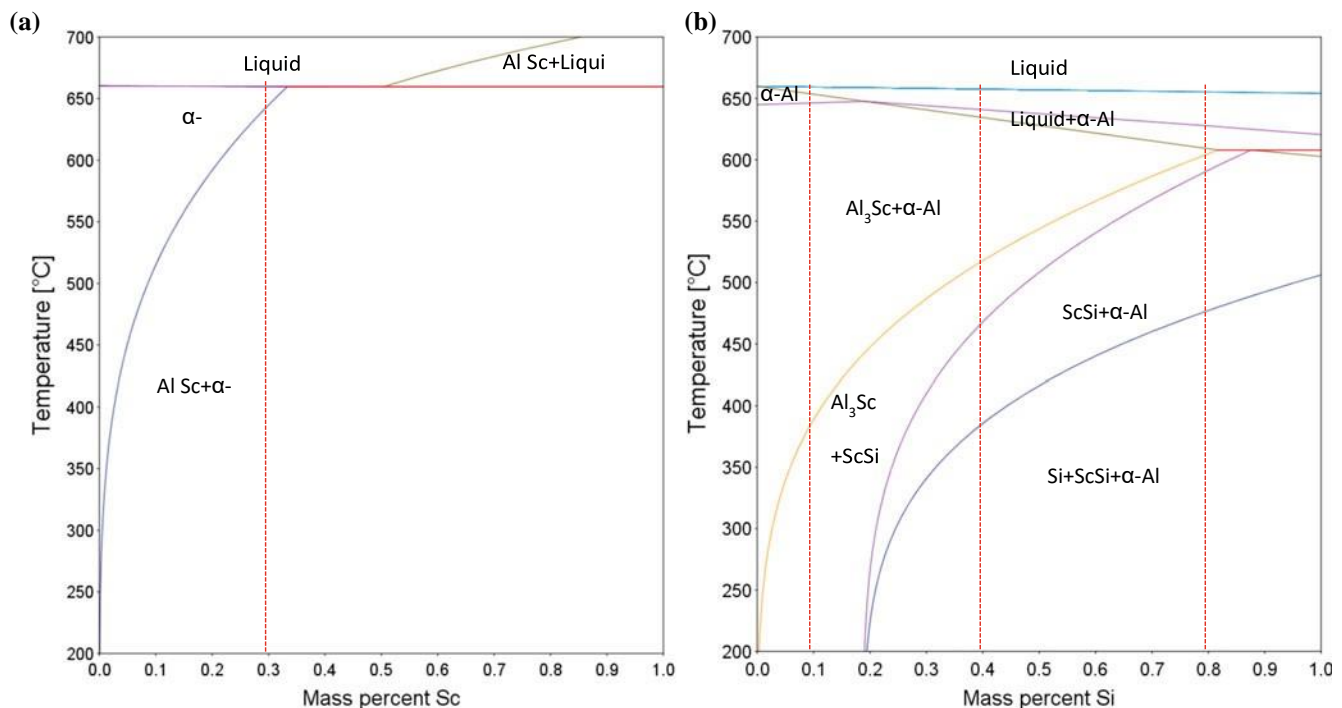


Fig. 2 Calculated Al-rich side of the **a** binary phase diagram of Al-Sc system, **b** pseudo-binary Al-Si system for constant 0.3 wt.% Sc

range. The equilibrium, coherent Al_3Sc (Scandium Aluminide) phase is directly formed during a eutectic reaction occurring at 660°C [15]. The Sc-content chosen for the alloys in this study is 0.3 wt.% which is a slightly reduced concentration than the maximum solubility limit of Sc in $\alpha\text{-Al}$. From Fig. 2a and b, it can be seen that the Al_3Sc solvus temperature of 648°C remains unchanged with the addition of Si and the vice versa is not true [16]. Thus, homogenisation of Al-Si-Sc alloys is practically difficult without increasing risk of local melting. Hence, a low-temperature homogenisation treatment of these alloys will be just enough to form $(\text{Al},\text{Si})_3\text{Sc}$ nano-dispersoids. The recrystallization temperature of Al-0.3Sc alloy is 580°C [6], giving a larger window of operating temperature for hot rolling for these alloys.

Equilibrium Phase Analysis in Sc-Containing Al-Si Alloys

The amount of $\text{Al}_9\text{Fe}_2\text{Si}_2$ intermetallic phase is similar in all the three alloys due to similar Fe-content as shown in Fig. 3a–c. The other Fe-rich phases ($\text{Al}_8\text{Fe}_2\text{Si}$ and $\text{Al}_{13}\text{Fe}_4$) are not stable at temperatures lower than 450°C . The amount of pure-Si phase depends on the Si-content in the alloy. The stable Al_3Sc primary phase is only present in the alloy with low Si-content (0.1 wt.%). Conversely, the ScSi intermetallic phase is higher in alloys with high Si-content (0.4 and 0.8 wt.%). The variation in the amount of the equilibrium phases at 350°C (the homogenisation treatment temperature) with changing Sc to Si ratio for the three Sc-containing alloys is

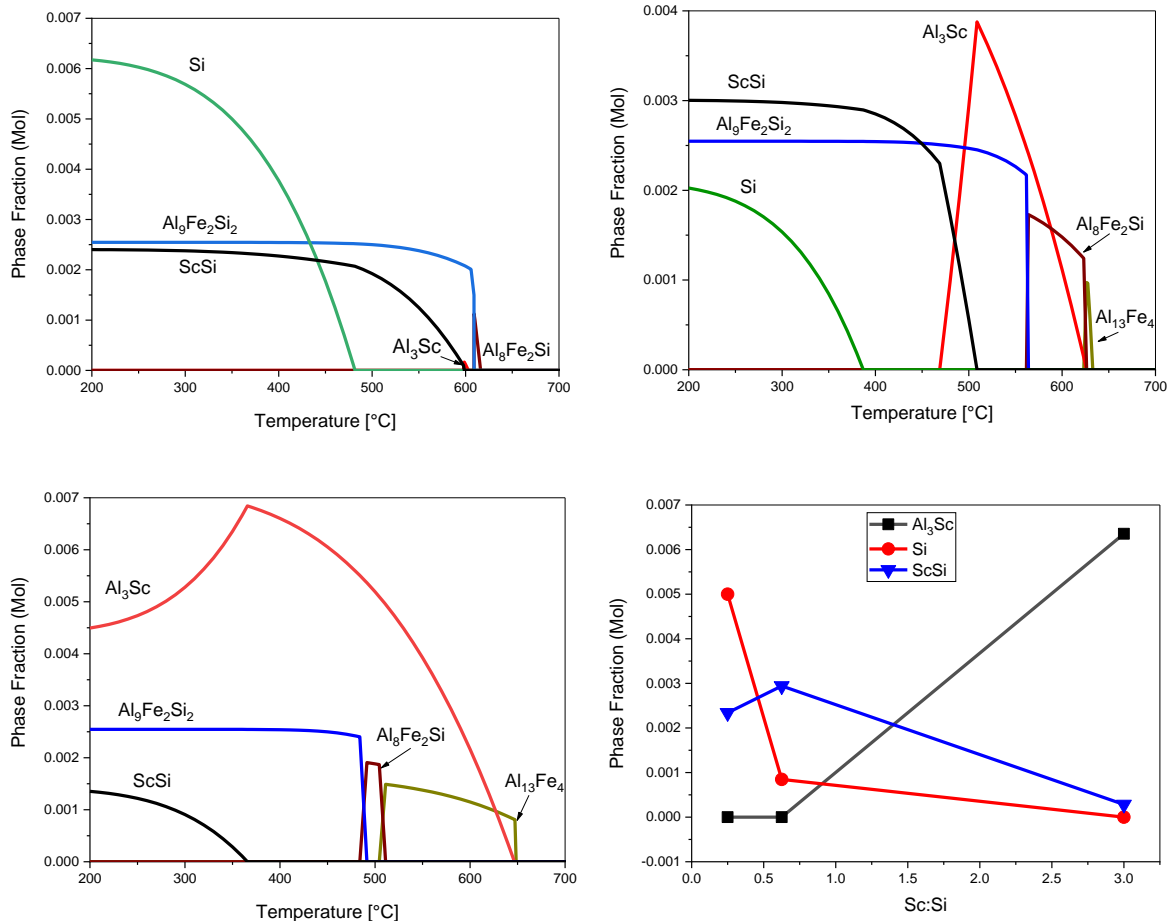


Fig. 3 Calculated equilibrium phase fractions **a** in Al-0.8Si-0.2Sc-0.08Fe **b** in Al-0.4Si-0.25Sc-0.08Fe **c** in Al-0.1Si-0.35Sc-0.08Fe model alloys and **d** with respect to Sc:Si ratio in Al-Si-Sc alloy system at 350°C

given in Fig. 3d. Both pure Si and ScSi phases are non-hardening phases. The phase contributing to the hardening effect is expected to be secondary $(Al,Si)_3Sc$ and cannot be predicted with this calculation. The amount of nano-sized secondary $(Al,Si)_3Sc$ hardening phase will be dependent on the amount of Sc available in the α -Al solid solution. The presence of ScSi and primary Al_3Sc particles will consume some of the required Sc leaving lower Sc-content in the solid solution of these alloys.

Hardness Results

The hardness of all Sc-containing alloys is higher than that of respective Sc-free alloys at all stages of processing as shown in Table 2 and Fig. 4. The as-cast hardness for Sc-containing alloys was 40–60% higher than that of the alloys without Sc mainly due to the solid solution strengthening effect of Sc [17]. Upon low-temperature homogenisation treatment, the hardness of Sc-containing alloys was increased by 30–68% as compared to their as-cast condition.

The strain-hardening behaviour of alloys depends on the amount of strain and deformation temperature [18, 19], which in this case was kept similar for all the alloys studied. Alloy Al-0.1Si-0.3Sc do not show any hardening effect during rolling (refer Fig. 4) probably due to the very low level of Si-content and due to the presence of a large number of $(Al,Si)_3Sc$ dispersoids which have been reported to show sluggish strain-hardening response [19]. In the case of Sc-free alloys, comparatively a stronger strain hardening effect was seen during rolling.

Microstructure Analysis

The predicted equilibrium phases were also found to be present in all the alloys when studied using SEM-EDX in the as-cast condition. In the Sc-containing alloys, heterogeneous distribution of $(Al,Si)_3Sc$ nano-sized dispersoids was also observed which might have been formed due to

discontinuous precipitation during casting [20, 21]. The higher hardness observed in the Sc-containing alloys in the as-cast condition might be also due to these $(Al,Si)_3Sc$ dispersoids.

All the Sc-free alloys show a completed homogenisation due to very high homogenisation temperature (600 °C). On the other hand, due to low-temperature homogenisation of Sc-containing alloys, sub-micron sized Si-precipitates shown in Fig. 5a were formed in the presence of primary Si (Fig. 5b), coarse ScSi and $Al_9Fe_2Si_2$ intermetallics at the dendrite boundaries (Fig. 6).

The low-temperature-homogenised Sc-containing alloys were further examined using TEM to study nano-sized $(Al,Si)_3Sc$ dispersoids. A large number density of $(Al,Si)_3Sc$ dispersoids was formed in all Al-Si-Sc alloys as shown in Fig. 7a along [100] zone axis. The coffee-bean shaped dispersoids in Fig. 8b have two arcs and a central no strain-contrast line normal to $g \cdot [\bar{1}1\bar{1}]$ as shown by Ashby and Brown (AB) strain contrast method. The AB contrast confirmed that the dispersoids are coherent with the α -Al matrix [4, 22, 23]. The Fast Fourier Transform (FFT) image

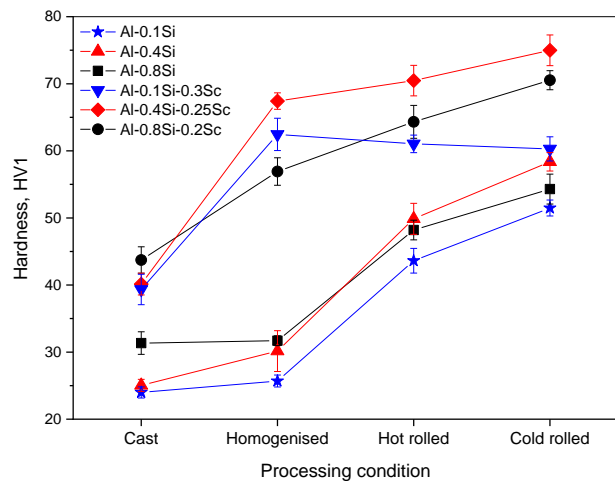


Fig. 4 Hardness evolution of Sc-free and Sc-containing Al-Si alloys with respect to processing stages

Table 2 Vickers microhardness values for the alloys in four different processing conditions

Model alloy system	Nominal composition (wt.%)	Vickers hardness (HV1)			
		Cast	Homogenised	Hot rolled	Cold rolled
Sc-free alloys	Al-0.8Si	31.3 ± 1.68	31.7 ± 0.74	48.2 ± 1.47	54.3 ± 2.22
	Al-0.4Si	25.0 ± 0.90	30.2 ± 3.04	49.9 ± 2.31	58.4 ± 1.38
	Al-0.1Si	24.0 ± 0.83	25.7 ± 0.89	43.6 ± 1.84	51.5 ± 1.19
Sc-containing alloys	Al-0.8Si-0.3Sc	43.7 ± 1.97	56.9 ± 2.05	64.3 ± 2.45	70.5 ± 1.42
	Al-0.4Si-0.3Sc	40.1 ± 1.62	67.4 ± 1.23	70.5 ± 2.28	75.0 ± 2.29
	Al-0.1Si-0.3Sc	39.3 ± 2.27	65.6 ± 6.97	61.0 ± 1.30	60.3 ± 1.80

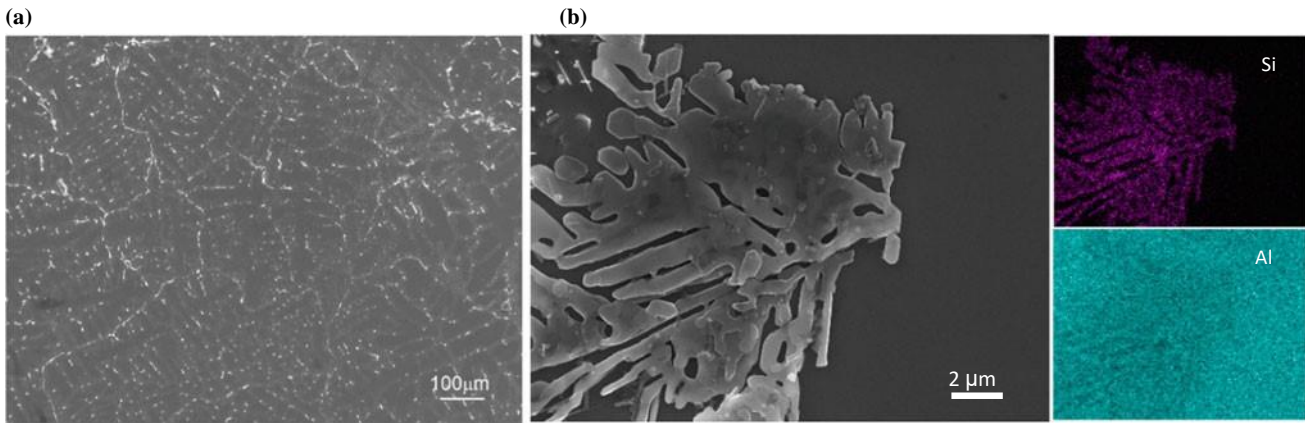


Fig. 5 Secondary electron images of the Al-0.8Si-0.3Sc alloy after low-temperature homogenisation treatment at 350 °C for 30 min showing **a** segregation of Si-precipitates and intermetallic phases at the dendrite boundaries, **b** presence of primary Si and corresponding energy dispersive spectroscopy maps of Al and Si

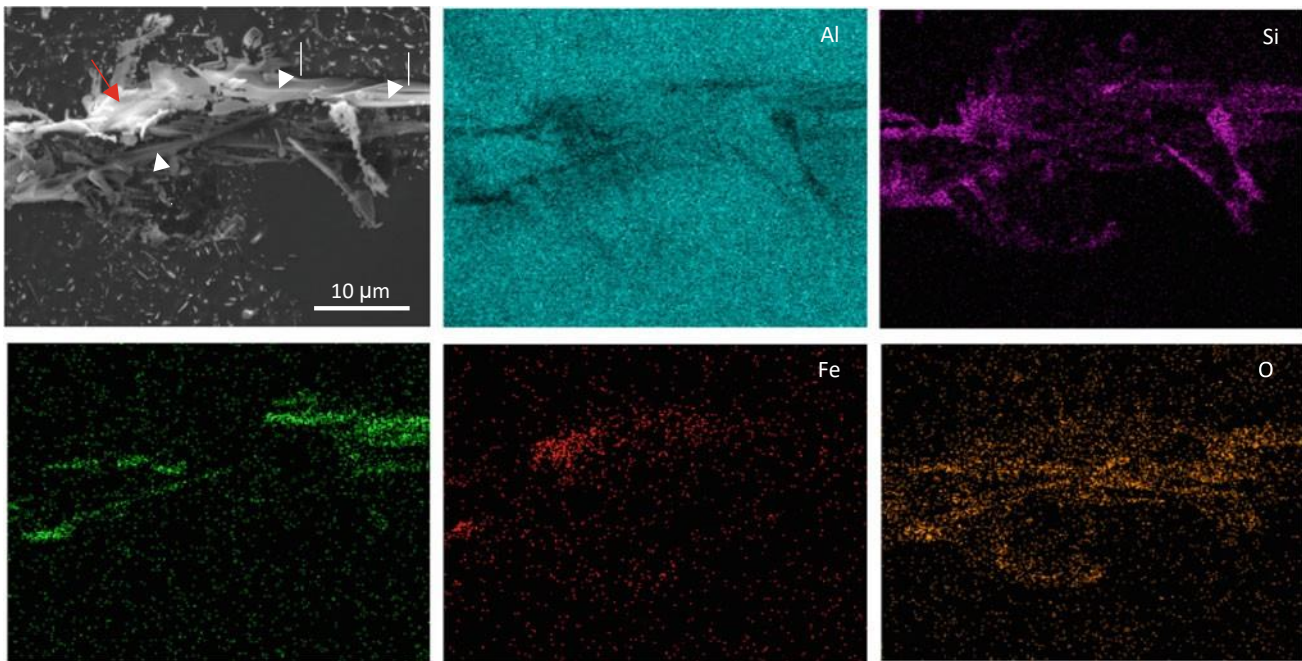


Fig. 6 Secondary electron image of intermetallic phases (Fe-rich $Al_9Fe_2Si_2$ indicated with a darker arrow and ScSi phase indicated with the white arrows) found together in Al-0.8Si-0.2Sc alloy after low-temperature homogenisation treatment at 350 °C for 30 min

Fig. 7 BF TEM image of $(\text{Al}, \text{Si})_3\text{Sc}$ nano-dispersoids in the Al-0.1Si-0.3Sc alloy in as-homogenised condition **a** showing large number density, **b** nano-dispersoids appear as coffee-bean shaped particles due to Ashby-Brown strain contrast effect which confirms their coherency with α -Al matrix and the inset image shows an FFT of the corresponding micrograph

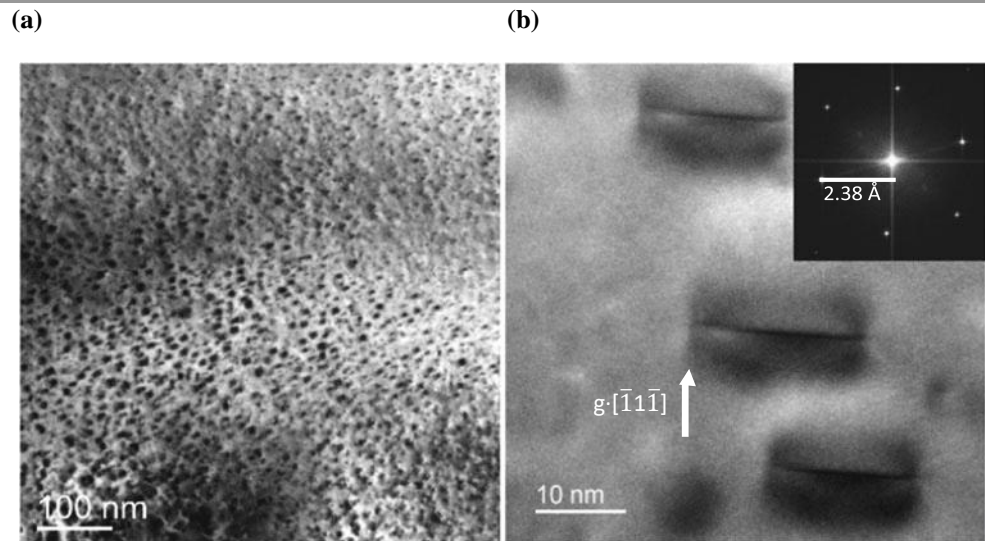
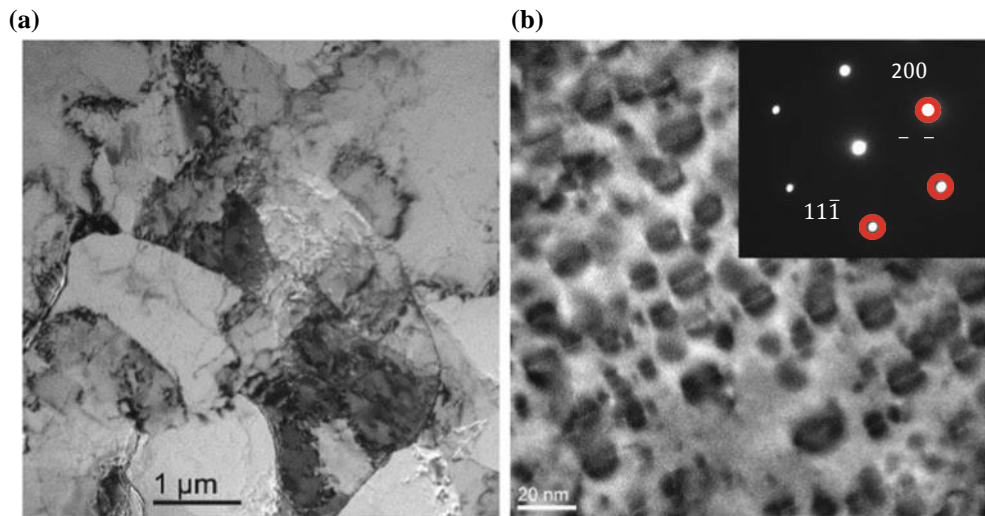


Fig. 8 BF TEM images of Al-0.1Si-0.3Sc alloy hot rolled at 350 °C **a** showing sub-grain formations and tangled dislocations, **b** the coherency of $(\text{Al}, \text{Si})_3\text{Sc}$ nano-dispersoids is retained after the hot rolling. Inset image shows a corresponding SADP



given as an inset in Fig. 7b confirms the zone axis in $[011]$ and a lattice distance between the $(11\bar{1})$ planes of 2.38 \AA as measured from the FFT spots.

During hot rolling, the formation of a sub-grain structure with regions of large dislocation density has been observed as shown in Fig. 8a in all the Sc-containing alloys. The alloys at higher magnifications shows that the matrix had a homogeneous distribution of nano-sized, coherent $(\text{Al}, \text{Si})_3\text{Sc}$ dispersoids along $[011]$ zone as indicated in Fig. 8b.

Conclusion

Scandium containing and Sc-free Al-Si model alloys were designed and processed using a conventional metallurgical route of wrought aluminium semiproducts with the aid of CALPHAD analysis. The Sc-containing alloys possessed superior hardness in the cast, homogenised and rolled

conditions (F-temper) as compared to Sc-free alloys. The improved hardness in the as-cast condition in the case of Sc-containing alloys is mainly attributed to the solid solution strengthening effect of Sc and the discontinuous precipitation of $(\text{Al}, \text{Si})_3\text{Sc}$ nano-dispersoids. The low-temperature homogenisation treatment at 350 °C for 0.5 h to Sc-containing alloys resulted in the formation of a homogeneous secondary $(\text{Al}, \text{Si})_3\text{Sc}$ nano-dispersoids in the α -Al matrix. These dispersoids were retained during the hot rolling process at 350 °C and contributed to the hardening in the case of Sc-containing alloys

Acknowledgements The authors acknowledge the use of facilities within the Monash Centre for Electron Microscopy. The MGS (Monash Graduate Scholarship), IMPRS (International Monash Postgraduate Research Scholarship) for the financial support required to conduct this work. The authors would like to acknowledge Clean TeQ Ltd. for providing in-kind Al-Sc master alloys.

References

1. I. Polmear, *Light alloys: Metallurgy of the light metals*, Edward Arnold, United Kingdom, 1995.
2. Z. Ahmad, A. Ul-Hamid, B. Abdul Aleem, The corrosion behavior of scandium alloyed Al 5052 in neutral sodium chloride solution, *Corros. Sci.* 43 (2001) 1227–1243. [https://doi.org/10.1016/s0010-938x\(00\)00147-5](https://doi.org/10.1016/s0010-938x(00)00147-5).
3. M. Cavanaugh, N. Birbilis, R. Buchheit, F. Bovard, Investigating localized corrosion susceptibility arising from Sc containing intermetallic Al₃Sc in high strength Al-alloys, *Scr. Mater.* 56 (2007) 995–998. <https://doi.org/10.1016/j.scriptamat.2007.01.036>.
4. S. Iwamura, Y. Miura, Loss in coherency and coarsening behavior of Al₃Sc precipitates, *Acta Mater.* 52 (2004) 591–600. <https://doi.org/10.1016/j.actamat.2003.09.042>.
5. L. Toropova, D. Eskin, M. Kharakterova, T. Dobatkina, *Advanced aluminium alloys containing Scandium*, Taylor & Francis Group, London & New York, 1998.
6. V. Davydov, T. Rostova, V. Zakharov, Y. Filatov, V. Yelagin, Scientific principles of making an alloying addition of scandium to aluminium alloys, *Mater. Sci. Eng. A.* 280 (2000) 30–36. [https://doi.org/10.1016/s0921-5093\(99\)00652-8](https://doi.org/10.1016/s0921-5093(99)00652-8).
7. T. Dorin, M. Ramajayam, A. Vahid, T. Langan, *Aluminium Scandium Alloys*, in: *Fundam. Alum. Metall.*, Woodhead Publishing, United Kingdom, 2018: pp. 439–494.
8. L. Rokhlin, N. Bochvar, O. Rybal'chenko, I. Tarytina, A. Sukhanov, Phase equilibria in aluminum-rich Al-Sc-Si alloys during solidification, *Russ. Metall.* 2012(7) (2012) 606–611. <https://doi.org/10.1134/s0036029512070129>.
9. M. Kharakterova, D. Eskin, L. Toropova, Precipitation hardening in ternary alloys of the Al-Sc-Cu and Al-Sc-Si systems, *Acta Met. Mater.* 42(7) (1994) 2285–2290.
10. C. Booth-Morrison, Z. Mao, M. Diaz, D. Dunand, C. Wolverton, Role of silicon in accelerating the nucleation of Al₃(Sc,Zr) precipitates in dilute Al-Sc-Zr alloys, *Acta Mater.* 60 (2012) 4740–4752. <https://doi.org/10.1016/j.actamat.2012.05.036>.
11. N. Vo, D. Dunand, D. Seidman, Improving aging and creep resistance in a dilute Al-Sc alloy by microalloying with Si, Zr and Er, *Acta Mater.* 63 (2014) 73–85. <https://doi.org/10.1016/j.actamat.2013.10.008>.
12. Q. Yao, Elastic Properties and Electronic Structure of L12 (Al,Si)₃Sc, *Adv. Mater. Res.* 284–286 (2011) 1987–1990. <https://doi.org/10.4028/www.scientific.net/amr.284-286.1987>.
13. G. Du, J. Deng, Y. Wang, D. Yan, L. Rong, Precipitation of (Al, Si)₃Sc in an Al-Sc-Si alloy, *Scr. Mater.* 61 (2009) 532–535. <https://doi.org/10.1016/j.scriptamat.2009.05.014>.
14. T. Dorin, M. Ramajayam, T.J. Langan, Effects of Mg, Si, and Cu on the formation of the Al₃Sc/Al₃Zr dispersoids, in: *6th Int. Alum. Alloy. Conf.*, Canadian Institute of Mining, Metallurgy & Petroleum, 2018.
15. H. Jo, S. Fujikawa, Kinetics of precipitation in Al-Sc alloys and low temperature solid solubility of scandium in aluminium studied by electrical resistivity measurements, *Mater. Sci. Eng. A.* 171 (1993) 151–161.
16. J. Royset, N. Ryum, Scandium in aluminium alloys, *Int. Mater. Rev.* 50(1) (2005) 19–44. <https://doi.org/10.1179/174328005x14311>.
17. T. Dorin, M. Ramajayam, J. Lamb, T. Langan, Effect of Sc and Zr additions on the microstructure/strength of Al-Cu binary alloys, *Mater. Sci. Eng. A.* 707 (2017) 58–64. <https://doi.org/10.1016/j.msea.2017.09.032>.
18. B. Li, Q. Pan, Z. Yin, Characterization of hot deformation behavior of as-homogenized Al-Cu-Li-Sc-Zr alloy using processing maps, *Mater. Sci. Eng. A.* 614 (2014) 199–206. <https://doi.org/10.1016/j.msea.2014.07.031>.
19. V. Jindal, P. De, K. Venkateswarlu, Effect of Al₃Sc precipitates on the work hardening behavior of aluminum-scandium alloys, *Mater. Lett.* 60 (2006) 3373–3375. <https://doi.org/10.1016/j.matlet.2006.03.017>.
20. E. Marquis, D. Seidman, Nanoscale structural evolution of Al₃Sc precipitates in Al(Sc) alloys, *Acta Mater.* 49 (2001) 1909–1919. [https://doi.org/10.1016/s1359-6454\(01\)00116-1](https://doi.org/10.1016/s1359-6454(01)00116-1).
21. J. Royset, N. Ryum, Kinetics and mechanisms of precipitation in an Al-0.2 wt. % Sc alloy, *Mater. Sci. Eng. A.* 396 (2005) 409–422. <https://doi.org/10.1016/j.msea.2005.02.015>.
22. D. Williams, B. Carter, *Transmission electron microscopy: Part 1- Basics*, 2nd ed., Springer, New York, 2009.
23. W. Zhang, Y. Ye, L. He, P. Li, X. Feng, L. Novikov, Dynamic response and microstructure control of Al-Sc binary alloy under high-speed impact, *Mater. Sci. Eng. A.* 578 (2013) 35–45. <https://doi.org/10.1016/j.msea.2013.04.067>.

6 Sc-containing phases in Al-Si-Sc alloys

6.1 Synopsis

This chapter develops an understanding regarding the precipitation mechanisms for $(\text{Al,Si})_3\text{Sc}$ and V-phase (AlSc_2Si_2) phases using *ex situ* heat treatment and *in situ* TEM studies of Al-Si-Sc alloys. Two alloys, namely Al-0.8Si-0.2Sc and Al-0.4Si-0.25Sc were cast and then heat-treated at 350 °C for 30 minutes to form coherent $(\text{Al,Si})_3\text{Sc}$ nano-precipitates. The alloys were then subsequently rolled and solutionised at 450-550 °C to form the V-phase. The hardening effect of $(\text{Al,Si})_3\text{Sc}$ phase was seen in the pre-heat treated alloys whereas the formation of V-phase led to the significant softening of the alloys as indicated by the hardness test results. The V-phase was studied in detail utilising electron microscopy techniques and the rod-shaped morphology was found for the first time along with six new ORs of V-phase with the α -Al matrix. The phase transformation studies were conducted using an *in situ* TEM heating technique indicated that the $(\text{Al,Si})_3\text{Sc}$ phase forms by a continuous precipitation mechanism from the supersaturated α -Al solid solution without the formation of any metastable phases. Similarly, the *in situ* TEM heating experiment conducted on the pre-heat-treated Al-0.8Si-0.2Sc alloy indicated the precipitation of V-phase by a classical nucleation and growth mechanism following the dissolution of Si-particles first and then of $(\text{Al,Si})_3\text{Sc}$ nano-precipitates.



Contents lists available at ScienceDirect

Journal of Alloys and Compounds

journal homepage: www.elsevier.com/locate/jalcom

Understanding the formation of $(\text{Al,Si})_3\text{Sc}$ and V-phase $(\text{AlSc}_2\text{Si}_2)$ in Al-Si-Sc alloys via *ex situ* heat treatments and *in situ* transmission electron microscopy studies



Jayshri Dumbre^{a,*}, Shravan K. Kairy^a, Elaf Anber^b, Timothy Langan^c, Mitra L. Taheri^b, Thomas Dorin^d, Nick Birbilis^e

^a Department of Materials Science and Engineering, Monash University, Clayton, VIC 3800, Australia

^b Department of Materials Science and Engineering, Johns Hopkins University, Baltimore, MD 21218, USA

^c Clean TeQ Holdings Ltd., Notting Hill, VIC 3168, Australia

^d Institute for Frontier Materials, Deakin University, Geelong, VIC 3216, Australia

^e College of Engineering and Computer Science, The Australian National University, Acton, ACT 2601, Australia

article info

Article history:

Received 9 August 2020

Received in revised form 27 November 2020

Accepted 23 December 2020

Available online 26 December 2020

Keywords:

Metals and alloys

Microstructure Precipitation

Transmission electron microscopy (TEM)

abstract

Scandium (Sc) containing Al-Si model alloys were heat-treated at various temperatures to determine the interaction between Si and Sc. The $(\text{Al,Si})_3\text{Sc}$ phase was formed at ~ 350 °C and V-phase $(\text{AlSc}_2\text{Si}_2)$ was observed to form at above ~ 450 °C, as determined from x-ray diffraction and selected area electron diffraction. Hardening of the alloys was observed due to the formation of coherent, nanoscale $(\text{Al,Si})_3\text{Sc}$ precipitates; whereas significant softening was observed upon the formation of coarse V-phase. Herein, the V-phase is studied in detail and has for the first time been revealed to have a rod morphology. The Transmission electron microscopy (TEM) allowed for the determination of six new orientation relationships (ORs) with the α -Al matrix for the V-phase. Additionally, *in situ* TEM heating experiments at 550 °C revealed that the formation of V-phase occurs due to a nucleation and growth mechanism following the dissolution of Si particles and nanoscale $(\text{Al,Si})_3\text{Sc}$ precipitates.

© 2021 Elsevier B.V. All rights reserved.

1. Introduction

Owing to their high specific strength, aluminium (Al) alloys remain critical materials for automotive and aerospace applications [1]. Ongoing efforts to increase the strength of Al-alloys, in addition to efforts to extend the balance of properties for Al-alloys, includes the broad exploration of alloying [2]. Of particular interest, the addition of scandium (Sc) to Al-alloys has resulted in reported improvements in room temperature strength [3–5], as well as the creep resistance at high temperatures [6–8], without deteriorating other properties [9]. The beneficial effects of Sc additions to Al have been attributed to the formation of well-dispersed, coherent, L_{12} structured Al_3Sc nano-sized precipitates [8,10]. Following the benefits initially observed in binary Al-Sc alloys, alloying additions of Sc have since been evaluated in various ternary and quaternary Al-alloy systems, such as the Al-Mg-Sc [11,12], Al-Cu-Sc [13,14] and Al-Zn-Mg-(Cu)-Sc-(Zr) [15–17] systems, whereby it was also

reported that Sc additions remain beneficial - with such alloys having some commercial applications. To date, however, attempts to study the role of Sc in so-called 6xxx series (Al-Si-Mg) alloys remain scarce, which is in part due to an apparently unfavourable interaction between silicon (Si) and Sc, which inhibits the formation of the beneficial L_{12} Al_3Sc nano-precipitates. If such an unfavourable Si-Sc interaction can be understood, and potentially eliminated, the impact in the context of Al-alloy property space (namely the strength vs. ductility field) would be significant. This is because 6xxx series Al-alloys represent a balance of medium strength and high ductility, high corrosion resistance, and are readily formable into a variety of shapes [2]. Exploiting beneficial additions of Sc to 6xxx-series Al-alloys would allow to further improvements in the strength, whilst maintaining other favourable properties.

The commercial Al-alloys always have some amount of Si in them. Of the studies reported to date, the presence of lower levels of Si in Al-Sc alloys increases the precipitation kinetics associated with Sc forming nanoscale Al_3Sc precipitates [18–22]. Although the nano-precipitates in these alloys are broadly called as Al_3Sc , they

* Corresponding author.

E-mail address: jayshri.dumbre@monash.edu (J. Dumbre).

are most likely $(\text{Al,Si})_3\text{Sc}$ due to the substitution of Si at Al sublattice sites, which was found to be more favourable, resulting in more relaxed, coherent, $L1_2$ structured $(\text{Al,Si})_3\text{Sc}$ precipitates with a composition of Al- 25 at% Sc- 6 at% Si [19–21]. The nano-precipitates in this particular study are thus referred to as $(\text{Al,Si})_3\text{Sc}$ throughout this document. A recent study revealed that the substitution of Si to Al was on the order of 25% for $(\text{Al,Si})_3\text{Sc}$ particles within the alloy in the as-cast state, which found to be decreasing as a function of ageing time [23,24]. The calculated shear modulus for $(\text{Al,Si})_3\text{Sc}$ precipitates is ~ 2.4 times than that of Al, making such precipitates an effective strengthening phase in the Al matrix [25]. Calculations suggest that the $(\text{Al,Si})_3\text{Sc}$ phase is less brittle than Al_3Sc , suggesting that dilute additions of Si in Al-Sc alloys may result in a better balance of mechanical properties than in Si-free Al-Sc alloys [19]. In contrast, the formation of a ternary compound, AlSc_2Si_2 , also known as V-phase (or less commonly, τ -phase) was reported with the addition of Si to Al-Sc alloys in a different study [26]. It was therein determined that the evolution of V-phase in the Al matrix was accompanied by a decrease in hardness of Al-Sc-Si alloys [27]. As a result, it was proposed that Si be limited to a maximum of 0.15 wt% in Al-Sc alloys [27]. However, a recent study indicated that the hardening can be achieved without the formation of V-phase for Al-Si-Sc wrought alloy system having Si content as high as 0.8 wt% by optimising the thermomechanical processing sequence [28]. In another study, it was reported that the formation of both non-coherent Si particles and V-phase, as a result of ageing an Al-9.72Si-0.45Sc alloy, contributed to an increase in hardness of ~ 150 MPa [26]. Additionally, another report revealed that refined Si particles and nano-sized V-phase in the hypereutectic Al-(13–22) Si-0.8Sc alloy prepared by spark plasma sintering had enhanced compressive strength without the loss of ductility, also with increased wear resistance [29]. Thermodynamically, V-phase is more stable and has a lower enthalpy of formation compared to that of Al_3Sc [30]. It has been reported that V-phase has slightly higher bulk, shear, and Young's modulus than those of Al_3Sc and is naturally brittle [30]. However, V-phase is anisotropic whereas Al_3Sc is isotropic when compared for elastic properties [30,31]. These apparently conflicting claims in the literature are likely owing to a lack of understanding regarding the formation of V-phase, more generally in the field of Al-alloys. Despite the works to date regarding V-phase and any deleterious effect upon mechanical properties, there is presently no detailed analysis regarding the morphology, structure and chemical characteristics of V-phase or its formation mechanisms.

In this work, two Al-Si-Sc model alloys were studied and specific heat treatments were performed to form nanoscale $(\text{Al,Si})_3\text{Sc}$ and V-phase. Hardness measurements were used to indirectly follow the formation kinetics of both phases. *Ex situ* electron microscopy and x-ray diffraction (XRD) techniques were utilised to characterise the phases observed, whilst *in situ* transmission electron microscopy (TEM) studies were performed to understand the formation mechanisms for both phases.

2. Materials and methods

2.1. Alloy synthesis

Two custom produced model alloys of Al-Si-Sc with Si to Sc ratio of 4.3 (0.8 wt% Si) and 1.92 (0.4 wt% Si) were cast using a lab-scale gravity die casting process. The alloys were prepared using 99.86 wt % commercially pure Al, pure Si, and Al-2 wt% Sc master alloy. The gravity die casting of the liquid melt was done into a rectangular-shaped mild steel mould of dimensions $150 \times 50 \times 10$ mm from a superheat temperature of 720 °C after a holding time of 30 min. The alloy composition in the as-cast condition was analysed by

Table 1

Chemical composition (wt%) of the two Sc-containing Al-alloys measured using inductively coupled plasma – optical emission spectroscopy (ICP-OES) test.

Alloy	Si	Sc	Fe	Al	Si:Sc
Al-0.8Si-0.2Sc	0.86	0.20	0.08	Balance	4.30
Al-0.4Si-0.25Sc	0.48	0.25	0.08	Balance	1.92

inductively coupled plasma - optical emission spectroscopy (ICP-OES) and is reported in Table 1.

The equilibrium pseudo-binary Al-Si phase diagram with a constant 0.25 wt% Sc was constructed using the ThermoCalc® software, based on the TCAL-4 thermodynamic database. The software aided in predicting probable phases and designing heat treatments for both the alloys varying in Si to Sc ratio. Controlled lab-scale heat treatments were performed on these model alloys to obtain the phases predicted by the software. At first, the pre-heat treatment of as-cast ingots was performed at 350 °C for 0.5 h to form $(\text{Al,Si})_3\text{Sc}$ nano-precipitates. The pre-heat-treated ingots were then hot-rolled at 350 °C to decrease the thickness from 10 mm to 4 mm, and then subsequently cold rolled to 1 mm using a lab-scale Buehler four-high rolling mill facility. The rolled sheets from the alloys with 0.4 wt% and 0.8 wt% Si were then solutionised at 450 °C and 550 °C, respectively, to form the V-phase. Subsequently, ageing treatments at 250 °C with varying time intervals were performed to study the variation in hardness in the presence of V-phase. The entire processing sequence for both the alloys is given in Fig. 1.

2.2. Hardness testing

The hardness of both the alloys in all processing conditions was measured using a Struers® Duramin A-300 Vickers hardness tester, employing a 1 kg applied load. Hardness values were recorded from 7 different locations upon each alloy and averaged.

2.3. Microstructural characterisation

Specimens for scanning electron microscope (SEM) were cut and electropolished to mirror-finish to observe under JEOL® 7001 F SEM in the secondary electron imaging (SEI) and energy dispersive spectroscopy (EDS) mode. Electropolishing was conducted with 30% nitric acid – 70% methanol electrolyte at –30 °C in a Struers® Tenupol 5 twin-jet electro-polishing unit. The cell voltage was set to 12.7 V, the current was 180–190 mA and the approximate electro-polishing time was 2 min.

For structural and chemical characterisation of phases using TEM, 3 mm diameter discs were punched from mechanically thinned alloy sheets of 200 μm thick. Two different techniques were used to prepare TEM specimens: (1) electropolishing and (2) ion milling. Electropolishing was used for specimens containing phases that are immune to the electropolishing solution, whilst ion milling was used for specimens containing phases that are reactive to the solution. Based on the experience, TEM specimens from the solutionised alloys which contained reactive phases were ion milled using Gatan® 691 precision ion polishing systems at –100 °C. All the other samples were electropolished with the parameters explained earlier in the case of SEM specimens. TEM specimens were then observed in Bright Field (BF) mode using an FEI® Tecnai G2 T20 TEM and FEI® Tecnai G2 F20 STEM operated at 200 kV. The high-resolution BF and high-angle annular dark-field (HAADF) – Scanning TEM (STEM) images were Fourier filtered with a circular aperture masking method for the spots in Fourier transform pattern in the Digital Micrograph software, in order to remove high-frequency noise. The EDS mode was used to understand the elemental analysis using a Bruker® Quantax 400 detector in the FEI® Tecnai G2 F20 STEM. To study the structural characteristics of the phases, the Crystal Maker®

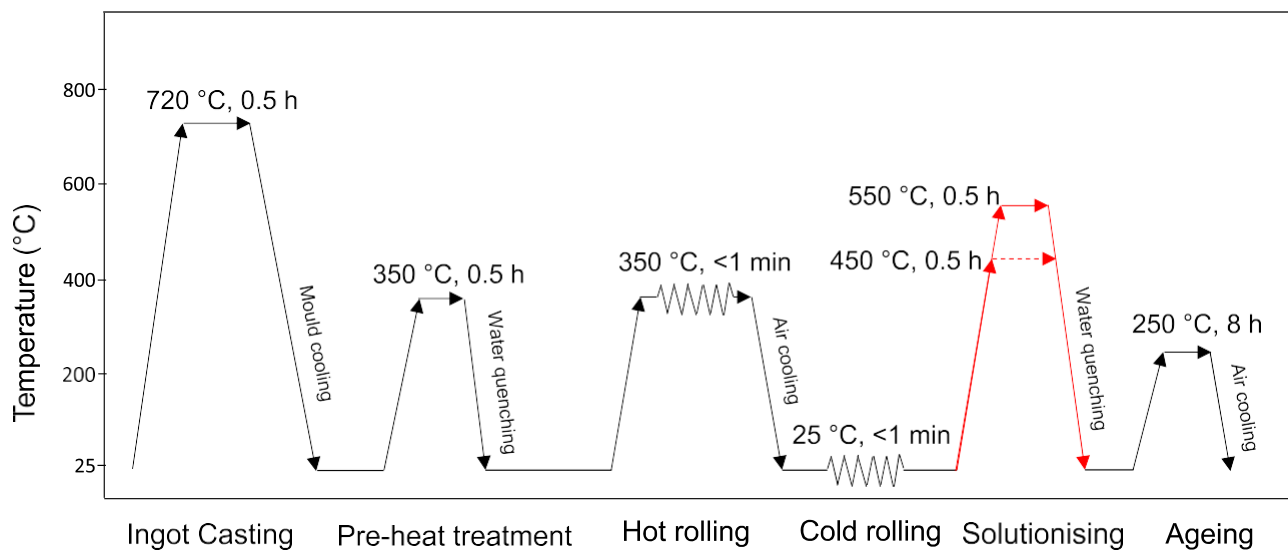


Fig. 1. Alloy production and processing diagram. The Al-0.4Si-0.25Sc alloy was solutionised at 450 °C for 0.5 h, and Al-0.8Si-0.2Sc was solutionised at 550 °C for 0.5 h.

software was utilised to build the simulated crystal structure as well as the diffraction patterns. The simulated structural information was compared with the experimental selected area diffraction patterns (SADP) of the phases in the α -Al matrix.

To analyse the phases in both the alloys using XRD technique, a sample of $20 \times 20 \times 10$ mm dimensions with a surface polished to 800 μm was used. The XRD equipment with a Cu $K\alpha$ radiation at 40 kV and 40 mA of Bruker® D8 Advance - DAVINCI design was utilised for conducting the scans. The international centre for diffraction data (ICDD) PDF-4 + 2018 RDB database with an analytical software Bruker® DIFFRAC.EVA V4.3 was utilised for the analysis of phases.

2.4. In situ TEM heating

To study phase transformations in the Al-Si-Sc model alloys, *in situ* TEM heat treatment experiments were conducted for both the alloys using a JEOL® 2100 LaB₆ TEM. Specimens for TEM were prepared by ion milling 3 mm diameter discs of 45 μm thick using a Fishione Model 110. Two different *in situ* heating experiments were carried out using a Gatan® heating holder model 628 and the corresponding microstructural changes were recorded *in situ* via a Debut digital screen capture software using a Gatan® Orius 832 fiber optic 10.7-megapixel CCD detector. For the first experiment, a TEM specimen from the as-cast Al-0.4Si-0.25Sc alloy was heated to 350 °C in the Gatan heating holder with a heating rate of 50 °C/min and was held for a duration of 1 h, to observe the nucleation and growth of the nanoscale (Al,Si)₃Sc phase. For the second experiment, the Al-0.8Si-0.2Sc alloy was first pre-heat treated *ex situ* in a muffle furnace at 350 °C for 30 min to form nanoscale (Al,Si)₃Sc phase precipitates and secondary Si particles. Specimens for TEM from this pre-heat treated Al-0.8Si-0.2Sc alloy was then *in situ* heated to 550 °C in the Gatan heating holder with a heating rate of 20 °C/min and held for 5 min to study the evolution of V-phase.

3. Results

3.1. Equilibrium phase diagram

The pseudo-binary Al-Si phase diagram with 0.25 wt% Sc is shown in Fig. 2 and was utilised as a reference for developing the solutionising heat treatment for the alloys studied. The Thermo-Calc® software predicted the stable regions for binary Al₃Sc and the

ScSi phases, however, the software could not predict the ternary V-phase. In contrast, the formation of V-phase was reported in Al-Si-Sc alloys in previous literature [32,33]. Therefore, the solutionising heat treatment experiments were designed in the ScSi phase stability range (region shaded with blue colour in Fig. 2) to explore the formation of the V-phase. It can be seen that the ScSi phase formation temperature increases with increasing Si content in the alloys. Thus, solutionising temperatures of 450 °C for the alloy with 0.4 wt% Si and 550 °C for the alloy with 0.8 wt% Si were selected to form the V-phase as indicated with the red dot in Fig. 2. Moreover, the red dot shows the stable ScSi phase region for both the selected compositions of the alloys for the respective solutionising temperatures.

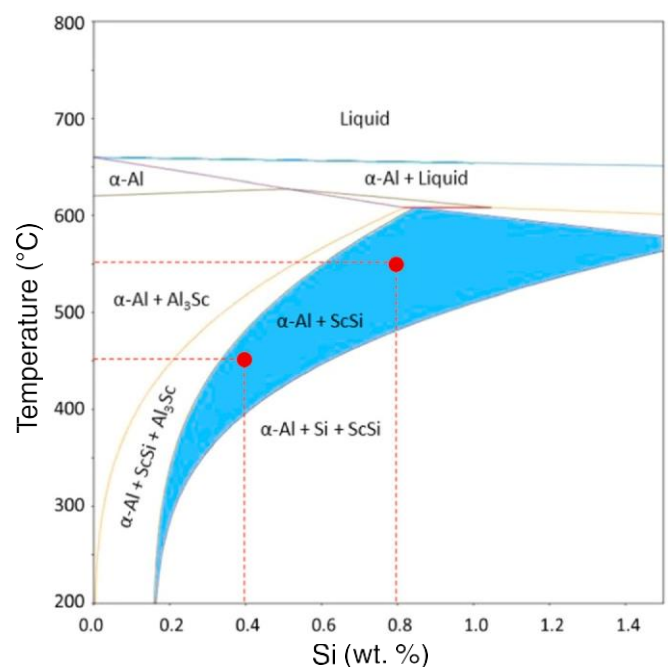


Fig. 2. Pseudo-binary phase diagram of Al-Si system with 0.25 wt% Sc. Diagram calculated using ThermoCalc®, indicating the ScSi phase region in α -Al matrix. (For interpretation of the references to colour in this figure, the reader is referred to the web version of this article)

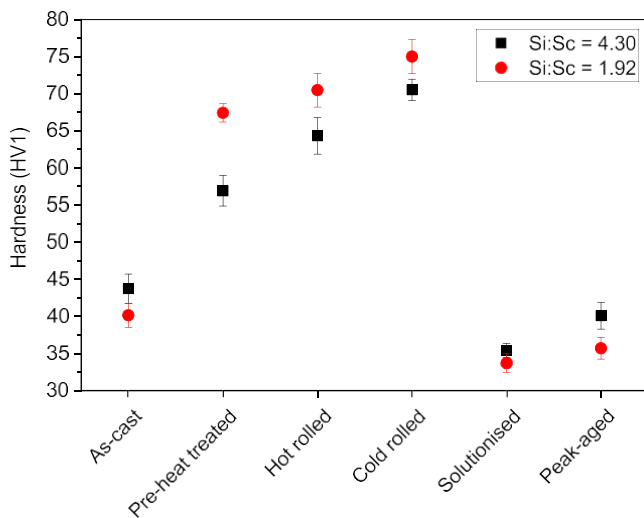


Fig. 3. Evolution of hardness as a function of processing during the thermo-mechanical treatments for both alloys studied.

3.2. Hardness results

To complement the microstructural development, hardness measurements were conducted after each step of the thermo-mechanical treatment and presented in Fig. 3.

The hardness was found to increase by ~30% and ~68% after the pre-heat treatment at 350 °C for the alloys with 0.8 wt% Si and 0.4 wt% Si, respectively, when compared to the hardness of the corresponding alloys in the as-cast condition. The increase in the hardness suggests the formation of strengthening phases, which could be the metastable Si-containing Al_3Sc particles. Further hardening of both the alloys of the order of 11–23% was observed, following hot and cold rolling processes due to increased workhardening response with strain which causes increased dislocation density [34,35]. Subsequently, the hardness of alloys decreased significantly after solutionising at 450–550 °C. The decrease in hardness suggests that the strengthening benefits from the $(\text{Al},\text{Si})_3\text{Sc}$ nano-precipitates were lost possibly due to their dissolution and formation of different phases. The hardness was then found to increase slightly during the

final ageing at 250 °C. To get a better understanding of the hardening behaviour following pre-heat treatment and softening following solutionising as a result of associated possible phase transformation phenomenon, XRD and electron microscopy techniques were applied.

3.3. XRD results

To understand the precipitation sequence, XRD was performed for the Al-0.8Si-0.2Sc alloy in two different heat treatment conditions, one being after the pre-heat treatment at 350 °C for 0.5 h and the other being after the high-temperature solutionising treatment at 550 °C for 0.5 h. The sample pre-heat treated at 350 °C has the presence of Si and $(\text{Al},\text{Si})_3\text{Sc}$ phases as shown in Fig. 4. In the case of the sample solutionised at 550 °C, peaks corresponding to Si were not present indicating a possible dissolution of the phase. The new peaks corresponding to the V-phase and $\text{Al}_9\text{Fe}_2\text{Si}_2$ intermetallic phase existed. The presence of $(\text{Al},\text{Si})_3\text{Sc}$ phase in the solutionised sample can not be confirmed since the peaks from V-phase overlaps to that from the $(\text{Al},\text{Si})_3\text{Sc}$ phase at the (111) and (200) spacings. The results from XRD analysis clearly confirmed the apparition of the V-phase during the post-rolling solution treatments. In order to further characterise this phase, electron microscopy techniques were applied.

3.4. Microstructure analysis

Intermetallic phases (Fe-rich β -phase $(\text{Al}_9\text{Fe}_2\text{Si}_2)$, primary Si particles, and ScSi-containing phase) were observed using SEM in both the alloys in the as-cast condition due to elemental segregation upon solidification. These phases continued to be present in the α -Al matrix as indicated by the white arrows in Fig. 5(a) after the pre-treatment and after all the subsequent process steps of sheet making. Any new intermetallics were not observed following thermo-mechanical processing. No significant dissolution of these intermetallics was observed during the solutionising treatment probably due to insufficient holding time. The formation of these intermetallics following casting has consumed some of the Sc and Si required for the precipitation of hardening phases. The matrix composition is thus required to be rich in Sc and Si solute to get maximum hardening effect following the precipitation treatment. The semi-quantitative SEM-EDS analysis for the areas free from

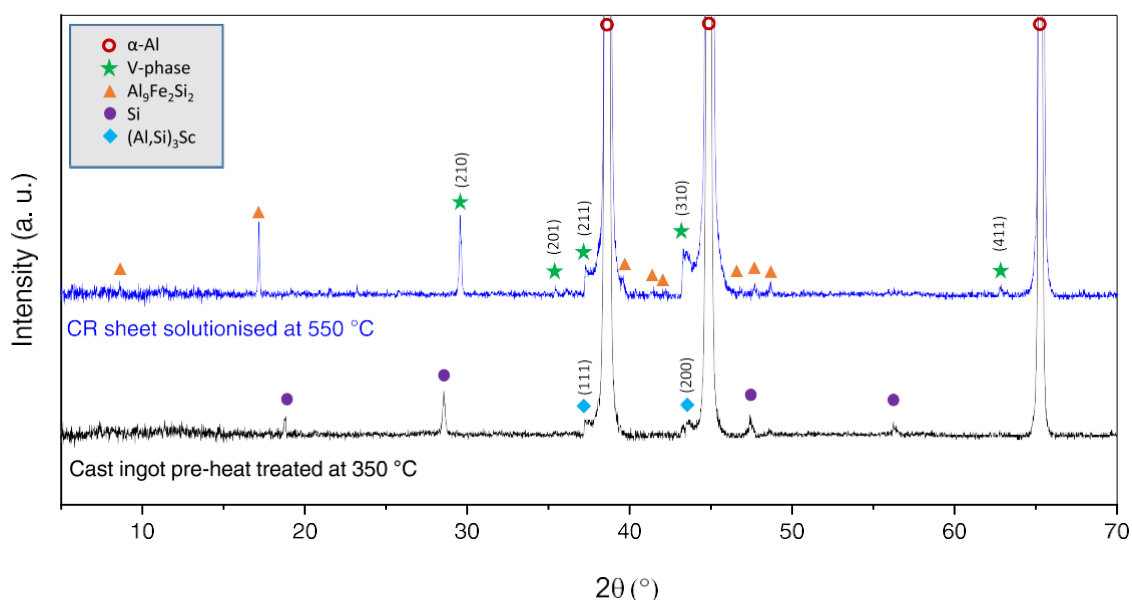


Fig. 4. Comparison of phases with the XRD results of Al-0.8Si-0.2Sc alloy in the pre-heat treated (350 °C for 0.5 h) and solutionised conditions (550 °C for 0.5 h).

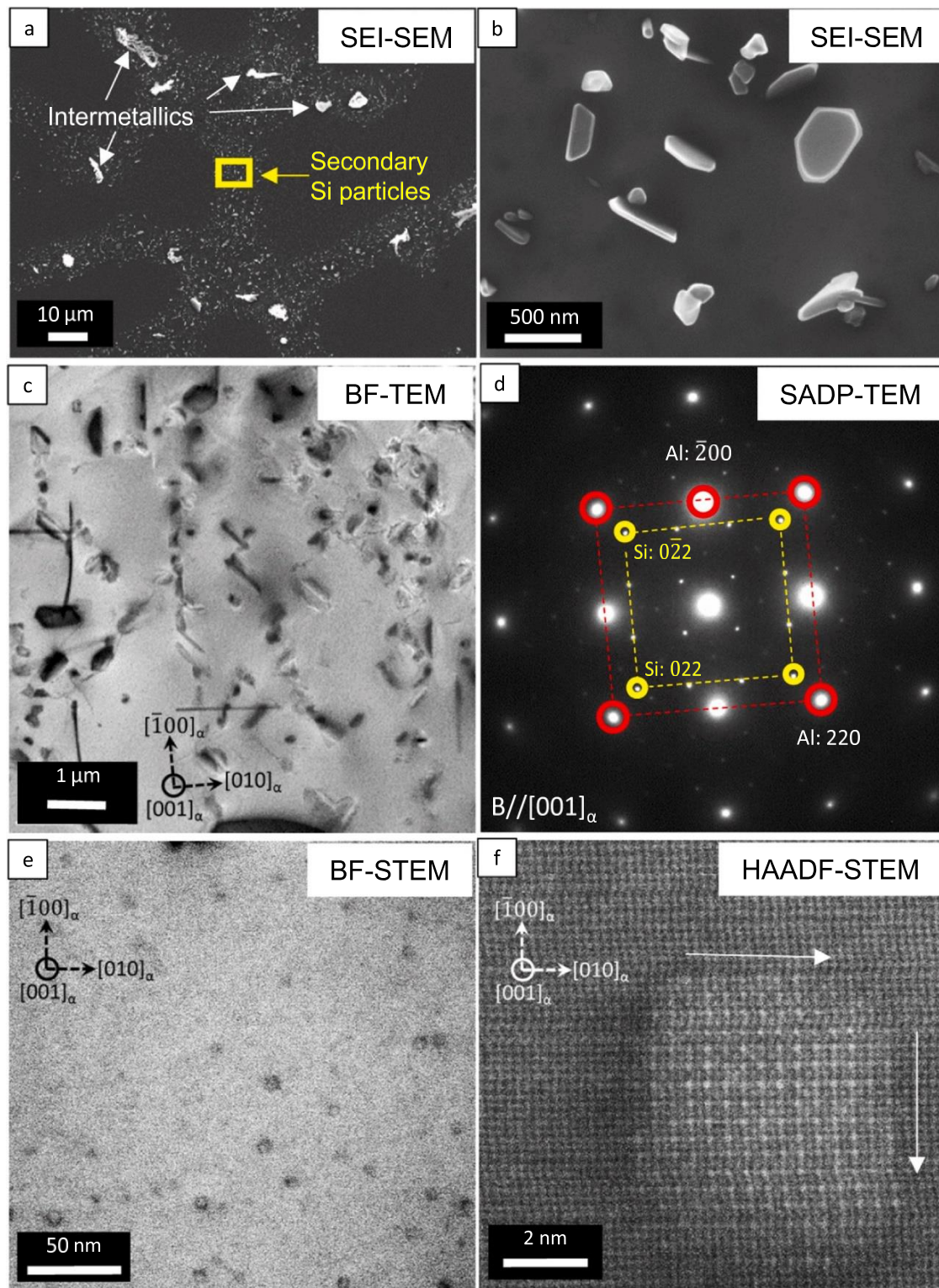


Fig. 5. Al-0.8Si-0.2Sc following pre-heat treatment at 350 °C for 0.5 h. (a) SEI-SEM image of the microstructure showing distribution of phases. White arrows indicate the coarse intermetallics (b) magnified SEI-SEM image of secondary Si particles marked by a rectangle in (a); (c) BF-TEM image of Si-precipitates and (d) corresponding SADP; (e) BF-STEM image of $(Al,Si)_3Sc$ nano-precipitates; (f) atomic-scale HAADF-STEM image showing the structure of coherent, nano-sized $(Al,Si)_3Sc$ faceted precipitate. (For interpretation of the references to colour in this figure, the reader is referred to the web version of this article).

precipitates was estimated for five regions in each as-cast sample and then averaged out. The approximate matrix composition was found to be Al- 0.6 at% Si- 0.1 at% Sc and Al- 0.34 at% Si- 0.14 at% Sc for Al-0.8Si-0.2Sc and Al-0.4Si-0.25Sc alloys respectively. Specimens after pre-heat treatment and solutionising were chosen for further

analysis using electron microscopy techniques as they exhibited the most significant variation in hardness (refer Fig. 3). The subsequent results of phase analysis in this section are thus mainly focused on the microstructure obtained during these two heat treatment processes.

3.4.1. Phase evolution following pre-heat treatment

Samples from the Al-0.8Si-0.2Sc alloy following pre-heat treatment at 350 °C for 0.5 h were observed under SEM. The microstructure shows the presence of coarse intermetallic phases (β -phase, primary-Si, and ScSi-containing phase) at grain boundaries as well as at dendrite boundaries, as shown in Fig. 5(a) using white arrows. Additionally, sub-micrometre sized and polygonal-shaped secondary Si particles were precipitated and segregated along the dendrite boundaries, as shown in Fig. 5(a) and in a magnified SEI mode image in Fig. 5(b). Typical secondary Si particles were 0.5–0.8 μm long and 0.2–0.4 μm wide. The SADP viewed along [001] zone axis of the α -Al matrix in Fig. 5(d) shows bright spots corresponding to the Al matrix (marked by red circles) and weak spots corresponding to the superlattice reflections of the diamond cubic structured Si-precipitates (indicated by yellow outer circles). The orientation relationship (OR) between the Si particles and the α -Al matrix was found to be a cube-cube which can be written as $[100]_{\text{Si}} \parallel [100]_{\alpha\text{-Al}}$ and $(011)_{\text{Si}} \parallel (220)_{\alpha\text{-Al}}$ in accordance with previously reported OR [36].

BF-STEM image of the sample indicates the formation of the nano-sized, $(\text{Al},\text{Si})_3\text{Sc}$ phase within the Al matrix as shown in Fig. 5(e). This is in contrast with the calculated equilibrium phase diagram in Fig. 2 which clearly indicates that the chosen alloy composition should be in the Al + Si + V-phase region during the pre-heat treatment at 350 °C and no $(\text{Al},\text{Si})_3\text{Sc}$ should form. However, previous experimental phase diagrams indicate the presence of a stable Al_3Sc phase in these type of alloys at 350 °C [32]. Moreover, during the gravity die casting of these alloys, the solidification rate was high enough to consume a very little Sc to form Sc-containing intermetallics in the as-cast alloys. Thus, a sufficient amount of Sc was still available in the solid solution of the alloy to form the $(\text{Al},\text{Si})_3\text{Sc}$ phase upon the pre-heat treatment at 350 °C. The OR of $(\text{Al},\text{Si})_3\text{Sc}$ phase with the α -Al matrix was found to be cube-cube, which is similar to the earlier reported results [37].

The STEM analysis of $(\text{Al},\text{Si})_3\text{Sc}$ precipitates further revealed their crystal structure, size, and shape. The Z-contrast HAADF method was utilised to identify the Sc columns in $(\text{Al},\text{Si})_3\text{Sc}$ nano-precipitate since the Z-contrast is roughly proportional to the square of Z (atomic numbers of atoms). Fig. 5(f) indicates brighter Sc atoms as compared to Al atoms, revealing the L_{12} crystal structure of the $(\text{Al},\text{Si})_3\text{Sc}$ precipitates, with the space group of $\text{Pm}\bar{3}\text{m}$ [33]. The atomic arrangement also confirms that the precipitates are perfectly coherent with the α -Al matrix with some amount of lattice mismatch at the interface, which resulted in the Ashby-Brown (AB) strain contrast around the precipitates [38]. The precipitates had an average diameter of 5 nm and those which were smaller than 3 nm, had no facets; however, those larger than 3 nm, had faceted cubic shape along $\langle 001 \rangle$ as observed in Fig. 5(f). Additional TEM observations revealed that the $(\text{Al},\text{Si})_3\text{Sc}$ precipitates had maintained their coherency with the α -Al matrix following the hot rolling at 350 °C and cold rolling at room temperature.

3.4.2. Phase evolution following solutionising

Phase changes were observed in the cold-rolled alloy sheets when exposed to high temperatures (450 °C for Al-0.4Si-0.25Sc alloy and 550 °C for Al-0.8Si-0.2Sc alloy) for a period of 0.5 h. The coherent, $(\text{Al},\text{Si})_3\text{Sc}$ phase as well as secondary Si particles that were formed, following pre-heat treatment, were rarely seen in the alloys after solutionising. Instead, a rod-shaped, anisotropic phase was discontinuously precipitated in the α -Al matrix as observed in the SEM image given in Fig. 6(a). The phase preferred the grain boundaries for the precipitation and appeared to be segregated along these boundaries. Fig. 6(b) gives the magnified image of the microstructure observed in Fig. 6(a). The length and thickness of these rods were much larger for the alloy treated at 550 °C (refer Fig. 6b) than that for the alloy treated

at 450 °C (refer Fig. 6c). The higher temperature has most likely led to the formation of longer and thicker rods due to a higher kinetic decomposition rate.

There is a possibility that this rod-shaped phase is a V-phase as its formation at high temperature in Al-alloys with high Si content was reported [27,33,39]. In all the reported literature, V-phase was described as coarse, oval [32] or spherical and ellipsoid shaped [33] phase. Some other studies indicated the formation of similar rod-shaped Al_3Sc [39,40], Al_3Zr [41,42], and $\text{Al}_3\text{Sc}_{(1-x)}\text{Zr}_x$ [43] phases in Al-Sc-(Zr)-(Mg) alloy systems. However, in the literature reported so far, there is no indication of the presence of V-phase in the rod-shaped morphology. Thus, it was important to analyse the rod-shaped phase formed in this case to confirm its chemical and structural properties *via* the use of TEM techniques. The elemental analysis conducted using STEM-EDS shows the area mapping results in Fig. 7. It can be seen that the rod-shaped precipitates are rich in both Si- and Sc-content. Further, line scan analysis using STEM-EDS was done to get the semi-quantitative results for the V-phase composition. The rod-shaped precipitate which was located in the thin area of the sample was chosen for the line-scan shown in Fig. 7(a) to get accurate elemental distribution. The line scan results in Fig. 7(c) verifies that there is an equal content of Sc and Si concentration in the precipitate. The matrix being α -Al, a large signal for Al was obtained which might not be the true representation of the stoichiometric content for the elements in the phase. The local EDS results of the rod-shaped precipitate thus suggests that the phase can have a stoichiometry of $\text{Al}_x\text{Si}_y\text{Sc}_y$. This agrees with the reported compositions of AlSc_2Si_2 (V-phase) and AlSiSc [33].

The observed softening during the high-temperature solutionising treatment comes from the loss of the coherent, nano-sized, $(\text{Al},\text{Si})_3\text{Sc}$ precipitates and the formation of the non-hardening V-phase. The microstructure observations using TEM, shown in Fig. 8(a) and (b), indicate only a few coarse $(\text{Al},\text{Si})_3\text{Sc}$ precipitates. The white arrows in Fig. 8(a) indicate semi-coherent $(\text{Al},\text{Si})_3\text{Sc}$ precipitates and red arrows show V-phase rods. The semi-coherent nature of the $(\text{Al},\text{Si})_3\text{Sc}$ nano-precipitates can be determined with the change in the AB strain contrast around these precipitates as seen in Fig. 8(b). The final ageing treatment at 250 °C could not recover the hardness drop experienced by both the alloys following solutionising, which confirmed that the microstructure remained unaffected after the peak ageing treatment.

3.4.3. V-phase characteristics

It is known that the V-phase has a tetragonal U_3Si_2 crystal structure, space group of $\text{P4}/\text{mbm}$ (No. 127), and lattice parameters of $a = 6.597 \text{ \AA}$, $c = 3.994 \text{ \AA}$ [33]. The Crystal Maker[®] was used to construct the simulated crystal structure and the associated diffraction patterns of the V-phase using the atomic coordinates of the V-phase [44].

The interatomic spacings (d-spacings) for the indexed planes of the V-phase were measured for the experimental SADPs and then compared with the d-spacings from the calculated diffraction patterns using Crystal Maker[®] and are produced in Table 2. A fair agreement (less than 2% variation) between the experimental and the calculated d-spacings from the SADPs confirmed the crystal structure of the V-phase. Additionally, the lattice parameters using experimental SADPs and high-resolution BF image were measured and compared against the previously reported values of V-phase [33] and are given in Table 3. The estimated lattice parameters using the experimental SADPs of this study were: $a = 6.56 \text{ \AA}$, $b = 6.64 \text{ \AA}$, and $c = 3.98 \text{ \AA}$; $\alpha = \beta = \gamma = 90^\circ$. The variation between measured 'a' and 'b' lattice parameters as well as the difference with the previously reported lattice parameters of the V-phase can be attributed to the low accuracy of the d-spacing measurement using SADP technique and due to the structural change occurred during the formation of metastable V-phase as reported previously [26]. The high-resolution BF image which was captured using STEM is given in Fig. 9. The image

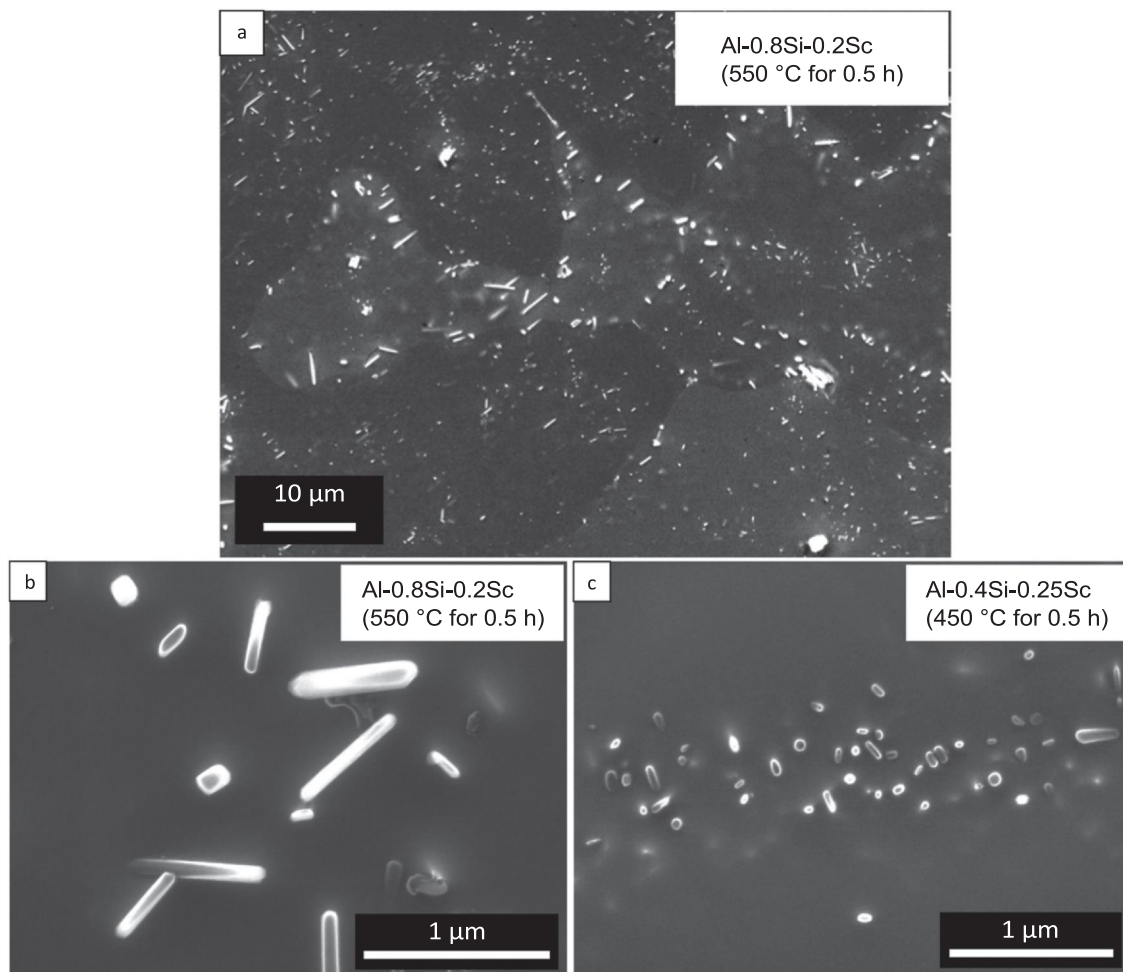


Fig. 6. SEI-SEM images of microstructure in (a) Al-0.8Si-0.2Sc alloy solution treated at 550 °C for 0.5 h (b) magnified view of Al-0.8Si-0.2Sc alloy solution treated at 550 °C for 0.5 h (c) Al-0.4Si-0.25Sc solution treated at 450 °C for 0.5 h.

was used to evaluate the lattice parameters of the V-phase; however, the estimation of 'c' is not available since the image is aligned along [001]_v zone axis. The remaining 'a' and 'b' parameters of the V-phase lattice structure were measured using an analysis tool of Digital Micrograph®. The measured values of 'a' and 'b' are 6.57 Å and 6.42 Å respectively, which differs from the previously reported lattice parameters of the V-phase [33] and the difference can be attributed to the inaccuracies of the measurement technique utilised in this study.

3.4.4. ORs of the rod-shaped phase with α-Al matrix

The SADPs were collected for the individual rods of the V-phase and were compared with the calculated diffraction patterns of the V-phase using Crystal Maker®, and a good match was found between the two. In total 11 individual rods were successfully analysed for the determination of ORs. It was seen that, most frequently, the V-phase precipitates were oriented in the [310] direction when viewed along different zone axis of the matrix as observed in Fig. 10 (a'), (b') and (c'), where the highlighted red pattern indicates an SADP of α-Al matrix and the highlighted yellow pattern indicates that of a V-phase. The phase had multiple and independent ORs with the α-Al matrix. In total, six new ORs were observed for the V-phase in Al-0.8Si-0.2Sc alloy when solutionised at 550 °C for 0.5 h and are listed below. Out of these six ORs, the OR1 was seen to be the most common.

$$[310]_{\text{AlSc}_2\text{Si}_2} || [001]_{\alpha\text{-Al}} \text{ and } (\bar{1}\bar{3}2)_{\text{AlSc}_2\text{Si}_2} || (\bar{2}\bar{2}0)_{\alpha\text{-Al}} \text{ as shown in Fig. 10 (a')} \quad \text{(OR1)}$$

$$[310]_{\text{AlSc}_2\text{Si}_2} || [001]_{\alpha\text{-Al}} \text{ and } (\bar{1}\bar{3}1)_{\text{AlSc}_2\text{Si}_2} || (\bar{2}\bar{2}0)_{\alpha\text{-Al}} \text{ as shown in Fig. 10 (b')} \quad \text{(OR2)}$$

$$[\bar{1}\bar{3}0]_{\text{AlSc}_2\text{Si}_2} || [011]_{\alpha\text{-Al}} \text{ and } (310)_{\text{AlSc}_2\text{Si}_2} || (\bar{2}00)_{\alpha\text{-Al}} \text{ as shown in Fig. 10 (c')} \quad \text{(OR3)}$$

$$[\bar{1}\bar{1}1]_{\text{AlSc}_2\text{Si}_2} || [013]_{\alpha\text{-Al}} \text{ and } (\bar{1}\bar{1}\bar{2})_{\text{AlSc}_2\text{Si}_2} || (200)_{\alpha\text{-Al}} \text{ as shown in Fig. 10 (d')} \quad \text{(OR4)}$$

$$[001]_{\text{AlSc}_2\text{Si}_2} || [001]_{\alpha\text{-Al}} \text{ and } (\bar{1}\bar{3}0)_{\text{AlSc}_2\text{Si}_2} || (\bar{2}00)_{\alpha\text{-Al}} \text{ as shown in Fig. 10 (e')} \quad \text{(OR5)}$$

$$[010]_{\text{AlSc}_2\text{Si}_2} || [011]_{\alpha\text{-Al}} \text{ and } (001)_{\text{AlSc}_2\text{Si}_2} || (\bar{1}\bar{1}1)_{\alpha\text{-Al}} \text{ as shown in Fig. 10 (f')} \quad \text{(OR6)}$$

When the matrix and the precipitate zone axes were aligned, the matching crystallographic planes and related misfits were calculated based on the identified OR [45]. For example, the misfit for OR1 along $(1\bar{3}2)_v || (\bar{2}\bar{2}0)_{\alpha\text{-Al}}$ was calculated as: $\text{misfit (\%)} = \{[d_{(220)\alpha} - d_{(132)_v}] / d_{(220)\alpha}\} \times 100$ [2], where $d_{(220)\alpha}$ and the $d_{(132)_v}$ are the lattice spacings of α-Al matrix along (220) plane and of V-phase along (132)

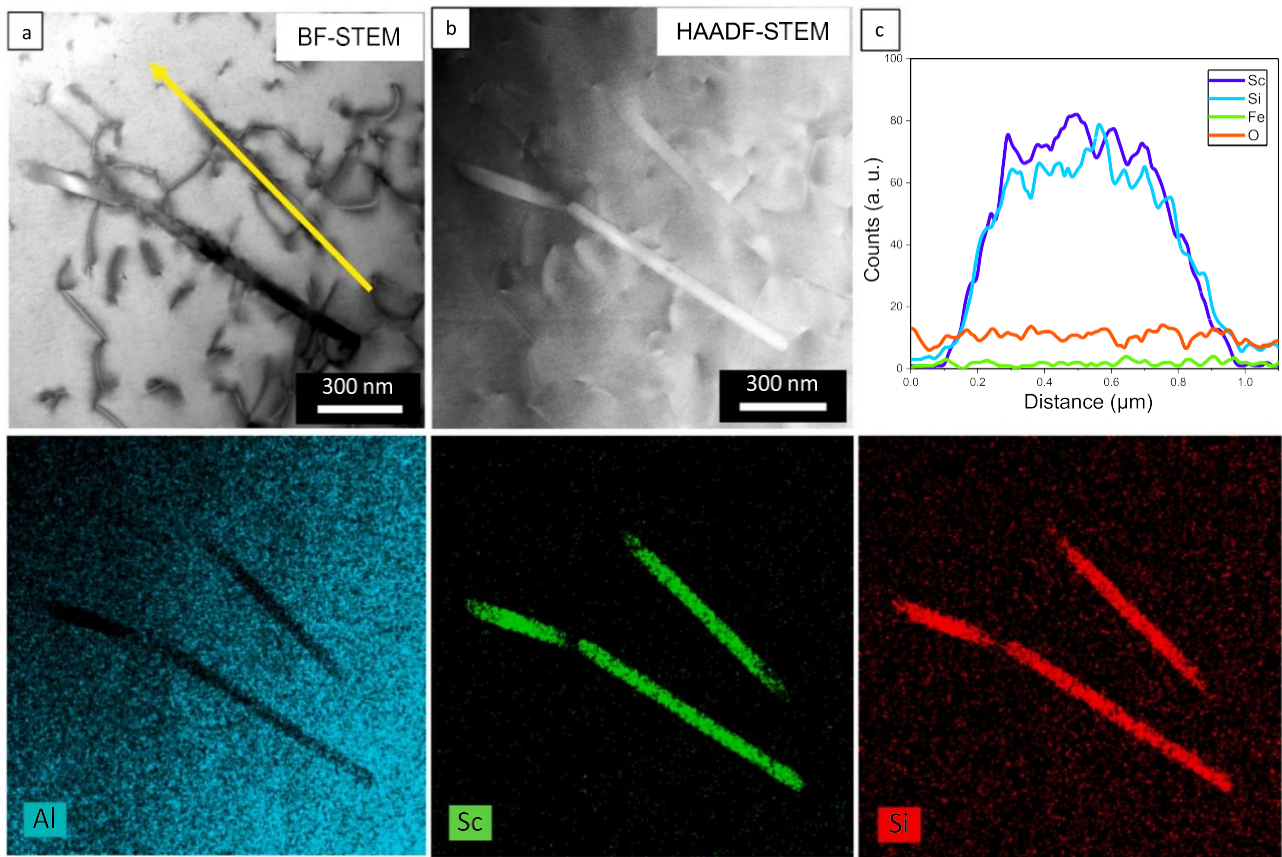


Fig. 7. (a) BF-STEM, (b) corresponding HAADF-STEM image, and (c) EDS line-scan results of the V-phase in the α -Al matrix in Al-0.8Si-0.2Sc solutionised at 550 °C for 0.5 h, with the corresponding EDS mapping results.

plane respectively. The d-spacings for the V-phase were obtained from the experimental SADPs given in Table 2 and that for the α -Al matrix were obtained from the earlier reported values ($a = 0.405$ nm) [46]. The matching crystallographic planes and the calculated lattice misfits for all the 6 ORs are given in Table 4. It was noticed that in most cases, V-phase formed as long rods with their long axis parallel

to $\langle 001 \rangle_{\alpha\text{-Al}}$ resulting in lower lattice misfit. The anisotropy in the shape of V-phase can be explained using the observed misfit values [47]. Especially OR1, OR3, OR4, and OR5 show a small difference ($< 3.5\%$) in lattice misfit, indicating the preference of rod-shaped phase to grow in the direction parallel to their long axis once nucleated. Whereas, OR2 and OR6 have comparatively larger misfit

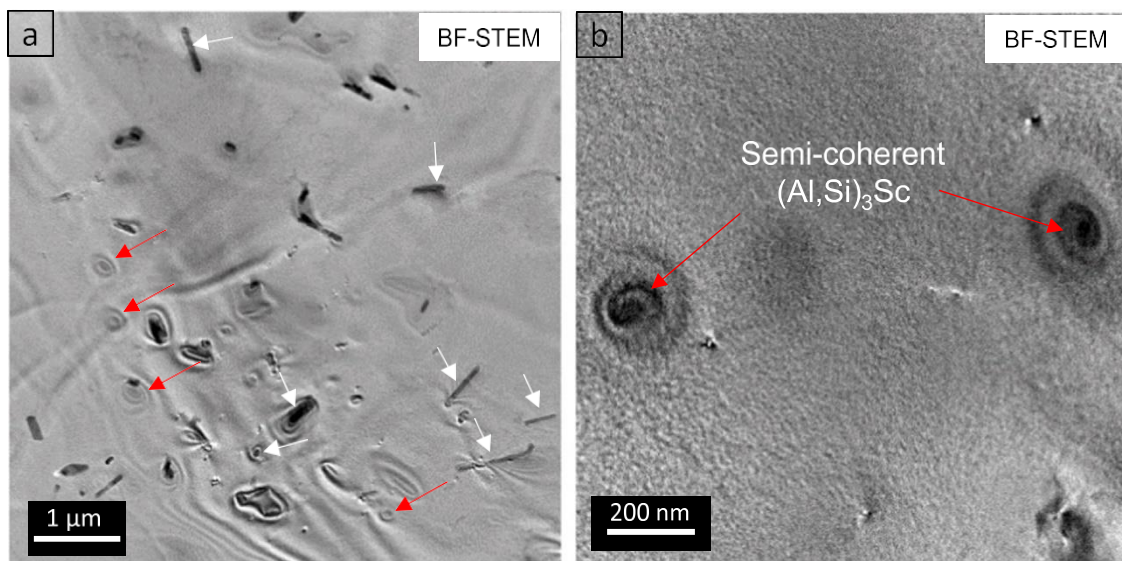


Fig. 8. BF-STEM images of Al-0.8Si-0.2Sc alloy solutionised at 550 °C for 0.5 h. (a) Low-magnification image of $(\text{Al,Si})_3\text{Sc}$ precipitates and V-phase and (b) semi-coherent $(\text{Al,Si})_3\text{Sc}$ precipitates. Red and white arrows indicate $(\text{Al,Si})_3\text{Sc}$ precipitates and V-phase respectively. (For interpretation of the references to colour in this figure legend, the reader is referred to the web version of this article).

Table 2

Experimental and calculated interplanar spacings (d-spacings) for the ternary V-phase.

(hkl)	d_{exp} (nm)	d_{cal} (nm) ^a
(110)	0.471	0.467
(001)	0.398	0.399
(200)	0.328	0.330
(020)	0.332	0.330
(120)	0.295	0.295
(201)	0.251	0.254
(211)	0.240	0.237
(130)	0.209	0.209
(131)	0.181	0.185
(112)	0.200	0.184
(320)	0.184	0.183
(202)	0.169	0.171
(140)	0.161	0.160
(132)	0.141	0.144
(213)	0.129	0.121
(242)	0.117	0.119
(530)	0.113	0.113

^aThe interplane spacings reproduced from ICDD PDF - 4 + 2018 RDB database file no. 04-018-3651

values of the order of 26% and 15% respectively indicating shorter growth along the respective axis.

In the previous studies, the experimental and calculated interplane distances were found to be different when compared [33] and the reported two ORs of the V-phase and the Al matrix were - $(\bar{1}2\bar{2})_{AlSc2Si2} || (010)_{\alpha-Al}; [221]_{AlSc2Si2} || [100]_{\alpha-Al}$ and $(1\bar{3}4)_{AlSc2Si2} || (010)_{\alpha-Al}; [221]_{AlSc2Si2} || [100]_{\alpha-Al}$ [26]. However, in this study both of these ORs were not observed. The ORs identified in this study are independent and different from each other even though viewed in the same zone axis of the α -Al matrix. This indicates random precipitation of V-phase in the α -Al matrix without a strong preference for any single OR. It is possible to find some more ORs of this discontinuously precipitated V-phase with the α -Al matrix if some more individual rods are analysed.

3.4.5. In situ TEM heating results

The microstructure analysis showed that the phases formed after the pre-heat treatment are nano-sized (Al,Si)₃Sc precipitates and the secondary Si particles. However, both of these phases were observed to be absent in both the alloys after the solutionising treatment, and instead, a rod-shaped V-phase was observed. To study the phase transformation mechanisms for the nano-sized (Al,Si)₃Sc precipitates and the V-phase rods, an *in situ* TEM heating technique was employed.

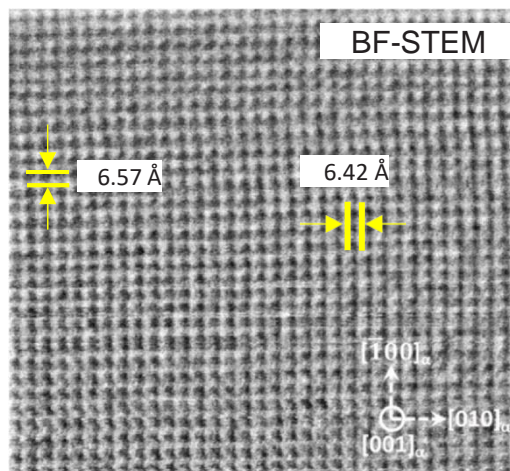
A TEM sample from the Al-0.4Si-0.25Sc alloy in the as-cast condition was *in situ* heated at 50 °C/min to 350 °C and held for 1 h at 350 °C to observe and record the precipitation of (Al,Si)₃Sc. Images from the recorded video were extracted from the start of the precipitate nucleation every 10 s up to 1000 s of holding time and the quantitative analysis of the precipitate diameter was done using

Table 3

Comparison of experimental and theoretical lattice parameters of V-phase.

Lattice parameters	Previously reported lattice parameters [33] (Å)	Experimental lattice parameters (Å)	
		Using SADPs	Using high-resolution BF image
a	6.597	6.56	6.57
b	6.597	6.64	6.42
c	3.994	3.98	--

Note: Estimation of 'c' using high-resolution BF image is not available since the image is aligned along [001]_v.

**Fig. 9.** Atomic resolution BF-STEM image of the V-phase in Al-0.8Si-0.2Sc alloy.

these calibrated images in the ImageJ software [48]. The (Al,Si)₃Sc nano-precipitates started to nucleate as soon as the temperature of 350 °C was reached as shown in Fig. 11 (a). The number density of the nano-precipitates increased with increasing holding time as shown in Fig. 11 (b) and (c). The quantitative measurement of all the nucleated precipitates was averaged and represented in Fig. 11 (d). A standard deviation of 5% was applied to all the measurements since the precipitate diameter measurements were done manually in the ImageJ software. It was noted that the average stable precipitate diameter for the *in situ* TEM heated sample was much larger (~15 nm) than that for the *ex situ* sample heated at 350 °C for 30 min (~5 nm). Also, a sharp increase in precipitate diameter in the first 100 s was observed and then the diameter remained constant with minimal growth up to a holding time of about 1000 s. The larger diameter and a shorter time to reach the stable diameter for the nano-precipitates in the case of *in situ* TEM heated sample can be due to the increased precipitation kinetics in the thin foil as compared to that in the bulk sample.

The second sample for *in situ* TEM heating experiment was from the Al-0.8Si-0.2Sc alloy, which was first *ex situ* pre-heat treated at 350 °C for 30 min in a muffle furnace. The microstructure of this sample was comprised of a mixture of the precipitated nano-sized (Al,Si)₃Sc phase and secondary Si particles as earlier shown in Fig. 5. The appropriate area containing both of these phases was selected for observation under TEM for the *in situ* experiment. While the sample foil was heating to reach 550 °C, the dissolution of secondary Si particles was observed. The noticeable size reduction of the Si particle was seen from a temperature of 180 °C and the complete dissolution of the same occurred at 396 °C as shown in Fig. 12 (a₁-a₆). During this period there were no changes to the nano-sized (Al,Si)₃Sc precipitates and they started to dissolve from a temperature of 458 °C, which resulted in the reduced number density of the (Al,Si)₃Sc precipitates with increasing temperature. Some of the nano-precipitates that were not dissolved in the early stages had experienced growth in diameter up to 35–40 nm. The reduced number density and the growth of these precipitates during the heating period from 458 °C to 520 °C are shown in Fig. 12 (b₁-b₃). Eventually, all the precipitates dissolved at 520 °C resulting in the α -Al matrix rich in a solid solution of Sc and Si, and no precipitation of new phases occurred until 548 °C temperature. However, at 549 °C, a small rod-shaped phase precipitated which then experienced growth at 550 °C as shown in Fig. 12 (c₁-c₃). The heating experiment was stopped after a holding time of 5 min because of the excessive growth of the rod-shaped V-phase and a very high drift of the foil due to the high holding temperature.

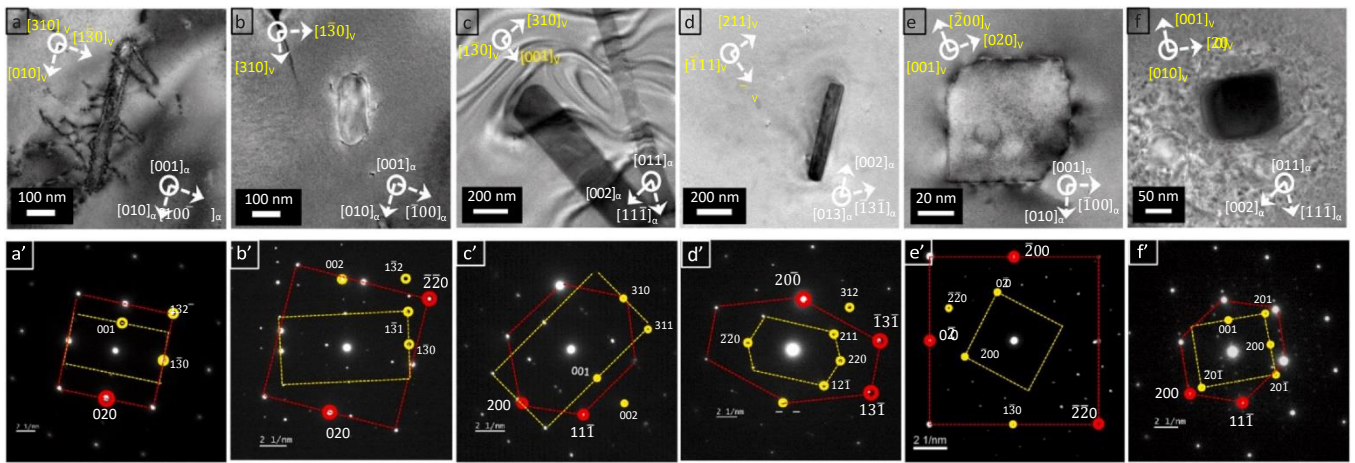


Fig. 10. Crystallographic ORs of the V-phase with the α -Al matrix in Al-0.8Si-0.2Sc alloy solutionised at 550 °C for 0.5 h (a–f) BF-TEM images of the V-phase, (a’–f’) respective SADPs of the images. (For interpretation of the references to colour in this figure, the reader is referred to the web version of this article).

Table 4

Misfit between matching crystallographic planes for the identified ORs of the AlSi_2Sc_2 (V-phase) and α -Al matrix.

OR No.	ORs of V-phase with α -Al matrix	d_a (nm)	d_v (nm)	Misfit (%)
OR1	$[310]_v \parallel [001]_a$ and $(1\ 2)_v \parallel (0)_{a\ \bar{3}}$	$d_{(220)} = 0.1432$	$d_{(132)} = 0.141$	1.5
OR2	$[310]_v \parallel [001]_a$ and $(1\ 1)_v \parallel (0)_{a\ \bar{3}}$	$d_{(220)} = 0.1432$	$d_{(131)} = 0.181$	-26.4
OR3	$[1\ 0]_v \parallel [011]_a$ and $(310)_v \parallel (00)_a$	$d_{(200)} = 0.2025$	$d_{(310)} = 0.209$	-3.2
OR4	$[11]_v \parallel [0\bar{1}3]_a$ and $(\bar{1}\ 1\bar{2})_v \parallel (200)_a$	$d_{(200)} = 0.2025$	$d_{(112)} = 0.200$	1.2
OR5	$[001]_v \parallel [001]_a$ and $(1\ 0)_v \parallel (00)_{a\ \bar{3}}$	$d_{(200)} = 0.2025$	$d_{(130)} = 0.209$	-3.2
OR6	$[010]_v \parallel [011]_a$ and $(001)_v \parallel (1)_{a\ \bar{3}}$	$2d_{(111)} = 0.4676$	$d_{(001)} = 0.398$	14.9

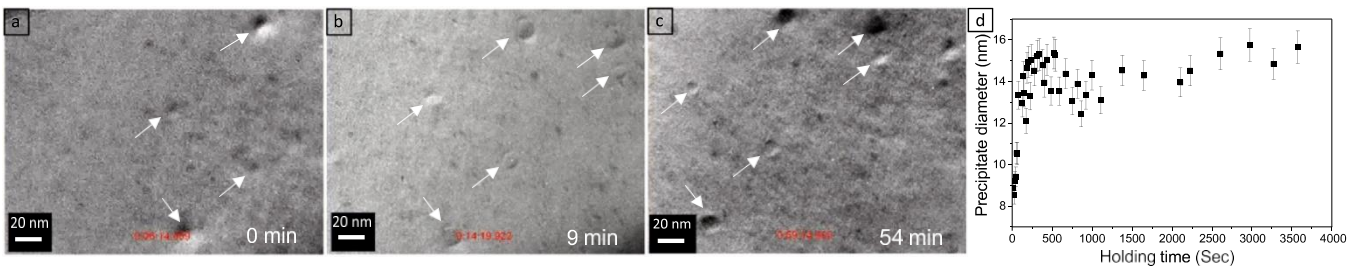


Fig. 11. (a–c) Images from *in situ* TEM heating experiment conducted on Al-0.4Si-0.25Sc alloy at 350 °C for 1 h showing nucleation and growth of $(\text{Al,Si})_3\text{Sc}$ nano-precipitates, (d) respective change in precipitate diameter as a function of holding time.

4. Discussion

It is evident from the hardness results and related micro-structures that the processing conditions, in particular, the heat

treatment temperature, play a major role in determining the final hardness for Al-Si-Sc alloys. The pre-heat treatment resulted in a significant hardening of both the alloys whereas a high-temperature solutionising treatment led to severe softening. The initial hardening

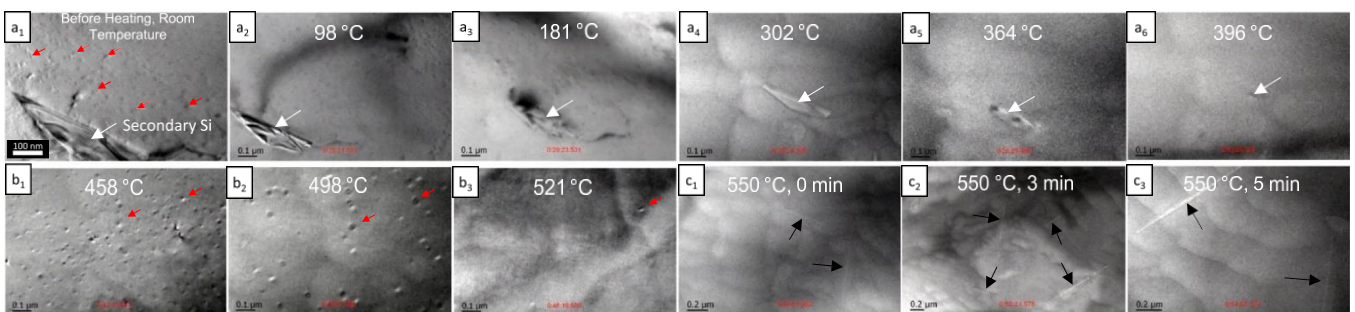


Fig. 12. Snapshots of video during *in situ* TEM heating of Al-0.8Si-0.2Sc alloy revealing (a₁–a₆) dissolution sequence for the secondary Si particle (b₁–b₃) dissolution sequence of the nano-sized $(\text{Al,Si})_3\text{Sc}$ precipitates (c₁–c₃) nucleation and growth sequence for the rod-shaped V-phase. Red, white and black arrows indicate the $(\text{Al,Si})_3\text{Sc}$ nano-precipitates, Si-particle and V-phase rods respectively. Note: As-cast Al-0.8Si-0.2Sc alloy was first *ex situ* heat treated at 350 °C for 30 min and then *in situ* heated at 550 °C. (For interpretation of the references to colour in this figure legend, the reader is referred to the web version of this article).

after pre-heat treatment comes from the formation of homogeneous (Al,Si)₃Sc nano-precipitates [8,33] as seen from the microstructure analysis in this study. Generally, the strengthening mechanisms related to precipitate formation is a function of the dominating precipitate-dislocation interaction mechanism – (1) precipitate shearing or (2) precipitate by-passing (or dislocation looping). The transition from predominantly precipitate shearing to precipitate by-passing occurs for a critical precipitate diameter [49]. Sometimes, a mixed mechanism of strengthening is also seen due to the presence of small and large precipitates in the alloy at the same time. The strengthening due to precipitate shearing is generally contributed by (1) Modulus hardening, (2) Coherency strengthening, and (3) Order strengthening [8,19]. In this case, the Orowan mechanism of precipitate by-passing is expected to be prevalent due to the presence of sufficiently larger precipitates formed after the pre-heat treatment [50]. The hardness improvement during the rolling process was mainly attributed to the strain hardening process [34,35].

4.1. Phase transformation mechanisms

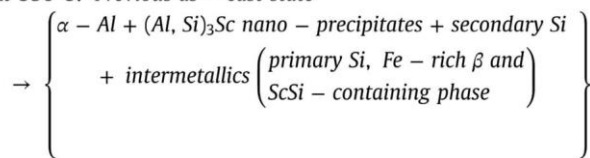
4.1.1. The formation mechanism for (Al,Si)₃Sc phase

The (Al,Si)₃Sc nano-precipitates formation mechanism in the case of binary Al-Sc and ternary Al-Sc-M (where M can be other major alloying addition to Al-alloys like Si, Cu, Zn, etc.) alloy systems are well studied and reported to be due to the decomposition of solute elements resulting in the direct formation of the nano-precipitates from the supersaturated solution of α -Al matrix [33,51,52]. However, it is important to study if the formation mechanism of (Al,Si)₃Sc nano-precipitates remains the same in the presence of high Si content in the alloys.

The *in situ* TEM heating experiment was thus conducted for the Al-0.4Si-0.25Sc as-cast alloy at an isothermal temperature of 350 °C in order to just form the (Al,Si)₃Sc nano-precipitates as obtained during *ex situ* treatment at the same temperature. The results as indicated in Fig. 11 (a) and (b), show the direct nucleation of (Al,Si)₃Sc phase from the supersaturated α -Al matrix at 350 °C with almost negligible holding time. It was observed that the nucleation was homogeneous, and occurred randomly throughout the Al matrix without the preferential grain boundary precipitation indicating that the foil specimen areas were rich in Si- and Sc-content. Thus, the precipitation sequence for the (Al,Si)₃Sc phase seen in this study can be written as follows:



At 350°C: Previous as – cast state



where $SS_{\alpha\text{-Al}}$ indicates a solid solution of Si and Sc in the α -Al matrix. The initial growth of the (Al,Si)₃Sc precipitates is very fast for the first 100 s until the precipitates reach a stable diameter of 13–16 nm as indicated in Fig. 11 (d). This confirms the classical nucleation and growth mechanism for the (Al,Si)₃Sc precipitates. An earlier study [53] indicated that the continuous precipitation of this phase when annealing is carried out at temperatures below 300 °C and the discontinuous precipitation of the same was observed at the grain boundaries for the annealing temperatures greater than 350 °C. On the contrary, in this study, in the case of (Al,Si)₃Sc nano-precipitates, the continuous precipitation has been seen even at the temperature of 350 °C. This can be partly due to the contribution of Si atoms in

accelerating the precipitation mechanism for (Al,Si)₃Sc nano-precipitates [19–21]. Once the stable diameter of nano-precipitates is reached, a negligible amount of growth in their diameter was observed which is contrary to the observations made in alloys leaner in Si where the spherical nano-precipitates grow in diameter as a function of ageing temperature, ageing time and Sc concentration [54].

4.1.2. The formation mechanism for V-phase

The formation of a rod-shaped V-phase heterogeneously distributed along the grain boundaries occurred in the case of Al-0.4Si-0.25Sc and Al-0.8Si-0.2Sc alloys when *ex situ* treated at 450 °C and 550 °C respectively. The ScSi region in the phase diagram calculated using ThermoCalc® (given in Fig. 2) is assumed to be the probable V-phase formation region. Thus, two different solutionising temperatures were used for these alloys depending on the ScSi phase region. The V-phase was formed at the expense of (Al,Si)₃Sc and secondary Si particles as indicated in the results Section 3.4.2.

The rod-shaped morphology was for the first time observed in the case of V-phase in this study. The earlier studies which indicate the formation of other rod-shaped phases in Al-alloys were analysed to see if the V-phase formation mechanism could be similar to those cases. There exists extensive research about the coherency loss and growth of nano-sized Al₃Sc precipitates [49,54–57]. In one study, rod-like Al₃Sc precipitates were formed in annealed Al-0.1 wt% Sc alloy along with some other morphologies [58]. In another study, similar rod-like precipitates of 300–500 nm in length and irregular widths in Al-2.2Mg-0.12Sc at% alloys were formed may be due to the coagulation of precipitates after the coherency loss [40]. The rod-shaped Al₃Sc_{(1-x)Zr_x} precipitates were discontinuously precipitated in the industrial AA5754 alloy modified with Sc and Zr additions [43], the mechanism of which was observed to be similar in the case of high-temperature annealed Al-3Mg-0.25Er-0.25Zr wt% alloy [59]. The tetragonal plates of Al₃Zr were formed from the rod-shaped Al₃Zr with the precipitation sequence as:

$SS_{\alpha\text{-Al}} \rightarrow$ spherical Al₃Zr with L1₂ structure \rightarrow Rod-shaped Al₃Zr with L1₂ structure \rightarrow plates of Al₃Zr with a tetragonal DO₂₃ structure [42]. The research done so far has raised two main possibilities for the rod-shaped V-phase formation mechanism in the Al-0.4Si-0.25Sc and Al-0.8Si-0.2Sc alloys when solutionised at 450 and 550 °C and are as stated below.

Possibility 1: The precipitation sequence similar to the earlier reported case of rod-shaped tetragonal Al₃Zr phase [41,42], which is given as:

$SS_{\alpha\text{-Al}} \rightarrow$ nucleation of L1₂ structured spherical (Al,Si)₃Sc nano-precipitates \rightarrow rod-shaped (Al,Si)₃Sc precipitates with L1₂ structure \rightarrow tetragonal V-phase.

Possibility 2: The classic nucleation and growth of rod-shaped V-phase which require the supersaturated solid solution of Si and Sc in the α -Al matrix to start the precipitation mechanism. Thus, suggesting that the secondary Si and the nano-precipitates rich in Sc if present need to dissolve first in order to form the V-phase. The precipitation sequence, in this case, is given as:

Previous state *i.e.* $\{SS_{\alpha\text{-Al}} + (\text{Al,Si})_3\text{Sc nano-precipitates} + \text{secondary Si} + \text{intermetallics}\} \rightarrow$ dissolution of secondary Si $\rightarrow \{SS_{\alpha\text{-Al}} \text{ rich in Si content} + (\text{Al,Si})_3\text{Sc nano-precipitates}\} \rightarrow$ dissolution of (Al,Si)₃Sc nano-precipitates $\rightarrow SS_{\alpha\text{-Al}} \rightarrow \{\alpha\text{Al} + \text{V-phase}\}$.

The *in situ* TEM heat treatment at 550 °C of pre-heat-treated Al-0.8Si-0.2Sc alloy clearly indicated the dissolution and precipitation sequence of the possible phases in the Al matrix. During heating, as the temperature increases, the solubility of Si increases as indicated by the increasing solvus line in Fig. 2. This resulted in the dissolution of secondary Si-phase, which was complete at a temperature of

396 °C as given in Fig. 12 (a₁–a₆). With increasing heating temperature, more Si was released back into the matrix and the (Al,Si)₃Sc nanoprecipitates became less stable, and, in turn, dissolved into the matrix at 520 °C as shown in Fig. 12 (b₁–b₃). The dissolution of both the phases resulted in the formation of a supersaturated solution of the α -Al matrix rich in Si and Sc. The spontaneous nucleation of the V-phase occurred once a threshold in the composition/nucleation barrier is reached followed by growth in the rod-shaped morphology at 549 °C without forming any other metastable phases. The observed dissolution and precipitation sequence of V-phase in the alloy studied here corresponds with the expected possibility (2) of the V-phase formation mechanism. It should be noted that the dissolution sequence discussed here depends on the heat treatment route and will vary if a different heat treatment (*e.g.* direct isothermal homogenization treatment of the as-cast sample at 550 °C) is utilized. Further, a high growth rate of the V-phase rods was observed within 5 s of holding time due to exposure of the specimen to the high heating temperature of 550 °C as shown in Fig. 12 (c₁–c₃).

The formation temperature for the V-phase was higher than that of (Al,Si)₃Sc phase for both the alloys as seen experimentally. The ScSi phase region predicted by ThermoCalc® in Fig. 2 corresponds well with the V-phase formation region previously assumed in this study. This assumption was also a basis for the heat treatment design for both the alloys to form either (Al,Si)₃Sc or V-phase in the α -Al matrix selectively. The secondary Si particles and the nano-scale (Al,Si)₃Sc precipitates co-existed when the alloys were pre-heat treated at 350 °C for 30 min without the formation of the V-phase. The nucleation of the V-phase was observed to occur at 450 °C and 550 °C for the alloy with 0.4 wt% Si and 0.8 wt% Si respectively. The solvus line temperature for Si-particles increases with increasing Si content and in order to form a stable V-phase both Si and Sc need to be in a solid solution. Therefore, the V-phase nucleation is temperature-dependent and increasing Si content resulted in the increased nucleation temperature of the V-phase. The simultaneous precipitation of (Al,Si)₃Sc phase and Si particles in an alloy can be obtained by optimising the heat treatment conditions below the V-phase nucleation temperature to improve the hardening response in Al-Si-Sc alloys. The understanding of the formation mechanisms of (Al,Si)₃Sc and V-phase is thus crucial for the successful use of Sc in the alloying of 6xxx series and other Si-containing Al-alloys.

5. Conclusions

The formation mechanisms for the nanoscale (Al,Si)₃Sc and V-phase were studied by means of electron microscopy, XRD, and *in situ* TEM for Al-Si-Sc alloys. The following conclusions may be drawn:

1. Nanoscale and coherent (Al,Si)₃Sc, along with sub-micrometre sized secondary Si precipitates, were formed in Al-(0.4–0.8)Si-(0.20–0.25)Sc wt% alloys following pre-heat treatment at 350 °C for 0.5 h, resulting in a significant hardening effect.
2. The hardness of pre-heat treated Al-Sc-Si alloys did not vary with subsequent hot and cold rolling processes due to the retention of (Al,Si)₃Sc precipitates in the Al matrix. However, a significant decrease in hardness was observed following solutionising at 450 °C and 550 °C - as a result of the formation of rod-shaped V-phase at the expense of secondary Si particles and (Al,Si)₃Sc nanoscale precipitates.
3. Rod-shaped V-phase (AlSc₂Si₂) having a tetragonal crystal structure with lattice parameters; $a = 6.56 \text{ \AA}$, $b = 6.64 \text{ \AA}$, and $c = 3.98 \text{ \AA}$; $\alpha = \beta = \gamma = 90^\circ$, was determined. In addition, six new ORs between V-phase and the Al matrix were identified.
4. Nanoscale (Al,Si)₃Sc precipitates were nucleated at 350 °C by the continuous precipitation mechanism, without the formation of any other metastable phases.

5. Rod-shaped V-phase was precipitated at 549 °C from Si- and Sc-rich Al matrix by a classical nucleation and growth mechanism, following a complete dissolution of secondary Si-particles and (Al,Si)₃Sc nanoscale precipitates.
6. Processing conditions at which both the desirable (Al,Si)₃Sc nanoscale precipitates and the undesirable rod-shaped V-phase form and their phase transformation mechanisms were determined.

CRedit authorship contribution statement

Jayshri Dumbre: Conceptualization, Methodology, Investigation, Writing - original draft. **Shravan K. Kairy:** Investigation, Writing - review & editing. **Elaf Anber:** Investigation. **Timothy Langan:** Resources, Funding acquisition. **Mitra L. Taheri:** Supervision, Writing - review & editing. **Thomas Dorin:** Conceptualization, Supervision, Writing - review & editing. **Nick Birbilis:** Conceptualization, Supervision, Writing - review & editing.

Declaration of Competing Interest

The authors declare that they have no known competing financial interests or personal relationships that could have appeared to influence the work reported in this paper.

Acknowledgements

The authors acknowledge the use of instruments and scientific and technical assistance at the Monash Centre for Electron Microscopy, a Node of Microscopy Australia and Monash X-Ray Platform (XRP), Monash University, Australia. This research used equipment funded by the Australian Research Council Grant (LE110100223). The authors are grateful to Clean TeQ Holdings Ltd., Australia for providing Al-Sc master alloys and acknowledge financial support through the ARC Linkage Project Scheme (LP160100104). Dr Thomas Dorin is the recipient of an Australian Research Council - Australian Discovery Early Career Award. The authors also acknowledge the use of the Centralized Research Facility (CRF) at Drexel University, Philadelphia, USA for *in situ* TEM experiments.

References

- [1] A. Poznak, D. Freiberg, P. Sanders, *Automotive wrought aluminium alloys*, *Fundam. Alum. Metall. Recent Adv.* (2018) 333–386.
- [2] I.J. Polmear, D. John, J.F. Nie, M. Qian, *Light Alloys: Metallurgy of the Light Metals*, 5th ed., Elsevier, 2017.
- [3] L. Willey, L. Pa, U. S. Pat.: Alum. Scandium Alloy 3619181 1968.
- [4] K. Venkateswarlu, L. Pathak, A. Ray, G. Das, P. Verma, M. Kumar, R. Ghosh, Microstructure, tensile strength and wear behaviour of Al-Sc alloy, *Mater. Sci. Eng. A* 383 (2004) 374–380, <https://doi.org/10.1016/j.msea.2004.05.075>
- [5] J. Ma, D. Yan, L. Rong, Y. Li, Effect of Sc addition on microstructure and mechanical properties of 1460 alloy, *Prog. Nat. Sci. Mater. Int.* 24 (2014) 13–18, <https://doi.org/10.1016/j.pnsc.2014.01.003>
- [6] E.A. Marquis, D.N. Seidman, D.C. Dunand, Effect of Mg addition on the creep and yield behavior of an Al-Sc alloy, *Acta Mater.* 51 (2003) 4751–4760, [https://doi.org/10.1016/S1359-6454\(03\)00288-X](https://doi.org/10.1016/S1359-6454(03)00288-X)
- [7] C.B. Fuller, D.N. Seidman, D.C. Dunand, Creep properties of coarse-grained Al(Sc) alloys at 300 °C, *Acta Metall.* 40 (1999) 691–696, [https://doi.org/10.1016/S1359-6462\(98\)00468-0](https://doi.org/10.1016/S1359-6462(98)00468-0)
- [8] D.N. Seidman, E.A. Marquis, D.C. Dunand, Precipitation strengthening at ambient and elevated temperatures of heat-treatable Al(Sc) alloys, *Acta Mater.* 50 (2002) 4021–4035, [https://doi.org/10.1016/S1359-6454\(02\)00201-X](https://doi.org/10.1016/S1359-6454(02)00201-X)
- [9] M. Cavanaugh, N. Birbilis, R. Buchheit, F. Bovard, Investigating localized corrosion susceptibility arising from Sc containing intermetallic Al₃Sc in high strength Al-alloys, *Scr. Mater.* 56 (2007) 995–998, <https://doi.org/10.1016/j.scriptamat.2007.01.036>
- [10] M. Nakayama, A. Furuta, Y. Miyura, Precipitation of Al₃Sc in Al-0.23 mass % Sc alloys, *Mater. Trans.* 38 (1997) 852–857.
- [11] R. Sawtell, C. Jensen, Mechanical properties and microstructures of Al-Mg-Sc alloys, *Metall. Trans. A* 21A (1990) 421–430 [https://doi.org/S0109-5641\(99\)00093-7](https://doi.org/S0109-5641(99)00093-7) [pii].
- [12] Y. Filatov, V. Yelagin, V. Zakharov, New Al – Mg – Sc alloys, *Mater. Sci. Eng. A* 280 (2000) 97–101.
- [13] B. Chen, L. Pan, R. Wang, G. Liu, P. Cheng, L. Xiao, J. Sun, Effect of solution treatment

- on precipitation behaviors and age hardening response of Al-Cu alloys with Sc addition, *Mater. Sci. Eng. A* 530 (2011) 607–617, <https://doi.org/10.1016/j.msea.2011.10.030>
- [14] C. Yang, P. Zhang, D. Shao, R. Wang, L. Cao, J. Zhang, G. Liu, B. Chen, J. Sun, The influence of Sc solute partitioning on the microalloying effect and mechanical properties of Al-Cu alloys with minor Sc addition, *Acta Mater.* 119 (2016) 68–79, <https://doi.org/10.1016/j.actamat.2016.08.013>
- [15] J. Liu, P. Yao, N. Zhao, C. Shi, H. Li, X. Li, D. Xi, S. Yang, Effect of minor Sc and Zr on recrystallization behavior and mechanical properties of novel Al-Zn-Mg-Cu alloys, *J. Alloy. Compd.* 657 (2016) 717–725, <https://doi.org/10.1016/j.jallcom.2015.10.122>
- [16] M. Zhang, T. Liu, C. He, J. Ding, E. Liu, C. Shi, J. Li, N. Zhao, Evolution of microstructure and properties of Al-Zn-Mg-Cu-Zr alloy during aging treatment, *J. Alloy. Compd.* 658 (2016) 946–951, <https://doi.org/10.1016/j.jallcom.2015.10.296>
- [17] G. Li, N. Zhao, T. Liu, J. Li, C. He, C. Shi, E. Liu, J. Sha, Effect of Sc/Zr ratio on the microstructure and mechanical properties of new type of Al-Zn-Mg-Sc-Zr alloys, *Mater. Sci. Eng. A* 617 (2014) 219–227, <https://doi.org/10.1016/j.msea.2014.08.041>
- [18] T. Dorin, M. Ramajayam, A. Vahid, T.J. Langan, *Aluminium scandium alloys, Fundamentals of Aluminium Metallurgy Recent Advances*, Woodhead Publishing, United Kingdom, 2018, pp. 439–494.
- [19] N. Vo, D. Dunand, D. Seidman, Improving aging and creep resistance in a dilute Al-Sc alloy by microalloying with Si, Zr and Er, *Acta Mater.* 63 (2014) 73–85, <https://doi.org/10.1016/j.actamat.2013.10.008>
- [20] G. Du, J. Deng, Y. Wang, D. Yan, L. Rong, Precipitation of (Al,Si)₃Sc in an Al-Sc-Si alloy, *Scr. Mater.* 61 (2009) 532–535, <https://doi.org/10.1016/j.scriptamat.2009.05.014>
- [21] C. Booth-morrison, Z. Mao, M. Diaz, D.C.C. Dunand, C. Wolverton, D.N. Seidman, Role of silicon in accelerating the nucleation of Al₃(Sc,Zr) precipitates in dilute Al-Sc-Zr alloys, *Acta Mater.* 60 (2012) 4740–4752, <https://doi.org/10.1016/j.actamat.2012.05.036>
- [22] T. Dorin, M. Ramajayam, S. Babaniaris, L. Jiang, T.J. Langan, Precipitation sequence in Al-Mg-Si-Sc-Zr alloys during isochronal aging, *Materialia* 8 (2019) 100437, <https://doi.org/10.1016/j.mta.2019.100437>
- [23] T. Dorin, M. Ramajayam, S. Babaniaris, T.J. Langan, Micro-segregation and precipitates in as-solidified Al-Sc-Zr-(Mg)-(Si)-(Cu) alloys, *Mater. Charact.* 154 (2019) 353–362, <https://doi.org/10.1016/j.matchar.2019.06.021>
- [24] T. Dorin, M. Ramajayam, T.J. Langan., 2018. Effects of Mg, Si, and Cu on the formation of the Al₃Sc/Al₃Zr dispersoids Proceedings of the 6th International Conference on Aluminium Alloys, Canadian Institute of Mining Metallurgy & Petroleum.
- [25] Q. Yao, Elastic properties and electronic structure of L1₂ (Al,Si)₃Sc, *Adv. Mater. Res.* 284–286 (2011) 1987–1990, <https://doi.org/10.4028/www.scientific.net/AMR.284-286.1987>
- [26] M.L. Kharakterova, D.G. Eskin, L.S. Toropova, Precipitation hardening in ternary alloys of the Al-Sc-Cu and Al-Sc-Si systems, *Acta Metall. Et Mater.* 42 (7) (1994) 2285–2290.
- [27] V.G. Davydov, T.D. Rostova, V.V. Zakharov, Y.A. Filatov, V.I. Yelagin, Scientific principles of making an alloying addition of scandium to aluminium alloys, *Mater. Sci. Eng. A* 280 (2000) 30–36, [https://doi.org/10.1016/S0921-5093\(99\)00652-8](https://doi.org/10.1016/S0921-5093(99)00652-8)
- [28] J. Dumbre, T. Langan, T. Dorin, N. Birbilis, Optimised composition and process design to develop Sc-enhanced wrought Al-Si alloys, *Miner. Met. Mater. Ser.* (2019) 1431–1438, https://doi.org/10.1007/978-3-030-05864-7_179
- [29] N. Raghukiran, R. Kumar, The role of the bimodal distribution of ultra-fine silicon phase and nano-scale V-phase (Al₃Si₂Sc) on spark plasma sintered hypereutectic Al-Si-Sc alloys, *Mater. Sci. Eng. A* 657 (2016) 123–135, <https://doi.org/10.1016/j.msea.2016.01.069>
- [30] D. Chen, C. Xia, Z. Chen, Y. Wu, M. Wang, N. Ma, H. Wang, Thermodynamic, elastic and electronic properties of AlSc₂Si₂, *Mater. Lett.* 138 (2015) 148–150, <https://doi.org/10.1016/j.matlet.2014.10.006>
- [31] X. Zhang, F. Wang, W. Jiang, First-principles investigations of structural, mechanical, electronic and optical properties of U₃Si₂-type AlSc₂Si₂ under high pressure, *Trans. Nonferrous Met. Soc. China* 27 (2017) 148–156, [https://doi.org/10.1016/S1003-6326\(17\)60017-7](https://doi.org/10.1016/S1003-6326(17)60017-7)
- [32] L. Rokhlin, N. Bochvar, O. Rybal'chenko, I. Tarytina, A. Sukhanov, Phase equilibria in aluminum-rich Al-Sc-Si alloys during solidification, *Russ. Metall.* 2012 (7) (2012) 606–611, <https://doi.org/10.1134/S0036029512070129>
- [33] L. Toropova, D. Eskin, M. Kharakterova, T. Dobatkina, *Advanced Aluminium Alloys Containing Scandium*, Taylor & Francis Group, London & New York, 1998.
- [34] V. Jindal, P. De, K. Venkateswarlu, Effect of Al₃Sc precipitates on the work hardening behavior of aluminum-scandium alloys, *Mater. Lett.* 60 (2006) 3373–3375, <https://doi.org/10.1016/j.matlet.2006.03.017>
- [35] V. Rajinikanth, V. Jindal, V.G. Akkirmardi, M. Ghosh, K. Venkateswarlu, Transmission electron microscopy studies on the effect of strain on Al and Al-1% Sc alloy, *Scr. Mater.* 57 (2007) 425–428, <https://doi.org/10.1016/j.scriptamat.2007.04.038>
- [36] C. Ho, B. Cantor, Heterogeneous nucleation of solidification of Si in Al-Si and Al-Si-P alloys, *Acta Metall. Mater.* 43 (1995) 3231–3246, [https://doi.org/10.1016/0956-7151\(94\)00480-6](https://doi.org/10.1016/0956-7151(94)00480-6)
- [37] D. Williams, B. Carter, *Transmission Electron Microscopy: Part 1- Basics*, 2nd ed., Springer, New York, 2009.
- [38] M. Ashby, L. Brown, Diffraction contrast from spherically symmetrical coherency strains, *Philos. Mag. A: J. Theor. Exp. Appl. Phys.* 8 (1963) 1083–1103.
- [39] E. Marquis, D. Seidman, Nanoscale structural evolution of Al₃Sc precipitates in Al (Sc) alloys, *Acta Mater.* 49 (2001) 1909–1919, [https://doi.org/10.1016/S1359-6454\(01\)00116-1](https://doi.org/10.1016/S1359-6454(01)00116-1)
- [40] E. Marquis, D. Seidman, Coarsening kinetics of nanoscale Al₃Sc precipitates in an Al-Mg-Sc alloy, *Acta Mater.* 53 (2005) 4259–4268, <https://doi.org/10.1016/j.actamat.2005.08.035>
- [41] N. Ryum, Precipitation and recrystallization in an Al-0.5 wt% Zr-alloy, *Acta Met.* 17 (1969) 269–278.
- [42] O. Izumi, D. Oelschägel, On the decomposition of a highly supersaturated AlZr solid solution, *Scr. Metall.* 3 (1969) 619–622, [https://doi.org/10.1016/0036-9748\(69\)90062-3](https://doi.org/10.1016/0036-9748(69)90062-3)
- [43] C. Fuller, A. Krause, D. Dunand, D. Seidman, Microstructure and mechanical properties of a 5754 aluminum alloy modified by Sc and Zr additions, *Mater. Sci. Eng. A* 338 (2002) 8–16, [https://doi.org/10.1016/S0921-5093\(02\)00056-4](https://doi.org/10.1016/S0921-5093(02)00056-4)
- [44] A. Tyvanchuk, T. Yanson, B. Kotur, O. Zarechnyuk, M. Kharakterova, Isothermal section of the Sc-Al-Si system at 770 K, *Russ. Met.* 4 (1988) 190–192.
- [45] B. Cheng, X. Zhao, Y. Zhang, H. Chen, I. Polmear, J. Nie, Co-segregation of Mg and Zn atoms at the planar η 1-precipitate/Al matrix interface in an aged Al-Zn-Mg alloy, *Scr. Mater.* 185 (2020) 51–55, <https://doi.org/10.1016/j.scriptamat.2020.04.004>
- [46] J. Edington, Electron Diffraction in the Electron Microscope, 1975.
- [47] K. Fujii, K. Matsuda, T. Gonoji, K. Watanabe, T. Kawabata, Y. Uetani, S. Ikeno, Crystallographic orientation relationship between discontinuous precipitates and matrix in commercial AZ91 Mg alloy, *Mater. Trans.* 52 (2011) 340–344, <https://doi.org/10.2320/matertrans.MB2010121>
- [48] C. Schneider, W. Rasband, K. Eliceiri, NIH image to imageJ: 25 years of image analysis, *Nat. Methods* 9 (2012) 671–675.
- [49] D.N. Seidman, E.A. Marquis, D.C. Dunand, Precipitation strengthening at ambient and elevated temperatures of heat-treatable Al (Sc) alloys, *Acta Mater.* 50 (2002) 4021–4035, [https://doi.org/10.1016/S1359-6454\(02\)00201-X](https://doi.org/10.1016/S1359-6454(02)00201-X)
- [50] T. Torma, E. Kovacs-Csetenyi, T. Turmezey, T. Ungar, I. Kovacs, Hardening mechanisms in Al-Sc alloys, *J. Mater. Sci.* 24 (1989) 3924–3927, <https://doi.org/10.1007/BF01168955>
- [51] H. Jo, S. Fujikawa, Kinetics of precipitation in Al-Sc alloys and low temperature solid solubility of scandium in aluminium studied by electrical resistivity measurements, *Mater. Sci. Eng. A* 171 (1993) 151–161.
- [52] V.I. Elagin, V.V. Zakharov, T.D. Rostova, Some features of decomposition for the solid solution of scandium in aluminium, *Met. Sci. Heat Treat.* 25 (1983) 57–60, <https://doi.org/10.1007/BF00741946>
- [53] J. Royset, N. Ryum, Scandium in aluminium alloys, *Int. Mater. Rev.* 50 (1) (2005) 19–44, <https://doi.org/10.1179/174328005x14311>
- [54] W.G. Zhang, Y.C. Ye, L.J. He, P.J. Li, X. Feng, L.S. Novikov, Dynamic response and microstructure control of Al-Sc binary alloy under high-speed impact, *Mater. Sci. Eng. A* 578 (2013) 35–45, <https://doi.org/10.1016/j.msea.2013.04.067>
- [55] S. Iwamura, Y. Miura, Loss in coherency and coarsening behavior of Al₃Sc precipitates, *Acta Mater.* 52 (2004) 591–600, <https://doi.org/10.1016/j.actamat.2003.09.042>
- [56] K.E. Knippling, D.N. Seidman, D.C. Dunand, Ambient- and high-temperature me-mechanical properties of isochronally aged Al-0.06Sc, Al-0.06Zr and Al-0.06Sc-0.06Zr (at%) alloys, *Acta Mater.* 59 (2011) 943–954, <https://doi.org/10.1016/j.actamat.2010.10.017>
- [57] A. Lohar, B. Mondal, D. Rafaja, V. Klemm, S. Panigrahi, Microstructural investigations on as-cast and annealed Al-Sc and Al-Sc-Zr alloys, *Mater. Charact.* 60 (2009) 1387–1394, <https://doi.org/10.1016/j.matchar.2009.06.012>
- [58] E.A. Marquis, D.N. Seidman, Nanoscale structural evolution of Al₃Sc precipitates in Al(Sc) alloys, *Acta Mater.* 49 (2001) 1909–1919, [https://doi.org/10.1016/S1359-6454\(01\)00116-1](https://doi.org/10.1016/S1359-6454(01)00116-1)
- [59] A. Mochugovskiy, A. Mikhaylovskaya, N. Tabachkova, V. Portnoy, The mechanism of L1₂ phase precipitation, microstructure and tensile properties of Al-Mg-Er-Zr alloy, *Mater. Sci. Eng. A* 744 (2019) 195–205, <https://doi.org/10.1016/j.msea.2018.11.135>

7 Effect of Si to Sc ratio on $(\text{Al},\text{Si})_3\text{Sc}$ nano-precipitates

7.1 Chapter synopsis

This chapter provides a detailed quantitative analysis of $(\text{Al},\text{Si})_3\text{Sc}$ nano-precipitates formed in Sc-containing alloys with varying Si to Sc ratio from 0.44 to 4.30. The three alloys were heat-treated at 350 °C for 30 minutes to form the $(\text{Al},\text{Si})_3\text{Sc}$ nano-precipitates. The diameter, number density, and volume fraction of $(\text{Al},\text{Si})_3\text{Sc}$ nano-precipitates were assessed and compared utilising TEM and SAXS techniques. The prediction of these characteristics was also aided by ThermoCalc[®] software, however as noted throughout this work, the results from CALPHAD are only a guide and often do not mimic empirical findings, most likely due to the limited database for the ternary Al-Si-Sc alloys (and little empirical data availability for such systems to date). The precipitate characteristics were found to be strongly correlated to the chemical composition of the alloys, processing conditions, and bulk hardness of the alloys. The $(\text{Al},\text{Si})_3\text{Sc}$ nano-precipitates revealed a strong coherency strain around them when seen under TEM in BF mode. To understand the local strain field distribution in the microstructure, PED technique was utilised and strain maps were acquired along the [001] direction of the α -Al matrix. The maximum local strain field was found to be related to the Si concentration in the alloy as well as in the nano-precipitates.

7.2 Abstract

This study investigates the role of Si on various characteristics of $(\text{Al,Si})_3\text{Sc}$ nano-precipitates in the model Al-Si-Sc alloys employing small-angle x-ray scattering, transmission electron microscopy, precession electron diffraction, and atom probe tomography. The understanding developed herein will help obtain the desirable microstructure thereby improving the hardening response. The diameter, volume fraction, and number density of nano-precipitates were found to be a function of processing condition, Si to Sc ratio, and resultant hardness. The local strain field at a nanometer scale along $[001]_{\alpha\text{-Al}}$ was seen to be increasing with Si content in the alloys and was related to the bulk hardness of the respective alloys and Si concentration in the nano-precipitates. Further, uniform distribution of Si and Sc concentration in the $(\text{Al,Si})_3\text{Sc}$ nano-precipitates without any partitioning at the interphase boundary was seen.

7.3 Introduction

The 6xxx series Al-alloys are most widely used in the automotive sector for the light-weighting purpose to replace heavier steel components in order to increase fuel efficiency and reduce CO₂ emissions. Efforts to enhance the strength of these alloys by the addition of alloying elements are common and studies indicate that alloying with Sc in small quantities can achieve significantly higher mechanical properties while maintaining corrosion resistance [2–5,75,86,96]. The strength increase occurs mainly due to the formation of Sc-containing, nano-sized, coherent, L1₂ structured Al₃Sc precipitates upon ageing heat treatment [6,84]. For the Al-Sc alloys with dilute addition of Si, the formation of the L1₂ precipitates was seen to be favourable, and Si atoms were reported to substitute to Al in the Al₃Sc precipitates [83,84,97]. Since most commercial Al-alloys always have some Si content at an impurity level, the precipitates formed in these alloys are actually (Al,Si)₃Sc even though they have been broadly reported as Al₃Sc in earlier studies. In this work, the Sc-rich L1₂ precipitates will hence be referred to as (Al,Si)₃Sc, with exception of the alloys where the presence of Si is either not accounted or has been known to be negligible.

A number of studies investigate the effect of Si on the formation kinetics of L1₂ precipitates in Al-Sc alloys. The (Al,Si)₃Sc precipitates were found to form during casting in the presence of 0.6 wt. % Si [88]. The accelerated precipitation of Sc-containing phases in the presence of Si occurs due to the reduced Sc migration energy forming the Si-Sc pairing [98]. The Si content in the precipitates was seen to be decreasing as a function of ageing time which confirms that Si mainly plays a role during the nucleation and early ageing stages [27]. The effect of Si on the diffusivity of Sc was found to sometimes result in a higher coarsening rate than that of the Al₃Sc or Al₃Sc_(1-x)Zr_x, or Al₃(Sc,Zr,Er) precipitates [97]. The (Al,Si)₃Sc precipitates result in a significant strengthening effect in Al-Sc alloys with dilute Si addition, which was superior to that of alloys without Si addition [97]. Additionally, the (Al,Si)₃Sc precipitates were also seen

to be less brittle than Al_3Sc . Although the effect of a low level of Si on the formation of Al_3Sc precipitates is well understood [83,84], there is still a lot of unknown about the effect of higher levels of Si in Sc-containing aluminium alloys. The presence of higher content of Si was often reported as deleterious due to the formation of the ternary V-phase (AlSi_2Sc_2) instead of the L_{12} phase [7,21]. The limited understanding of the precipitation sequence in Al-Si-Sc alloys with a high content of Si limits the use of Sc in 6xxx series Al-alloys which have Si content of 0.6 to 0.8 wt. %. The present work will hence investigate the effect of alloying with a higher level of Si on the precipitates in Al-Sc alloys.

The L_{12} structured coherent precipitates have strain associated with them due to their slightly increased lattice parameters as compared to the Al matrix. Although the effect of various alloying additions on the lattice parameters of the L_{12} phase in the Al-Sc alloys has been studied [99,100], the effects of Si on the lattice parameters of L_{12} nano-precipitates are not yet studied. The presence of elastic strain in the microstructure has a profound effect on the strengthening response [26,52,57,97,101]. The strain level associated with nano-precipitates depends on their level of coherency status with semi-coherent precipitates having a larger strain compared to fully coherent precipitates [22,102]. Thus reducing the lattice misfit between precipitate and matrix usually helps maintain the lower strain levels and higher coarsening resistance of the precipitates [25,103,104]. Apart from room temperature strength, the local strain levels also influence the stress corrosion cracking, deformation response, and creep performance [105]. The measurement of local strain distribution can help improve the understanding of the $(\text{Al,Si})_3\text{Sc}$ phase and one of the techniques to do so is PED. In PED technique, an electron beam is rotated at a fixed small angle around the axis normal to the sample surface and the resultant diffraction pattern generates crystallographic information about the sample [106]. The technique can measure the slight distortions in the diffraction pattern which are related to the

nano-scale lattice strain and is traditionally been applied to single-crystalline semiconductor materials [107,108] with some recent use for polycrystalline alloy samples as well [109–112].

In this study, a detailed analysis of the local strain distribution due to the presence of $(\text{Al,Si})_3\text{Sc}$ nano-precipitates is conducted using PED technique. The $(\text{Al,Si})_3\text{Sc}$ phase is further characterised using a SAXS, APT, and various electron microscopy techniques to understand the effect of Si and Sc content on the various characteristics of $(\text{Al,Si})_3\text{Sc}$ nano-precipitates, which can be related to the resultant hardening effect.

7.4 Materials and methods

7.4.1 Alloys composition

The selected Si concentration was 0.1, 0.4, and 0.8 wt. % in three Al-Si-Sc model alloys to match the Si content to that of commercial 6xxx series Al-alloys. The Sc concentration of 0.3 wt. % was used for all three alloys to maximise the Si to Sc interactions. The bulk alloy composition in the as-cast condition was analysed by ICP-OES and is reported in Table 7.1.

Table 7.1: Chemical composition (wt. %) of Al-Si-Sc alloys measured using ICP-OES test.

Nominal composition of the alloys	Measured alloy composition			
	Si	Sc	Fe	Si:Sc ratio
Al-0.8Si-0.3Sc	0.86	0.20	0.08	4.30
Al-0.4Si-0.3Sc	0.48	0.25	0.08	1.92
Al-0.1Si-0.3Sc	0.14	0.32	0.08	0.44

7.4.2 Alloys processing

All three alloys were cast using a lab-scale gravity die casting facility. The liquid melt at 720 °C after a holding time of 30 minutes was poured into a rectangular-shaped mild steel mould of dimensions 150 × 50 × 10 mm maintained at room temperature. It is known that the Al-Sc alloys when exposed to a temperature higher than 400 °C, Al₃Sc precipitates do experience coarsening and coherency loss. At 350 °C, some degree of softening, as a result of Al₃Sc precipitate growth and coherency loss, was seen when exposed for a prolonged time [13,25,26,53,54]. Therefore, a heat treatment at 350 °C for a short duration was considered to be an appropriate treatment for Al-Si-Sc alloys in this study. To restrict the coarsening of (Al,Si)₃Sc precipitates, a short holding time of 0.5 h corresponding to the obtained peak

hardness, was selected. Thus, the three alloy ingots were heat-treated at 350 °C for 0.5 h in a salt bath furnace followed by quenching in a water bath maintained at room temperature within a quench delay of 10 s. The ThermoCalc[®] software with the precipitation module (TC-PRISMA[®]) and the TCAL4 thermodynamic database was utilised for the prediction of the Al₃Sc precipitate characteristics such as size distribution and volume fraction for the three alloys at 350 °C for 0.5 h.

7.4.3 Characterisation

7.4.3.1 Hardness test

Bulk hardness measurements for the alloys in the as-cast and heat-treated conditions were conducted using Struers[®] Duramin A-300 Vickers hardness tester. The sample surface was polished on both sides using SiC emery paper up to 800 µm before measurements. Hardness values were taken at 10 locations for each sample with an applied load of 1 kg and then averaged.

7.4.3.2 Microstructure analysis

The specimens for microstructure imaging using TEM were prepared from the three alloys in the heat-treated condition. The 3 mm disc specimens were punched from thin alloy sheets and ground to 120 – 170 µm thickness. The discs were electro-polished with an electrolyte composed of 30% nitric acid and 70% methanol at -30 °C till the formation of a central hole in the foil. The Struers[®] Tenupol electro-polishing unit uses a twin-jet flow system for the electrolyte. The cell voltage was 12.7 V, the current was 180-190 mA and the approximate electro-polishing time was 3 to 4 minutes depending on the foil thickness. The microstructures were analysed in BF and DF modes using FEI[®] Tecnai G² T20 TEM operated at 200 kV.

The quantitative analysis of the (Al,Si)₃Sc nano-precipitates was conducted using TEM images taken at a similar sample thickness. The approximate sample thickness was 100 nm with some

level of uncertainty and hence quantitative comparisons done for various samples might have some inaccuracies. The diameter of nano-precipitates was estimated to be similar to the length of the no-contrast strain line to simplify the measurements and approximately 125 nano-precipitates from each alloy sample were analysed for the measurements. The number density of the precipitates was estimated by counting the actual number of precipitates in an image frame over the frame area. Four frames for each alloy sample were used for the measurements and the average values were estimated. The volume fraction of the precipitates was calculated using their size and number density and the precipitates were assumed to be spherical. It should be noted that the TEM images cover only a small local area in a thin foil and might not be a true representation of the precipitates in the bulk alloys. Hence, SAXS technique was utilised in order to understand the $(\text{Al,Si})_3\text{Sc}$ nano-precipitate characteristics at a bulk level. The results were then used to calculate the strengthening response of the heat-treated alloys.

7.4.3.3 Small-angle x-ray scattering

Thin samples of size $9 \times 9 \mu\text{m}$ were cut using a low speed saw cutting machine along the transverse section from alloy ingots in the cast as well as heat-treated condition. The samples were then manually thinned down to approximately $75 \mu\text{m}$ thickness with an emery paper of $800 \mu\text{m}$ size. The SAXS instrument of Bruker[®] N8 Horizon with Cu microbeam radiation and Vantec-500 2D detector was utilised. The data analysis was conducted using Bruker[®] DIFFRAC.SAXS V1.0 software.

7.4.3.4 Local strain fields

The strain distributions at the nanometer scale were measured for the area containing nano-precipitates and the surrounding matrix in the three heat-treated alloy samples using PED NanoMEGAS[®] DigiSTAR[™] system on a JEOL[®] 2100 F TEM. The TEM foil samples were prepared for the strain measurements using the electropolishing technique as explained in

section 7.4.3.2. Appropriate specimen areas of size $100 \times 100 \text{ nm}^2$ and $50 \times 50 \text{ nm}^2$ containing nano-scale $(\text{Al,Si})_3\text{Sc}$ precipitates were selected for measurements with a scan step size of 1 nm and 0.5 nm respectively. Multiple measurements were done in a specimen on various areas for repeatability purposes. For all the specimens, the beam was aligned in $[011]_{\alpha\text{-Al}}$ zone axis, and the strain measurements were carried out in $[001]$ direction thus measuring the d-spacing of (001) planes. The strain analysis was conducted using a Topspin[®] software package with reference lattice parameters of the Al matrix in the respective specimens and was replotted for comparison using Matlab[®] software.

7.4.3.5 Atom probe tomography

Thin needle samples were prepared for the composition analysis of the nano-precipitates using APT. The needles were first wire cut using the electron discharge machining (EDM) technique to a cross-section area of $300 \times 300 \mu\text{m}^2$ and a length of 1 cm. The electropolishing of the needles was then carried out in two stages at room temperature using the Struers[®] Lectropol 5 electrolytic polishing unit. The first stage of electropolishing was done using an electrolyte composed of 33% nitric acid and 67% methanol at a cell voltage of 7-10 V to achieve a roughly thinner needle. The second stage of electropolishing was conducted using 2% perchloric acid and 98% methanol solution at a cell voltage of 10-20 V under an optical microscope until a neck formation and subsequent fracture occurred to form a thin needle with an approximate tip radius of 40-80 nm. The APT was carried out on a CAMECA[®] LEAP 4000 HR[™] instrument at a pulse rate of 200 kHz, a temperature of 25 K, and a pulse fraction of 20%. The 3DAP reconstruction of the acquired data was done using IVAS[™] 3.8.2 software. The default image compression factor of 1.40 and the default electric field factor of 4.3 was used.

7.5 Results

7.5.1 Hardness results

The Vickers hardness results obtained for the three Al-Si-Sc alloys in the as-cast as well as in the heat-treated condition are given in Figure 7.1. The hardness of the alloys in the as-cast condition increases gradually with increasing the Si to Sc ratios of the alloys. Upon heat treatment, all three alloys show increased hardness as compared to that of the as-cast condition. However, the hardness in the heat-treated alloys decreased gradually with increasing Si to Sc ratio in the alloys. Thus, it is evident that the hardness response of the Al-Si-Sc alloys upon solidification is different than that following the heat treatment and is expected to be strongly related to the microstructure evolution. The subsequent sections thus study the microstructure of the three alloys using ThermoCalc[®] predictions, TEM, SAXS, PED, and APT to relate the phase characteristics to the hardness results.

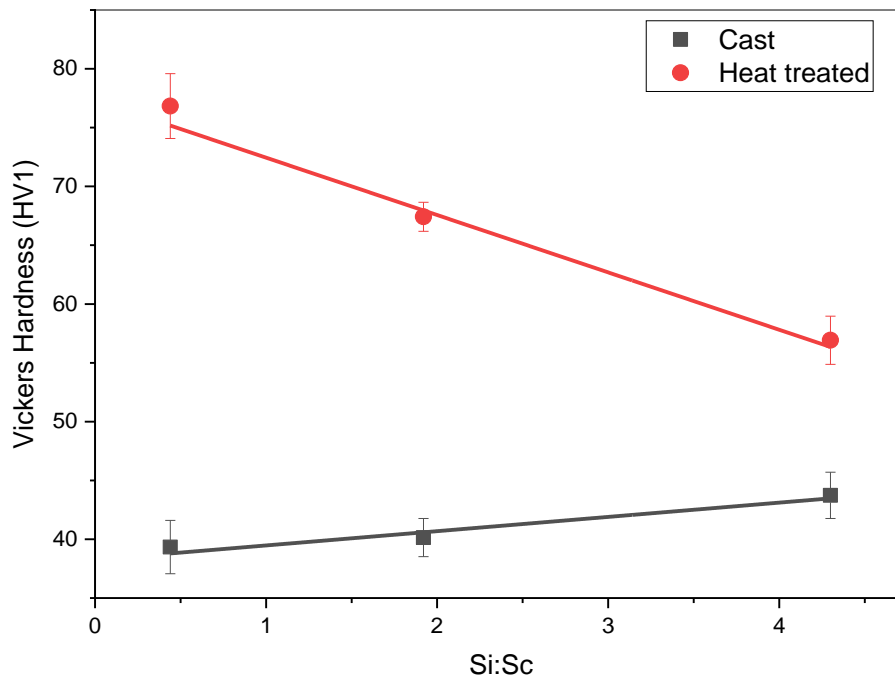


Figure 7.1: Vickers hardness results with respect to Si to Sc ratios of the Al-Si-Sc alloys in as-cast and heat-treated conditions.

7.5.2 Precipitation prediction using ThermoCalc®

The precipitation module (TC – PRISMA) within ThermoCalc® software was utilised for the precipitation prediction for the Al-Si-Sc alloys. The software could not predict the $(Al,Si)_3Sc$ phase although the selected alloys have sufficiently high Si content. Instead, the prediction of Al_3Sc precipitates was done for their radius, volume fraction, and number density at 350 °C for 30 minutes holding time. The results in Figure 7.2 (a) indicates a normal distribution of Al_3Sc precipitates size for the three alloys with a negligible change in the mean radius of the precipitates. Figure 7.2 (b) shows that the three characteristics of the precipitates (radius, volume fraction, and number density) decrease linearly with increasing Si to Sc ratios. However, the change in the radius and volume fraction of these nano-precipitates for the three alloys is negligible. On the other hand, the number density of nano-precipitates decreased significantly with increasing Si to Sc ratios, which is mainly due to the decreasing Sc content in the alloys.

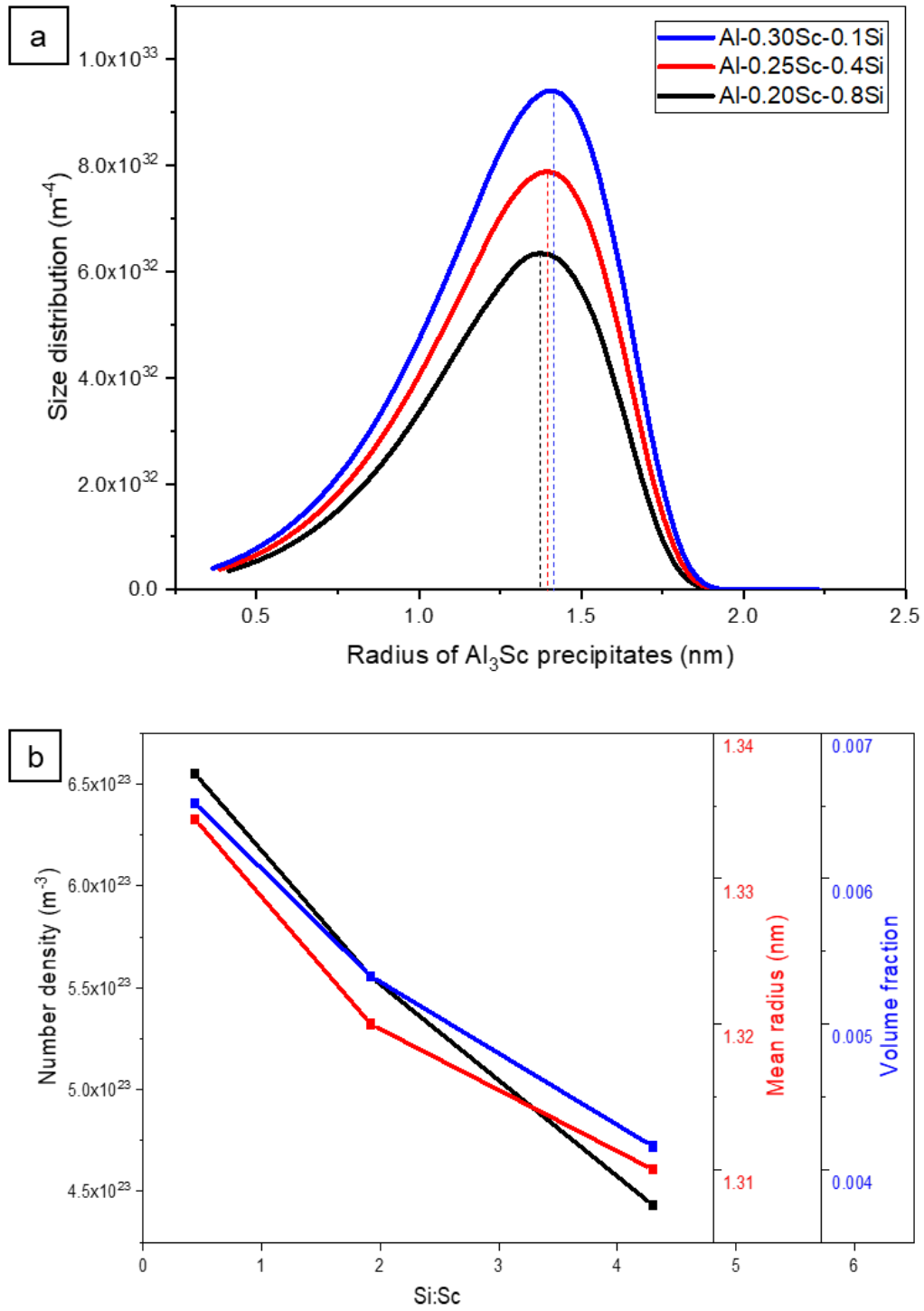


Figure 7.2: Al₃Sc precipitation simulation results at 350 °C for 30 minutes using ThermoCalc[®]: (a) size distribution, (b) radius, number density, and volume fraction with respect to Si to Sc ratios of the alloys.

7.5.3 Transmission electron microscopy

The qualitative analysis of the $(\text{Al,Si})_3\text{Sc}$ nano-precipitates in the Al-0.1Si-0.3Sc, Al-0.4Si-0.25Sc, and Al-0.8Si-0.2Sc alloys heat-treated at 350 °C for 0.5 h was done using TEM. A BF TEM image in Figure 7.3 (a) indicates a high number density of the fine $(\text{Al,Si})_3\text{Sc}$ precipitates distributed within the area. The nano-precipitates in Al-0.4Si-0.25Sc alloy are coarser as compared to that in the other two alloys as shown in Figure 7.3 (c) and additionally, some of them had developed facets depending on their size when observed at higher magnification (refer Figure 7.3 d). The nano-precipitates in the Al-0.8Si-0.2Sc alloy are finer as compared to the Al-0.4Si-0.25Sc alloy while their number density has been reduced as compared to the Al-0.1Si-0.3Sc alloy (refer Figure 7.3 e).

It is known that these precipitates are coherent with the matrix due to the similarity of the crystal structure and lattice parameters between the precipitate and the surrounding α -Al matrix. However, there exists a small lattice mismatch between the precipitates and the α -Al matrix, which results in a small coherency strain around these precipitates [100]. The nano-precipitates are seen to be coherent with the α -Al matrix as indicated by AB strain contrast [113] around the nano-precipitates in all three alloys (refer Figure 7.3 b and f).

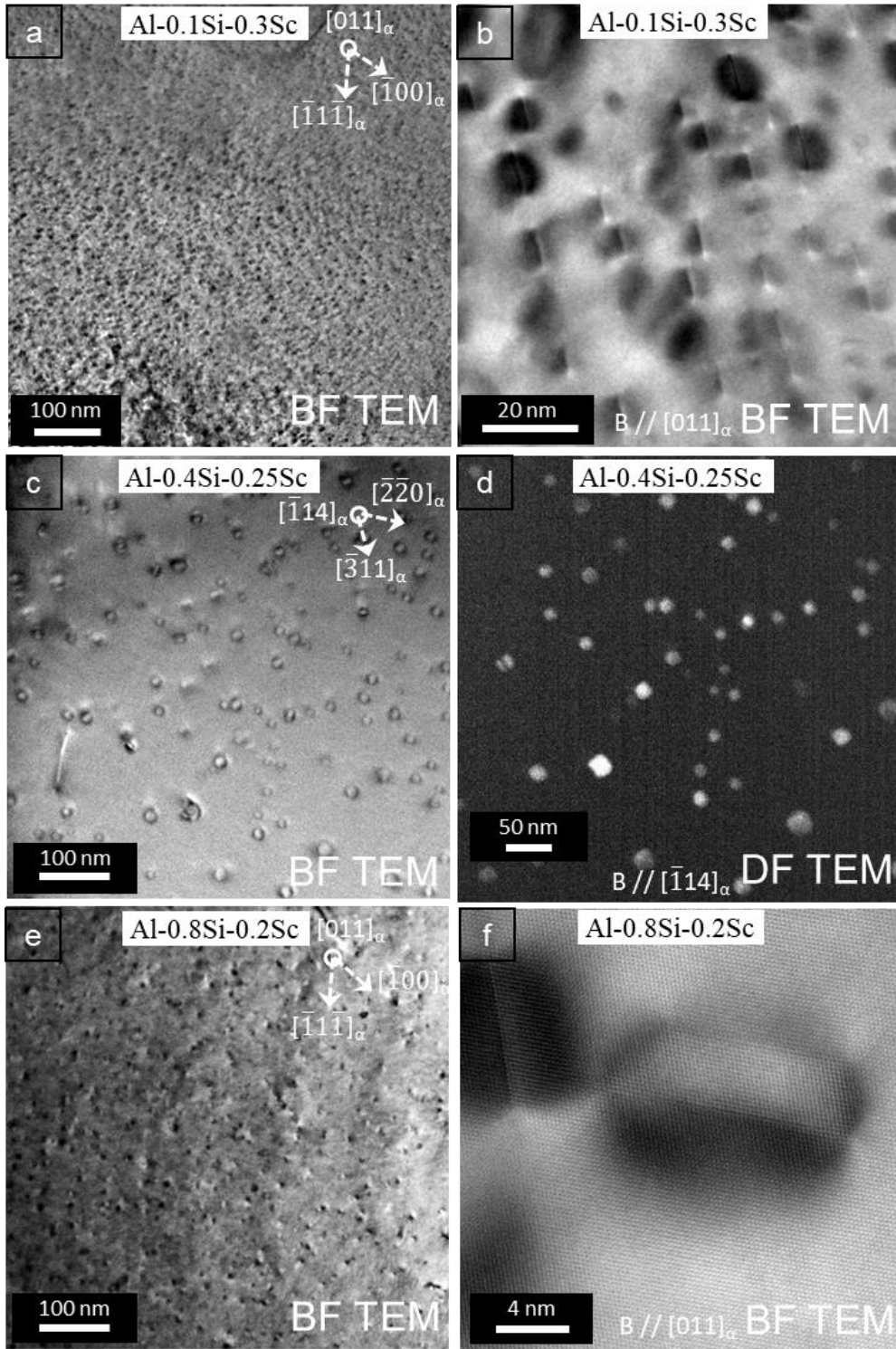


Figure 7.3: $(\text{Al,Si})_3\text{Sc}$ nano-precipitates following heat treatment at 350 °C, 0.5 h: (a) uniform local distribution of precipitates, (b) precipitates revealing coherency as seen with the AB strain contrast, (c) coarser precipitates, (d) DF image indicating faceted precipitates, (e) relatively fine precipitates, and (f) lattice fringes in the high-resolution TEM image showing coherency of precipitate with Al matrix.

The crystal structure information of the $(\text{Al,Si})_3\text{Sc}$ nano-precipitate was obtained utilising high-resolution TEM (HRTEM). A single nano-precipitate in the heat-treated Al-0.8Si-0.2Sc alloy along $[011]_{\alpha\text{-Al}}$ zone axis is shown in Figure 7.4 (a). The fast Fourier transformation (FFT) of Figure 7.4 (a) given in Figure 7.4 (b) confirms the diffraction pattern of the $L1_2$ structured $(\text{Al,Si})_3\text{Sc}$ phase with a space group $\text{Pm}\bar{3}\text{m}$ [57]. Further post-processing of Figure 7.4 (a) is done by masking the weak spots generated by $(\text{Al,Si})_3\text{Sc}$ phase in Figure 7.4 (b). The resultant Fourier-filtered image in Figure 7.4 (c) and the corresponding colourmap in Figure 7.4 (d) is then used to measure the d-spacings between the major lattice planes and $d_{[200]}$ was measured as 2.08\AA and for $d_{[220]}$ was 1.41\AA . The $(\text{Al,Si})_3\text{Sc}$ phase was oriented with the $\alpha\text{-Al}$ matrix and the OR was found to be cube-cube which agrees with the previously report OR for Al_3Sc precipitates [114]. The OR can be written as: $[011]_{(\text{Al,Si})_3\text{Sc}} \parallel [011]_{\alpha\text{-Al}}$ and $(100)_{(\text{Al,Si})_3\text{Sc}} \parallel (100)_{\alpha\text{-Al}}$.

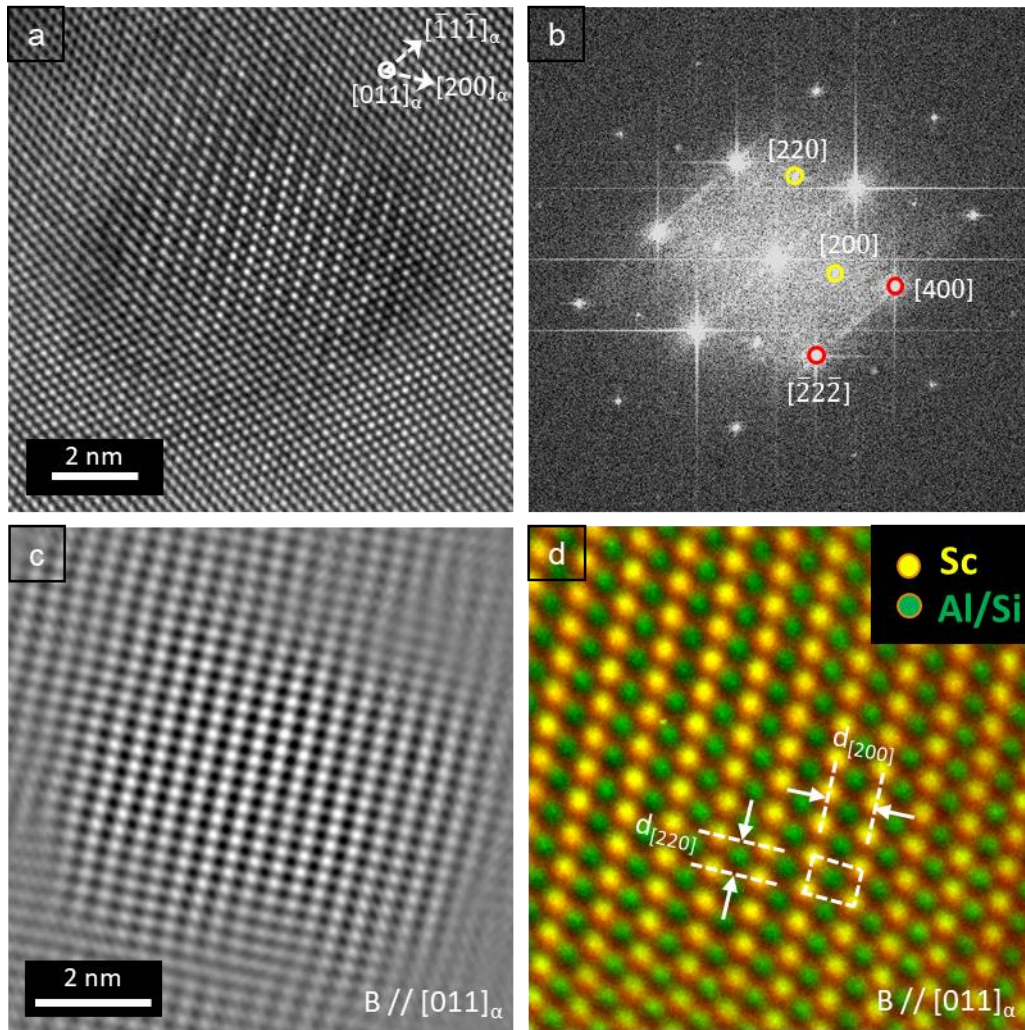


Figure 7.4: $(\text{Al,Si})_3\text{Sc}$ nano-precipitate in Al-0.8Si-0.2Sc alloy heat-treated at 350 °C for 0.5 h: (a) HRTEM image, (b) corresponding diffraction pattern obtained by the Fourier transformation of the image in (a), (c) Fourier-filtered image of (a) after masking diffraction spots from $L1_2$ phase, (d) colourmap revealing atomic arrangement in $L1_2$ crystal structure with interplanar spacings: $d_{[200]} = 2.08\text{\AA}$ and $d_{[220]} = 1.41\text{\AA}$.

7.5.4 Quantification of nano-precipitates

The quantitative analysis of precipitates was conducted using SAXS as well as TEM in order to understand the role of Si and Sc content on the precipitate evolution. The SAXS technique was utilised for the three Al-Si-Sc alloys in the as-cast as well as the heat-treated conditions and the results are summarised in Table 7.2, whereas analysis using TEM was done on the heat-treated samples only. The two techniques were compared for the precipitates in the heat-treated condition, which is discussed in the latter part of this section.

Table 7.2: Effect on volume fraction, size and number density of precipitates with increasing Si content in the Al-Si-Sc alloys analysed using SAXS.

Sr. No.	Alloy	Condition	Invariant, Q ($\times 10^{-10} \text{Å}^{-4}$)	Normalised volume fraction, f_v	Radius, R (Å)	Number density, (10^3Å^{-2})
1	Al-0.1Si-0.3Sc	As-cast	3.47	0.067	98.99	8.2
2	Al-0.1Si-0.3Sc	Heat-treated	5.19	0.100	33.05	327.7
3	Al-0.4Si-0.25Sc	As-cast	2.43	0.047	76.42	12.4
4	Al-0.4Si-0.25Sc	Heat-treated	3.69	0.071	61.84	35.6
5	Al-0.8Si-0.2Sc	As-cast	2.82	0.054	52.38	44.7
6	Al-0.8Si-0.2Sc	Heat-treated	3.35	0.065	43.49	92.8

The precipitate radius measured using Guinier radius (R_g) from the Guinier plot for the three alloys in the as-cast and the heat-treated conditions is plotted in Figure 7.5 (a). The precipitate radius in the as-cast specimens is larger for all three specimens than that of the heat-treated specimens and has a decreasing tendency with increasing Si content in the alloys. The precipitate radius in the heat-treated specimens does not exhibit similar behaviour or any specific trend. The heat-treated specimen with the lowest Si to Sc ratio shows the finest sized precipitates out of all and the one with the medium Si to Sc ratio shows the coarsest precipitates. The change occurred in the precipitate radius (as-cast radius – radius after heat treatment) is shown in Figure 7.5 (b) which decreases gradually with the increase in the Si to Sc ratio in the alloys. The volume fraction of the precipitates in the as-cast condition has no definite trend with Si to Sc ratios of the alloys, however, all the three alloy samples show an increase in the

volume fraction after the heat treatment as a result of precipitation of $(Al,Si)_3Sc$ phase. The volume fraction of the phase decreases with decreasing Sc content in the heat-treated alloys as given in Figure 7.5 (c). Similarly, the precipitate number density increases gradually with increasing Si to Sc ratios for as-cast specimens due to increasing Si content, whereas it has a decreasing trend for the heat-treated specimens due to decreasing Sc content (refer Figure 7.5 d). The results indicate that in the as-cast condition, the Si content plays a major role, whereas, for the heat-treated condition, the Sc content plays a major role in defining the $(Al,Si)_3Sc$ precipitate characteristics.

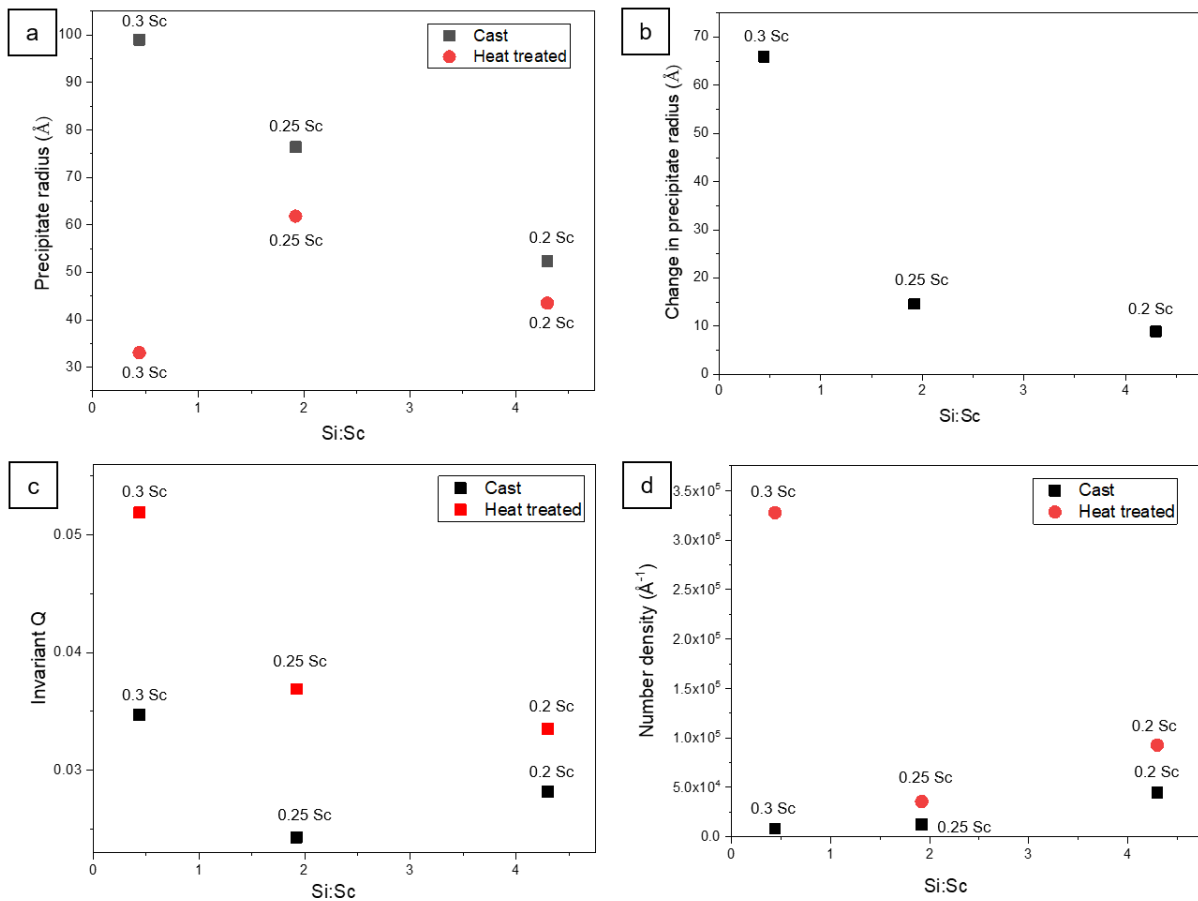


Figure 7.5: SAXS analysis for the effect of Si:Sc ratios on $(Al,Si)_3Sc$ precipitates characteristics: (a) radius, (b) change in precipitate radius (cast precipitate radius – heat-treated precipitate radius), (c) invariant Q which is proportional to the volume fraction and (d) number density.

The assessment of the size and volume fraction of the precipitates can be confirmed using Kratky plots as given in Figure 7.6 for the three alloys compared in as-cast and heat-treated condition. The value of Q_{\max} is inversely proportional to the precipitate radius and the higher the value of Q_{\max} , the finer is the precipitate size [95]. As can be seen, all the heat-treated specimens show the finer precipitate size as compared to that in the as-cast specimens. This confirms the previous estimation of precipitate size using R_g from Guinier plot. Similarly, the area under the curve in the Kratky plot is proportional to the volume fraction of the precipitates, and all the heat-treated specimens show an increased volume fraction of the precipitates as compared to that in their respective as-cast alloy specimens due to the precipitation of $(\text{Al,Si})_3\text{Sc}$ phase during the heat treatment.

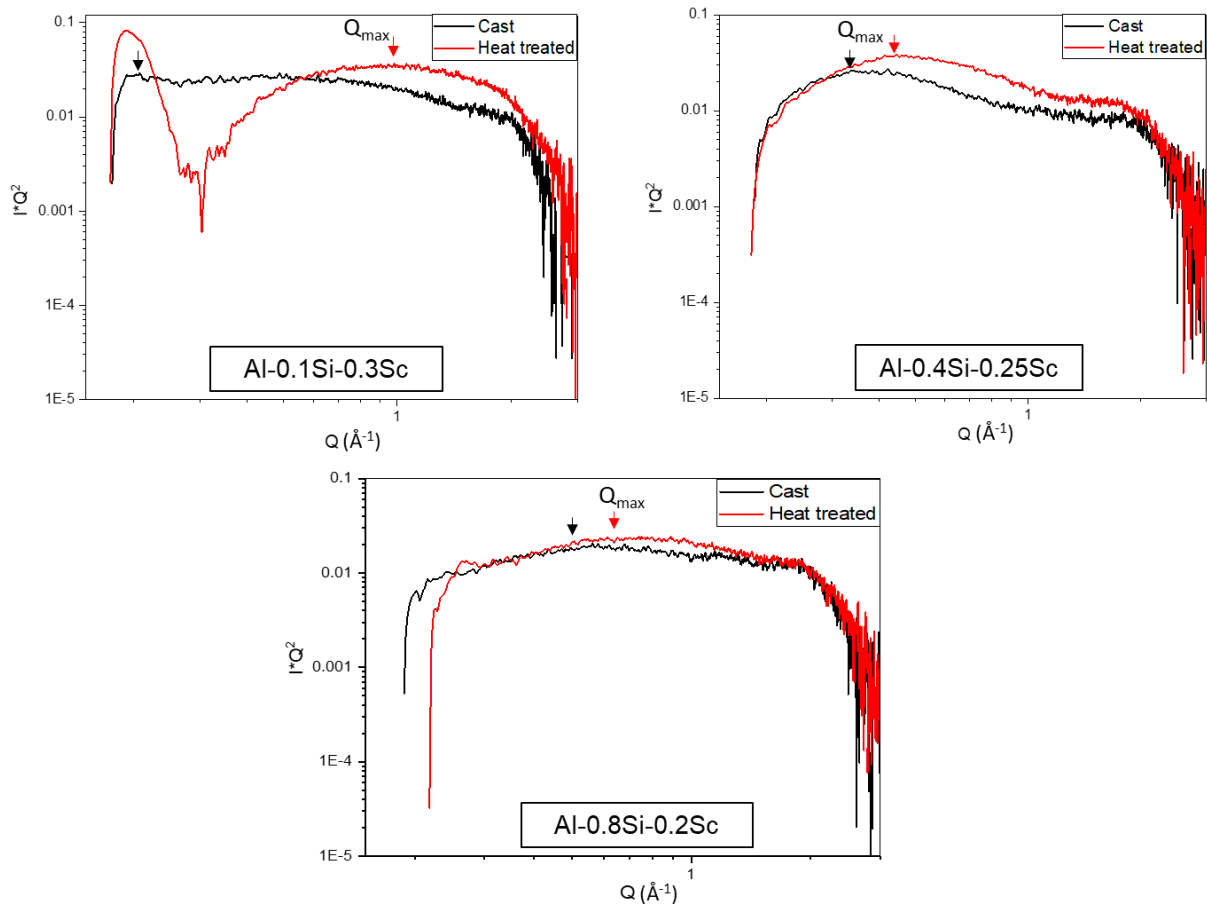


Figure 7.6: Precipitates volume comparison in as-cast and heat-treated conditions for the Al-Si-Sc alloys using Kratky plots.

The Kratky plots of the three alloys in the as-cast condition are compared in Figure 7.7 (a). It can be seen that the specimen with the highest Sc content (Al-0.1Si-0.3Sc) shows the highest area under the curve and thus has the highest volume fraction of the precipitates. Whereas the other two specimens show a similar area under the curve, indicating that there is a marginal difference between the volume fraction of the precipitates in these two alloys. Similar observations can be made for the three alloys in the heat-treated condition given in Figure 7.7 (b) where the specimen with the lowest Si to Sc ratio (Al-0.1Si-0.3Sc) shows a higher volume fraction of the precipitates due to the higher Sc content as compared to that in the other two alloys.

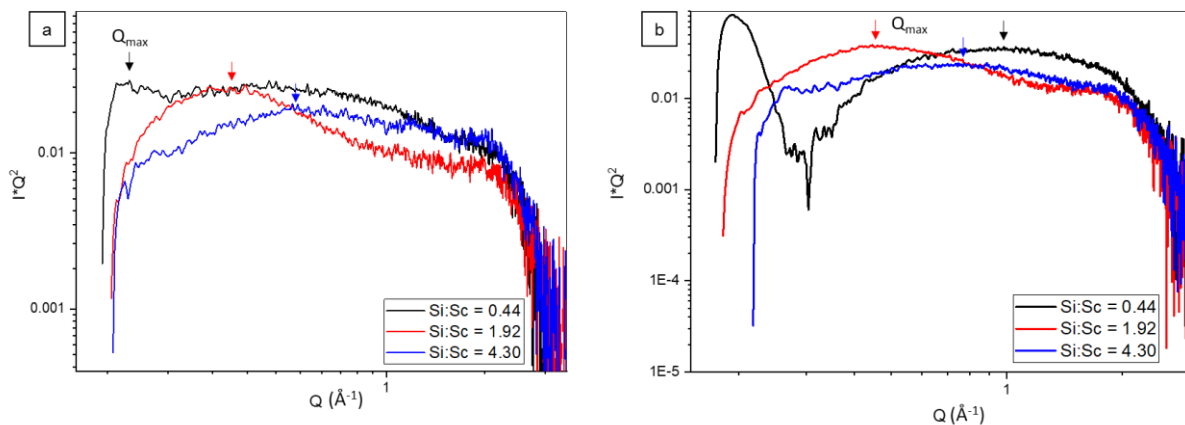


Figure 7.7: Comparison of Kratky plots in all the three alloys in (a) as-cast condition and (b) after heat treatment at 350 °C for 0.5 h.

The nano-precipitate diameter, volume fraction, and number density in the heat-treated specimens were compared using TEM, SAXS, and ThermoCalc[®] simulation results and are given in Figure 7.8. As can be seen in Figure 7.8 (a, b, c), although the precipitation simulation results follow similar trends with the experimental results, there are clear differences between the simulation and experimental results. This indicates that perhaps the ThermoCalc[®] database is incomplete to consider the role of Si in the Al-Si-Sc ternary alloy systems. On the other hand, the TEM and SAXS results agree with each other and confirm the variation in the nano-precipitate characteristics (refer to Figure 7.8 a, b, and d). The average number density and the

volume fraction had a decreasing trend with increasing Si to Sc ratios. Since the Sc content varies across the three alloys i.e. 0.3, 0.25, and 0.2 wt. % for the alloys with Si to Sc ratio of 0.44, 1.92, and 4.3 respectively; the decreased number density and volume fraction can be attributed to the decreasing Sc content. However, the diameter of $(Al,Si)_3Sc$ nano-precipitates has no direct relationship with the composition of alloys and the nano-precipitates in Al-0.4Si-0.25Sc alloy showed the largest diameter, which matches with the earlier visual observations made using TEM in section 7.5.3. The nano-precipitate size variation in this alloy is also seen to be higher as compared to that in the other two alloys. The change in the nano-precipitate size, volume fraction, and the number density with changing Si to Sc ratios reveal possible Si and Sc interactions during the precipitation heat treatment. Therefore, the nano-precipitates were further studied using PED and APT for the nano-scale strain distribution and atomic-scale composition variation respectively.

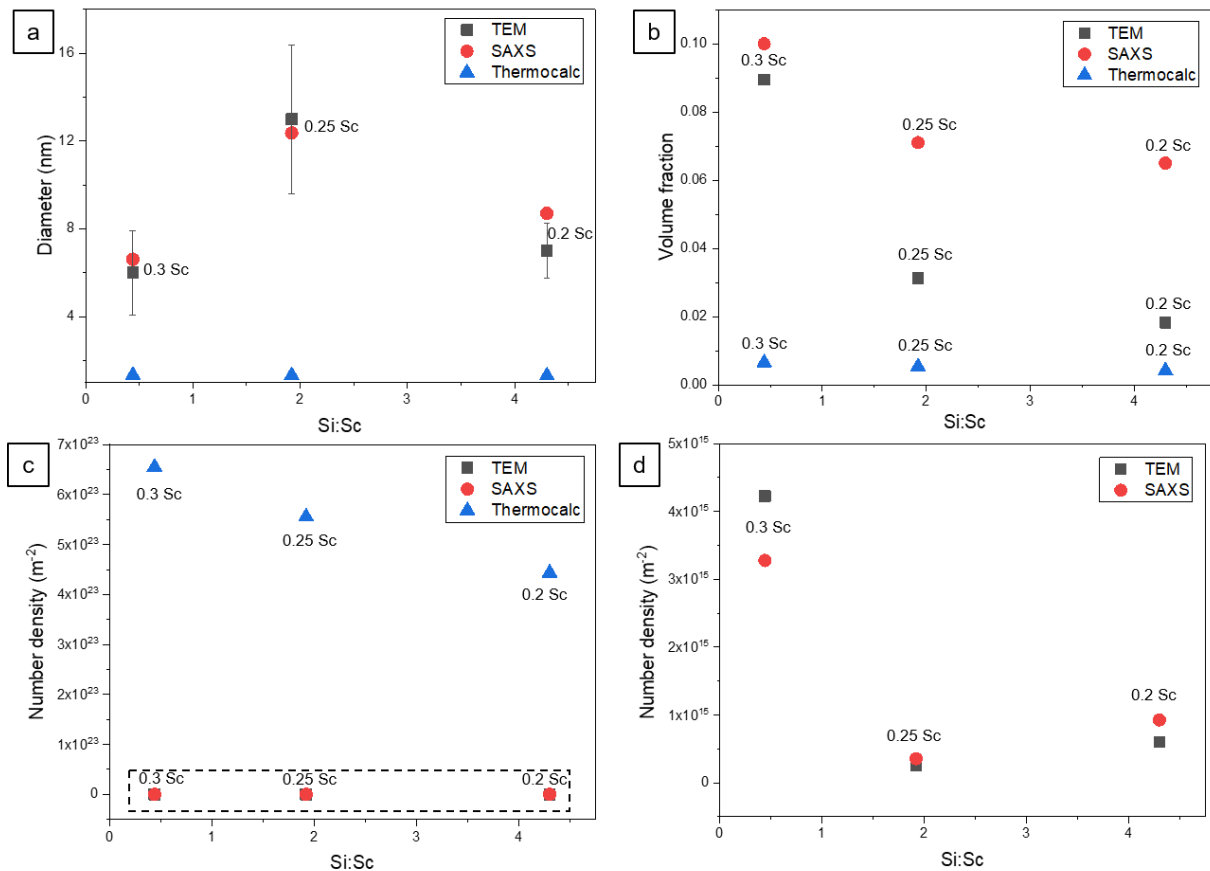


Figure 7.8: Comparison using TEM, SAXS, and ThermoCalc[®] for (Al,Si)₃Sc precipitate characteristics in heat-treated alloys: (a) size, (b) volume fraction, (c) number density, and (d) magnified view of the data in the dashed rectangle in the graph in (c).

7.5.5 Local strain distribution

The local strain distributions in the microstructures were mapped using PED for the three heat-treated Al-Si-Sc alloy specimens against the reference lattice parameters of the α -Al matrix. Since the strain measurements were done in a specific direction of $[001]_{\alpha\text{-Al}}$, only x-component of the strain is being presented here. The area showing the highest strain values was identified visually from each scanned area and the quantitative results of this strain along $[001]_{\alpha\text{-Al}}$ i.e. $\text{Strain}_{\text{max}}$. are given in Table 7.3. An increased strain was observed in all the scans due to the presence of (Al,Si)₃Sc nano-precipitates which have slightly higher lattice parameters than that of Al matrix [115]. Additionally, the average $\text{strain}_{\text{max}}$. was seen to be increasing with increasing Si content in the alloys. For the alloy with 0.1 wt. % Si, the strain level was comparatively low ($0.19 \pm 0.05\%$), however, with the Si addition of 0.4 wt. %, the strain level in the microstructure increased significantly to $1.15 \pm 0.36\%$. With further increased addition of Si to 0.8 wt. %, the strain level was marginally increased to $1.43 \pm 0.18\%$.

Table 7.3: Maximum strain from various scans collected for the three Al-Si-Sc alloys in heat-treated condition along $[001]_{\alpha\text{-Al}}$

Alloy composition	Scan No.	Step size (nm)	$\text{Strain}_{\text{max}}$. (%)	Average $\text{strain}_{\text{max}}$. (%)
Al-0.1Si-0.3Sc	1	1	0.19	0.19 ± 0.05
	2	0.5	0.12	
	3	1	0.27	
	4	0.5	0.18	
	5	1	0.19	
Al-0.4Si-0.25Sc	1	1	0.72	1.15 ± 0.36
	2	1	1.18	
	3	0.5	1.64	

	4	0.5	0.77	
	5	0.5	1.14	
	6	1	1.43	
Al-0.8Si-0.2Sc	1	0.5	1.30	1.43 ± 0.18
	2	1	1.55	

The three representative scans of 100×100 nm size from BF TEM images of each alloy specimen are given in Figure 7.9 (A, B, and C). These strain maps were collected along $[001]_{\alpha\text{-Al}}$ with a step size of 1 nm and were normalised against the reference lattice parameters of the Al matrix. The maximum strain in the scans was seen to be present at the locations of nano-precipitates. The visual comparison of strain in the three specimens in Figure 7.9 (A), (B), and (C) indicates that Al-0.8Si-0.2Sc alloy shows the highest $\text{strain}_{\text{max}}$, followed by Al-0.4Si-0.25Sc and Al-0.1Si-0.3Sc alloys similar to the results in Table 7.3. Thus, it can be safely said that the microstructure attains a higher elastic $\text{strain}_{\text{max}}$ due to the presence of $(\text{Al,Si})_3\text{Sc}$ nano-precipitates and it increases with the increasing Si content of the three alloys.

To better understand the strain quantitatively, a rectangular area containing $\text{strain}_{\text{max}}$ occupied by the nano-precipitates as well as the near-zero strain region of the $\alpha\text{-Al}$ matrix over a distance of ~ 85 nm was selected (refer Figure 7.9 A, B, and C). The strain profiles for these three areas are given in Figure 7.9 (d). All the specimens show a gradual decrease in the strain as the mapping distance is moved from the precipitate to the matrix. A stable matrix should result in a near-zero strain and the same can be seen for Al-0.1Si-0.3Sc alloy. However, for Al-0.4Si-0.25Sc and Al-0.8Si-0.2Sc alloys, the matrix is at a higher strain indicating the presence of some unstable regions. It is clear from the plot that the $\text{strain}_{\text{max}}$ in the microstructure increases with the Si addition in the alloys. In order to better understand the local strain field with the Si addition, the alloys with 0.4 and 0.8 wt. % Si were analysed using APT to understand the atomic-scale chemical characteristics of the nano-precipitates.

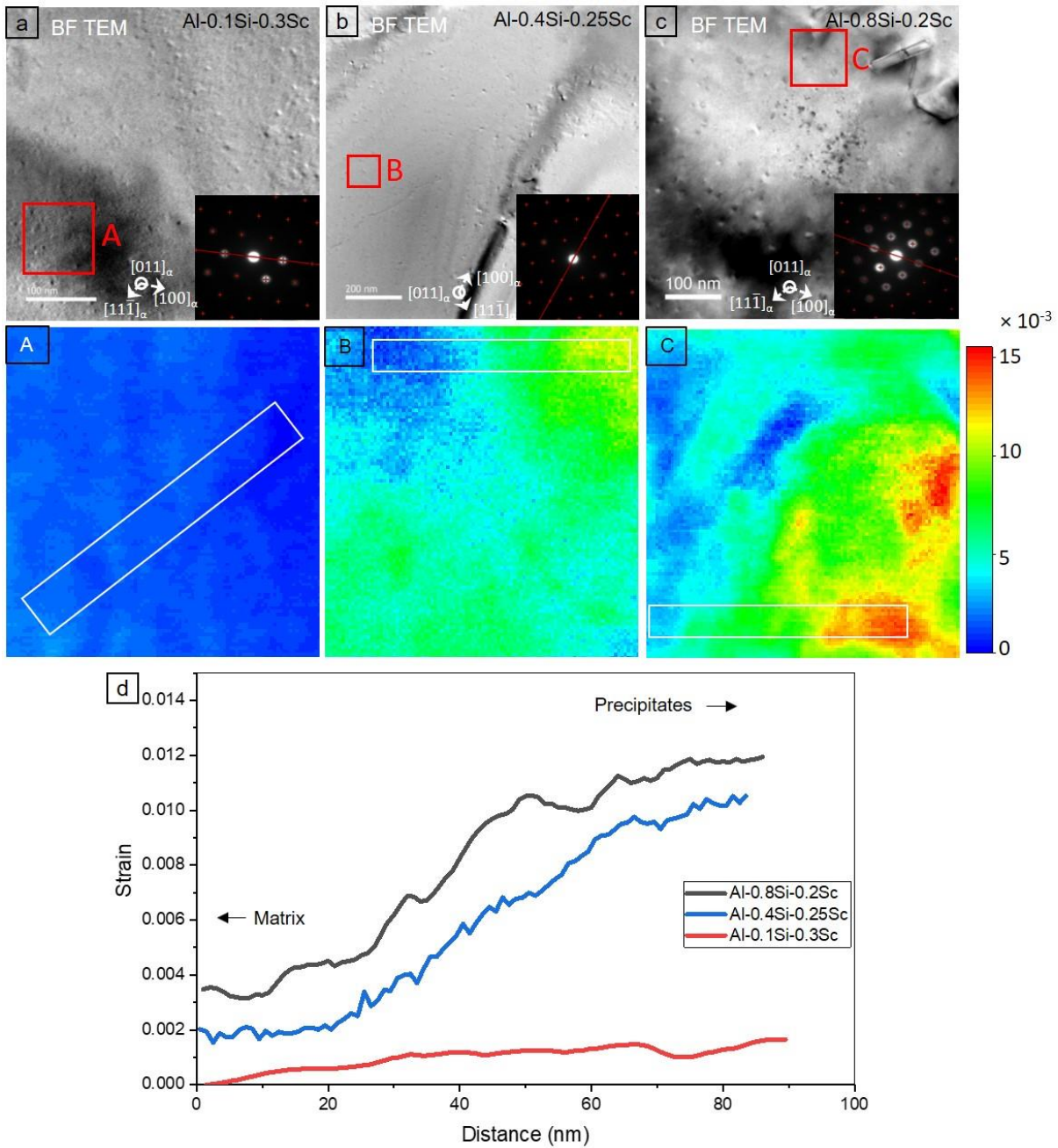


Figure 7.9: Area selected for the strain mapping in (a) Al-0.1Si-0.3Sc, (b) Al-0.4Si-0.25Sc, (c) Al-0.8Si-0.2Sc alloys in heat-treated condition, (A, B, and C) respective normalised strain maps of scan size 100×100 nm along $[001]_{\alpha\text{-Al}}$, (d) 2D plots of the average strain distribution of the white rectangles marked in A, B, and C.

7.5.6 Composition of nano-precipitates

The APT volume reconstruction of a nano-tip in Figure 7.10 (a) and (b) shows well-distributed nano-precipitates in the Al matrix. The separated maps of Si and Sc in Figure 7.10 coincide

with each other for the segregation of Si and Sc atoms respectively indicating the presence of Si in the nano-precipitates.

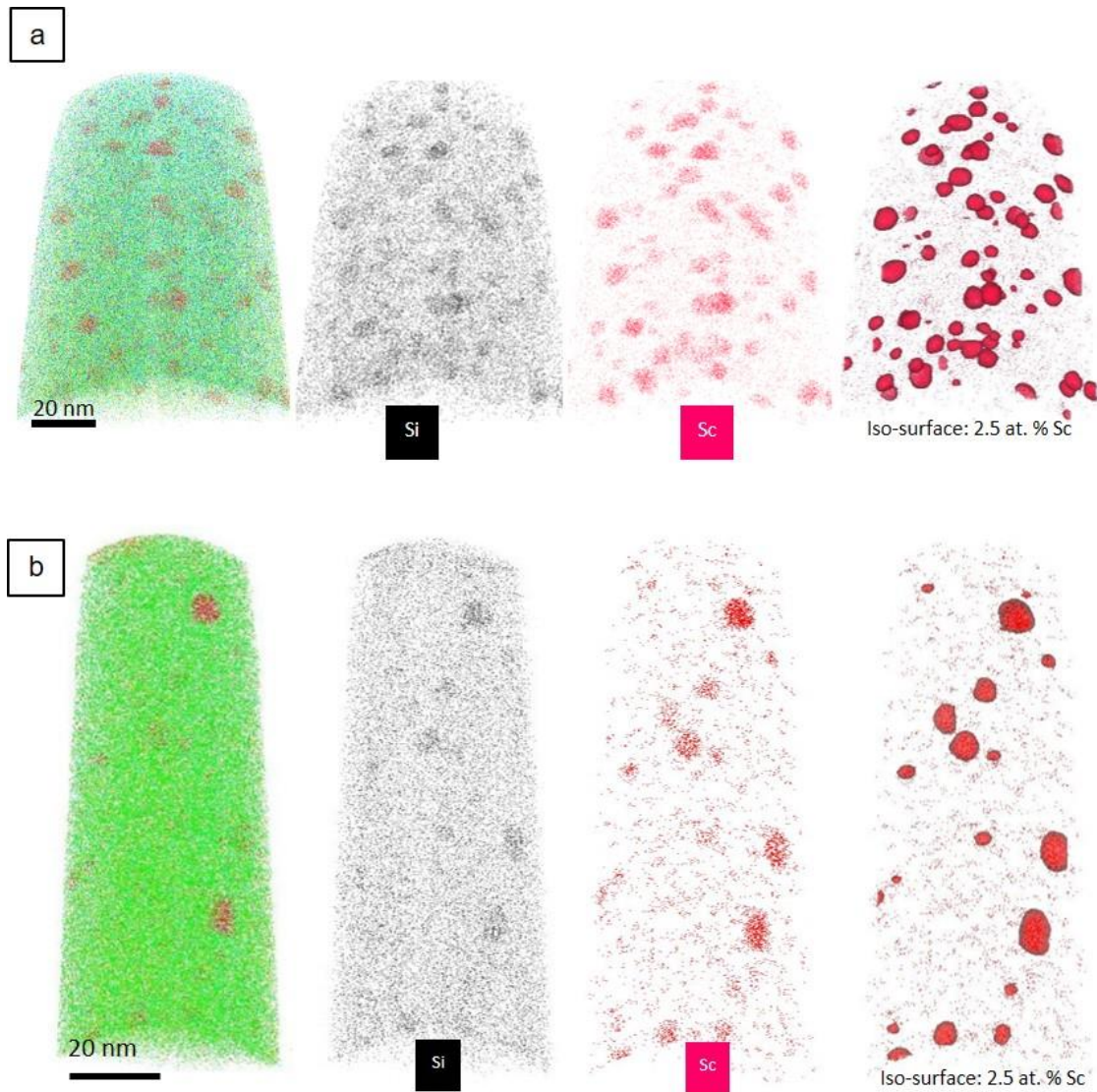


Figure 7.10: 3DAP volume constructed for heat-treated (a) Al-0.4Si-0.25Sc, (b) Al-0.8Si-0.2Sc alloys.

The composition of nano-precipitates was determined by the iso-concentration surface approach. The iso-surface of 2.5 at. % Sc was used to compute the composition proxygrams for all the precipitates in the constructed 3DAP volume represented in Figure 7.11. A total of 75 nano-precipitates in the case of Al-0.4Si-0.25Sc alloy sample and of 20 nano-precipitates in the case of Al-0.8Si-0.2Sc alloy sample were analysed and error bars indicate the standard

deviation of the elemental concentration for the analysed precipitates. A matrix rich in Al and lean in the alloying additions can be seen; however, as the interface approaches, the Al concentration reduces gradually, and Sc and Si concentration increases in both the specimens. It can also be seen that the distribution of Si, as well as Sc in the nano-precipitate, is uniform without any partitioning at the core or the interface between matrix and precipitate. The average composition of the nano-precipitate in Al-0.4Si-0.25Sc alloy was Al - 7.4 at. % Si – 18.5 at. % Sc, with uncertainty for Si concentration is ± 0.60 at. % and for Sc is ± 0.92 at. % calculated using the standard deviation within the iso-concentration surface. Whereas, in the Al-0.8Si-0.2Sc alloy, the nano-precipitate composition was Al – 12 at. % Si – 20.3 at. % Sc with uncertainty for Si concentration is ± 1.47 at. % and for Sc is ± 1.86 at. % within the iso-concentration surface. Most previous reported Al substitution by Si is below 10 at. % probably due to the lower Si content within the alloys studies [83–85,116]. Yet another study indicated a higher Al substitution by Si (20 to 25 at. %) in the precipitates formed during the casting process [88]. The results indicate that for a given heat treatment condition, the Si content in the nano-precipitates is related to the Si content in the alloy - more the Si in the alloy, the more it is in the $(Al,Si)_3Sc$ nano-precipitates.

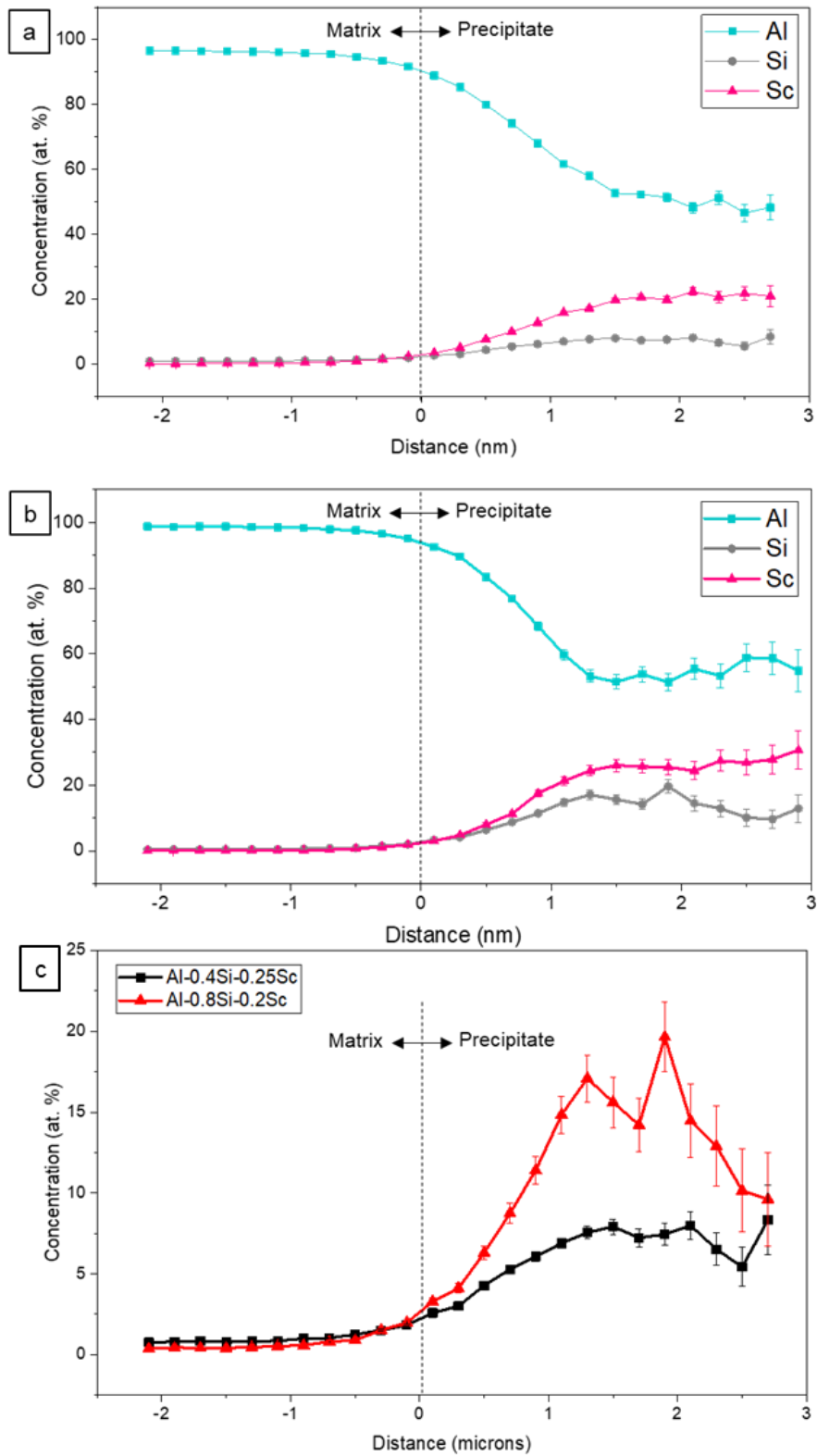


Figure 7.11: Proxigrams of the nano-precipitates from Figure 7.10: (a) Al, Si, and Sc in Al-0.4Si-0.25Sc, (b) Al, Si, and Sc in Al-0.8Si-0.2Sc, (c) overlay of Si concentration.

7.6 Discussions

Quantitative analysis of $(\text{Al,Si})_3\text{Sc}$ nano-precipitates in Al-Si-Sc heat-treated alloys was done using TEM, SAXS, and compared with that of ThermoCalc[®] predictions. The findings could help understand the relevant precipitation kinetics. Further, the local strain fields associated with the precipitates were analysed and then correlated to the Si content, the hardness of the alloys, and APT results.

7.6.1 Effect of Si to Sc ratio on $(\text{Al,Si})_3\text{Sc}$ precipitation

It is known that the presence of Si in the Al-Sc alloys accelerates the precipitation kinetics of $(\text{Al,Si})_3\text{Sc}$ phase due to increased Sc diffusion kinetics [84,89]. Thus, with increasing the Si content in the alloy, the Si-Sc cluster formations should increase resulting in the increased precipitation of $(\text{Al,Si})_3\text{Sc}$ phase; effectively refining their size. This has been verified for the three alloys in this study, where the precipitates formed after the casting process became finer in size as the Si content was increased.

The faster precipitate growth kinetics during the heat treatment in the presence of Si results in the coarser precipitates [97]. The precipitate size after the heat treatment would be a function of (1) precipitate size in the as-cast condition, (2) number of Si-Sc clusters formed during heat treatment, and (3) precipitate growth rate during the heat treatment. These factors are dependent on the Si and Sc content if the same processing conditions are applied. As seen earlier in Figure 7.8 (d), the precipitate number density in heat-treated samples had reduced due to the reduced Sc content in the alloys. Thus, the precipitate size after the heat treatment remains mainly a function of precipitate size after casting and the precipitate growth during the heat treatment.

The smallest-sized precipitates were formed in the heat-treated Al-0.1Si-0.3Sc alloy as seen in Figure 7.8 (a). Usually, a small quantity of Si is sufficient to accelerate the precipitation kinetics of $(\text{Al,Si})_3\text{Sc}$ phase [84]. Moreover, this alloy had the highest Sc content resulting in the highest

number density as compared to that in the other two alloys (refer Figure 7.8 d). In the as-cast condition, this alloy had a low number density of coarser precipitates, as seen from Figure 7.5 (d), which may have resulted in only a small contribution to the precipitate diameter after the heat treatment. The heat-treated Al-0.4Si-0.25Sc alloy had comparatively lower Sc content lowering the number density of nano-precipitates. This alloy had increased Si content which might be responsible for increased growth of the nano-precipitates, which resulted in coarsest precipitates out of the three alloys. On the other hand, the heat-treated Al-0.8Si-0.2Sc alloy was expected to have the coarsest precipitates but observed to have finer precipitates as compared to that of Al-0.4Si-0.25Sc alloy. This could be due to the contribution from a large number density of fine precipitates after the casting which continued to be present in the heat-treated condition.

7.6.2 Effect of Si content on local strain

The strain maps acquired using PED in Figure 7.9 (A, B, and C) show the presence of local strain variations in the heat-treated Al-Si-Sc alloys as a result of the formation of $(Al,Si)_3Sc$ nano-precipitates in the α -Al matrix. The maximum strain was seen to be located at the nano-precipitates and the region away from the precipitates towards Al matrix shows a gradual decrease in strain levels nearing zero which is the reference strain level. The maximum strain along $[001]_{\alpha-Al}$ is plotted against the Si content in the alloys and is also compared with the hardness obtained for respective heat-treated alloys in Figure 7.12. A good agreement between the local strain levels, Si content in the alloys, and the hardness values was seen. It was observed that the local strain_{max} increased with increasing Si content in the alloys. As a result, the corresponding hardness was seen to be decreasing with increasing strain.

The hardness of the alloys in the heat-treated condition was mainly a function of volume fraction and number density of $(Al,Si)_3Sc$ nano-precipitates and can be controlled by the addition of Sc in the alloys as seen from the SAXS results. On the other hand, PED analysis

indicated that the hardness of the alloys was also related to the strain associated with the nano-precipitates and can be controlled by the addition of Si to the alloys. To further understand the role of Si in the nano-precipitates, the results from proxygrams generated by APT were utilised. It was seen that the Si concentration in the nano-precipitates increased with increasing Si content in the bulk alloys. Thus, it seems that the presence of a higher level of Si in the nano-precipitates can possibly increase their lattice parameters resulting in an increased lattice mismatch between precipitate and matrix. A detailed study of evaluating exact lattice parameters for the $(\text{Al,Si})_3\text{Sc}$ nano-precipitates containing different levels of Si concentrations can help understand the relationship between the chemical and crystallographic nature of these nano-precipitates.

An earlier study indicated that the presence of Si is effective at an early stage of precipitate nucleation, however, the Si concentration in the nano-precipitates depleted with increasing ageing time [88]. This possibly can be explained with the strain results acquired in this work. As the increased Si content in the alloys accelerates the nucleation kinetics, Si is always present in the nano-precipitates at the early stages. However, a further increase in the size of the nano-precipitates occurs due to enhanced growth kinetics in the presence of Si, and the nano-precipitates can remain stable up to a certain size only. This study shows that the nano-precipitates tend to increase the associated strain in a presence of a higher level of Si concentration. Thus, the depletion of Si atoms from the nano-precipitate at a longer ageing time is probably favourable to reduce the associated strain levels. Further studies on the discrete effect of precipitate size on the Si concentration of precipitates and associated strain can be useful to confirm this understanding. Another study of interfacial strain across a β -phase precipitate in a polycrystalline 5xxx series Al-alloy indicated the presence of a negative strain region due to the formation of a solute depleted region [117]. Such a negative strain region was

not identified in this study probably due to an absence of any solute depleted region at the interface of nano-precipitates as confirmed by the APT proxygrams.

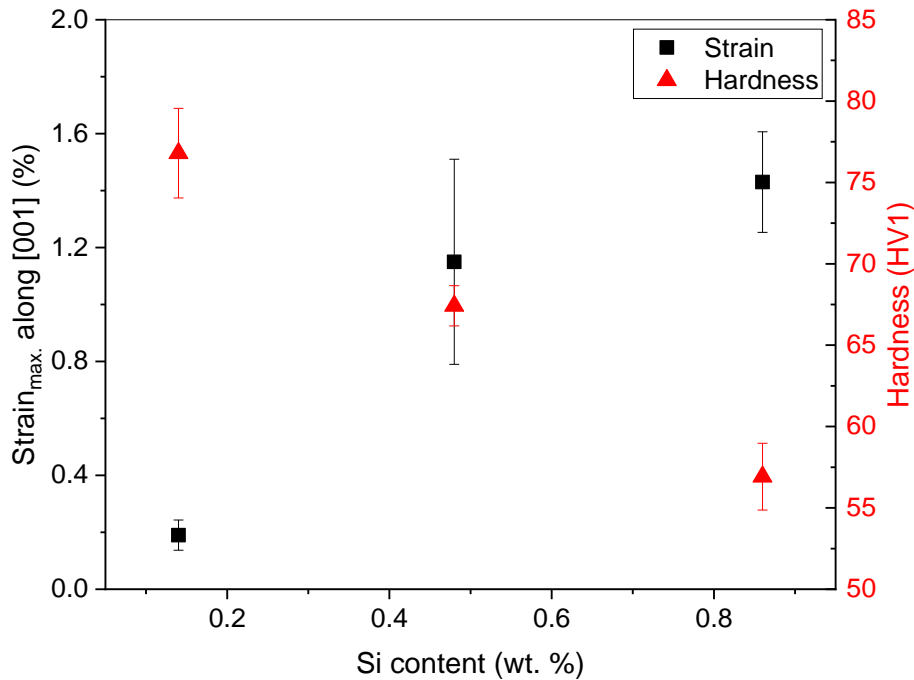


Figure 7.12: Maximum strain as a function of Si content and hardness following the heat treatment of Al-Si-Sc alloys.

7.6.3 Effect of Si to Sc ratio on hardening response

The hardness of all the three alloys in the as-cast condition increased with increasing Si to Sc ratio in the alloys as shown in Figure 7.1. Earlier reported studies indicated that the presence of Si in the matrix help accelerate the nucleation of Sc-containing precipitates during the thermal treatments [84]. The increased hardness with increasing Si content in alloys can be related to the decreased diameter of $(Al,Si)_3Sc$ precipitates and an increased number density as given in Figure 7.5 (a) and (c) respectively.

The hardening in the heat-treated samples came from the formation of homogeneous $(Al,Si)_3Sc$ nano-precipitates [26,57]. The hardness was seen to be a function of diameter, number density, and volume fraction of the $(Al,Si)_3Sc$ precipitates. ThermoCalc[®] simulation analysis for the prediction of precipitation at 350 °C for 30 minutes was not effective enough to establish the

trends for the precipitate diameter and the volume fraction of the $(\text{Al,Si})_3\text{Sc}$ phase. However, the prediction of decreasing the number density of the nano-precipitates with increasing Si to Sc ratios matched well with the decreasing bulk hardness of the heat-treated alloys. Figure 7.1 shows that the alloy with the lowest Si to Sc ratio (Al-0.1Si-0.3Sc alloy) has the highest hardness as compared to that of the other two alloys, which can be attributed to the finest size, highest volume fraction, and highest number density of the $(\text{Al,Si})_3\text{Sc}$ precipitates. Since the other two alloys have the coarser and lesser $(\text{Al,Si})_3\text{Sc}$ precipitates with the lower volume fraction, the resultant hardness of these two alloys is lower than that of the Al-0.1Si-0.3Sc alloy.

7.6.4 Strengthening mechanisms

Generally, two types of strength mechanisms are prevalent in the alloys strengthened due to precipitate formation depending on the precipitate size – (1) precipitate shearing which occurs in smaller precipitates, and (2) dislocation looping around the precipitates in the case of larger precipitates also known as the Orowan mechanism. Sometimes, a mixed mechanism of strengthening is also seen due to the presence of small and large precipitates in the alloy at the same time. An investigation has been done to identify the prevalent strengthening mechanism contributed by the $(\text{Al,Si})_3\text{Sc}$ for the three heat-treated Al-Si-Sc alloys.

a. Precipitate shearing

The strengthening due to precipitate shearing is usually contributed by (1) coherency strengthening which comes from the coherency strains at the precipitate-matrix interface, (2) order strengthening which comes from the work done in creating anti-phase boundaries (APB) in ordered precipitates, (3) modulus mismatch strengthening due to the difference between the shear modulus of matrix and precipitates [26,97].

The large coherency strain around the nano-precipitates was seen in the case of all heat-treated specimens as indicated by the AB strain contrast in Figure 7.3. The strain measurements done

using PED indicated that the local strain field increased with increasing Si content of the alloys and is related to the bulk hardness (refer Figure 7.12). Thus, the coherency strain is expected to play a role in the strengthening mechanism and hence is considered here for estimation. The strengthening due to coherency (σ_{coh}) was calculated using [26,99],

$$\sigma_{coh} = M\alpha_{\varepsilon} (G\varepsilon)^{\frac{3}{2}} \sqrt{\frac{rVv}{0.18Gb^2}} \quad \text{Equation 5}$$

where,

M = Matrix orientation factor and is 3.06 for random texture sample

α_{ε} = Constant taken as 2.6

G = Shear Modulus of Al and is 25.4 GPa

ε = Constrained lattice parameter mismatch is given by $\left(\frac{2}{3}\right)\left(\frac{\Delta a}{a}\right)$

$\frac{\Delta a}{a}$ = Lattice parameter mismatch at room temperature taken as 0.0125 [118]

r = Mean radius of precipitates as determined from SAXS data

V_v = Volume fraction of precipitates as determined from ThermoCalc[®]

b = Magnitude of Burger's vector and is 0.286 nm

Strengthening due to ordered, coherent, (Al,Si)₃Sc nano-precipitates can occur if the precipitates are fine enough to shear by a dislocation creating an APB [118]. Most order strengthening occurs in the alloys having precipitates of the L1₂ crystal structure. The order strengthening (σ_{ord}) was calculated using [26,99],

$$\sigma_{ord} = 0.81 M \frac{\gamma_{abp}}{2b} \sqrt{\frac{3\pi Vv}{8}} \quad \text{Equation 6}$$

where,

γ_{abp} = Average value of Al₃Sc APB energy for (111) plane taken as 0.5 J/m² [26]

The strengthening due to modulus mismatch (σ_{mod}) between the α -Al matrix and the $(Al,Si)_3Sc$ precipitates was calculated using [26,99],

$$\sigma_{mod} = 0.0055 M (\Delta G)^{\frac{3}{2}} \left(\frac{2Vv}{Gb^2}\right)^{\frac{1}{2}} b \left(\frac{r}{b}\right)^{\frac{3m}{2}-1} \quad \text{Equation 7}$$

where,

ΔG = Shear modulus mismatch between the matrix and precipitates and is taken as 42.5 GPa

m = Constant of value 0.85

b. Dislocation looping

An earlier study indicated that the strengthening due to precipitates was not significant when aged at below 300 °C for Al-Sc alloys and theoretical calculations indicated that the Orowan mechanism was operative for ageing above 300 °C and precipitate diameter larger than 6.8 nm [52]. In the current study, since the heat treatment of the alloys was carried out at a temperature greater than 300 °C resulting in a larger diameter of precipitates (6 to 10 nm) in the specimens, the Orowan mechanism may be operative and needs to be considered. The strengthening due to the Orowan looping mechanism (σ_{oro}), was calculated using [26,99],

$$\sigma_{oro} = M \frac{0.4Gb}{\pi\lambda} \frac{\ln\left(\frac{2r}{b}\right)}{\sqrt{1-\nu}} \quad \text{Equation 8}$$

where,

λ = Inter-precipitate spacing and is calculated using $2r\left(\frac{\pi}{4Vv}\right)^{\frac{1}{2}} - 1$

ν = Poisson's ratio of Al taken as 0.345 for these calculations

All the calculated values for the strength of the Al-Si-Sc alloys contributing due to various strengthening mechanisms are compared in Table 7.3. The strength contribution by the modulus mismatch strengthening mechanism is much lower to the experimental results and hence can be neglected. Instead, contribution by the order and coherency strengthening

mechanism appears to be the highest. This indicates that the presence of coherent, ordered, $L1_2$, $(Al,Si)_3Sc$ nano-precipitates in a large number density probably resulted in the dislocation shearing mechanism as a primary strengthening mechanism for the three alloys. The overall estimation of strength contributions is still on a higher side as compared to the experimental hardness results. This probably is related to the calculated volume fraction of the nano-precipitates using ThermoCalc[®], as the Sc lost in the formation of intermetallics is not considered in the calculations instead the entire Sc content is considered to be utilised by the $(Al,Si)_3Sc$ nano-precipitates.

Table 7.3: Comparison of the calculated strength from various contributions and the experimental hardness results.

Alloy	Si to Sc ratio	σ_{oro} (MPa)	σ_{ord} (MPa)	σ_{coh} (MPa)	σ_{mod} (MPa)	HV1
Al-0.8Si-0.2Sc	4.30	108	152	164	15	56.9 ± 2.05
Al-0.4Si-0.25Sc	1.92	96	172	221	19	67.4 ± 1.23
Al-0.1Si-0.3Sc	0.44	167	190	179	17	76.83 ± 2.76

The size, volume fraction and the number density of $(Al,Si)_3Sc$ nano-precipitates in the microstructure determine the mechanical properties in the Al-Si-Sc alloys by controlling the prevalent strengthening mechanism. In general, finer sized precipitates in a large number density with higher volume fraction gives rise to enhanced strengthening in these alloys. The precipitate characteristics were seen to be a function of the composition of the alloys (Si content and Sc content), processing conditions (as-cast or heat-treated), and heat treatment parameters (heating temperature and holding time). Thus, optimising the alloy composition, processing route, and the heat treatment practice should be utilised to get the desired characteristics of $(Al,Si)_3Sc$ nano-precipitates in the microstructure in order to achieve balanced mechanical

properties. The alloys optimised for their mechanical properties are expected to perform better in the application space.

7.7 Conclusions

The $(\text{Al,Si})_3\text{Sc}$ precipitate characteristics such as their size, number density, volume fraction, associated local strain fields, and chemical composition in the Al-Si-Sc model alloys were estimated utilizing TEM, SAXS, PED, and APT techniques. The following key conclusions were drawn from this study:

1. The as-cast bulk hardness of the alloys increased with increasing Si content in the alloys and can be related to the precipitate characteristics. The diameter of $(\text{Al,Si})_3\text{Sc}$ precipitates decreased and the number density increased with increasing Si content in the alloys resulting in the enhanced hardness.
2. The hardness of the heat-treated alloys decreased with increasing Si to Sc ratios. The decreased hardening response was attributed to the decreased Sc content in the alloys, which resulted in the decreased volume fraction and number density of the $(\text{Al,Si})_3\text{Sc}$ nano-precipitates.
3. The maximum local strain along $[001]_{\alpha\text{-Al}}$ in the heat-treated alloys increased up to $\sim 1.43 \pm 0.18\%$ with increasing Si content of the alloys and was also related to the gradual decrease in the corresponding hardness. The increased Si concentration in the $(\text{Al,Si})_3\text{Sc}$ nano-precipitates could be contributing to the increased strain in the microstructures.
4. The Si and Sc concentration measured using the APT technique was found to be uniform in the $(\text{Al,Si})_3\text{Sc}$ nano-precipitates without any partitioning at the interface boundary of precipitate and matrix. The Si concentration in the $(\text{Al,Si})_3\text{Sc}$ nano-precipitates was seen to be proportional to the Si content in the bulk alloys.
5. The calculated contribution from various strengthening mechanisms compared against the experimental hardening response indicated that the order and coherency strengthening mechanism of precipitate shearing by a dislocation in the matrix seems to be prevalent in

this case. This might be a result of the ordered, coherent, $L1_2$ structured $(Al,Si)_3Sc$ nano-precipitates distributed in the α -Al matrix.

8 Summary and future work

8.1 Summary

The research work documented in this thesis is focused on understanding the role of Si in the precipitation of Sc-containing phases in model Al-Si-Sc alloys; which will serve to the ultimate goal of developing high-strength 6xxx series Al-alloys for automotive and aerospace use in the long term. The key areas discussed in the results chapters (chapter 5 to 7) are: (1) The use of CALPHAD to design and develop the optimised processing conditions to get improved hardness in Al-Si-Sc alloys as compared to that in the Al-Si alloys; (2) The *ex situ* heat treatments on the alloys with high Si content (Al-0.8Si-0.2Sc and Al-0.4Si-0.25Sc) in order to form both the desirable $(\text{Al,Si})_3\text{Sc}$ and deleterious V-phase; (3) The *in situ* TEM heating experiments to study the formation mechanisms for $(\text{Al,Si})_3\text{Sc}$ nano-precipitates and V-phase; (4) Quantification of $(\text{Al,Si})_3\text{Sc}$ nano-precipitates utilising SAXS and TEM and their relationship with the Si and Sc content; (5) Understanding the local strain distribution and compositional variation for the coherent $(\text{Al,Si})_3\text{Sc}$ nano-precipitates utilising PED and APT techniques. The conclusions obtained from these specific studies may be summarised as below.

1. CALPHAD tools were used to design and process the Sc-containing and Sc-free Al-Si model alloys at lab scale using a conventional metallurgical route of wrought Al semi-products. The Sc-containing alloys possessed superior hardness in the cast, pre-heat-treated, and rolled conditions (F-temper) as compared to Sc-free alloys, which was mainly attributed to the formation of $(\text{Al,Si})_3\text{Sc}$ nano-precipitates. The low-temperature homogenisation treatment at 350 °C for 0.5 h to the Sc-containing alloys resulted in the formation of coherent $(\text{Al,Si})_3\text{Sc}$ nano-precipitates. The hardness of pre-heat treated Al-Sc-Si alloys did not vary with subsequent hot and cold rolling processes due to the retention of $(\text{Al,Si})_3\text{Sc}$ precipitates in the Al matrix.

2. The solutionising treatment at 450 °C and 550 °C resulted in a significant decrease in the hardness in the case of Al-0.4Si-0.25Sc and Al-0.8Si-0.2Sc alloys - as a result of the formation of a rod-shaped V-phase (AlSc_2Si_2) at the expense of secondary Si particles and $(\text{Al,Si})_3\text{Sc}$ nanoscale precipitates. The V-phase was determined to have a tetragonal crystal structure with lattice parameters; $a = 6.56 \text{ \AA}$, $b = 6.64 \text{ \AA}$, and $c = 3.98 \text{ \AA}$; $\alpha = \beta = \gamma = 90^\circ$. Besides, six new ORs between V-phase and the Al matrix were identified.
3. The *in situ* TEM heating experiments indicated that the nanoscale $(\text{Al,Si})_3\text{Sc}$ precipitates were nucleated at 350 °C by the continuous precipitation mechanism, without the formation of any other metastable phases. On the other hand, the rod-shaped V-phase was precipitated at ~ 550 °C in the Al-0.8Si-0.2Sc alloy from the Si- and Sc-rich Al matrix by a classical nucleation and growth mechanism, following a complete dissolution of secondary Si particles and $(\text{Al,Si})_3\text{Sc}$ nano-precipitates. Thus, it has been seen that utilising the heat treatment temperature higher than the solvus line temperature of Al-Si-Sc alloys having a Si content greater than 0.4 wt. % results in the formation of V-phase and thus softening of the alloys.
4. The quantitative analysis of $(\text{Al,Si})_3\text{Sc}$ nano-precipitate characteristics (size, volume fraction, and number density) in the as-cast condition of the Al-Si-Sc alloys using SAXS technique revealed that the diameter of $(\text{Al,Si})_3\text{Sc}$ precipitates decreased and the number density increased with increasing Si content in the alloys. Whereas, the decreased hardness in the heat-treated alloys with increasing Si to Sc ratio was mainly attributed to the decreased Sc content in the alloys, which resulted in the lower volume fraction and decreased number density of the nano-scale $(\text{Al,Si})_3\text{Sc}$ precipitates as evaluated using SAXS and TEM.
5. The maximum local strain along $[001]_{\alpha\text{-Al}}$ as determined by PED was increased up to ~ 1.43 \pm 0.18% for the heat-treated Al-Si-Sc alloys and was related to the gradual decrease in the

hardness of the respective alloys. The increased local strain field in the microstructure may be related to the increased Si concentration in the $(\text{Al,Si})_3\text{Sc}$ nano-precipitates, which was seen to be proportional to the Si content in the bulk alloys as measured using APT. The Si and Sc concentration measured using the APT technique was found to be uniform in the $(\text{Al,Si})_3\text{Sc}$ nano-precipitates without any partitioning at the interface boundary of the precipitate and matrix indicating that the presence of Si might not improve the coarsening resistance of these precipitates.

It was seen that the secondary Si particles and the nano-scale $(\text{Al,Si})_3\text{Sc}$ precipitates co-existed when the alloys were pre-heat treated at 350 °C for 30 min without the formation of V-phase. On the other hand, the nucleation of the V-phase was observed to occur at 450 °C and 550 °C for the alloy with 0.4 and 0.8 wt. % Si respectively. Additionally, the V-phase nucleation was seen to be temperature-dependent, and increasing Si content resulted in the increased nucleation temperature of the V-phase. Thus, there exists a compositional and processing window to improve the hardening response in Al-Si-(Mg)-Sc alloys. Simultaneous precipitation of $(\text{Al,Si})_3\text{Sc}$ and Mg_2Si phase in the 6xxx series Al-alloys can be obtained by optimising the ageing heat treatment conditions below the V-phase nucleation temperature for the selected composition.

8.2 Future work

The research herein has provided critical information regarding $(\text{Al,Si})_3\text{Sc}$ nano-precipitates and V-phase with respect to alloy composition, processing conditions, and heat treatment parameters. The detailed characterisation of these phases was an important aspect to enhance the understanding of various characteristics of these phases, their formation mechanisms, and their effect on the hardness. However, several unanswered research questions remain and such future work will help in further developing Sc-enhanced 6xxx series Al-alloys.

1. Effect of Sc and Si content on the corrosion performance of the Al-Si-(Mg)-Sc alloys

The work in the present study indicated a positive effect on the hardness of the Al-Si-Sc alloys due to the addition of Sc. Further studies are required to assess the corrosion performance of the Al-Si-(Mg)-Sc wrought alloys in the aqueous solution to see if the enhanced mechanical properties can be achieved without compromising the corrosion performance.

2. Effect of Sc addition on the micro-texture evolution during the thermomechanical processing

The microstructure analysis of the rolled sheets indicated the retention of $(\text{Al,Si})_3\text{Sc}$ nano-precipitates which were formed before the thermomechanical processing. The $(\text{Al,Si})_3\text{Sc}$ nano-precipitates are expected to alter the recrystallization texture and grain boundary distribution in the Al-Si-Sc alloys as against that in Al-Si alloys. A detailed study on the recrystallization, micro-texture and grain boundary evolution through the casting, homogenisation, and rolling processes can be carried out to understand the role of Sc addition on these modifications which then can be correlated to the mechanical properties of the alloys.

3. Effect of Sc addition on the bulk residual stress in the Al-Si-Sc alloys

The local strain levels have been seen to be increasing with increasing Si to Sc ratio due to the presence of $(\text{Al,Si})_3\text{Sc}$ nano-precipitates. This is likely to affect the bulk residual stress in the alloy samples which is related to the mechanical properties. The analysis of residual stress with respect to Si content, Sc content, and heat treatment condition can be conducted in the Sc-containing and Sc-free Al-Si alloys.

4. Heat treatment optimisation for Al-Si-Mg-Sc alloys

The work in this study was done on Al-Si-Sc alloys in order to focus on the Si and Sc interactions, even though the ultimate goal was enhanced mechanical properties in the 6xxx series Al-alloys. It is however known from the realm of commercial (wrought) Al-alloys that are produced at scale, that thermomechanical process optimisation is a critical aspect in the attainment of properties. As such, commencing with lab-scale model alloys of Al-Si-Mg-Sc compositions can be designed and processed and a study needs to be conducted to see if the Si-Sc interactions alter in the presence of Mg. The optimised heat treatments can then be developed for this alloy system to concurrently form the $(\text{Al,Si})_3\text{Sc}$ nano-precipitates as well as the β (Mg_2Si) precipitates – at scale.

References

- [1] I.J. Polmear, D. St.John, J.F. Nie, M. Qian, Light alloys: Metallurgy of the light metals, 5th ed., Elsevier, 2017.
- [2] S. Mondol, T. Alam, R. Banerjee, S. Kumar, K. Chattopadhyay, Development of a high temperature high strength Al alloy by addition of small amounts of Sc and Mg to 2219 alloy, *Mater. Sci. Eng. A.* 687 (2017) 221–231. <https://doi.org/10.1016/j.msea.2017.01.037>.
- [3] V. Singh, K. Prasad, A. Gokhale, Effect of minor Sc additions on structure, age hardening and tensile properties of aluminium alloy AA8090 plate, *Scr. Mater.* 50 (2004) 903–908. <https://doi.org/10.1016/j.scriptamat.2003.12.001>.
- [4] C. Fuller, A. Krause, D. Dunand, D. Seidman, Microstructure and mechanical properties of a 5754 aluminum alloy modified by Sc and Zr additions, *Mater. Sci. Eng. A.* 338 (2002) 8–16. [https://doi.org/10.1016/S0921-5093\(02\)00056-4](https://doi.org/10.1016/S0921-5093(02)00056-4).
- [5] M. Cavanaugh, N. Birbilis, R. Buchheit, F. Bovard, Investigating localized corrosion susceptibility arising from Sc containing intermetallic Al₃Sc in high strength Al-alloys, *Scr. Mater.* 56 (2007) 995–998. <https://doi.org/10.1016/j.scriptamat.2007.01.036>.
- [6] L. Willey, L. Pa, United States patent: Aluminium scandium alloy, 3619181, 1968.
- [7] V.G. Davydov, T.D. Rostova, V. V. Zakharov, Y.A. Filatov, V.I. Yelagin, Scientific principles of making an alloying addition of scandium to aluminium alloys, *Mater. Sci. Eng. A.* 280 (2000) 30–36. [https://doi.org/10.1016/S0921-5093\(99\)00652-8](https://doi.org/10.1016/S0921-5093(99)00652-8).
- [8] A. Norman, P. Prangnell, R. McEwen, The solidification behaviour of dilute aluminium–scandium alloys, *Acta Mater.* 46 (1998) 5715–5732. [https://doi.org/10.1016/S1359-6454\(98\)00257-2](https://doi.org/10.1016/S1359-6454(98)00257-2).
- [9] S.I. Fujikawa, M. Sugaya, H. Takei, K.I. Hirano, Solid solubility and residual resistivity of scandium in aluminium, *J. Less-Common Met.* 63 (1979) 87–97.
- [10] J. Røyset, N. Ryum, Scandium in aluminium alloys, *Int. Mater. Rev.* 50 (2005) 19–44. <https://doi.org/10.1179/174328005X14311>.
- [11] H. Jo, S. Fujikawa, Kinetics of precipitation in Al-Sc alloys and low temperature solid solubility of scandium in aluminium studied by electrical resistivity measurements, *Mater. Sci. Eng. A.* 171 (1993) 151–161.
- [12] S. Costa, H. Puga, J. Barbosa, A.M.P. Pinto, The effect of Sc additions on the microstructure and age hardening behaviour of as cast Al-Sc alloys, *Mater. Des.* 42 (2012) 347–352. <https://doi.org/10.1016/j.matdes.2012.06.019>.
- [13] W.G. Zhang, Y.C. Ye, L.J. He, P.J. Li, X. Feng, L.S. Novikov, Dynamic response and microstructure control of Al–Sc binary alloy under high-speed impact, *Mater. Sci. Eng. A.* 578 (2013) 35–45. <https://doi.org/10.1016/j.msea.2013.04.067>.
- [14] U. Patakham, J. Kajornchaiyakul, C. Limmaneevichitr, Grain refinement mechanism in an Al-Si-Mg alloy with scandium, *J. Alloys Compd.* 542 (2012) 177–186. <https://doi.org/10.1016/j.jallcom.2012.07.018>.
- [15] J. zhi Dang, Y.Y. feng HUANG, J. CHENG, Effect of Sc and Zr on microstructures and mechanical properties of as-cast Al-Mg-Si-Mn alloys, *Trans. Nonferrous Met. Soc. China (English Ed.)* 19 (2009) 540–544. [https://doi.org/10.1016/S1003-6326\(08\)60309-](https://doi.org/10.1016/S1003-6326(08)60309-)

X.

- [16] M. Kaiser, A. Kurny, Effect of scandium on the grain refining and ageing behaviour of cast Al-Si-Mg alloy, Iran. J. Mater. Sci. Eng. 8 (2011) 1–8. <https://doi.org/10.1016/j.matchar.2008.03.006>.
- [17] K. Chanyathunyaraj, U. Patakham, S. Kou, C. Limmaneevichitr, Microstructural evolution of iron-rich intermetallic compounds in scandium modified Al-7Si-0.3Mg alloys, J. Alloys Compd. 692 (2017) 865–875. <https://doi.org/10.1016/j.jallcom.2016.09.132>.
- [18] H. Li, F. Cao, S. Guo, Z. Ning, Z. Liu, Y. Jia, S. Scudino, T. Gemming, J. Sun, Microstructures and properties evolution of spray-deposited Al-Zn-Mg-Cu-Zr alloys with scandium addition, J. Alloys Compd. 691 (2017) 482–488. <https://doi.org/10.1016/j.jallcom.2016.08.255>.
- [19] T. Dorin, M. Ramajayam, K. Mester, B. Rouxel, J. Lamb, T.J. Langan, The effect of scandium and zirconium on the microstructure, mechanical properties and formability of a model Al-Cu alloy, Light Met. (2018) 1595–1599.
- [20] C. Xu, W. Xiao, R. Zheng, S. Hanada, H. Yamagata, C. Ma, The synergic effects of Sc and Zr on the microstructure and mechanical properties of Al-Si-Mg alloy, Mater. Des. 88 (2015) 485–492. <https://doi.org/10.1016/j.matdes.2015.09.045>.
- [21] M.L. Kharakterova, D.G. Eskin, L.S. Toropova, Precipitation hardening in ternary alloys of the Al-Sc-Cu and Al-Sc-Si systems, Acta Met. Mater. 42(7) (1994) 2285–2290.
- [22] M. Drits; L. Toropova; Y. Bykov, Homogenization of alloys in the system Al-Mg-Sc, Plenum Publ. Corp. (1984) 60–63.
- [23] Y. Tzeng, C. Wu, S. Lee, The effect of trace Sc on the quench sensitivity of AL-7Si-0.6 Mg alloys, Mater. Lett. 161 (2015) 340–342. <https://doi.org/10.1016/j.matlet.2015.08.108>.
- [24] V.I. Elagin, V. V. Zakharov, T.D. Rostova, Some features of decomposition for the solid solution of scandium in aluminum, Met. Sci. Heat Treat. 25 (1983) 57–60. <https://doi.org/10.1007/BF00741946>.
- [25] S. Iwamura, Y. Miura, Loss in coherency and coarsening behavior of Al₃Sc precipitates, Acta Mater. 52 (2004) 591–600. <https://doi.org/10.1016/j.actamat.2003.09.042>.
- [26] D.N. Seidman, E.A. Marquis, D.C. Dunand, Precipitation strengthening at ambient and elevated temperatures of heat-treatable Al(Sc) alloys, Acta Mater. 50 (2002) 4021–4035. [https://doi.org/10.1016/S1359-6454\(02\)00201-X](https://doi.org/10.1016/S1359-6454(02)00201-X).
- [27] T. Dorin, M. Ramajayam, T.J. Langan, Effects of Mg, Si, and Cu on the formation of the Al₃Sc/Al₃Zr dispersoids, in: 6th Int. Alum. Alloy. Conf., Canadian Institute of Mining, Metallurgy & Petroleum, 2018.
- [28] F. Fazeli, W.J. Poole, C.W. Sinclair, Modeling the effect of Al₃Sc precipitates on the yield stress and work hardening of an Al-Mg-Sc alloy, Acta Mater. 56 (2008) 1909–1918. <https://doi.org/10.1016/j.actamat.2007.12.039>.
- [29] Z. Ahmad, A. Ul-Hamid, B.J. Abdul Aleem, The corrosion behavior of scandium alloyed Al 5052 in neutral sodium chloride solution, Corros. Sci. 43 (2001) 1227–1243. [https://doi.org/10.1016/S0010-938X\(00\)00147-5](https://doi.org/10.1016/S0010-938X(00)00147-5).
- [30] Y. Shi, Q. Pan, M. Li, X. Huang, B. Li, Effect of Sc and Zr additions on corrosion behaviour of Al-Zn-Mg-Cu alloys, J. Alloys Compd. 612 (2014) 42–50.

<https://doi.org/10.1016/j.jallcom.2014.05.128>.

- [31] F. Sun, G. Nash, Q. Li, E. Liu, C. He, C. Shi, N. Zhao, Effect of Sc and Zr additions on microstructures and corrosion behavior of Al-Cu-Mg-Sc-Zr alloys, *J. Mater. Sci. Technol.* (2016). <https://doi.org/10.1016/j.jmst.2016.12.003>.
- [32] S.K. Kairy, B. Rouxel, J. Dumbre, J. Lamb, T.J. Langan, T. Dorin, N. Birbilis, Simultaneous improvement in corrosion resistance and hardness of a model 2xxx series Al-Cu alloy with the microstructural variation caused by Sc and Zr additions, *Corros. Sci.* 158 (2019) 108095. <https://doi.org/10.1016/j.corsci.2019.108095>.
- [33] J. Wloka, S. Virtanen, Influence of scandium on the pitting behaviour of Al-Zn-Mg-Cu alloys, *Acta Mater.* 55 (2007) 6666–6672. <https://doi.org/10.1016/j.actamat.2007.08.021>.
- [34] A. Mochugovskiy, A. Mikhaylovskaya, N. Tabachkova, V. Portnoy, The mechanism of L12 phase precipitation, microstructure and tensile properties of Al-Mg-Er-Zr alloy, *Mater. Sci. Eng. A.* 744 (2019) 195–205. <https://doi.org/10.1016/j.msea.2018.11.135>.
- [35] A.J. Ardell, Precipitation hardening, *Metall. Trans. A.* 16A (1985) 2131–2165. <https://doi.org/10.1007/BF02670416>.
- [36] C.B. Fuller, D.N. Seidman, D.C. Dunand, Creep properties of coarse-grained Al(Sc) alloys at 300 ° C, *Acta Metall.* 40 (1999) 691–696. [https://doi.org/10.1016/S1359-6462\(98\)00468-0](https://doi.org/10.1016/S1359-6462(98)00468-0).
- [37] N.Q. Vo, D.N. Seidman, D.C. Dunand, Effect of Si micro-addition on creep resistance of a dilute Al-Sc-Zr-Er alloy, *Mater. Sci. Eng. A.* 734 (2018) 27–33. <https://doi.org/10.1016/j.msea.2018.07.053>.
- [38] G. Xu, X. Cao, T. Zhang, Y. Duan, X. Peng, Y. Deng, Z. Yin, Achieving high strain rate superplasticity of an Al-Mg-Sc-Zr alloy by a new asymmetrical rolling technology, *Mater. Sci. Eng. A.* 672 (2016). <https://doi.org/10.1016/j.msea.2016.06.070>.
- [39] Y. Peng, Z. Yin, B. Nie, L. Zhong, Effect of minor Sc and Zr on superplasticity of Al-Mg-Mn alloys, *Trans. Nonferrous Met. Soc. China.* 17 (2007) 744–750. [https://doi.org/10.1016/S1003-6326\(07\)60167-8](https://doi.org/10.1016/S1003-6326(07)60167-8).
- [40] R. Sawtell, C. Jensen, Mechanical properties and microstructures of Al-Mg-Sc alloys, *Metall. Trans. A.* 21A (1990) 421–430. [https://doi.org/S0109-5641\(99\)00093-7](https://doi.org/S0109-5641(99)00093-7) [pii].
- [41] D. Yuzbekova, A. Mogucheveva, R. Kaibyshev, Superplasticity of ultrafine-grained Al-Mg-Sc-Zr alloy, *Mater. Sci. Eng. A.* 675 (2016) 228–242. <https://doi.org/10.1016/j.msea.2016.08.074>.
- [42] Y. Filatov, V. Yelagin, V. Zakharov, New Al – Mg – Sc alloys, *Mater. Sci. Eng. A.* 280 (2000) 97–101.
- [43] K. Venkateswarlu, L. Pathak, A. Ray, G. Das, P. Verma, M. Kumar, R. Ghosh, Microstructure, tensile strength and wear behaviour of Al-Sc alloy, *Mater. Sci. Eng. A.* 383 (2004) 374–380. <https://doi.org/10.1016/j.msea.2004.05.075>.
- [44] A. Norman, K. Hyde, F. Costello, S. Thompson, S. Birley, P. Prangnell, Examination of the effect of Sc on 2000 and 7000 series aluminium alloy castings: For improvements in fusion welding, *Mater. Sci. Eng. A.* 354 (2003) 188–198. [https://doi.org/10.1016/S0921-5093\(02\)00942-5](https://doi.org/10.1016/S0921-5093(02)00942-5).
- [45] K.B. Hyde, A.F. Norman, P.B. Prangnell, The effect of cooling rate on the morphology of primary Al₃Sc intermetallic particles in Al – Sc alloys, *Acta Mater.* 49 (2001) 1327–

1337. [https://doi.org/https://doi.org/10.1016/S1359-6454\(01\)00050-7](https://doi.org/https://doi.org/10.1016/S1359-6454(01)00050-7).
- [46] P. Zięba, Recent Developments on Discontinuous Precipitation, *Arch. Metall. Mater.* 62 (2017) 955–968. <https://doi.org/10.1515/amm-2017-0138>.
- [47] Z. Yin, Q. Pan, Y. Zhang, F. Jiang, Effect of minor Sc and Zr on the microstructure and mechanical properties of Al–Mg based alloys, *Mater. Sci. Eng. A.* 280 (2000) 151–155. [https://doi.org/10.1016/S0921-5093\(99\)00682-6](https://doi.org/10.1016/S0921-5093(99)00682-6).
- [48] J. Royset, N. Ryum, Scandium in aluminium alloys, *Int. Mater. Rev.* 50(1) (2005) 19–44. <https://doi.org/10.1179/174328005X14311>.
- [49] E.A. Marquis, D.N. Seidman, Nanoscale structural evolution of Al₃Sc precipitates in Al(Sc) alloys, *Acta Mater.* 49 (2001) 1909–1919. [https://doi.org/10.1016/S1359-6454\(01\)00116-1](https://doi.org/10.1016/S1359-6454(01)00116-1).
- [50] W. Zhang, Y. Wu, H. Lu, G. Lao, K. Wang, Y. Ye, P. Li, Discontinuous precipitation of Nano-Al₃Sc particles in Al-Sc alloy and its effect on mechanical property, *Int. J. Nanosci.* 17 (2018) 1–9. <https://doi.org/10.1142/S0219581X18500473>.
- [51] R.W. Hyland JR, M. Asta, S.M. Foiles, C.L. Rohrer, Al(f.c.c.):Al₃Sc(L12) interphase boundary energy calculations, *Acta Metall.* 46 (1998) 3667–3678.
- [52] T. Torma, E. Kovacs-Csetenyi, T. Turmezey, T. Ungar, I. Kovacs, Hardening mechanisms in Al-Sc alloys, *J. Mater. Sci.* 24 (1989) 3924–3927. <https://doi.org/10.1007/BF01168955>.
- [53] A. Lohar, B. Mondal, D. Rafaja, V. Klemm, S. Panigrahi, Microstructural investigations on as-cast and annealed Al-Sc and Al-Sc-Zr alloys, *Mater. Charact.* 60 (2009) 1387–1394. <https://doi.org/10.1016/j.matchar.2009.06.012>.
- [54] K.E. Knipling, D.N. Seidman, D.C. Dunand, Ambient- and high-temperature mechanical properties of isochronally aged Al-0.06Sc, Al-0.06Zr and Al-0.06Sc-0.06Zr (at.%) alloys, *Acta Mater.* 59 (2011) 943–954. <https://doi.org/10.1016/j.actamat.2010.10.017>.
- [55] M.J. Jones, F.J. Humphreys, Interaction of recrystallization and precipitation: The effect of Al₃Sc on the recrystallization behaviour of deformed aluminium, *Acta Mater.* 51 (2003) 2149–2159. [https://doi.org/10.1016/S1359-6454\(03\)00002-8](https://doi.org/10.1016/S1359-6454(03)00002-8).
- [56] P. Xu, F. Jiang, Z. Tang, N. Yan, J. Jiang, X. Xu, Y. Peng, Coarsening of Al₃Sc precipitates in Al-Mg-Sc alloys, *J. Alloys Compd.* 781 (2019) 209–215. <https://doi.org/10.1016/j.jallcom.2018.12.133>.
- [57] L. Toropova, D. Eskin, M. Kharakterova, T. Dobatkina, *Advanced aluminium alloys containing scandium*, Taylor & Francis Group, London & New York, 1998.
- [58] M. van Dalen, D. Dunand, D. Seidman, Effects of Ti additions on the nanostructure and creep properties of precipitation-strengthened Al-Sc alloys, *Acta Mater.* 53 (2005) 4225–4235. <https://doi.org/10.1016/j.actamat.2005.05.022>.
- [59] M. van Dalen, D. Seidman, D. Dunand, Creep- and coarsening properties of Al-0.06 at.% Sc-0.06 at.% Ti at 300-450 °C, *Acta Mater.* 56 (2008) 4369–4377. <https://doi.org/10.1016/j.actamat.2008.05.002>.
- [60] D. Erdeniz, W. Nasim, J. Malik, A.R. Yost, S. Park, A. De Luca, N.Q. Vo, I. Karaman, B. Mansoor, D.N. Seidman, D.C. Dunand, Effect of vanadium micro-alloying on the microstructural evolution and creep behavior of Al-Er-Sc-Zr-Si alloys, *Acta Mater.* 124 (2017) 501–512. <https://doi.org/10.1016/j.actamat.2017.05.055>.

- [61] H. Hallem, W. Lefebvre, B. Forbord, F. Danoix, K. Marthinsen, The formation of Al₃(Sc_xZr_yHf_{1-x-y})-dispersoids in aluminium alloys, *Mater. Sci. Eng. A.* 421 (2006) 154–160. <https://doi.org/10.1016/j.msea.2005.11.063>.
- [62] A. Tolley, V. Radmilovic, U. Dahmen, Segregation in Al₃(Sc,Zr) precipitates in Al-Sc-Zr alloys, *Scr. Mater.* 52 (2005) 621–625. <https://doi.org/10.1016/j.scriptamat.2004.11.021>.
- [63] W. Prukkanon, N. Srisukhumbowornchai, C. Limmaneevichitr, Modification of hypoeutectic Al-Si alloys with scandium, *J. Alloys Compd.* 477 (2009) 454–460. <https://doi.org/10.1016/j.jallcom.2008.10.016>.
- [64] L. Rokhlin, N. Bochvar, N. Leonova, I. Tarytina, Joint effect of scandium and zirconium on the aging and recrystallization of aluminum Al-Mg₂Si alloys, *Russ. Metall.* 2015 (2015) 51–59. <https://doi.org/10.1134/S0036029511010149>.
- [65] C. Fuller, D. Seidman, D. Dunand, Mechanical properties of Al(Sc,Zr) alloys at ambient and elevated temperatures, *Acta Mater.* 51 (2003) 4803–4814. [https://doi.org/10.1016/S1359-6454\(03\)00320-3](https://doi.org/10.1016/S1359-6454(03)00320-3).
- [66] J. Robson, Optimizing the homogenization of zirconium containing commercial aluminium alloys using a novel process model, *Mater. Sci. Eng. A.* 338 (2002) 219–229. [https://doi.org/10.1016/S0921-5093\(02\)00061-8](https://doi.org/10.1016/S0921-5093(02)00061-8).
- [67] X. Sauvage, A. Dédé, A.C. Muñoz, B. Huneau, Precipitate stability and recrystallisation in the weld nuggets of friction stir welded Al-Mg-Si and Al-Mg-Sc alloys, *Mater. Sci. Eng. A.* 491 (2008) 364–371. <https://doi.org/10.1016/j.msea.2008.02.006>.
- [68] V. Rajinikanth, V. Jindal, V.G. Akkimardi, M. Ghosh, K. Venkateswarlu, Transmission electron microscopy studies on the effect of strain on Al and Al-1% Sc alloy, *Scr. Mater.* 57 (2007) 425–428. <https://doi.org/10.1016/j.scriptamat.2007.04.038>.
- [69] V. Jindal, P. De, K. Venkateswarlu, Effect of Al₃Sc precipitates on the work hardening behavior of aluminum-scandium alloys, *Mater. Lett.* 60 (2006) 3373–3375. <https://doi.org/10.1016/j.matlet.2006.03.017>.
- [70] B. Li, Q. Pan, Z. Yin, Characterization of hot deformation behavior of as-homogenized Al-Cu-Li-Sc-Zr alloy using processing maps, *Mater. Sci. Eng. A.* 614 (2014) 199–206. <https://doi.org/10.1016/j.msea.2014.07.031>.
- [71] B. Forbord, H. Hallem, N. Ryum, K. Marthinsen, Precipitation and recrystallisation in Al-Mn-Zr with and without Sc, *Mater. Sci. Eng. A.* 387–389 (2004) 936–939. <https://doi.org/10.1016/j.msea.2003.10.374>.
- [72] K. Ihara, Y. Miura, Dynamic recrystallization in Al-Mg-Sc alloys, *Mater. Sci. Eng. A.* 387–389 (2004) 647–650. <https://doi.org/10.1016/j.msea.2004.05.082>.
- [73] K. Ikeda, R. Akiyoshi, T. Takashita, M. Mitsuhara, S. Hata, H. Nakashima, K. Yamada, K. Kaneko, Precipitation morphology in Al-Mg-Si-Sc-Zr hot-rolled sheet, in: 13th Int. Conf. Alum. Alloy. (ICAA 13), 2012: pp. 1181–1185.
- [74] J. Royset, U. Tundal, S.R. Skjervold, G. Waterloo, C. Braathen, O. Reiso, An investigation of Sc addition on the extrudability, recrystallisation resistance and mechanical properties of a 6082- and a 7108-alloy, *Mater. Forum.* 28 (2004) 246–251.
- [75] T. Dorin, M. Ramajayam, A. Vahid, T.J. Langan, Aluminium Scandium Alloys, in: *Fundam. Alum. Metall. Recent Adv.*, Woodhead Publishing, United Kingdom, 2018: pp. 439–494.

- [76] J. Royset, Scandium in Aluminium alloys overview: Physical Metallurgy, Properties and applications, *Metall. Sci. Technol.* 25 (2007) 11–21.
- [77] L.L. Rokhlin, N.R. Bochvar, E. V. Lysova, N.P. Leonova, I.G. Korol'kova, Phase equilibria in the ternary Al-Sc-Mn system, *Russ. Metall.* 2008 (2008) 84–88. <https://doi.org/10.1007/BF00773773>.
- [78] K. Chanyathunyaroj, U. Patakham, S. Kou, C. Limmaneevichitr, Microstructural evolution of iron-rich intermetallic compounds in scandium modified Al-7Si-0.3Mg alloys, *J. Alloys Compd.* 692 (2017) 865–875. <https://doi.org/10.1016/j.jallcom.2016.09.132>.
- [79] U. Patakham, C. Limmaneevichitr, Effects of iron on intermetallic compound formation in scandium modified Al-Si-Mg Alloys, *J. Alloys Compd.* 616 (2014) 198–207. <https://doi.org/10.1016/j.jallcom.2014.07.037>.
- [80] B. Rouxel, K. Mester, A. Vahid, J. Lamb, T. Dorin, Influence of the Al₃(Sc,Zr) dispersoids and the stretching on the natural ageing behavior of a binary Al-4Wt% Cu alloys, *Light Met.* 3 (2018) 1601–1607.
- [81] F. Lasagni, B. Mingler, M. Dumont, H.P. Degischer, Precipitation kinetics of Si in aluminium alloys, *Mater. Sci. Eng. A.* 480 (2008) 383–391. <https://doi.org/10.1016/j.msea.2007.07.008>.
- [82] I.N. Fridlyander, O.A. Noskova, N.B. Kuznetsova, Effect of iron and silicon impurities on the mechanical properties of an alloy in the system Al-Zn-Mg-Cu, *Metalloved. i Termicheskaya Obrab. Met.* (1987) 439–440.
- [83] G. Du, J. Deng, Y. Wang, D. Yan, L. Rong, Precipitation of (Al,Si)₃Sc in an Al-Sc-Si alloy, *Scr. Mater.* 61 (2009) 532–535. <https://doi.org/10.1016/j.scriptamat.2009.05.014>.
- [84] C. Booth-morrison, Z. Mao, M. Diaz, D.C.C. Dunand, C. Wolverton, D.N. Seidman, Role of silicon in accelerating the nucleation of Al₃(Sc,Zr) precipitates in dilute Al-Sc-Zr alloys, *Acta Mater.* 60 (2012) 4740–4752. <https://doi.org/10.1016/j.actamat.2012.05.036>.
- [85] N. Vo, D. Dunand, D. Seidman, Improving aging and creep resistance in a dilute Al-Sc alloy by microalloying with Si, Zr and Er, *Acta Mater.* 63 (2014) 73–85. <https://doi.org/10.1016/j.actamat.2013.10.008>.
- [86] Q. Yao, Elastic Properties and Electronic Structure of L1₂ (Al,Si)₃Sc, *Adv. Mater. Res.* 284–286 (2011) 1987–1990. <https://doi.org/10.4028/www.scientific.net/AMR.284-286.1987>.
- [87] R.A. Michi, A. De Luca, D.N. Seidman, D.C. Dunand, Effects of Si and Fe micro-additions on the aging response of a dilute Al-0.08Zr-0.08Hf-0.045Er at.% alloy, *Mater. Charact.* 147 (2019) 72–83. <https://doi.org/10.1016/j.matchar.2018.10.016>.
- [88] T. Dorin, M. Ramajayam, S. Babaniaris, T.J. Langan, Micro-segregation and precipitates in as-solidified Al-Sc-Zr-(Mg)-(Si)-(Cu) alloys, *Mater. Charact.* 154 (2019) 353–362. <https://doi.org/10.1016/j.matchar.2019.06.021>.
- [89] O. Beeri, D.C. Dunand, D.N. Seidman, Roles of impurities on precipitation kinetics of dilute Al-Sc alloys, *Mater. Sci. Eng. A.* 527 (2010) 3501–3509. <https://doi.org/10.1016/j.msea.2010.02.027>.
- [90] P. Leo, E. Cerri, P. De Marco, H. Roven, Properties and deformation behaviour of severe plastic deformed aluminium alloys, *J. Mater. Process. Technol.* 182 (2007) 207–214.

<https://doi.org/10.1016/j.jmatprotec.2006.07.038>.

- [91] L. Lityńska-Dobrzyńska, Effect of heat treatment on the sequence of phases formation in Al-Mg-Si alloy with Sc and Zr additions, *Arch. Metall. Mater.* 51 (2006) 555–560.
- [92] N.I. Kolobnev, L.B. Khokhlatova, S.V. Samokhvalov, A.A. Alekseev, S.V. Sbitneva, T.I. Tararaeva, V.I. Popov, Heat treatment effect on properties of Al-Mg-Si-Cu 1370 alloy, *Mater. Sci. Forum.* 519–521 (2006) 519–524. <https://doi.org/10.4028/www.scientific.net/MSF.519-521.519>.
- [93] C. Yeung, W. Lee, The effect of homogenization on the recrystallization behaviour of AA4006 Al – Si alloy, *J. Mater. Process. Technol.* 82 (1998) 102–106.
- [94] L. Rokhlin, N. Bochvar, O. Rybal'chenko, I. Tarytina, A. Sukhanov, Phase equilibria in aluminum-rich Al-Sc-Si alloys during solidification, *Russ. Metall.* 2012(7) (2012) 606–611. <https://doi.org/10.1134/S0036029512070129>.
- [95] F. De Geuser, A. Deschamps, Precipitate characterisation in metallic systems by small-angle X-ray or neutron scattering, *Comptes Rendus Phys.* 13 (2012) 246–256. <https://doi.org/10.1016/j.crhy.2011.12.008>.
- [96] J. Dumbre, T. Langan, T. Dorin, N. Birbilis, Optimised Composition and Process Design to Develop Sc-Enhanced Wrought Al-Si Alloys, in: *Miner. Met. Mater. Ser.*, 2019: pp. 1431–1438. https://doi.org/10.1007/978-3-030-05864-7_179.
- [97] N.Q. Vo, D.C. Dunand, D.N. Seidman, Improving aging and creep resistance in a dilute Al-Sc alloy by microalloying with Si, Zr and Er, *Acta Mater.* 63 (2014) 73–85. <https://doi.org/10.1016/j.actamat.2013.10.008>.
- [98] T. Dorin, M. Ramajayam, S. Babaniaris, L. Jiang, T.J. Langan, Precipitation sequence in Al–Mg–Si–Sc–Zr alloys during isochronal aging, *Materialia.* 8 (2019) 100437. <https://doi.org/10.1016/j.mtla.2019.100437>.
- [99] C.B. Fuller, D.N. Seidman, D.C. Dunand, Mechanical properties of Al(Sc,Zr) alloys at ambient and elevated temperatures, *Acta Mater.* 51 (2003) 4803–4814. [https://doi.org/10.1016/S1359-6454\(03\)00320-3](https://doi.org/10.1016/S1359-6454(03)00320-3).
- [100] Y. Harada, D.C. Dunand, Microstructure of Al₃Sc with ternary transition-metal additions, *Mater. Sci. Eng. A.* 329–331 (2002) 686–695.
- [101] C. Monachon, M. Krug, D. Seidman, D. Dunand, Chemistry and structure of core/double-shell nanoscale precipitates in Al-6.5Li-0.07Sc-0.02Yb (at.%), *Acta Mater.* 59 (2011) 3398–3409. <https://doi.org/10.1016/j.actamat.2011.02.015>.
- [102] S. Jiang, H. Wang, Y. Wu, X. Liu, H. Chen, M. Yao, B. Gault, D. Ponge, D. Raabe, A. Hirata, M. Chen, Y. Wang, Z. Lu, Ultrastrong steel via minimal lattice misfit and high-density nanoprecipitation, *Nature.* 544 (2017) 460–464. <https://doi.org/10.1038/nature22032>.
- [103] E.A. Marquis, D.N. Seidman, D.C. Dunand, Effect of Mg addition on the creep and yield behavior of an Al-Sc alloy, *Acta Mater.* 51 (2003) 4751–4760. [https://doi.org/10.1016/S1359-6454\(03\)00288-X](https://doi.org/10.1016/S1359-6454(03)00288-X).
- [104] E. Marquis, D. Seidman, Coarsening kinetics of nanoscale Al₃Sc precipitates in an Al-Mg-Sc alloy, *Acta Mater.* 53 (2005) 4259–4268. <https://doi.org/10.1016/j.actamat.2005.08.035>.
- [105] C. Booth-Morrison, D.N. Seidman, D.C. Dunand, Effect of Er additions on ambient and high-temperature strength of precipitation-strengthened Al-Zr-Sc-Si alloys, *Acta Mater.*

- 60 (2012) 3643–3654. <https://doi.org/10.1016/j.actamat.2012.02.030>.
- [106] R. Vincent, P.A. Midgley, Double conical beam-rocking system for measurement of integrated electron diffraction intensities, *Ultramicroscopy*. 53 (1994) 271–282. [https://doi.org/10.1016/0304-3991\(94\)90039-6](https://doi.org/10.1016/0304-3991(94)90039-6).
- [107] J.-L. Rouviere, A. Béché, Y. Martin, T. Denneulin, D. Cooper, Improved strain precision with high spatial resolution using nanobeam precession electron diffraction, *Appl. Phys. Lett.* 103 (2013) 241913. <https://doi.org/10.1063/1.4829154>.
- [108] Y.Y. Wang, D. Cooper, J. Rouviere, C.E. Murray, N. Bernier, J. Bruley, Nanoscale strain mapping in embedded SiGe devices by dual lens dark field electron holography and precession electron diffraction, *Microsc. Microanal.* 21 (2015) 1963–1964. <https://doi.org/10.1017/s1431927615010594>.
- [109] S. Wenner, R. Holmestad, Accurately measured precipitate-matrix misfit in an Al-Mg-Si alloy by electron microscopy, *Scr. Mater.* 118 (2016) 5–8. <https://doi.org/10.1016/j.scriptamat.2016.02.031>.
- [110] L.G. Hector, Y.-L.L. Chen, S. Agarwal, C.L. Briant, Friction stir processed AA5182-O and AA6111-T4 aluminum alloys. Part 2: Tensile properties and strain field evolution, *J. Mater. Eng. Perform.* 16 (2007) 404–417. <https://doi.org/10.1007/s11665-007-9060-0>.
- [111] P.F. Rottmann, K.J. Hemker, Nanoscale elastic strain mapping of polycrystalline materials, *Mater. Res. Lett.* 6 (2018) 249–254. <https://doi.org/10.1080/21663831.2018.1436609>.
- [112] J. Kang, D.S. Wilkinson, M. Bruhis, M. Jain, P.D. Wu, J.D. Embury, R.K. Mishra, A.K. Sachdev, Shear Localization and Damage in AA5754 Aluminum Alloy Sheets, *J. Mater. Eng. Perform.* 17 (2008) 395–401. <https://doi.org/10.1007/s11665-008-9224-6>.
- [113] M. Ashby, L. Brown, Diffraction contrast from spherically symmetrical coherency strains, *Philos. Mag. A J. Theor. Exp. Appl. Phys.* 8 (1963) 1083–1103.
- [114] D. Williams, B. Carter, *Transmission electron microscopy: Part 1- Basics*, 2nd ed., Springer, New York, 2009.
- [115] S. Saha, T.Z. Todorova, J.W. Zwanziger, Temperature dependent lattice misfit and coherency of Al₃X (X = Sc, Zr, Ti and Nb) particles in an Al matrix, *Acta Mater.* 89 (2015) 109–115. <https://doi.org/10.1016/j.actamat.2015.02.004>.
- [116] O. Beeri, D.C. Dunand, D.N. Seidman, Roles of impurities on precipitation kinetics of dilute Al-Sc alloys, *Mater. Sci. Eng. A*. 527 (2010) 3501–3509. <https://doi.org/10.1016/j.msea.2010.02.027>.
- [117] D.L. Foley, A.C. Leff, A.C. Lang, M.L. Taheri, Evolution of β -phase precipitates in an aluminum-magnesium alloy at the nanoscale, *Acta Mater.* 185 (2020) 279–286. <https://doi.org/10.1016/j.actamat.2019.10.024>.
- [118] M. Sharma, M. Amateau, T. Eden, Hardening mechanisms of spray formed Al-Zn-Mg-Cu alloys with scandium and other elemental additions, *J. Alloys Compd.* 416 (2006) 135–142. <https://doi.org/10.1016/j.jallcom.2005.08.045>.

Appendix 1:

The following manuscript is a result of work that was conducted in parallel to the thesis, but which does not form part of the examinable dissertation content. The work relates to the effect of Sc and Zr addition in 2xxx series (Al-Cu) Al-alloys, and the impact on microstructure and corrosion.



Contents lists available at ScienceDirect

Corrosion Science



Simultaneous improvement in corrosion resistance and hardness of a model 2xxx series Al-Cu alloy with the microstructural variation caused by Sc and Zr additions

S.K. Kairy^{a,*}, B. Rouxel^b, J. Dumbre^a, J. Lamb^c, T.J. Langan^d, T. Dorin^b, N. Birbilis^e

^a Department of Materials Science and Engineering, Monash University, Clayton, VIC, 3800, Australia

^b Institute for Frontier Materials, Deakin University, Waurn Ponds, VIC, 3216, Australia

^c Universal Alloy Corporation, Canton, GA, 30114, USA

^d Clean TeQ, Notting Hill, VIC, 3168, Australia

^e College of Engineering and Computer Science, The Australian National University, Acton, ACT, 2601, Australia

ARTICLE INFO

Keywords:

A: Aluminium A:
Alloy
B: STEM
B: Polarisation
C: Pitting corrosion
C: Intergranular corrosion.

ABSTRACT

The microstructural variation caused by Sc and Zr additions to a 2xxx series Al-Cu alloy was studied in the context of corrosion and hardness. The addition of Sc and Zr led to microstructural refinement, a decrease in corrosion current density, and a reduction in the extent of pitting and intergranular corrosion; whilst hardness increased. Such an improvement in properties was attributed to the variation of alloy microstructure. It was also noted that an often unreported W-phase ($\text{Al}_x\text{Cu}_{5-6}\text{ScZr}_{y=0.3}$), containing Zr, was 'cathodic' relative to the Al-matrix in the Al-Cu-Sc-Zr alloy.

1. Introduction

Precipitation hardenable 2xxx aluminium (Al) alloys based on the Al-Cu system are an important class of Al-alloys, achieving strengths that make them suitable for applications in aircraft structural components [1–4]. Aluminium alloy AA 2219 (Al-6 wt.%Cu) is considered to be the most preferred alloy for the construction of fuel tanks that carry cryogenic fuel, such as liquid oxygen and liquid hydrogen [5]. The strength of Al-Cu alloys is increased with the formation of nanoscale precipitates of metastable θ' -phase (Al_2Cu), which are dictated by ageing temperature and time [3,4,6]. Recently, it was identified that Sc and Zr additions, in combination with multi-step homogenisation heat treatments, further improved the strength of extruded Al-Cu alloys [7–9]. The improvement in strength was attributed to the formation of core-shell $\text{Al}_3(\text{Sc,Zr})$ nanoscale particles, which refined the size and increased the number density of θ' -phase precipitates in the Al-matrix [7–9]. Core-shell $\text{Al}_3(\text{Sc,Zr})$ particles were thermally stable and aided in inhibiting recrystallization of Al-alloys, even during high temperature mechanical processing [7,9–14]. In addition, $\text{Al}_3(\text{Sc,Zr})$ particles were also found to stabilise θ' -phase precipitates even up to 300 °C in as-cast Al-Cu-Sc-(Zr) alloys [15,16], making the alloys suitable for high temperature applications. Furthermore, it was identified that Sc can enhance the weldability of Al-alloys and improve mechanical properties of

weld metal [14,17]. Considering the beneficial aspects, and with the decrease in price of Sc in coming years [7–9], the potential commercial applications of Al-Cu-Sc-Zr alloys in the aerospace sector is promising. Based on the growing interest in the newly developed Al-Cu-Sc-Zr alloys and the criticality of their associated applications, in addition to mechanical properties, it is of utmost importance to study corrosion and understand its mechanisms associated with the microstructural variation caused by Sc and Zr additions.

Pitting and intergranular corrosion (IGC) are the most common forms of corrosion observed in Al-Cu alloys, and are associated with the microstructural features in the Al-matrix [18–21]. In Al-Cu alloys, constituent particles such as Fe-containing intermetallics and Al_2Cu particles that are formed during solidification are cathodic to the Al-matrix and pure Al in NaCl [18–25]. Therefore, pitting is associated with the dissolution of the Al-matrix at the periphery of the noble constituents. Pitting is also expected to initiate by dissolving the Al-matrix at the periphery of Al_2Cu precipitates, which are formed during ageing. Intergranular corrosion was associated with the dissolution of solute depleted zones adjacent to grain boundaries (GBs) containing Al_2Cu precipitates [19–22], in artificially aged Al-Cu alloys. In fact, IGC can even originate at the very early stage of ageing as a result of Cu segregation along GBs, prior to the formation of the precipitates, similar to Al-Si-Mg-Cu alloys [26,27]. The electrochemical response and the

* Corresponding author.

E-mail address: shravan.kairy@monash.edu (S.K. Kairy).

<https://doi.org/10.1016/j.corsci.2019.108095>

Received 5 April 2019; Received in revised form 8 July 2019; Accepted 12 July 2019

Available online 16 July 2019

0022-0748/© 2019 Elsevier Ltd. All rights reserved.

degree of IGC and pitting of Al and its alloys were determined to be influenced by many microstructural features such as precipitate size, number density and continuity along GBs; grain size; GB type (i.e. high angle and low angle) and length; texture; environment; impurity segregation and residual stress [22–41]. Therefore, detailed understanding of the microstructure within grains and GBs is important in designing corrosion resistant alloys.

There is a consensus that the corrosion behaviour of Al, Al-Mg, Al-Cu-Mg and Al-Zn-Mg-(Cu) alloys was improved with the addition of Sc- (Zr) [42–46], with an exception that Sc additions deteriorated an Al-Zn-Mg-Cu-Zr alloy [47]. The electrochemical behaviour of Al_3Sc and $Al_3(Sc,Zr)$ particles was studied and determined to be slightly cathodic to the Al-matrix in Al-Sc and Al-Mg-Zn-Sc alloys, respectively [46,47]. In addition, Al_3Sc and $Al_3(Sc,Zr)$ particles were determined to possess good electrochemical compatibility with the Al-matrix in most of the Al-alloy systems, as a result of the particles' poor ability to support the cathodic reaction, oxygen reduction, at appreciable rates [46,47]. To the authors' knowledge, there is only one study that is partly focussed on the role of Sc on pitting and metastable pitting of different grain sized Al-Cu-Sc alloys [48], relating the size of nanoscale θ' -phase precipitates with the evolution of metastable pitting events. However, that study did not investigate pitting caused by different second phase particles, such as Fe-containing intermetallics, Al_2Cu , Al_3Sc and W-phase particles, which are expected to evolve in the Al-matrix of Al-Cu-Sc alloys during solidification and homogenisation treatments. In addition, the role of Sc on other electrochemical parameters, such as corrosion potential (E_{corr}) and corrosion current density (i_{corr}), which are also important to understand the corrosion behaviour of Al-alloys, was not determined. Furthermore, the role of Sc and Zr additions on pitting and IGC of Al-Cu alloys was also not studied to date.

Herein, the microstructure, corrosion and hardness of a model 2xxx Al-Cu alloy in an artificially aged condition were explicitly studied with and without Sc and Zr, in order to investigate the role of Sc and Zr in microstructural evolution and alloy properties.

2. Material and methods

2.1. Material synthesis and ageing

Two Al-Cu alloys were cast with and without Sc and Zr. The chemical composition of the alloys as measured by inductively coupled plasma – atomic emission spectroscopy is shown in Table 1. Billets with 30 mm diameter were machined from the castings and were given multi-step homogenisation heat treatments. The latter step was carefully designed aiming at eliminating the segregation of Cu from the solidification and forming a fine distribution of $Al_3(Sc,Zr)$ particles with a core-shell structure. Homogenised 30 mm billets were extruded through a 5.5 mm diameter circular die, resulting in rods with an extrusion ratio of 32. As-extruded alloys were solution treated in salt bath at 500 °C for 1 h and subsequently water quenched. Solution treated alloys were then allowed to naturally age for 3 days, and then aged at 190 °C for 18 h in oil bath and quenched in water.

2.2. Microstructural characterisation

2.2.1. Electron backscattered diffraction

Electron backscattered diffraction (EBSD) was performed upon the

Table 1

Nominal composition (in wt.%) of Al-Cu and Al-Cu-Sc-Zr alloys as measured using inductively coupled plasma – atomic emission spectroscopy.

Sample I.D	Cu	Sc	Zr	Fe	Ti	Al
Al-Cu	4	0	0	0.07	0.005	Bal.
Al-Cu-Sc-Zr	4	0.1	0.13	0.07	0.005	Bal.

surface, perpendicular to the extrusion direction, of specimens from Al-Cu and Al-Cu-Sc-Zr alloys using a JEOL® 7001 F SEM at an operating voltage of 20 kV. An HKL NordlysMax² EBSD camera in conjunction with the Oxford instruments' Aztec software was used for the EBSD data acquisition, and the HKL Channel5 software was used to analyse the acquired data. Specimens for EBSD were prepared by electro-polishing in 3:1 methanol to nitric acid maintained at –28 °C and with an applied voltage of 12 V.

2.2.2. Scanning electron microscopy

Scanning Electron microscopy (SEM), in the backscattered electron (BSE) mode, was performed upon the surface, perpendicular to the extrusion direction, of specimens from Al-Cu and Al-Cu-Sc-Zr alloys using a JEOL® 7001 F SEM at an operating voltage of 15 kV. Energy-dispersive X-ray spectroscopy (EDXS) was performed using an Oxford Instruments' X-Max 80 silicon drift detector in conjunction with the 7001 F, and the collected EDXS data was analysed using the AZtec EDXS software. Specimens for SEM were prepared by grinding them to 4000 grit SiC paper in ethanol and then polishing to 0.01 µm surface finish using colloidal silica suspension, and finally ultrasonic cleaning in ethanol and drying in air.

2.2.3. Transmission electron microscopy

Transmission electron microscopy (TEM) was performed upon Al-Cu and Al-Cu-Sc-Zr alloys using three different FEI® electron microscopes. For bright-field TEM and electron diffraction, an FEI® G² T20 TWIN LaB₆ operated at 200 kV was used. High-angle annular dark-field - scanning transmission electron microscopy (HAADF-STEM), providing atomic number contrast information, was performed using an FEI® Tecnai G² F20 S-TWIN FEG operated at 200 kV and a double aberration corrected FEI® Titan³ 80-300 microscope operated at 300 kV. Energy-dispersive X-ray spectroscopy (EDXS) was performed using a Bruker® X-flash X-ray detector in conjunction with the F20, and the collected EDXS data with drift correction on was analysed using the Bruker® Esprit X-ray software. Specimens for TEM were prepared by punching 3 mm discs from thin slices, which were cut perpendicular to the extrusion direction, of Al-Cu and Al-Cu-Sc-Zr alloys. Discs were mechanically thinned to ≈ 50 µm using 2000 grit SiC paper in ethanol, and then argon ion milled at –100 °C using a Gatan® precision ion polishing system (PIPS). Prior to HAADF-STEM, specimens were plasma cleaned for 2 min with an Ar and O₂ gas mixture using a Gatan® solaris 950 advanced plasma system.

2.3. Corrosion testing

2.3.1. Potentiodynamic polarisation test

Potentiodynamic polarisation tests were performed upon Al-Cu and Al-Cu-Sc-Zr alloys in 0.1 M NaCl using BioLogic® VMP3 potentiostat. A three-electrode electrochemical Princeton Applied Research® K0235 flat cell, with 1 cm² exposed area for a working electrode, a platinum mesh counter electrode and a saturated calomel electrode (SCE) as a reference electrode, was used. Alloy specimens with a diameter of 5.3 mm were cold mounted in an epoxy resin, exposing their cross-sectional surface perpendicular to the extrusion direction. Exposed surfaces were then ground to 2000 grit SiC paper and ultrasonically cleaned in ethanol, air-dried, measured open circuit potential (OCP) in 0.1 M NaCl for 10 min. Subsequently, potentiodynamic polarisation tests were performed at a scan rate of 1 mV/sec commencing from –200 mV (vs. OCP) to ≈ –0.55 V_{SCE}. Tests were also performed in deaerated, using argon gas, 0.1 M NaCl at a scan rate of 1 mV/sec commencing from –20 mV (vs. OCP) to ≈ –0.55 V_{SCE} to readily discern pitting potential (E_{pit}) of the alloys. All tests were performed in triplicate for reproducibility.

2.3.2. Immersion test and optical profilometry

Optical profilometry, in the vertical scanning interferometry mode, was performed using a Veeco Wyko NT1100 upon the surface, perpendicular to the extrusion direction, of specimens from Al-Cu and Al-Cu-Sc-Zr alloys prior to and following immersion in 0.1 M NaCl for 7 days, to quantify pitting developed upon the surfaces. For this test, specimens were ground to 1 μm surface finish in water, ultrasonically cleaned in ethanol, air-dried and then immersed in 0.1 M NaCl for 7 days. Following immersion, specimens were taken from NaCl, ultrasonically cleaned in ethanol and air dried, and then immersed in 15% HNO_3 for 1 min to remove corrosion products and finally cleaned in distilled water and air-dried. The 15% HNO_3 treatment for 1 min completely removed corrosion products upon specimen surfaces with negligible attack to the Al-matrix (observed using SEM prior to and following the treatment, and are not shown herein). Optical profilometry was then performed at 4 different locations upon each alloy specimen surface, and pits were identified and analysed.

2.3.3. Intergranular corrosion test

The IGC behaviour of Al-Cu and Al-Cu-Sc-Zr alloys was assessed according to the standard test for age hardenable Al-alloys, ASTM G110 [49]. Specimens for the test were ground to 1200 grit SiC paper and cleaned in ethanol and air-dried. Prior to the test, specimens were immersed in an etching solution made of 50 mL HNO_3 (70%) and 950 mL distilled water, at 93 $^\circ\text{C}$ for 1 min and subsequently rinsed in distilled water. The use of HF acid in the etching solution was eliminated because of occupational health and safety criteria. Specimens were then immersed for 1 min in concentrated HNO_3 (70%) at room temperature, followed by rinsing in distilled water and drying in air. Subsequently, specimens were then immersed for 27 h in the test solution, 57 g NaCl +10 mL H_2O_2 (30%) +990 mL distilled water, maintained at 30 $^\circ\text{C}$. Following the test, specimens were removed from the test solution, cleaned in distilled water and air-dried for the inspection of IGC depth and mass loss. For observing IGC, cross-sectional surfaces that were perpendicular to the extrusion direction were ground in ethanol up to 1 μm surface finish using diamond paste, cleaned in ethanol and air dried, and then observed using an optical microscope, Olympus[®] GX51. Image analysis software, ImageJ 1.48v was used for measuring IGC depths. Mass loss was measured by measuring mass of each specimen prior to and following immersion in the test solution. To ensure accuracy in mass loss, corrosion products were removed by mechanically rubbing the specimens using a soft brush and then immersing them in 15% HNO_3 for 1 min, and finally cleaning them in distilled water and drying completely in air.

2.4. Hardness test

Vickers hardness of Al-Cu and Al-Cu-Sc-Zr alloys was measured using a Struers[®] Duramin A300 with an applied load of 1 kg and dwell time of 10 s. The cross-sectional surface, perpendicular to the extrusion direction, of specimens from both the alloys were ground to 800 grit SiC paper and cleaned in ethanol, and air-dried prior to the hardness measurement. A total of 7 measurements were collected for each alloy.

3. Results and discussion

3.1. Electron backscattered diffraction studies

Electron backscattered diffraction orientation maps of specimens from Al-Cu and Al-Cu-Sc-Zr alloys are presented in Fig. 1(a) and (b), respectively. High angle GBs, with a misorientation angle greater than 15 $^\circ$, were indicated by black lines in orientation maps (Fig. 1(a and b)). Whilst, low angle GBs corresponding to the misorientation angle 2 $^\circ$ to 15 $^\circ$ were not indicated, as they heavily populate in the Al-Cu-Sc-Zr alloy. The average length of HAGBs and LAGBs in the Al-Cu alloy was 1.06 ± 0.24 μm and 0.12 ± 0.02 μm , respectively, measured over an area of ≈ 0.499 mm^2 . Whilst, for the Al-Cu-Sc-Zr alloy, the average length of HAGBs and LAGBs was 1.86 ± 0.52 μm and 10.53 ± 0.59 μm , respectively. Over the same area, the average number of grains in Al-Cu and Al-Cu-Sc-Zr alloys was 50 ± 15 and 270 ± 23 , respectively, and their corresponding average grain size was 112 ± 68 μm and 33 ± 22 μm , respectively. From the orientation maps and statistics on grains and GBs, it can be inferred that the Al-Cu alloy was completely recrystallised and whilst the Al-Cu-Sc-Zr alloy exhibited deformed and unrecrystallised grains with a strong extrusion texture. Such microstructural variation is mainly attributed to the formation of nanoscale $\text{Al}_3(\text{Sc,Zr})$ particles [7,9–14], which were formed in the Al-Cu-Sc-Zr alloy during multi-step homogenisation treatments. From the corrosion point of view, it is important to understand such microstructural variation.

3.2. Scanning electron microscopy studies

Backscattered electron-SEM images of specimens from Al-Cu and Al-Cu-Sc-Zr alloys are shown in Fig. 2(a and c) and (b and d), respectively. The composition of different phases that were observed in both the alloys was determined using EDXS point analysis and is presented in Table 2.

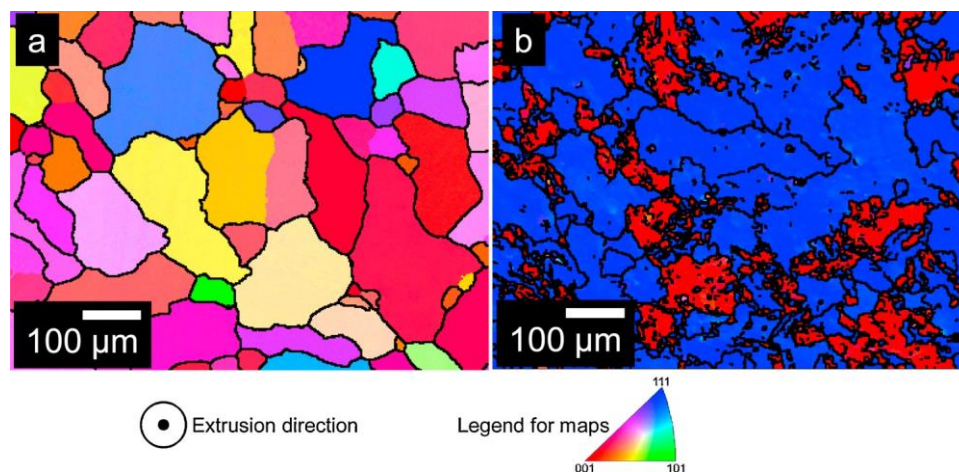


Fig. 1. (a) and (b) are EBSD orientation maps of Al-Cu and Al-Cu-Sc-Zr alloys, respectively.

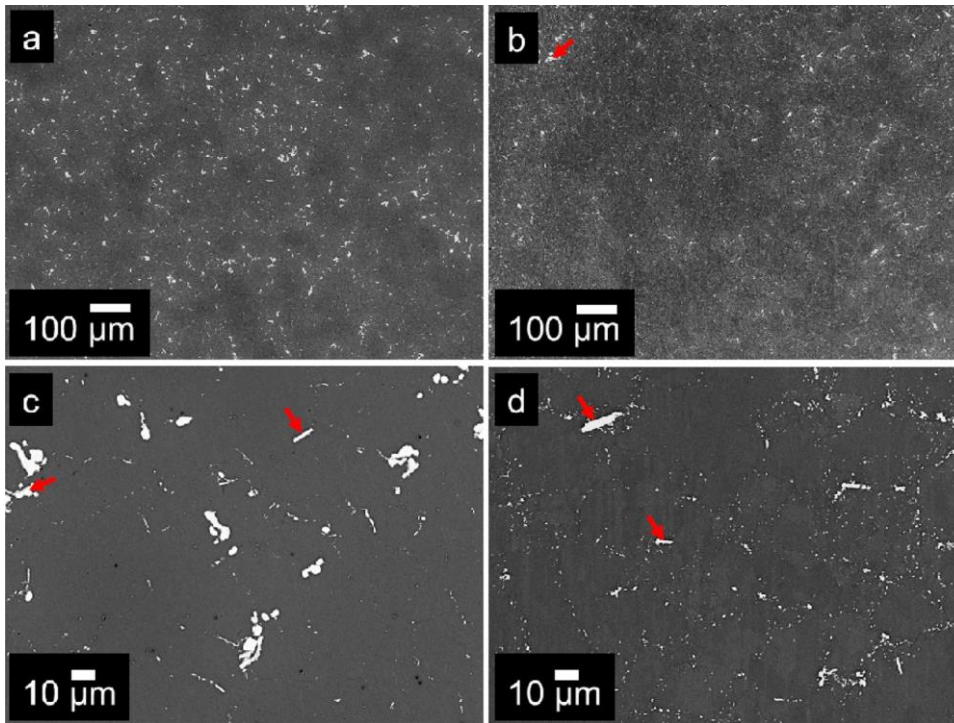


Fig. 2. (a) and (b) are low magnification BSE-SEM images of Al-Cu and Al-Cu-Sc-Zr alloys, respectively. High magnification BSE-SEM images of Al-Cu and Al-Cu-Sc-Zr alloys are shown in 'c' and 'd', respectively. The arrow in 'b' point to Al_2Cu . Arrows in 'c' point to $\text{Al}_x\text{Fe}_{3-4}\text{Cu}$, and the remaining particles in 'c' are Al_2Cu . In 'd', arrows point to $\text{Al}_x\text{Fe}_{3-4}\text{Cu}$, and most of the remaining very fine particles correspond to $\text{Al}_x\text{Cu}_{5-8}\text{ScZr}_y$.

Table 2
SEM-EDXS point analysis (in at.%) of different phases as observed in Al-Cu and Al-Cu-Sc-Zr alloys.

Sample I.D.	Al	Cu	Fe	Sc	Zr	Ti	Phase
Al-Cu	66.7	33.3	0	0	0	0	Al_2Cu
76.3		5.4	18.3	0	0	0	$\text{Al}_x\text{Fe}_{3-4}\text{Cu}$
98.2		0.8	0	0	0	0	Al-Matrix
Al-Cu-Sc-Zr	65	35	0	0	0	0	Al_2Cu
78		5.1	16.9	0	0	0	$\text{Al}_x\text{Fe}_{3-4}\text{Cu}$
76.1		20.6	0.1	3.0	0.2	0	$\text{Al}_x\text{Cu}_{5-8}\text{ScZr}_y$
98.2		1.6	0	0.1	0.1	0	Al-Matrix

Second phase particles, such as Al_2Cu and $\text{Al}_x\text{Fe}_{3-4}\text{Cu}$ were observed in the Al-matrix of the Al-Cu alloy. Whilst, the Al-Cu-Sc-Zr alloy contained Al_2Cu (marked by the arrow in Fig. 2b), $\text{Al}_x\text{Fe}_{3-4}\text{Cu}$ (marked by arrows in Fig. 2d) and W-phase ($\text{Al}_x\text{Cu}_{5-8}\text{ScZr}_y$, the very fine particles in Fig. 2d). The size of the second phase particles decreased and their number density increased with the addition of Sc and Zr to the Al-Cu alloy (Fig. 2(a–d)). The second phase particles observed in the Al-matrix of Al-Cu and Al-Cu-Sc-Zr alloys were formed during the solidification of the melt and homogenisation thermal treatments. All the second phases determined in the present study were frequently observed in Al-Cu and Al-Cu-Sc cast and wrought alloys [3,4,13,14,17,50,51]. However, the unique finding in the present study is that W-phase also contains Zr. The exact concentration of Zr in W-phase could not be determined by this technique. This finding demonstrates that it is still possible to determine more phases with chemical variations caused by solute additions in well-established aluminium alloys. Such identification is important as further detailed understanding the structure and composition of the phase can aid in understanding its formation mechanism and then in tailoring mechanical and corrosion properties of Al alloys.

3.3. Transmission electron microscopy studies

Bright field (BF)-TEM images of specimens from Al-Cu and Al-Cu-Sc-Zr alloys are shown in Fig. 3(a) and (b), respectively. The insets in Fig. 3(a) and (b) are selected area diffraction patterns (SADPs) obtained from the

corresponding BF-TEM images. Atomic number contrast HAADF-STEM images of specimens from the Al-Cu-Sc-Zr alloy are shown in Fig. 3(c–f). All TEM/STEM observations were performed along the $\langle 001 \rangle_\alpha$ direction (α corresponds to Al-matrix).

Based on the SADP analysis, precipitates in the Al-matrix of both Al-Cu and Al-Cu-Sc-Zr alloys were confirmed to be of θ' -phase (Fig. 3(a–b)). In addition, the diffraction spots from $\text{Al}_3(\text{Sc,Zr})$ particles were also identified in the SADP of Fig. 3b. Nanoscale $\text{Al}_3(\text{Sc,Zr})$ particles, which were marked by yellow arrows in Fig. 3b, were found to coexist with θ' -phase precipitates in the Al-matrix of the Al-Cu-Sc-Zr alloy. Precipitates of θ' -phase were bigger and lower in number density in the Al-matrix of the Al-Cu alloy than Al-Cu-Sc-Zr (Fig. 3(a–b)). High resolution HAADF-STEM imaging revealed the presence of θ'' -phase precipitates (marked by white arrows) in addition to θ' -phase precipitates (marked by red arrows) and $\text{Al}_3(\text{Sc,Zr})$ particles (marked by yellow arrows) in the Al-matrix of the Al-Cu-Sc-Zr alloy (Fig. 3c). Similar to θ' -phase, θ'' -phase precipitates were also found to coexist with $\text{Al}_3(\text{Sc,Zr})$ particles (Fig. 3c), indicating that $\text{Al}_3(\text{Sc,Zr})$ particles act as heterogeneous nucleation sites for the formation of the precipitates. High magnification and atomic resolution HAADF-STEM imaging aided in determining the precise dimensions of θ'' -phase precipitates (length: 41 ± 14 nm and thickness: 2.9 ± 0.4 nm), θ' -phase precipitates (length: 146 ± 65 nm and thickness: 2.1 ± 1.1 nm) and $\text{Al}_3(\text{Sc,Zr})$ particles (diameter: 12.4 ± 1.9 nm) in the Al-matrix of the Al-Cu-Sc-Zr alloy. Whilst, the average length and thickness of θ' -phase precipitates in the Al-matrix of the Al-Cu alloy as determined from BF-TEM images were 374 ± 135 nm and 26 ± 4 nm, respectively. Metastable θ'' - and θ' -phase precipitates were previously found to nucleate on Al_3Sc or $\text{Al}_3(\text{Sc,Zr})$ particles [7,9,15,16,52]. In general, such an interaction of Al_3Sc or $\text{Al}_3(\text{Sc,Zr})$ particles with the precipitates not only increases the strength of Al-Cu-Sc-(Zr) alloys [7,9,52], but also improves pitting resistance when compared to Al-Cu alloys - as the precipitate thickness decreases to the range of critical values to initiate pitting in Al-alloys [37–41].

Atomic resolution HAADF-STEM imaging of $\text{Al}_3(\text{Sc,Zr})$ particles at different locations in the Al-matrix of the Al-Cu-Sc-Zr alloy revealed their coexistence with either of Guinier-Preston (GP) zones or θ'' - or θ' -phase precipitates (Fig. 3(d–f)). The presence of GP zones on $\text{Al}_3(\text{Sc,Zr})$

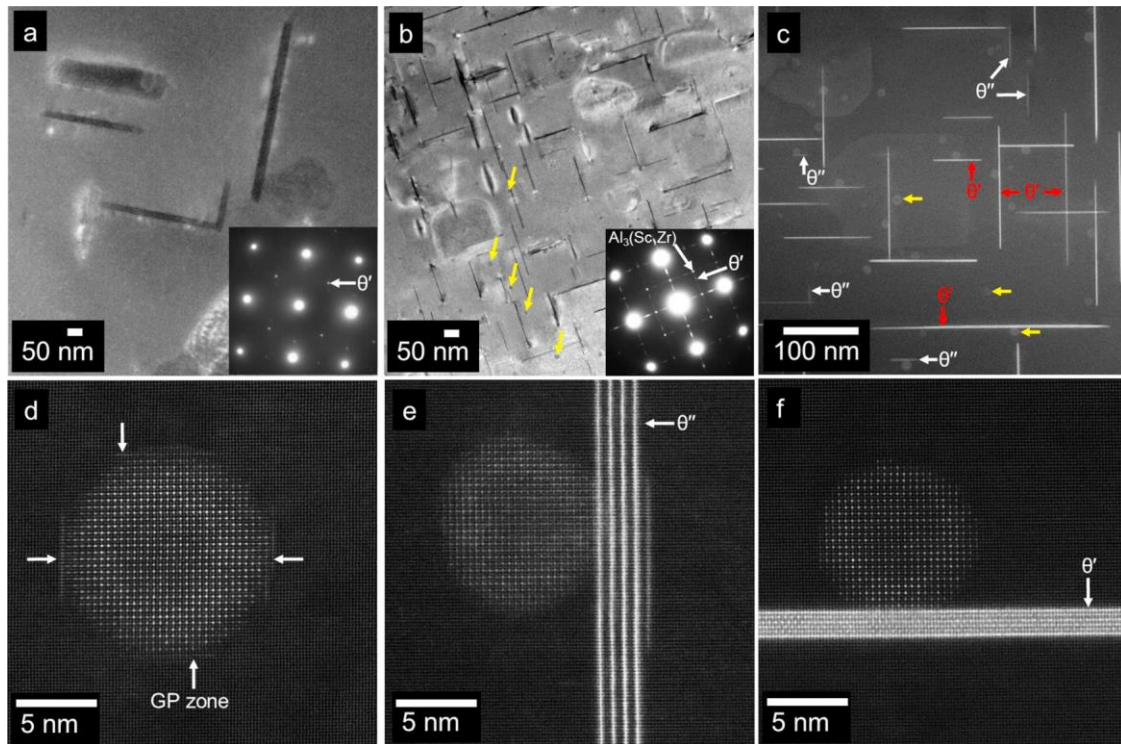


Fig. 3. (a) and (b) are BF-TEM images of Al-Cu and Al-Cu-Sc-Zr alloys, respectively. Insets in 'a' and 'b' are SADPs corresponding to the TEM images. (c–f) HAADF-STEM images of the Al-Cu-Sc-Zr alloy. Yellow arrows in 'b' and 'c' point to $\text{Al}_3(\text{Sc,Zr})$ particles. White arrows in 'd' point to GP zones that were nucleated over an $\text{Al}_3(\text{Sc,Zr})$ particle. (For interpretation of the references to colour in this figure legend, the reader is referred to the web version of this article.)

particles was not observed before. The unique microstructural observation herein led to rationalising the evolution mechanism of θ' -phase precipitates upon $\text{Al}_3(\text{Sc,Zr})$ particles. During ageing, GP zones, which comprise of a single atomic layer of Cu atoms, nucleate upon $\{001\}$ planes of $\text{Al}_3(\text{Sc,Zr})$ particles and with time GP zones transform to θ'' -phase and then to θ' -phase precipitates, aided by Cu segregation and rearrangement. However, different stages of the θ' -phase precipitate evolution were observed in specimens from the Al-Cu-Sc-Zr alloy (Fig. 3(c–f)), indicating that the nucleation and growth kinetics upon different $\text{Al}_3(\text{Sc,Zr})$ particles is not same. Upon close observation, atoms at the core of $\text{Al}_3(\text{Sc,Zr})$ particles are low in contrast when compared to their periphery (Fig. 3(d–f)), indicating that the higher atomic number element, i.e. Zr is present at the periphery of the particles. The abrupt change in contrast within $\text{Al}_3(\text{Sc,Zr})$ particles in high resolution HAADF-STEM images allowed us to precisely determine the diameter of Sc-rich core (6.3 ± 0.7 nm) and thickness of Zr-rich shell (3.1 ± 0.9 nm). In fact, it was reported that Zr dissolves in Al_3Sc by replacing Sc atoms [53–55], and thereby forming $\text{Al}_3(\text{Sc}_{1-x}\text{Zr}_x)$ core. Such core-shell particles were formed as a result of multi-step homogenisation heat treatments [7,9,10]. As the diffusivity of Zr is lower than Sc in the Al-matrix [10], Al_3Sc particles initially form in the Al-matrix during the early step of the homogenisation treatment. Upon further homogenisation at higher temperature, Zr atoms segregate to the interface of the particles and Al-matrix, and thereby forming Zr-rich shells, Al_3Zr , with the core comprised of Al_3Sc or $\text{Al}_3(\text{Sc}_{1-x}\text{Zr}_x)$. The Zr-rich shell was determined to improve the thermal stability of core-shell $\text{Al}_3(\text{Sc,Zr})$ particles and stabilise θ' -phase precipitates at high temperature [7,9,15,16,55,56].

Detailed HAADF-STEM characterisation and composition of W-phase constituent particle and PFZ observed within a grain of the Al-Cu-Sc-Zr alloy are presented in Fig. 4 and Table 3, respectively.

Constituent W-phase particles were also observed within grains of the Al-Cu-Sc-Zr alloy (marked by the white arrow in Fig. 4a). The EDXS-point analysis of the constituents revealed a stoichiometric composition

of $\text{Al}_x\text{Cu}_{5-6}\text{ScZr}_{y=0.3}$ (Table 3). The evolution of such constituents resulted in the formation of PFZs within grains (marked by the yellow arrow in Fig. 4a). The unusual formation of PFZs within grains is a result of the consumption of Cu by the constituents from the Al-matrix. Therefore, it is important to note that the formation of W-phase can be considered as detrimental to mechanical properties as its evolution results in the formation of PFZs within grains. The size of such PFZs depends on the size of the constituent particles; the bigger the particle, the larger the PFZ. Constituent W-phase particles were also observed in several important industrial Al-alloys containing Sc and Cu [17,50,56,57]. It was identified that W-phase forms during a high temperature homogenisation treatment [51,56–58]. There exists a little consensus on the exact amount of Cu and Sc that is required to trigger the formation of W-phase in Al-Cu-Sc alloys [13,14,17,50,56–58]. The structural and chemical information of W-phase was previously identified and studied in Al-Sc-Cu alloys by optical microscopy, X-ray diffraction and electron microprobe analysis techniques [50]. The stoichiometric composition (in at.%) of W-phase, with the tetragonal crystal structure and the space group of $I4/mmm$, was determined to be of $\text{Al}_{5.8}\text{Cu}_{7.4}\text{Sc}$ [50].

Atomic resolution HAADF-STEM image of the W-phase constituent particle along the $[\bar{1}11]_w$ zone axis and the corresponding fast Fourier transform analysis are presented in Fig. 4(c) and (d), respectively. The unique atomic arrangement in the HAADF-STEM image reveals tetragonal structure, with the projected unit cell represented by dashed yellow lines (Fig. 4c). Aberration corrected HAADF-STEM imaging allowed us to measure the interplanar spacing of W-phase, $d_{110} = 0.647$ nm and $d_{101} = 0.462$ nm. From the experimentally determined d-spacing, lattice parameters of W-phase were calculated to be $a = 0.915$ nm and $b = 0.535$ nm. The calculated lattice parameters differ from those of the values ($a = 0.855 - 0.862$ nm and $c = 0.504 - 0.509$ nm) reported previously for W-phase [50]. The variation in lattice parameters determined herein with that of previously reported could be due to the variation in the composition of W-phase.

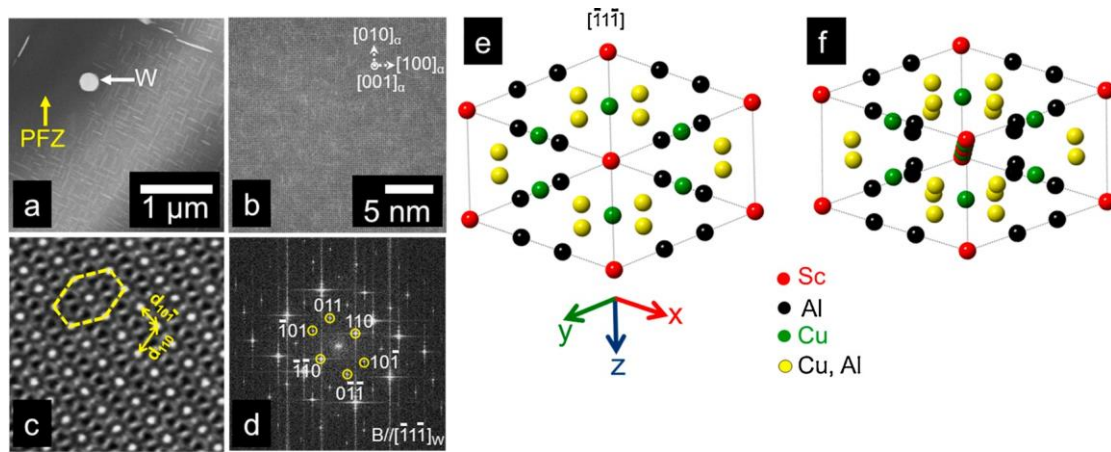


Fig. 4. (a) HAADF-STEM image of the Al-Cu-Sc-Zr alloy. (b) High resolution HAADF-STEM image of the PFZ shown by the yellow arrow in 'a'. (c) Atomic resolution HAADF-STEM imaging of W-phase along the $[111]_W$ direction reveals a unique atomic column arrangement of the tetrahedron structure (space group: $I4/mmm$) with interplanar spacings, $d_{101} = 0.462$ nm and $d_{110} = 0.647$ nm. The projected unit cell of W-phase is shown by yellow dashed lines in 'c'. (d) The diffraction pattern obtained by the Fourier transformation of the STEM image in 'c'. (e) The simulated unit cell of W-phase along the $[111]_W$ direction shows unique arrangement of atoms. (f) The simulated unit cell of W-phase slightly tilted from the $[111]_W$ direction. (For interpretation of the references to colour in this figure legend, the reader is referred to the web version of this article.)

Table 3

TEM-EDXS point analysis (in at.%) of second phase particles and precipitates, and PFZs along high angle grain boundaries (HAGBs) and low angle grain boundaries (LAGBs) in Al-Cu and Al-Cu-Sc-Zr alloys. The composition of constituent second phase particles within grains of both the alloys, and of PFZs that were formed as a result of W-phase within grains of the Al-Cu-Sc-Zr alloy is also presented.

Sample I.D.	Region	Phase	Al	Cu	Fe	Sc	Zr	Ti	
Al-Cu	HAGBs	θ'	78.7	20.7	0.4	0	0.2	0	
		PFZ	99.3	0.4	0.2	0	0.1	0	
	Grains	Al_3Cu_3Fe	73.5	20.0	6.3	0	0.2	0	
Al-Cu-Sc-Zr	HAGBs	θ'	69.9	29.3	0.5	0	0.3	0	
		$Al_3(Sc,Zr)$	95.2	1.4	0.2	1.9	1.3	0	
		$Al_xCu_6ScZr_{y=0.3}$ (W)	54.3	37.6	0.8	5.6	1.7	0	
	PFZ		98.3	0.8	0.2	0.3	0.4	0	
		LAGBs	θ'	89.0	10.6	0.3	0	0.1	0
			$Al_3(Sc,Zr)$	94.6	0.7	0.2	1.8	2.7	0
	PFZ		99.1	0.5	0.2	0	0.2	0	
Grains	$Al_xCu_{2-3}Fe$	90.8	6.3	2.8	0	0.1	0		
	$Al_xCu_{5-6}ScZr_{y=0.3}$ (W)	54.2	36.2	0.8	6.7	2.1	0		
	PFZ	98.8	0.9	0.2	0	0.1	0		

Therefore, the composition and lattice parameters that were experimentally determined herein for W-phase are unique.

To rationalise the chemical ordering in the atomic-resolution HAADF-STEM image in Fig. 4c, a projected unit cell of W-phase along the $[111]_W$ direction was simulated using the CrystalMaker® software and is presented in Fig. 4e. The simulation was performed from the experimentally determined lattice parameters from the present study, and the structural data of W-phase with stoichiometric composition

Table 4

Structural parameters of W-phase ($Al_{6.5}Cu_{5.5}Sc$) [50].

Atoms	x/a	y/b	z/c	Wyckoff notation
Sc	0	0	0	2a
Cu	0.25	0.25	0.25	8i
Al	0.357	0	0	8j
Cu, Al	0.284	0.5	0	8f

$Al_{6.5}Cu_{5.5}Sc$ provided in Table 4 [50]. The simulated unit cell of W-phase in Fig. 4e matches closely with the projected unit cell as marked by dashed yellow lines in Fig. 4c. For better visualisation, the simulated unit cell was slightly tilted off the $[111]_W$ zone axis (Fig. 4f). The red, black and green spheres represent Sc, Al and Cu atoms, respectively, and yellow spheres correspond to either of Cu and Al atoms (Fig. 4(e-f)). The intensities corresponding to the atomic column position (0,0,0) are strong because of the presence of Sc and Cu atoms (Fig. 4(c and f)). In this study, W-phase was also found to contain a minor amount of Zr, whose exact position in the unit cell could not be determined.

The GB microstructure and microchemistry of Al-Cu and Al-Cu-Sc-Zr alloys are presented in Figs. (5–7) and Table 3.

The Al-Cu alloy contained sub-micrometre to micrometre sized θ' -phase precipitates along its HAGBs (Fig. 5 and Table 3). Whilst, HAGBs in the Al-Cu-Sc-Zr alloy contained sub-micrometre sized θ' -phase precipitates and W-phase ($Al_xCu_6ScZr_{y=0.3}$) constituent particles, and nanometre scale $Al_3(Sc,Zr)$ particles (Fig. 6 and Table 3).

Precipitates of θ' -phase along HAGBs were less in number and not closely spaced in the Al-Cu-Sc-Zr alloy when compared to the precipitates along HAGBs in the Al-Cu alloy (Figs. 5 and 6), as a result of the formation of W-phase along HAGBs in the Al-Cu-Sc-Zr alloy. The width of PFZs was higher adjacent to HAGBs containing W-phase constituent particles when compared to θ' -phase precipitates (Fig. 6). In addition, the PFZ width also varied based on the size of precipitates and constituents along HAGBs; the larger the size of precipitates and constituent particles, the more the width of PFZs.

In contrast to HAGBs, θ' -phase precipitates were finer and closely spaced along LAGBs in the Al-Cu-Sc-Zr alloy (Figs. 6 and 7), resulting in PFZs of smaller width adjacent to LAGBs. In addition, W-phase constituents were not observed along LAGBs in the Al-Cu-Sc-Zr alloy, indicating that the constituents are preferred to nucleate and grow along HAGBs. Microstructure and microchemistry of LAGBs in the Al-Cu alloy were not studied as such GBs were less in number and hence not observed in any of the TEM specimens. However, smaller and closely spaced θ' -phase precipitates can be predicated along LAGBs with PFZs of smaller width when compared to HAGBs of the Al-Cu alloy. Such detailed characterisation in understanding the GB microstructure and microchemistry of the alloys studied herein is important in assessing the IGC behaviour, and was not performed before.

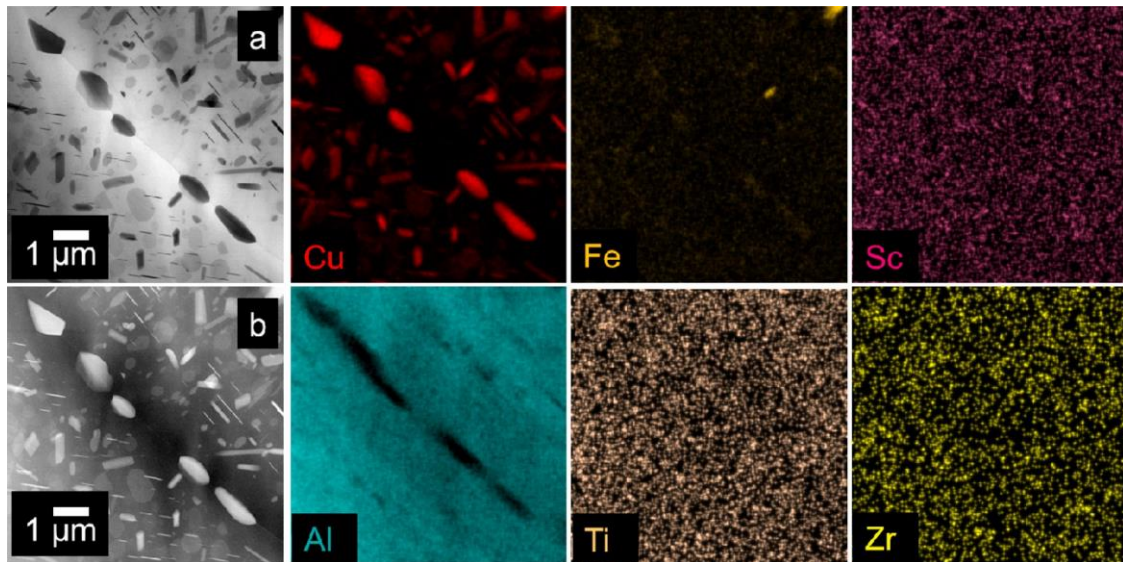


Fig. 5. (a) and (b) are BF-STEM and HAADF-STEM images of a high angle grain boundary in the Al-Cu alloy, respectively. The EDXS maps correspond to the STEM images.

3.4. Corrosion and electrochemical characteristics

3.4.1. Potentiodynamic polarisation assessment

Potentiodynamic polarisation response of Al-Cu and Al-Cu-Sc-Zr alloys in naturally-aerated and deaerated 0.1 M NaCl is shown in Fig. 8, and the results evaluated from the polarisation response are presented in Table 5.

The i_{corr} was determined to be twice more for the Al-Cu alloy than the Al-Cu-Sc-Zr alloy, based on tests in naturally-aerated NaCl, indicating that corrosion resistance is improved with Sc and Zr additions. In addition, E_{corr} and OCP were determined to be similar for both Al-Cu

and Al-Cu-Sc-Zr alloys. The E_{pit} was difficult to discern for both Al-Cu and Al-Cu-Sc-Zr alloys as it was close to their E_{corr} in the naturally-aerated NaCl. Therefore, 0.1 M NaCl was deaerated to shift the E_{corr} less noble than the E_{pit} by retarding or eliminating the oxygen reduction reaction (reaction 1). In such deaerated NaCl, water reduction (reaction 2) becomes a prominent cathodic reaction upon Al alloys. The anodic reaction corresponding to the dissolution of Al from Al alloys is represented by reaction 3.

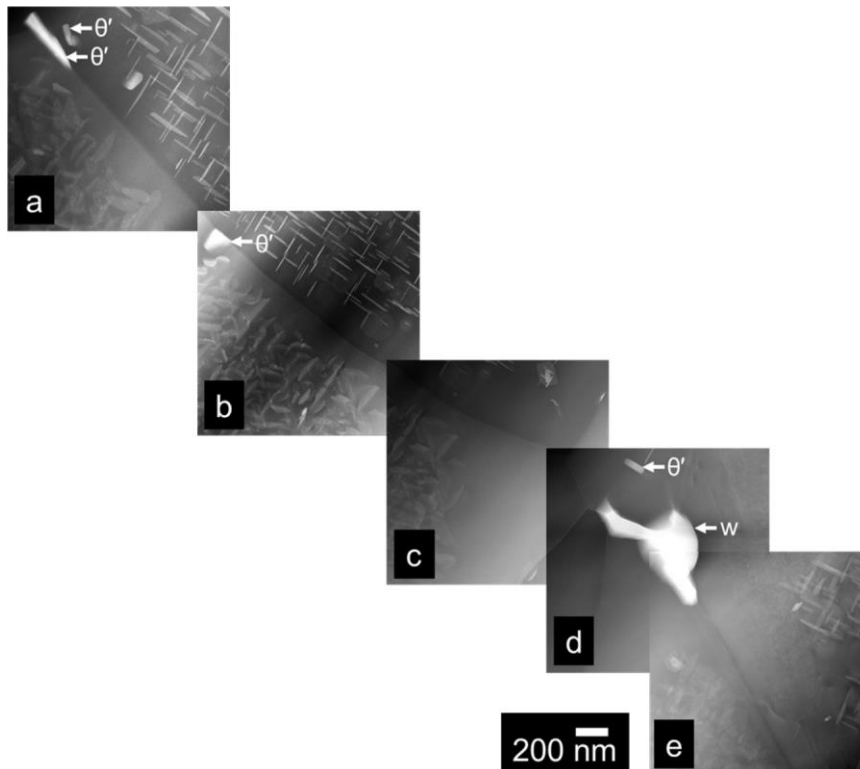


Fig. 6. (a–e) Montage of HAADF-STEM images of high angle grain boundaries in the Al-Cu-Sc-Zr alloy.

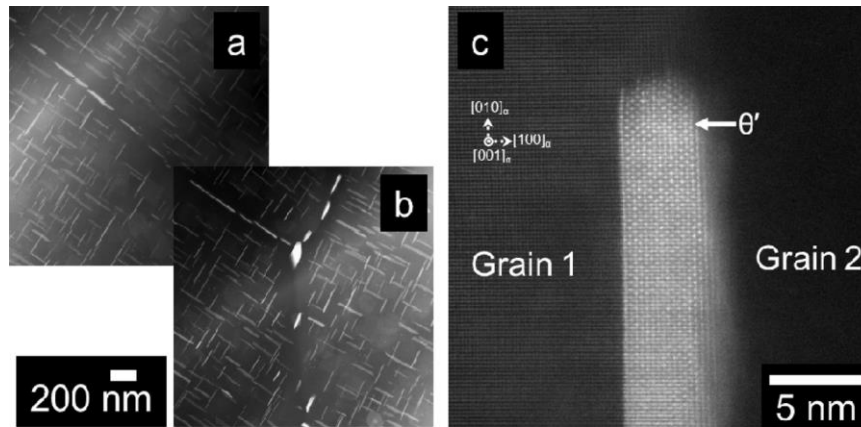


Fig. 7. (a–b) Montage of HAADF-STEM images of low angle grain boundaries in the Al-Cu-Sc-Zr alloy. Atomic resolution HAADF-STEM image of one of the precipitates in ‘a’ is shown in ‘c’.

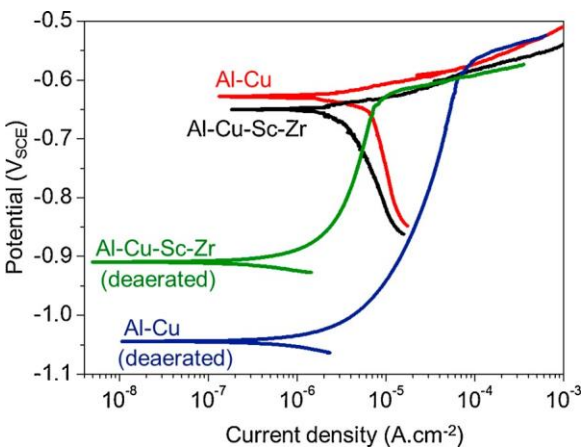
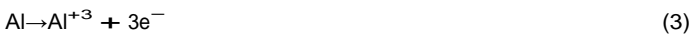


Fig. 8. Potentiodynamic polarisation response of Al-Cu and Al-Cu-Sc-Zr alloys in naturally-aerated and deaerated 0.1 M NaCl.



The E_{pit} was determined to be ≈ 50 mV less noble for the Al-Cu-Sc-Zr

alloy than the Al-Cu alloy, indicating that pitting resistance decreases with Sc and Zr additions. However, the passive current density was determined to be lower for the Al-Cu-Sc-Zr alloy than the Al-Cu alloy in deaerated conditions, indicating that the passive film developed upon the Al-Cu-Sc-Zr alloy is more protective than that of the Al-Cu alloy.

Microstructure and microchemistry of Al-Cu and Al-Cu-Sc-Zr alloys influenced the potentiodynamic polarisation response. The decrease in the grain size and thereby increasing the GB length would decrease the i_{corr} , as GBs aid in rapid formation of a protective oxide layer upon metals and alloys that exhibit corrosion rates lower than $10 \mu\text{A}/\text{cm}^2$ [32]. Therefore, the decrease in the i_{corr} of the Al-Cu-Sc-Zr alloy compared to the Al-Cu alloy is a result of the decrease in grain size and increase in the length of GBs. Such influence of grain and GB parameters on the i_{corr} was determined to be associated with the variation in anodic reaction kinetics [32,33]. In addition, the texture, i.e. crystallographic orientation of grains generated by processing techniques, and

Table 5:

Corrosion current density (i_{corr}), corrosion potential (E_{corr}), open circuit potential (OCP) and pitting potential (E_{pit}) of Al-Cu and Al-Cu-Sc-Zr alloys in 0.1 M NaCl.

Sample I.D	i_{corr} ($\times 10^{-6}$ A. cm^{-2})	E_{corr} (V _{SCE})	OCP (V _{SCE})	E_{pit} (V _{SCE}) [*]
Al-Cu	6.78 ± 0.44	-0.624 ± 0.004	-0.657 ± 0.002	-0.568 ± 0.005
Al-Cu-Sc-Zr	3.29 ± 0.63	-0.643 ± 0.007	-0.669 ± 0.003	-0.619 ± 0.009

* measured in the deaerated condition.

residual stress and strain were also known to influence the i_{corr} [32–36]. However, a definitive understanding on the role of such microstructural parameters on the i_{corr} is complicated, as it is difficult to decouple the variation in one with another. Such microstructural parameters play a primary role in influencing the corrosion of pure metals. In alloys, in addition to such microstructural parameters, second phase particles and composition that are dictated by alloying additions and thermal treatments also influence the corrosion behaviour.

The role of Sc on the potentiodynamic polarisation response of high purity Al was previously studied [42]; E_{corr} and E_{pit} were ennobled and the i_{corr} was decreased with the addition of Sc, indicating an improvement in the corrosion behaviour of Al with the addition of Sc. The improvement in the corrosion behaviour was attributed to the formation of protective Sc-containing oxide layer [42]. It was later speculated the formation of Sc(OH)₃ layer that might be the reason for the improvement in corrosion behaviour of a (Sc, Zr)-containing 7xxx alloy that was free of second phase particles [47]. Such a speculation was made as Sc did not improve the corrosion behaviour of the alloy containing second phase particles and Sc(OH)₃ was considered to be less soluble than Sc₂O₃ in water [47]. In the Al-Cu system, Sc addition ennobled the E_{pit} [48], contradicting the present study (Fig. 8 and Table 5). This discrepancy could be due to the variation of alloy com-

position, processing, ageing and microstructure. In addition, the E_{pit} is a qualitative parameter and does not give information on the number and size of pits, and hence the extent of damage caused by pitting. Therefore, quantification of pitting, following a period of immersion in NaCl is essential to access the pitting of Al-Cu and Al-Cu-Sc-Zr alloys.

3.4.2. Immersion test and optical profilometry studies

The evolution of pits upon Al-Cu and Al-Cu-Sc-Zr alloys following 7 days immersion in 0.1 M NaCl was studied using optical profilometry and is shown in Fig. 9.

It is evident that there were only sub-micrometre scale features and grinding scratches, following preparation up to 1 μm surface finish, upon pristine surfaces of Al-Cu and Al-Cu-Sc-Zr alloys (Fig. 9a and b). Following 7 days immersion in 0.1 M NaCl, pits developed upon both the Al-Cu and Al-Cu-Sc-Zr alloys (Fig. 9c and d). Statistics on pits upon Al-Cu and Al-Cu-Sc-Zr alloys over an area of $\approx 4.62 \text{ mm}^2$ are presented

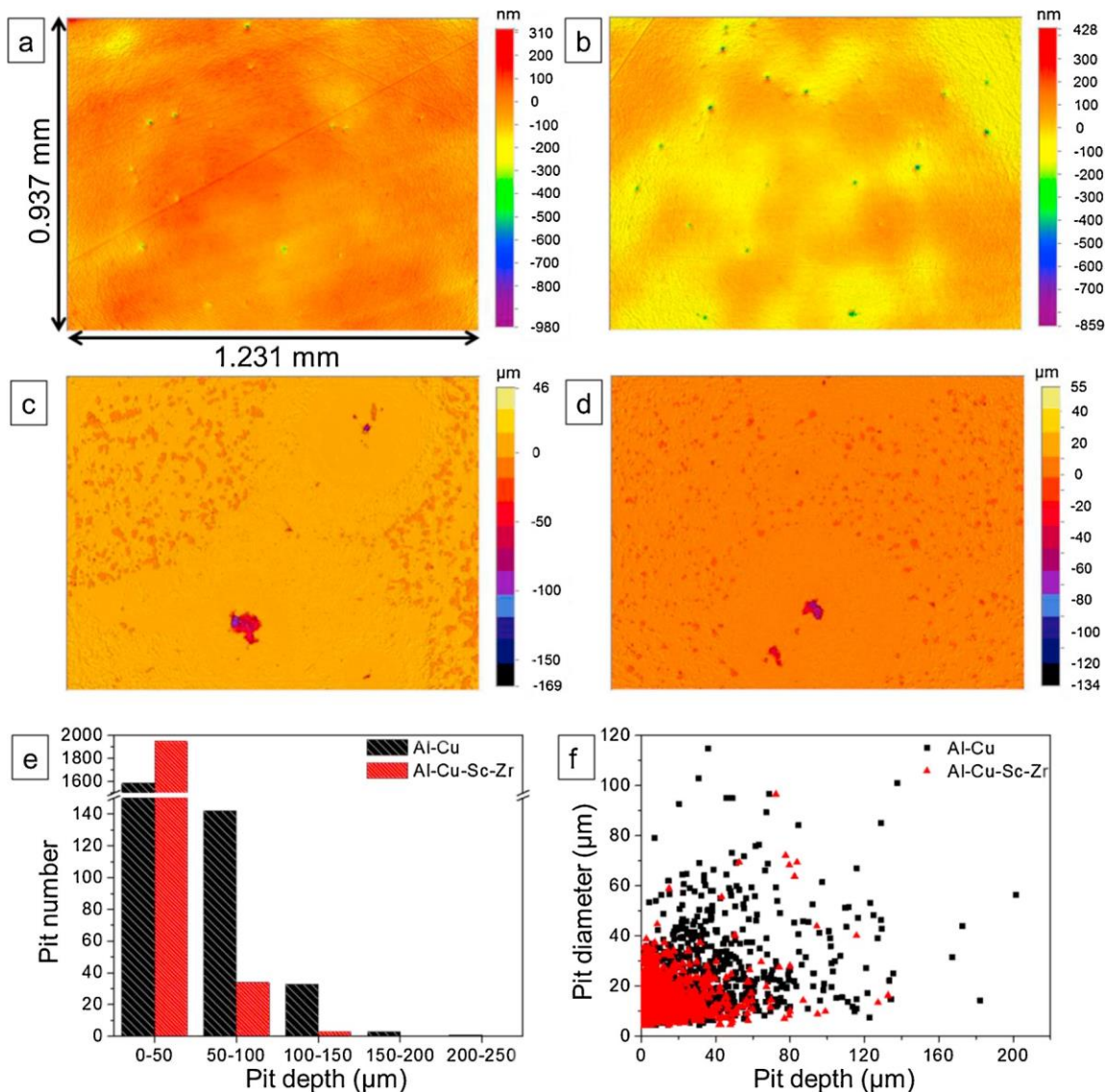


Fig. 9. (a and c) and (b and d) are representative vertical scanning interferometry – optical profilometry images of Al-Cu and Al-Cu-Sc-Zr, respectively. Images (a and b) and (c and d) were taken prior to and following 7 days immersion of both alloys in 0.1 M NaCl, respectively. Statistical analysis of pits that evolved over an area of $\approx 4.62 \text{ mm}^2$ (four different regions) following 7 days immersion are presented in e and f.

in Fig. 9e and f. The average total number of pits developed upon the Al-Cu-Sc-Zr alloy (431 mm^{-2}) is higher than the Al-Cu alloy (389 mm^{-2}). However, the extent of damage caused by pits does not solely depend on the number of pits but also on their diameter and depth. From Fig. 9(e and f), pits with depths up to $\approx 200 \text{ }\mu\text{m}$ and $\approx 132 \text{ }\mu\text{m}$ were observed upon Al-Cu and Al-Cu-Sc-Zr alloys following 7 days immersion, respectively. In addition, more pits with depths greater than $1 \text{ }\mu\text{m}$ were observed upon the Al-Cu alloy than the Al-Cu-Sc-Zr alloy. Furthermore, pits with higher diameter were observed upon the Al-Cu alloy than the Al-Cu-Sc-Zr alloy. Based on the statistics on pit number, size and depth of Al-Cu and Al-Cu-Sc-Zr alloys, it can be concluded that the extent of damage caused by pitting is more for the Al-Cu alloy than the Al-Cu-Sc-Zr alloy. Therefore, the refinement in size of the particles and precipitates in the Al-matrix, albeit their increase in number density and evolution of W-phase and $\text{Al}_3(\text{Sc,Zr})$ phase, improved the extent of damage caused by pitting with Sc and Zr additions. The difference in solid solution composition and variation in the texture of Al-Cu and Al-Cu-Sc-Zr alloys would also have influenced the dissolution kinetics of the Al-matrix.

3.4.3. Investigation of pitting origin

To identify the origin of pitting, Al-Cu and Al-Cu-Sc-Zr alloy specimens, which were metallographically prepared to a $0.01 \text{ }\mu\text{m}$ surface finish in colloidal silica suspension, were immersed in 0.1 M NaCl for 10 h and subsequently examined using SEM (Fig. 10).

Pits originated in the Al-matrix and developed in the form of trenches at the periphery of all second phase particles, in both Al-Cu and Al-Cu-Sc-Zr alloys, indicating that Al_2Cu , $\text{Al}_x\text{Fe}_{3-4}\text{Cu}$ and W-phase ($\text{Al}_x\text{Cu}_{5-8}\text{ScZr}_y$) particles are cathodic, more noble, to the Al-matrix. The electrochemical characteristics of Al_2Cu and (Fe- and Cu)-containing particles, and in the context of localised corrosion of Al-alloys, was previously studied [22–24]. It was determined that Al_2Cu and (Fe- and Cu)-containing particles were cathodic to the Al-matrix, resulting in the dissolution of Al-matrix at their periphery [22–24]. During dissolution of the Al-matrix, the oxygen reduction reaction upon Fe-containing and Cu-containing particles was determined to be strong enough to increase the pH locally, exacerbating the dissolution of the Al-matrix at their periphery [22–24]. Herein, it is for the first time that we report that W-phase is cathodic, more noble, to the Al-matrix.

Pitting can also initiate by dissolving the Al-matrix at the periphery

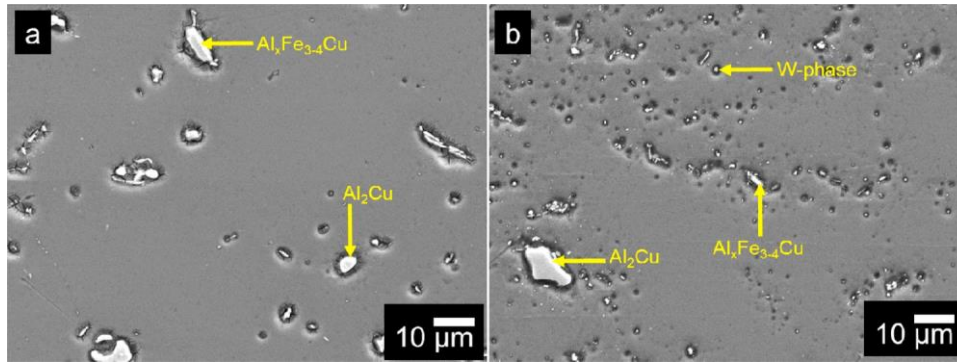


Fig. 10. Secondary electron - SEM images of (a) Al-Cu and (b) Al-Cu-Sc-Zr alloys following 10 h exposure to 0.1 M NaCl.

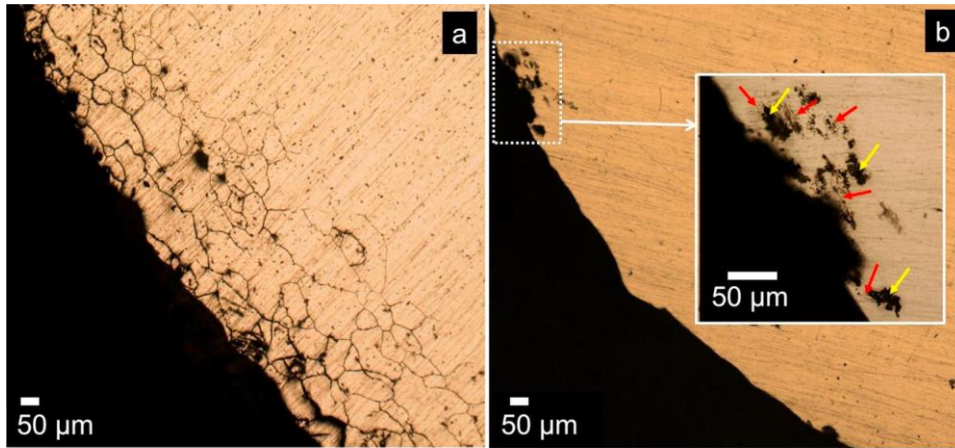
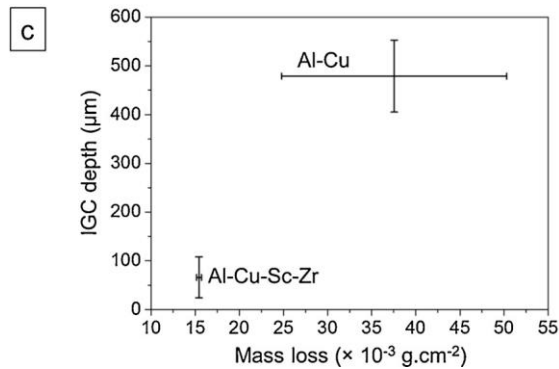


Fig. 11. Optical micrographs showing cross-sectional surfaces of (a) Al-Cu and (b) Al-Cu-Sc-Zr alloys, following ASTM G110 immersion test for 27 h. The inset in image 'b' is the high magnification image of the region within the dotted rectangular box. Red and yellow arrows in the inset in 'b' point to IGC and pitting, respectively. Image 'c' shows IGC depth vs. mass loss for both the alloys, following the test. (For interpretation of the references to colour in this figure legend, the reader is referred to the web version of this article.)



of sub-micrometre scale θ' -phase precipitates in the Al-Cu alloy. In the case of Al-Cu-Sc-Zr alloy, most of θ' - and θ'' -phase precipitates did not contribute to discernible pitting, as their thickness was fine and below the critical thickness to initiate pitting in Al-alloys [37–41]. In addition, nanoscale $\text{Al}_3(\text{Sc,Zr})$ are known to be electrochemically inactive and not associated with pitting, as they become spontaneously passive when anodically polarized and also do not support the oxygen reduction reaction at appreciable rates when cathodically polarized [46,47].

3.4.4. Intergranular corrosion assessment

Optical micrographs of cross-sectional surfaces of Al-Cu and Al-Cu-Sc-Zr alloys exhibiting IGC and IGC + pitting, respectively, following ASTM G110 immersion test for 27 h are shown in Fig. 11a and b. The IGC depth vs. mass loss of the alloys following the test is presented in Fig. 11c. The mode of corrosion in the Al-Cu alloy was IGC, whilst that in the Al-Cu-Sc-Zr alloy was IGC + pitting. It is also noted that the IGC attack is uniform in the Al-Cu alloy, whilst, IGC + pitting attack was not

uniform in the Al-Cu-Sc-Zr alloy (Fig. 11 a–b). The average depth of IGC for the Al-Cu alloy and IGC + pitting for the Al-Cu-Sc-Zr alloy was $478.94 \pm 73.71 \mu\text{m}$ and $66.29 \pm 42.13 \mu\text{m}$, respectively. In addition, the average mass loss of Al-Cu and Al-Cu-Sc-Zr alloys was $37.55 \pm 12.75 \text{ mg.cm}^{-2}$ and $15.43 \pm 0.28 \text{ mg.cm}^{-2}$, respectively. Therefore, the extent of damage caused by IGC was more for the Al-Cu alloy than combined IGC + pitting in the Al-Cu-Sc-Zr alloy. The variation in the mode and extent of corrosion with Sc and Zr additions is a result of the variation in GB type and length, in addition to the formation of different phases along GBs and within grains. Based on the reported electrochemical characteristics of Al_2Cu , (Fe- and Cu)-containing particles and $\text{Al}_3(\text{Sc,Zr})$ in Al-alloys [22–24,46,47], and of W-phase from the present study, the phenomenology of IGC in the Al-Cu alloy and IGC + pitting in the Al-Cu-Sc-Zr alloy may be deduced from the electron microscopy results. In the Al-Cu alloy, IGC was associated with the dissolution of PFZs adjacent to noble θ' -phase precipitates along GBs. Whilst in the Al-Cu-Sc-Zr alloy, IGC was associated with the dissolution of PFZs along GBs containing noble θ' -phase

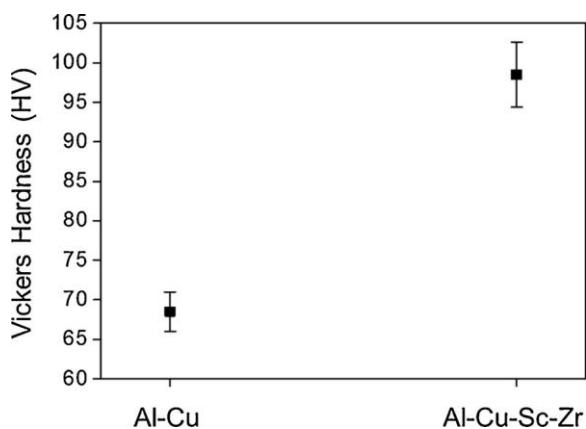


Fig. 12. Vickers hardness of Al-Cu and Al-Cu-Sc-Zr alloys with an applied load of 1 kg.

precipitates and W-phase particles, and pitting was associated with the dissolution of PFZs at the periphery of noble W-phase particles formed within grains. In the Al-Cu-Sc-Zr alloy, $\text{Al}_3(\text{Sc,Zr})$ particles were considered to be electrochemically compatible with the Al-matrix [46,47], and hence with the PFZ, and do not contribute to IGC. In addition, constituent $\text{Al}_x\text{Cu}_3\text{Fe}$ particles were not observed along any of the GBs in Al-Cu and Al-Cu-Sc-Zr alloys, as the particles are not influenced by thermal treatments and form significantly less in number when compared to precipitates. Therefore, the role of Fe-containing particles in the propagation of IGC is negligible, though their rare encounter along GBs aid in the dissolution of the PFZ. The depth of attack was lesser for the Al-Cu-Sc-Zr alloy than the Al-Cu alloy as a result of the formation of smaller grains and increase in the length of GBs, making the IGC path circuitous.

3.5. Hardness evaluation

Vickers hardness values as determined for Al-Cu and Al-Cu-Sc-Zr alloys are presented in Fig. 12.

The hardness values of Al-Cu and Al-Cu-Sc-Zr alloys are 68.5 ± 2.5 and 98.5 ± 4.4 , respectively. In a different study, the tensile strength of the Al-Cu-Sc-Zr alloy was determined to be higher than the Al-Cu alloy [7]. The significant increase in mechanical properties of the Al-Cu-Sc-Zr alloy when compared to the Al-Cu alloy is a result of microstructural variation, such as an increase in the number density and a decrease in size of θ' -phase precipitates, presence of nanometre scale core-shell $\text{Al}_3(\text{Sc,Zr})$ particles, a decrease in grain size and presence of deformed grain structure with Sc and Zr additions.

All the above findings indicate that Sc and Zr additions can significantly improve the corrosion behaviour and strength, via modifying the microstructure, of 2xxx series Al-Cu alloys, despite the formation of W-phase. Further increase in the properties can be achieved by inhibiting W-phase formation. The probable methods that can aid in inhibiting the formation of W-phase are by decreasing the Cu content in the alloy, adding minor solute elements that can consume extra Cu and designing specific processes and thermal treatments.

4. Conclusions

Herein, the microstructural variation caused by Sc and Zr additions to a model 2xxx series Al-Cu alloy aged at 190 °C for 18 h was explicitly studied in the context of corrosion and hardness. The following conclusions can be drawn:

- 1 The addition of Sc and Zr to the Al-Cu alloy led to significant microstructural variation by inhibiting the recrystallization, retaining deformed grains and extrusion texture, refining grains and thereby

varying grain boundary (GB) type and length. Second phase particles and precipitates decreased in size and increased in number with Sc and Zr additions to the Al-Cu alloy. Core-shell $\text{Al}_3(\text{Sc,Zr})$ particles nucleated Guinier-Preston zones, which were transformed to θ'' - and θ' -phase precipitates. Constituent W-phase ($\text{Al}_x\text{Cu}_{5-6}\text{ScZr}_{y=0.3}$) was also observed within grains and along high angle GBs of the Al-Cu-Sc-Zr alloy.

- 2 The corrosion current density decreased by ≈ 2 -fold, the pitting potential demeaned by ≈ 50 mV and the passive current density decreased with Sc and Zr additions to the Al-Cu alloy. Such variation in the electrochemical response was attributed to the microstructural variation caused by Sc and Zr additions to the Al-Cu alloy. However, no significant variation in corrosion and open circuit potentials was observed with Sc and Zr additions to the Al-Cu alloy.
- 3 The extent of damage caused by pitting decreased with Sc and Zr additions to the Al-Cu alloy. Pits were developed in the form of trenches upon Al-Cu and Al-Cu-Sc-Zr alloys, dissolving the Al-matrix at the periphery of Al_2Cu , $\text{Al}_x\text{Fe}_{3-4}\text{Cu}$ and W-phase ($\text{Al}_x\text{Cu}_{5-6}\text{ScZr}_y$) particles.
- 4 The addition of Sc and Zr to the Al-Cu alloy led to the transformation of the corrosion mode from intergranular corrosion (IGC) to IGC + pitting. Such a transformation was attributed to the dissolution of anodic precipitate free zones adjacent to cathodic W-phase particles that were formed within grains and along high angle GBs of the Al-Cu-Sc-Zr alloy. However, the amount of mass loss and the depth of attack decreased with Sc and Zr additions to the Al-Cu alloy.
- 5 The increase in hardness with Sc and Zr additions to the Al-Cu alloy was attributed to the refinement in size and increase in number density of nanoscale θ'' - and θ' -phase precipitates, and the presence of nanoscale $\text{Al}_3(\text{Sc,Zr})$ particles. The decrease in grain size and presence of deformed grain microstructure also contributed to the increase in hardness.

Data availability

The raw/processed data required to reproduce these findings cannot be shared at this time as the data also forms part of an ongoing study.

Acknowledgements

The authors would like to thank the Australian Research Council for funding this study (LP160100104). The Monash Centre for Electron Microscopy (MCEM) is gratefully acknowledged.

References

- [1] E.A. Starke, J.T. Staley, Application of modern aluminium alloys to aircraft, *Prog. Aerospace Sci.* 32 (1996) 131–172.
- [2] J.C. Williams, E.A. Starke, Progress in structural materials for aerospace systems, *Acta Mater.* 51 (2003) 5775–5799.
- [3] I.J. Polmear, D. St John, J. Nie, M. Qian, Light Alloys From Traditional Alloys to Nanocrystals, fifth ed., Elsevier, Oxford, 2017.
- [4] J.F. Nie, Physical metallurgy in light alloys, in: D.E. Laughlin, K. Hono (Eds.), *Physical Metallurgy*, Elsevier, Amsterdam, 2014, pp. 2009–2156.
- [5] P.S. Rao, K.G. Sivasadan, P.K. Balasubramanian, Structure-property correlation of AA 2219 aluminium alloy weldments, *Bull. Mater. Sci.* 19 (1996) 549–557.
- [6] A. Biswas, D.J. Siegel, C. Wolverton, D.V. Seidman, Precipitates in Al-Cu alloys revisited: atom-probe tomographic experiments and first-principles calculations of compositional evolution and interfacial segregation, *Acta Mater.* 59 (2011) 6187–6204.
- [7] T. Dorin, M. Ramajayam, J. Lamb, T. Langan, Effect of Sc and Zr additions on the microstructure/strength of Al-Cu binary alloys, *Mater. Sci. Eng. A* 707 (2017) 58–64.
- [8] T. Dorin, M. Ramajayam, K. Mester, B. Rouxel, J. Lamb, T.J. Langan, The effect of scandium and zirconium on the microstructure, mechanical properties and formability of a model Al-Cu alloy, in: O. Martin (Ed.), *Light Metals and TMS 2018, The Minerals, Metals and Materials Series*, Springer, 2018, pp. 1595–1599.
- [9] T. Dorin, A. Vahid, M. Ramajayam, T. Langan, Aluminium scandium alloys, in: R.N. Lumley (Ed.), *Fundamentals of Aluminium Metallurgy: Recent Advances*, Elsevier, Cambridge, 2018, pp. 439–494.

- [10] A. Tolley, V. Radmilovic, U. Dahmen, Segregation in $Al_3(Sc,Zr)$ precipitates in Al-Sc-Zr alloys, *Scripta Mater.* 52 (2005) 621–625.
- [11] K.E. Knippling, R.A. Karnesky, C.P. Lee, D.C. Dunand, D.N. Seidman, Precipitation evolution in Al-0.1Sc, Al-0.1Zr and Al-0.1Sc-0.1Zr (at%) alloys during isochronal aging, *Acta Mater.* 58 (2010) 5184–5195.
- [12] M. Suresh, A. Sharma, A.M. More, N. Nayan, S. Suwas, Effect of scandium addition on evolution of microstructure, texture and mechanical properties of thermo-mechanically processed Al-Li alloy AA2195, *J. Alloys. Compd.* 740 (2018) 364–374.
- [13] J. Royset, N. Ryum, Scandium in aluminium alloys, *Int. Mater. Rev.* 50 (2005) 19–44.
- [14] A.F. Norman, P.B. Prangnell, R.S. McEwen, The solidification behaviour of dilute aluminium-scandium alloys, *Acta Mater.* 46 (1998) 5715–5732.
- [15] S. Mondal, S. Kashyap, S. Kumar, K. Chattopadhyay, Improvement of high temperature strength of 2219 alloy by Sc and Zr addition through a novel three-stage heat treatment route, *Mater. Sci. Eng. A* 732 (2018) 157–166.
- [16] Y.H. Gao, C. Yang, J.Y. Zhang, L.F. Cao, G. Liu, J. Sun, E. Ma, Stabilizing nano-precipitates in Al-Cu alloys for creep resistance at 300°C, *Mater. Res. Lett.* 7 (2018) 18–25.
- [17] A.F. Norman, K. Hyde, F. Costello, S. Thompson, S. Birley, P.B. Prangnell, Examination of the effect of Sc on 2000 and 7000 series aluminium alloy castings: for improvements in fusion welding, *Mater. Sci. Eng. A* 354 (2003) 188–198.
- [18] J. Kang, Z. Feng, G.S. Frankel, J. Li, G. Zou, A. Wu, Effect of precipitate evolution on the pitting corrosion of friction stir welded joints of an Al-Cu alloy, *Corrosion* 72 (2016) 719–731.
- [19] J.R. Galvele, S.M.D. Micheli, Mechanism of intergranular corrosion of Al-Cu alloys, *Corros. Sci.* 10 (1970) 795–807.
- [20] I.L. Muller, J.R. Galvele, Pitting potential of high purity binary aluminium alloys-I. Al-Cu alloys. Pitting and Intergranular corrosion, *Corros. Sci.* 17 (1977) 179–193.
- [21] J.R. Davis, *Corrosion of Aluminium and Aluminium Alloys*, 1st ed., ASM International, Materials Park, 1999.
- [22] J.R. Scully, T.O. Knight, R.G. Buchheit, D.E. Peebles, Electrochemical characteristics of the Al_2Cu , Al_3Ta and Al_3Zr intermetallic phases and their relevancy to the localised corrosion of Al alloys, *Corros. Sci.* 35 (1993) 185–195.
- [23] N. Birbilis, R.G. Buchheit, Electrochemical characteristics of intermetallic phases in aluminium alloys, *J. Electrochem. Soc.* 152 (2005) B140–B151.
- [24] N. Birbilis, M.K. Cavanaugh, R.G. Buchheit, Electrochemical behaviour and localised corrosion associated with $AlCu_2Fe$ particles in aluminium alloy 7075-T651, *Corros. Sci.* 48 (2006) 4202–4215.
- [25] Y. Back, G.S. Frankel, Electrochemical quartz crystal microbalance study of corrosion of phases in AA2024, *J. Electrochem. Soc.* 150 (2003) B1–B9.
- [26] S.K. Kairy, T. Alam, P.A. Rometsch, C.H.J. Davies, R. Banerjee, N. Birbilis, Understanding the origins of intergranular corrosion in copper-containing Al-Mg-Si alloys, *Metall. Mater. Trans. A* 47 (2016) 985–989.
- [27] S.K. Kairy, P.A. Rometsch, C.H.J. Davies, N. Birbilis, On the intergranular corrosion and hardness evolution of 6xxx series Al-alloys as a function of Si:Mg ratio, Cu content and ageing condition, *Corrosion* 73 (2017) 1280–1295.
- [28] S.K. Kairy, S. Turk, N. Birbilis, A. Shekhter, The role of microstructure and microchemistry on intergranular corrosion of aluminium alloy AA7085-T7452, *Corros. Sci.* 143 (2018) 414–427.
- [29] R. Zhang, R.K. Gupta, C.H.J. Davies, A.M. Hodge, M. Tort, K. Xia, N. Birbilis, The influence of grain size and grain orientation on sensitization in AA5083, *Corrosion* 72 (2016) 160–168.
- [30] W. Zhang, S. Ruan, D.A. Wolfe, G.S. Frankel, Statistical model for intergranular corrosion growth kinetics, *Corros. Sci.* 45 (2003) 353–370.
- [31] S. Ruan, D.A. Wolfe, G.S. Frankel, Statistical modelling and computer simulation of intergranular corrosion growth in AA2024-T3 aluminium alloy, *J. Stat. Plan. Infer.* 126 (2004) 553–568.
- [32] K.D. Ralston, N. Birbilis, Effect of grain size on corrosion: a Review, *Corrosion* 66 (2010) 075005-075005-13.
- [33] K.D. Ralston, N. Birbilis, C.H.J. Davies, Revealing the relationship between grain size and corrosion rate of metals, *Scripta Mater.* 63 (2010) 1201–1204.
- [34] K.D. Ralston, D. Fabijanic, N. Birbilis, Effect of grain size on corrosion of high purity aluminium, *Electrochim. Acta* 56 (2011) 1729–1736.
- [35] K.D. Ralston, J.G. Brunner, S. Virtanen, N. Birbilis, Effect of processing on grain size and corrosion of AA2024-T3, *Corrosion* 67 (2011) 105001-105001-10.
- [36] J.G. Brunner, N. Birbilis, K.D. Ralston, S. Virtanen, Impact of ultrafine-grained microstructure on the corrosion of aluminium alloy AA2024, *Corros. Sci.* 57 (2012) 209–214.
- [37] S.K. Kairy, P.A. Rometsch, K. Diao, J.F. Nie, C.H.J. Davies, N. Birbilis, Exploring the electrochemistry of 6xxx series aluminium alloys as a function of Si to Mg ratio, Cu content, ageing conditions and microstructure, *Electrochim. Acta* 190 (2016) 92–103.
- [38] K.D. Ralston, N. Birbilis, M.K. Cavanaugh, M. Weyland, B.C. Muddle, R.K.W. Marceau, Role of nanostructure in pitting of Al-Cu-Mg alloys, *Electrochim. Acta* 55 (2010) 7834.
- [39] K.D. Ralston, N. Birbilis, M. Weyland, C.R. Hutchinson, The effect of precipitate size on the yield strength-pitting corrosion correlation in Al-Cu-Mg alloys, *Acta Mater.* 58 (2010) 5941.
- [40] R.K. Gupta, N.L. Sukiman, M.K. Cavanaugh, B.R.W. Hinton, C.R. Hutchinson, N. Birbilis, Metastable pitting characteristics of aluminium alloys measured using current transients during potentiostatic polarisation, *Electrochim. Acta* 66 (2012) 245.
- [41] R.K. Gupta, A. Deschamps, M.K. Cavanaugh, S.P. Lynch, N. Birbilis, Relating the early evolution of microstructure with the electrochemical response and mechanical performance of a Cu-rich and Cu-lean 7xxx aluminium alloy, *J. Electrochem. Soc.* 159 (2012) C492.
- [42] I.N. Ganiev, Corrosion-Electrochemical behaviour of special-purity aluminium and its AK1 alloy alloyed with scandium, *Russ. J. Appl. Chem.* 77 (2004) 925–929.
- [43] Y. Shi, Q. Pan, M. Li, X. Huang, B. Li, Effect of Sc and Zr additions on corrosion behaviour of Al-Zn-Mg-Cu alloys, *J. Alloys. Compd.* 612 (2014) 42–50.
- [44] Y. Deng, R. ye, G. Xu, J. Yang, Q. Pan, B. Peng, X. Cao, Y. Duan, Y. Wang, L. Lu, Z. Yin, Corrosion behaviour and mechanism of new aerospace Al-Zn-Mg alloy friction stir welded joints and the effects of secondary Al_3ScZr_{1-x} nanoparticles, *Corros. Sci.* 90 (2015) 359–374.
- [45] Y. Deng, Z. Yin, K. Zhao, J. Duan, J. Hu, Z. He, Effects of sc and Zr microalloying additions and ageing time at 120°C on the corrosion behaviour of an Al-Zn-Mg alloy, *Corros. Sci.* 65 (2012) 288–298.
- [46] M.K. Cavanaugh, N. Birbilis, R.G. Buchheit, F. Bovard, Investigating localised corrosion susceptibility arising from Sc containing intermetallic Al_3Sc in high strength Al-alloys, *Scripta Mater.* 56 (2007) 995–998.
- [47] J. Wloka, S. Virtanen, Influence of scandium on the pitting behaviour of Al-Zn-Mg-Cu alloys, *Acta Mater.* 55 (2007) 6666–6672.
- [48] S.H. Wu, P. Zhang, D. Shao, P.M. Cheng, J. Kuang, K. Wu, J.Y. Zhang, G. Liu, J. Sun, Grain size-dependent Sc microalloying effect on the yield strength-pitting corrosion correlation in Al-Cu alloys, *Mater. Sci. Eng. A* 721 (2018) 200–214.
- [49] Standard Practice for Evaluating Intergranular Corrosion Resistance of Heat Treatable Aluminium Alloys by Immersion in Sodium Chloride + Hydrogen Peroxide Solution, ASTM international, West Conshohocken, PA, 2009 ASTM G 110:2009.
- [50] L.S. Toropova, D.G. Eskin, M.L. Kharakterova, T.V. Dobatkina, *Advanced Aluminium Alloys Containing Scandium*, Taylor and Francis Publishers, Oxford, 1998.
- [51] Y.H. Gao, J. Kuang, G. Liy, J. Sun, Effect of minor Sc and Fe co-addition on the microstructure and mechanical properties of Al-Cu alloys during homogenisation treatment, *Mater. Sci. Eng. A* 746 (2019) 11–26.
- [52] B.A. Chen, L. Pan, R.H. Wang, G. Liu, P.M. Cheng, L. Xiao, J. Sun, Effect of solution treatment on precipitation behaviours and age hardening response of Al-Cu alloys with Sc addition, *Mater. Sci. Eng. A* 530 (2011) 607–617.
- [53] Y. Harada, D.C. Dunand, Microstructure of Al_3Sc with ternary transition-metal additions, *Mater. Sci. Eng. A* 329-331 (2002) 686–695.
- [54] C.B. Fuller, J.L. Murray, D.N. Seidman, Temporal evolution of the nanostructure of Al(Sc,Zr) alloys: part I-Chemical compositions of $Al_3(Sc_{1-x}Zr_x)$ precipitates, *Acta Mater.* 53 (2005) 5401–5413.
- [55] C.B. Fuller, D.N. Seidman, Temporal evolution of the nanostructure of Al(Sc,Zr) alloys: part II-Coarsening of $Al_3(Sc_{1-x}Zr_x)$ precipitates, *Acta Mater.* 53 (2005) 5415–5428.
- [56] M. Jia, Z. Zheng, Z. Gong, Microstructure evolution of the 1469 Al-Cu-Li-Sc alloy during homogenization, *J. Alloys. Compd.* 614 (2014) 131–139.
- [57] B. Jiang, D. Yi, X. Yi, F. Zheng, H. Wang, B. Wang, H. Liu, Z. Hu, Effect of trace amounts of added Sc on microstructure and mechanical properties of 2055 aluminium alloy, *Mater. Charact.* 141 (2018) 248–259.
- [58] M. Gazizov, V. Teleshov, V. Zakharov, R. Kaibyshev, Solidification behaviour and the effects of homogenisation on the structure of an Al-Cu-Mg-Ag-Sc alloy, *J. Alloys. Compd.* 509 (2011) 9497–9507.